

Waveform Diversity and Range-Coupled Adaptive Radar Signal Processing

by

Thomas Higgins

Submitted to the graduate degree program in Electrical Engineering & Computer Science and the Graduate Faculty of the University of Kansas in partial fulfillment of the requirements for the degree of Doctor of Philosophy.

---

Chairperson: Shannon Blunt

---

Christopher Allen

---

Tyrone Duncan

---

David Petr

---

James Stiles

Date defended: December 5, 2011

The Dissertation Committee for Thomas Higgins  
certifies that this is the approved version of the following dissertation:

Waveform Diversity and Range-Coupled Adaptive Radar Signal Processing

---

Chairperson: Shannon Blunt

Date approved: December 05, 2011

## **Abstract**

Waveform diversity may offer several benefits to radar systems though often at the cost of reduced sensitivity. Multi-dimensional processing schemes are known to offer many degrees of freedom, which can be exploited to suppress the ambiguity inherent to pulse compression, array processing, and Doppler frequency estimation.

Spatial waveform diversity can be achieved by transmitting different but correlated waveforms from each element of an antenna array. A simple yet effective scheme is employed to transmit different waveforms in different spatial directions. A new reiterative minimum mean squared error approach entitled Space-Range Adaptive Processing, which adapts simultaneously in range and angle, is derived and shown in simulation to offer enhanced performance when spatial waveform diversity is employed relative to both conventional matched filtering and sequentially adapting in angle and then range. The same mathematical framework is utilized to develop Time-Range Adaptive Processing (TRAP) algorithm which is capable of simultaneously adapting in Doppler frequency and range. TRAP is useful when pulse-to-pulse changing of the center frequency or waveform coding is used to achieve enhanced range resolution or unambiguous ranging, respectively.

The inherent computational complexity of the new multi-dimensional algorithms is addressed by segmenting the full-dimension cost functions, yielding a reduced-dimensional variants of each. Finally, a non-adaptive approach based on the multi-dimensional TRAP signal model is utilized to develop an efficient clutter cancellation technique capable of suppressing multiple range intervals of clutter when waveform diversity is applied to pulse-Doppler radar.

## Acknowledgments

I would like to thank Dr. Blunt for setting me on a course for success beginning with my master's degree and continuing throughout the PhD process. I'm positive that many more students will benefit from his mentorship throughout his career as a professor. Many members of my committee have had an impact on my engineering education. I have asked them to serve on this committee because I expect to be judged with the superior academic standards and fairness they have exhibited in the many experiences I have shared with them throughout the last decade.

The latter portion of this work was conducted while working in the Radar Division at the Naval Research Laboratory, which has provided a phenomenal knowledge base. Many ideas have been discovered in discussions with my colleagues. I would like to thank the following people from the Radar Division: Dr. Aaron Shackelford for his aptitude in identifying research issues and being an understanding supervisor, Dr. Karl Gerlach for his signal processing wisdom, and Dr. Eric Mokole for facilitating my interaction with the research community. I would also like to thank Tegan Webster for her help in editing the final copy of this dissertation.

I am fortunate to have a wonderful family which has supported me throughout this process. My parents and sisters have offered relentless encouragement and support without which I could not have completed this work. Last but not least, I am indebted to my friends that chose to devote the several years I spent in school to a greater cause — defending the United States of America. Thank you Aaron Shuey (US Army), Jason Randall (US Navy), and Adam Minard (US Army).

# TABLE OF CONTENTS

Table of Contents .....	v
Chapter 1 Introduction.....	1
1.1 Pulse Compression.....	2
1.2 Doppler Processing .....	5
1.3 Array Processing.....	7
1.4 Motivation.....	10
1.5 Organization of Document.....	13
1.6 Adaptive Signal Processing Background.....	14
1.6.1 Adaptive Pulse Compression .....	15
1.6.2 Re-Iterative Super Resolution.....	17
Chapter 2 Gain-Constrained Adaptive Pulse Compression and Fast Adaptive Pulse Compression .....	20
2.1 Gain-Constrained APC Cost Function.....	21
2.2 Fast APC Signal Model and Cost Function .....	23
2.3 Gain-Constrained Fast APC.....	24
2.4 Implementation .....	27
2.5 Simulation Results .....	28
2.6 Conclusions.....	32
Chapter 3 Analysis of Range-Angle Coupled Beamforming MIMO Architectures .....	33
3.1 Frequency Diverse Array Chirp Structure .....	34
3.1.1 FDA Beampattern and Ambiguity Analysis .....	38
3.2 Digital Waveform Diverse Array.....	46
3.2.1 DWDA Beampattern and Ambiguity Analysis.....	48
3.3 Conclusions.....	58

Chapter 4	Space-Range Adaptive Processing .....	60
4.1	Space-Range Signal Model .....	61
4.2	Space-Range Adaptive Processing.....	63
4.2.1	Implementation .....	66
4.2.2	Fast Matrix Update .....	67
4.3	Reduced Dimensionality SRAP .....	69
4.3.1	Fast Matrix Update for RD-SRAP .....	72
4.4	Computational Complexity .....	73
4.5	Assessment of Joint Adaptive Processing.....	77
4.5.1	Sequential Angle-Range Adaptive Processing .....	78
4.5.2	Filter Response .....	79
4.5.3	Sequential RISR-APC.....	81
4.5.4	Filter Response Simulation Analysis .....	82
4.6	Simulation Results .....	91
4.6.1	Imaging Scenario .....	91
4.6.2	Surveillance Scenario.....	96
4.6.3	MTI Scenario .....	99
4.7	Conclusions.....	111
Chapter 5	Time-Range Adaptive Processing .....	113
5.1	Time-Range Signal model .....	114
5.2	Time-Range Adaptive Processing.....	116
5.2.1	Implementation .....	118
5.2.2	Fast Matrix Update .....	119
5.3	Reduced Dimensionality TRAP.....	121
5.3.1	Fast Matrix Update for RD-TRAP.....	125
5.4	Eclipsing Repair.....	126
5.5	Sequential APC and RISR .....	130
5.6	Simulation Results .....	132

5.7	Conclusions.....	144
Chapter 6	Non-Identical Multiple Pulse Compression and Clutter Cancellation.....	145
6.1	Non-Identical Multiple Pulse Compression.....	146
6.1.1	Clutter Cancellation .....	148
6.1.2	Extension to Multiple Clutter Intervals.....	150
6.1.3	Fast Implementation.....	152
6.2	Simulation Results .....	154
6.2.1	Synthetic Wideband Scenario .....	155
6.2.2	Pulse Agile Scenario .....	169
6.3	Conclusion .....	178
Chapter 7	Conclusions.....	180
References	.....	182

## CHAPTER 1 INTRODUCTION

Radar systems transmit electromagnetic energy to obtain information about the environment in which they are operated. The majority of radar systems fall into the pulse-Doppler category. Pulsed radars transmit short high-power pulses of electromagnetic energy after which the antenna that was used to transmit is switched to a radar receiver that records the energy that is reflected from the environment. The delay from the time the pulse is transmitted by the radar to the time that a particular echo is received is measured to determine what range the echo originated from. For a given delay  $\tau$  the range can be computed as  $R=c\tau/2$  where  $c \approx 3 \times 10^8$  m/s is the speed of light and the factor of 2 in the denominator accounts for the two way path from the radar to the target and then back to the radar. The energy of the received echoes can also be used to determine the radar cross-section (RCS) of scatterers illuminated by the radar. Ideally, the radar transmits an infinitely short, infinite energy signal however, practical limitations confine the timewidth (temporal duration), peak power, and bandwidth of the radar pulse. The peak power is closely related to detection performance and the bandwidth is inversely proportional to the range resolution of the radar system. The ratio of the received energy of a radar echo from a target to the noise energy of the radar receiver, commonly referred to as signal-to-noise ratio (SNR), determines if a target can be detected by the radar receiver. The pre-processing SNR at the radar receiver is predicted by the radar range equation [1] that is expressed as

$$SNR = \frac{P_t G^2 \lambda^2}{(4\pi)^2 R^4 k T B F} \sigma, \quad (1.1)$$

where  $P_r$  is the peak transmitted power,  $G$  is the antenna gain,  $\lambda$  is the wavelength associated with the radar's center frequency,  $\sigma$  is the RCS of the target,  $R$  is the range to the target,  $k$  is Boltzmann's constant,  $T$  is the absolute temperature of the radar receiver in Kelvin,  $B$  is the noise bandwidth, and  $F$  is the receiver noise figure. The SNR in (1.1) can benefit from transmitting modulated waveforms and performing pulse compression receiver processing.

The received echoes can also be used to measure the radial velocity (with respect to the radar) of targets. This measurement typically requires that the radar examine the change in phase of a particular echo over time, hence multiple pulses are used to provide a well resolved estimate of the pulse to pulse phase change of a particular received echo. The rate of the phase change with respect to time is referred to as the Doppler frequency and is denoted as  $f_d = 2v/\lambda$ , where  $v$  is the radial velocity of the target and  $\lambda$  is the wavelength associated with the carrier frequency of the radar [1]. The radar is also required to isolate returns from different spatial locations, this is achieved by utilizing an antenna with a narrow beamwidth such that only a small angular sector is illuminated on transmit and processed on receive. The antenna can be mechanically or electronically scanned to cover a desired volume. Electronic scanning requires an antenna array with phase shifting capability on each element. The next three sections will discuss pulse compression, Doppler processing, and array processing concepts in more detail.

### *1.1 PULSE COMPRESSION*

Pulse compression waveforms or modulated pulses are used to exploit the statistical properties of uncorrelated receiver noise and modulation bandwidth by employing signal processing techniques to allow a relatively long modulated waveform to achieve the SNR and range resolution commensurate with a short high power pulse. This gain is achieved by correlating a

digital version of the transmitted waveform with the digitally recorded radar echoes and is referred to as matched filtering or pulse compression [2]. Pulse compression transforms the delayed, scaled pulses in the received signal to delayed and scaled versions of the auto-correlation of the transmitted waveform. Figure 1.1 displays the auto-correlation of a typical radar waveform and Figure 1.2 illustrates an example of received radar data before and after pulse compression. The time bandwidth product ( $TB$ ) of a radar pulse indicates the SNR improvement that can be achieved when matched filtering is employed. Unfortunately, the matched filter exhibits range sidelobes, evidenced by the auto-correlation function in Fig. 1.1, that can mask surrounding scatterers.

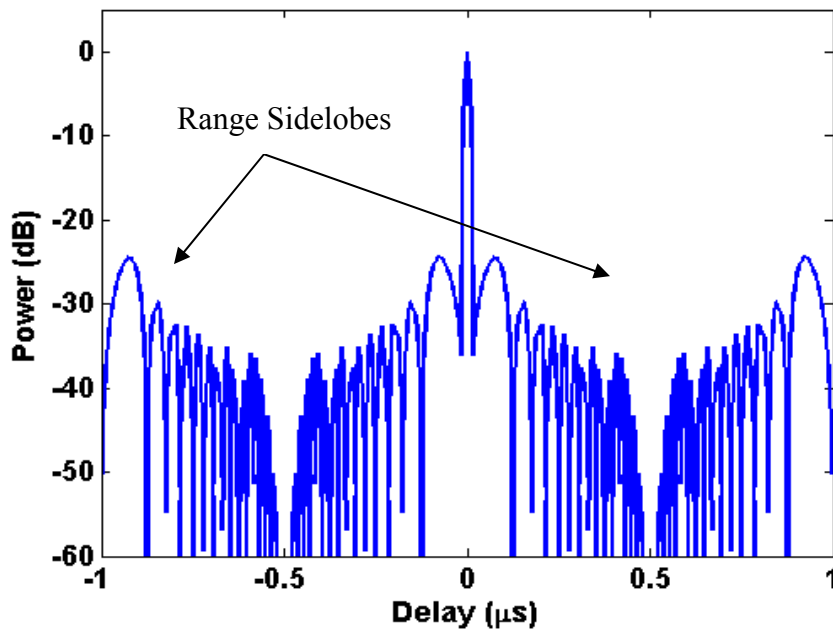


Figure 1.1 Auto-correlation of a typical radar waveform

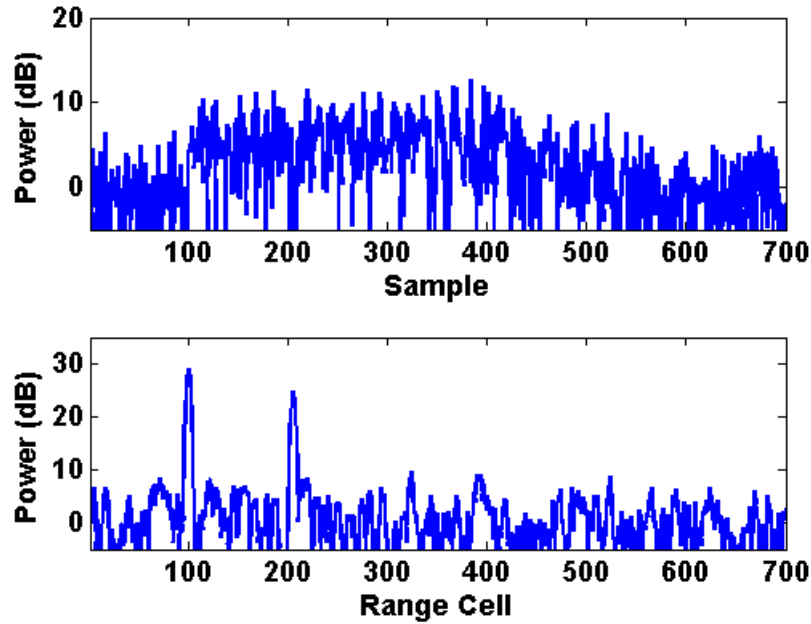


Figure 1.2 Example of radar data before (top) and after (bottom) pulse compression

The structure of the matched filter sidelobes is dependent upon the choice of transmitted waveform, as a result much work has been done on radar waveform design. Radar waveform design is usually limited to constant modulus waveforms to allow the transmit power amplifiers to be operated in saturation for efficiency. The most popular continuous phase pulse compression waveform is the linear frequency modulation or “chirp” waveform. Binary phase-coded waveforms, such as Barker codes [3], have also been shown to possess low sidelobe levels. Other types of waveforms that have been explored include non-linear frequency modulation waveforms [4], Costas codes [5], Frank codes [6], and complementary codes [7]. The waveform used in the example shown in Figs. 1.1 and 1.2 is a P3 polyphase code [8], which is a sampled (at the Nyquist rate) version of a chirp. Alternative pulse compression filters, that do not match the transmitted waveform, can be employed to suppress range sidelobes, however the transmitted waveform still plays an important role.

## 1.2 DOPPLER PROCESSING

The pulse to pulse phase shift caused by moving targets can be used to resolve targets that exhibit different radial velocities. The duration between transmitted pulses, or pulse repetition interval (PRI), determines the maximum unambiguous range and velocity. The number of pulses used is referred to the coherent processing interval (CPI). Doppler processing is achieved by applying a digital filter bank across the pulses in the CPI for each range cell. When the target motion is linear throughout the CPI, the pulsed radar returns possess a tone-like structure associated with the Doppler frequency. Hence, the fast Fourier transform (FFT) can be used to realize a bank of frequency filters that separate returns with different velocities. Due to the finite duration of the pulsed-radar measurement the frequency response of targets exhibit Doppler sidelobes that can obscure small targets at different speeds in the same range cell. Windowing can be applied to suppress these sidelobes at the cost of reduced frequency resolution.

The properties of the aforementioned phase shift induced by a moving target can be determined by analyzing a simple case. Consider a pulsed carrier radar waveform denoted as

$$s(t) = p(t) \cos(2\pi f_c t), \quad (1.2)$$

where  $f_c$  is the carrier frequency and

$$p(t) = U(t) - U(t - T_p), \quad (1.3)$$

in which  $U(t)$  is the unit step function and  $T_p$  is the pulsewidth of the transmitted waveform.

Under the typical assumption that the fast-time Doppler shift is negligible, the received echo for the  $m^{\text{th}}$  pulse in a CPI from a moving target with an initial range of  $R$  can be expressed as

$$y_m(t) = p\left(t - \frac{2R - 2vmT}{c}\right) \cos\left(2\pi f_c \left(t - \frac{2R - 2vmT}{c}\right)\right), \quad (1.4)$$

where  $v$  is the radial component (towards the radar) of the target velocity,  $c$  is the speed of light, and  $T$  is the PRI. Rearranging the terms and substituting  $\frac{1}{\lambda_c} = \frac{f_c}{c}$  into (1.4) yields

$$y_m(t) = p\left(t - \frac{2R - 2vmT}{c}\right) \cos\left(2\pi f_c t - 2\pi \frac{2R}{\lambda_c} + 2\pi \frac{2v}{\lambda_c} mT\right). \quad (1.5)$$

Observe that the term  $mT$  in (1.5) represents a discrete time progression with a sampling rate of  $PRF = 1/T$  thus the term associated with the slow-time pulse to pulse phase change can be expressed as

$$\phi = 2\pi \frac{2v}{\lambda_c} \frac{m}{PRF}. \quad (1.6)$$

The normalized Doppler frequency associated with this term is

$$k_d = \frac{2v}{\lambda_c} \frac{1}{PRF}. \quad (1.7)$$

The principles of sampling theory dictate that in order to avoid aliasing  $k_d$  must satisfy

$-\frac{1}{2} < k_d < \frac{1}{2}$ . Consequently, if  $|v| \geq \frac{PRF}{2} \frac{\lambda_c}{2}$  the velocity measurement will be aliased; the

quantity  $\frac{PRF}{2} \frac{\lambda_c}{2}$  is referred to as the ambiguous velocity and can be controlled by adjusting the radar PRF.

Doppler processing is implemented using the discrete Fourier transform (DFT) of the digitized echoes recorded in a CPI. The DFT of an input signal  $x(n)$  is defined as

$$X(k) = \sum_{n=1}^N x(n) e^{-j2\pi \frac{k}{N} n}, \quad k = 0, 1, \dots, N-1, \quad (1.8)$$

where  $k$  is normalized frequency. Figure 1.3 shows the Doppler frequency response for a range cell containing a target traveling towards an X-band (10 GHz) radar at 200 m/s. For this example the PRF is 40 kHz and there are 20 pulses in the CPI.

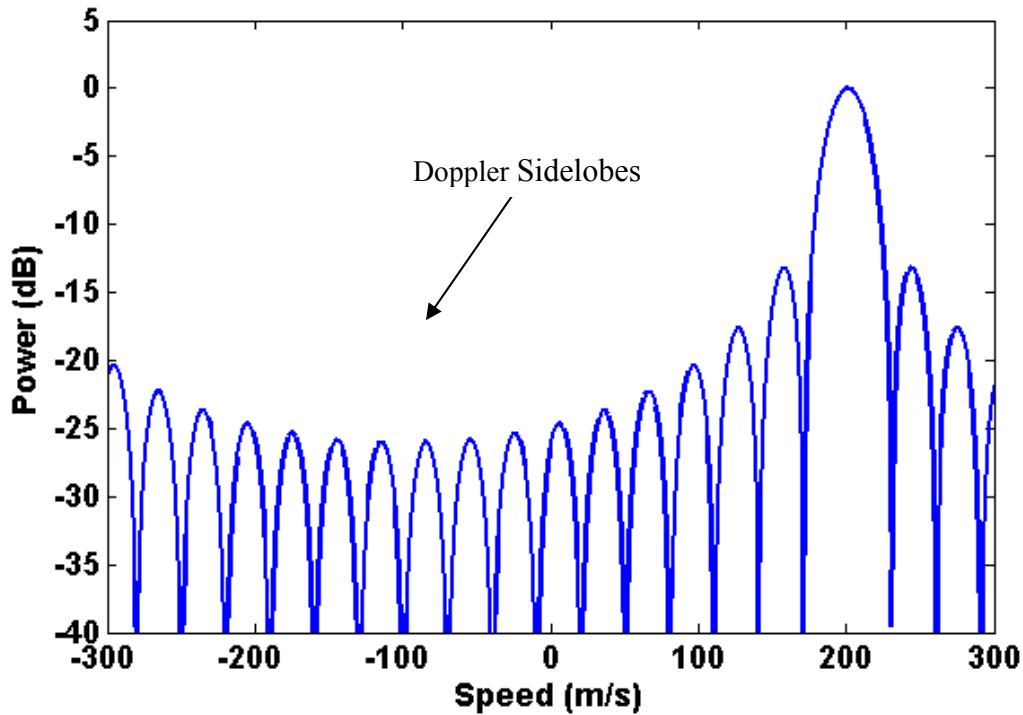


**Figure 1.3** Doppler frequency response for a 200 m/s target measured with a 40 kHz PRF at X-band

### 1.3 ARRAY PROCESSING

Antenna arrays are widely used in radar systems to facilitate electronic scanning and spatial discrimination. Typically the same waveform is transmitted on each element with an elemental phase shift to focus energy in a desired direction. A number of pulses are processed before steering the beam to a different spatial direction.

The notional array geometry used throughout this report is defined as follows. Figure 1.4 depicts a linear array in which the blue line represents a phase front of a far field plane wave traveling in the theta direction (relative to boresight) and  $d$  is the element spacing. Note that the convention used here is that the array element indices are increasing from left to right and the spatial angle theta is referenced from boresight that is indicated by the dashed line. Throughout this document it is assumed that signals being transmitted from the array have a relatively narrow bandwidth when compared to their center frequency. As illustrated in Fig. 1.4, the physical path length difference from two adjacent elements to a phase front in the far field plane wave is given by the relationship  $d \sin \theta$ . Under the narrowband assumption the electrical angle associated with this distance is approximately  $\frac{2\pi}{\lambda} d \sin \theta$  where  $\lambda$  is the wavelength associated with the radar carrier frequency.

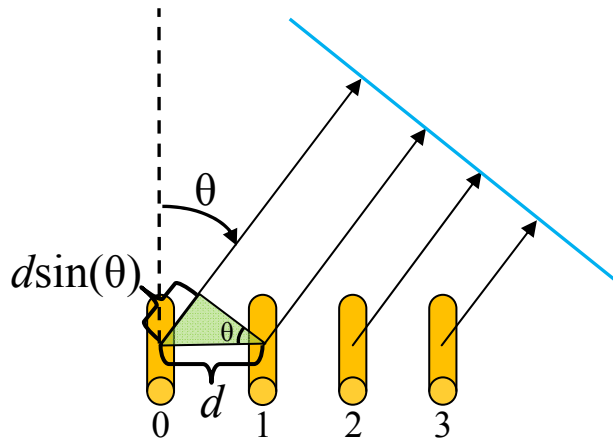


**Figure 1.4** Linear array illustration

The phase shift between the signals received at adjacent elements is analogous to that derived for moving targets in the previous section. Consider a sinusoidal source  $s(t) = \cos(2\pi f_c t)$  in the

far field of the array at angle  $\theta$  and range  $R$  (from element 0). The received signal at the  $m^{\text{th}}$  element can be expressed as

$$y_m(t) = \cos\left(2\pi f_c \left(t - \frac{R - md \sin(\theta)}{c}\right)\right), \quad (1.9)$$

where  $md \sin(\theta)$  is the path length distance between adjacent elements. Substituting  $\frac{1}{\lambda_c} = \frac{f_c}{c}$

into (1.9) and rearranging results in

$$y_m(t) = \cos\left(2\pi f_c t - 2\pi \frac{R}{\lambda_c} + 2\pi \frac{md \sin(\theta)}{\lambda_c}\right). \quad (1.10)$$

The element to element phase progression is likewise similar to the pulse-to-pulse phase progression in (1.6) for moving targets where here  $md$  give the location of the spatial samples, the spatial frequency is given by the expression

$$k_s = \frac{d}{\lambda_c} \sin(\theta), \quad (1.11)$$

which, to avoid aliasing, is bounded as  $\frac{1}{2} < \frac{d}{\lambda_c} \sin(\theta) < \frac{1}{2}$ . Hence,  $d$  is typically chosen to be  $\frac{\lambda_c}{2}$

(half-wave spacing) such that signals between  $\pm 90^\circ$  of boresight will not be aliased. Unlike the relationship between radial velocity and Doppler frequency, the mapping from spatial angle to spatial frequency is non-linear as a result of the geometric relationship between the angle of incidence and the path length difference between array elements. This relationship developed for sinusoidal sources applies to received radar echoes as well (under the assumption that the received signal are sufficiently narrowband). Additionally, due to antenna reciprocity [9] the phase progression associated with the spatial frequency in (1.11) can be used to electronically steer

transmitted radar pulses to different spatial angles. Beamforming can be achieved using phase shifters on each element after which the channels can be combined into a single channel digitizer. However, many advanced array processing techniques require that multiple channels are digitized. The DFT can be used to perform digital beamforming when the data received by each element of a linear array with half-wave spacing is digitized. The normalized response received at a 20 element linear array (with half-wave spacing) for a target at  $-20^\circ$  is displayed in Fig. 1.5.

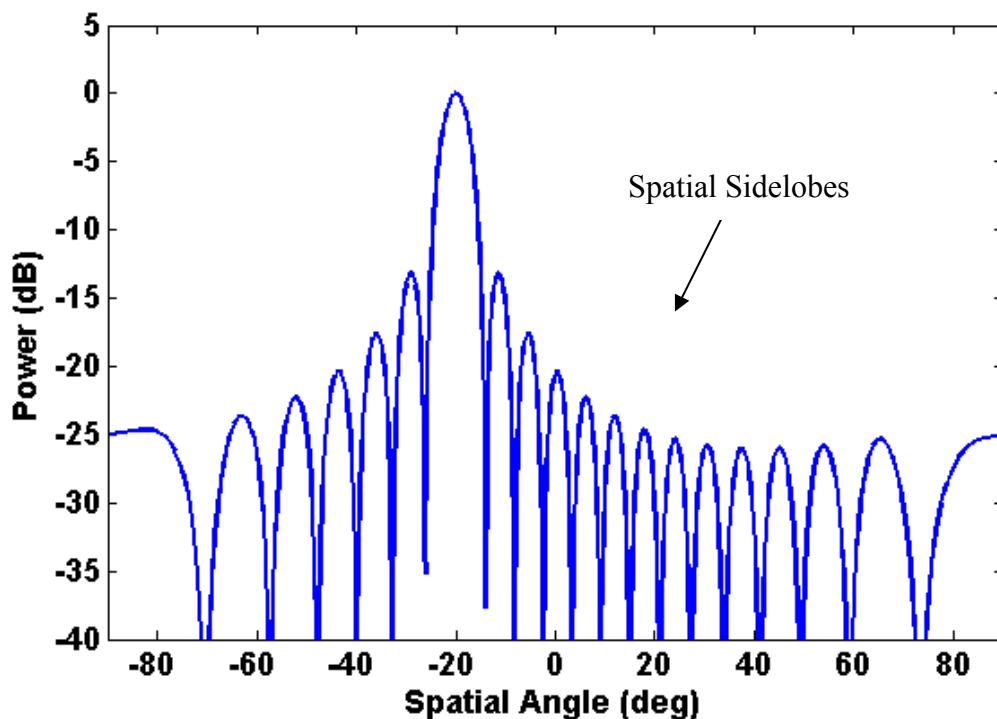


**Figure 1.5** Spatial frequency response from a 20 element linear array with half-wave spacing for a target at  $-20^\circ$

#### 1.4 MOTIVATION

Historically pulse-Doppler radar systems have been carefully designed to transmit the same waveform from each element of an antenna array and minimize pulse to pulse changes in the transmitted waveform. Advances in computing power and hardware design will potentially allow more complex transmission schemes to be employed at a reasonable cost. For example,

transmitting different waveforms from different elements of a radar array has been proposed as a means to achieve transmit beam pattern flexibility [10-12]. These waveforms are often referred to as multiple input multiple output (MIMO) waveforms. Additionally, transmitting different waveforms on a pulse to pulse basis can also have benefits. However, altering the transmit framework of radar waveforms comes at the cost of reduced matched filter sensitivity and greater calibration requirements.

MIMO radar waveforms can be used to control the spatial distribution of the energy transmitted from an antenna array. This concept allows a great deal of flexibility in the transmit beam pattern as well as the ability to transmit different waveforms to different spatial directions within a single transmit pulse. Advantages of this architecture include shorter search times, longer dwell times, reduced sensitivity to passive exploitation, and potentially simultaneous multi-mode capability. Short search times are valuable when close-in threats are lost and need to be re-acquired, whereas long dwell times can be used to provide increased Doppler resolution. A major disadvantage of beamspiling is the reduction in power delivered to any particular spatial angle; this loss in power can be overcome by increasing the dwell time (as long as the radar remains coherent). Additionally, applications exist that do not require the same amount of power be delivered to all angles, for example, consider the elevation coverage pattern depicted in Fig. 1.6 for a ship-based radar. Note that at high elevations the detection range is shorter than near the horizon, hence beamspiling is tolerable as the radar scans away from the horizon.

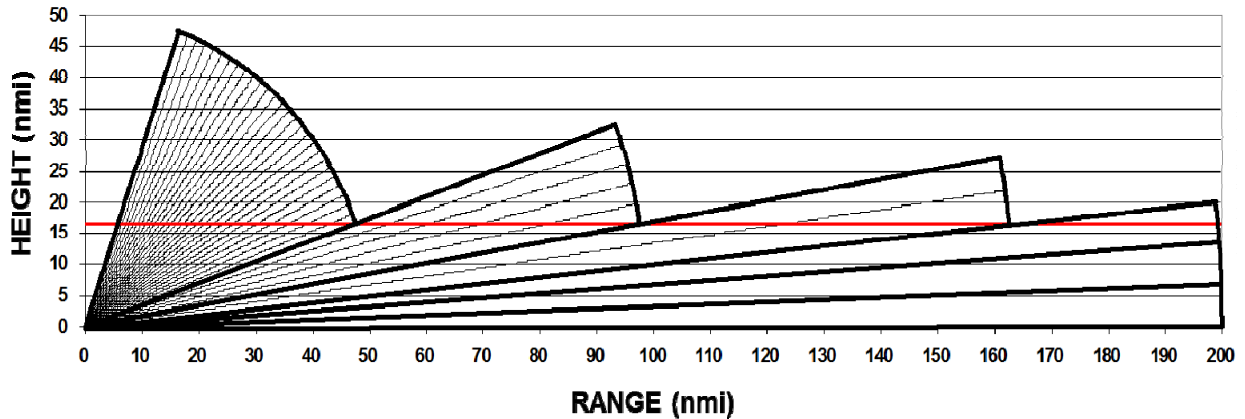


**Figure 1.6** Example of ship-based radar elevation coverage pattern  
(graphic courtesy of James Alter, Naval Research Laboratory)

Diversity benefits have also been suggested for changing the radar waveform on a pulse to pulse basis, albeit this has a significant impact on clutter cancellation. Pulse to pulse waveform diversity can be used to mitigate range ambiguities, facilitate radar embedded communications, and enhanced range resolution. Ambiguity resolution and radar-embedded communications employ different coding on each pulse while enhanced range resolution is achieved by changing the center frequency of each waveform.

This report will examine the effect of the aforementioned waveform diversity techniques on radar operations. Transmitting different waveforms from an array and pulse to pulse waveform changes have deleterious effects on radar sensitivity because conventional processing techniques exhibit sidelobes that obscure nearby targets. Numerous pulse compression techniques that reduce range sidelobes have been presented [13-16] and array and Doppler processing techniques typically employ windowing to reduce sidelobes. It is determined later that adapting independently does not yield the degrees of freedom required to suppress sidelobes for some waveform diversity techniques. A vast amount of work has been done regarding Space-Time Adaptive Processing (STAP) [17] however, aside from [18-20], very little work has been done on

adapting simultaneously in space and range or time and range. In [18-20] a data-weighted Least-Squares based approach entitled Iterative Adaptive Approach (IAA) is used to adaptively perform beamforming, fast-time Doppler processing, and pulse compression simultaneously. However, the dimensionality of the matrix inverse required by this approach is extremely large resulting in a per-iteration computational complexity that is related to the number of range cells processed by the radar, cubed. Furthermore, it is not readily apparent that the underlying signal model used for IAA can be augmented to account for eclipsed targets without becoming ill-conditioned; as such, this approach will not be considered. In this document, a re-iterative minimum mean square error framework is used to develop adaptive space-range and time-range coupled processing techniques denoted as Space-Range Adaptive Processing (SRAP) and Time-Range Adaptive Processing (TRAP). The new algorithms are shown to offer enhanced sensitivity at a modest increase in computation relative to adapting in each domain independently. Additionally, a deterministic approach entitled Non-Identical Multiple Pulse Compression (NIMPC) for cancelling range ambiguous pulse-agile clutter is presented. All approaches presented here can be augmented to account for eclipsed targets.

### *1.5 ORGANIZATION OF DOCUMENT*

The rest of this document is organized in the following manner. The remainder of this chapter presents the Adaptive Pulse Compression (APC) [13] and Re-Iterative Super Resolution (RISR) [21] algorithms as background. The following chapter details the inclusion of a gain constraint to the APC and Fast APC (FAPC) [22] algorithms via a minimum variance distortionless response (MVDR) framework. Chapter 3 discusses partially correlated MIMO transmit strategies for beamspoiling. Next, Space-Range Adaptive Processing (SRAP) is presented and compared to sequential adaptation in the spatial and range domains using APC and RISR. The Time Range

Adaptive Processing (TRAP) and Non-Identical Multiple Pulse Compression (NIMPC) algorithms are highlighted in Chapters 5 and 6, respectively. Conclusions and proposed future work are stated in the final chapter.

## *1.6 ADAPTIVE SIGNAL PROCESSING BACKGROUND*

In the context of radar, adaptive signal processing refers to any technique that utilizes information that is obtained from a measurement of the environment to improve performance. Much of the work in this dissertation is based on adaptivity of range, spatial, and temporal receiver filter structures. In particular, the following chapters will discuss approaches that are capable of adapting in multiple dimensions simultaneously within a re-iterative minimum mean squared error (RMMSE) framework. RMMSE approaches that independently address pulse compression and array processing have been considered.

Adaptive Pulse Compression (APC) is an RMMSE approach to pulse compression that produces a unique pulse compression filter for each range cell of interest and has been shown to suppress range sidelobes into the noise floor [13]. The RMMSE framework has also been applied to the direction of arrival problem; this approach entitled Re-Iterative Super Resolution (RISR) [21] can be formulated in the context of radar array or Doppler processing.

The new work in this dissertation is closely related to these algorithms and can be viewed as a combination of the independent approaches into coupled-domain processing architectures that exhibit a large number of degrees of freedom. The remainder of this chapter lays out the previously conceived algorithms as background.

### 1.6.1 ADAPTIVE PULSE COMPRESSION

Much work has been done to develop pulse compression methods that alleviate the effects of range sidelobes, though pulse compression filters that deviate from the matched filter consequently suffer from varying degrees of mismatch loss. The Minimum Mean-Square Error (MMSE) based Adaptive Pulse Compression (APC) algorithm is capable of suppressing range sidelobes into the noise by employing a unique pulse compression filter for each range cell. The radar return signal can be modeled as a discrete convolution of the transmitted waveform with the illuminated range profile. The return from the  $\ell^{\text{th}}$  range cell can thus be denoted as

$$\mathbf{y}(\ell) = \mathbf{x}^T(\ell) \mathbf{s} + \mathbf{v}(\ell), \quad (1.12)$$

where  $\ell$  is the range cell index,  $(\bullet)^T$  is the transpose operator,  $\mathbf{s} = [s_0 \ s_1 \ \dots \ s_{N-1}]^T$  is the length- $N$  sampled version of the transmit waveform,  $\mathbf{x}(\ell) = [x(\ell) \ x(\ell-1) \ \dots \ x(\ell-N+1)]^T$  is a collection of complex amplitudes corresponding to the scatterers in the range profile that the waveform convolves with at delay  $\ell$ , and  $\mathbf{v}(\ell)$  is a sample of additive noise. The assumed received signal model for APC [13] is formed by grouping  $N$  contiguous samples of the radar receive model in (1.12) and is expressed as

$$\mathbf{y}(\ell) = [y(\ell) \ y(\ell+1) \ \dots \ y(\ell+N-1)]^T = \mathbf{X}^T(\ell) \mathbf{s} + \mathbf{v}(\ell), \quad (1.13)$$

where  $\mathbf{v}(\ell)$  is an  $N \times 1$  vector of additive noise samples, and  $\mathbf{X}(\ell)$  is the  $N \times N$  matrix

$$\mathbf{X}(\ell) = [\mathbf{x}(\ell) \ \mathbf{x}(\ell+1) \ \dots \ \mathbf{x}(\ell+N-1)] = \begin{bmatrix} x(\ell) & x(\ell+1) & \dots & x(\ell+N-1) \\ x(\ell-1) & x(\ell) & \dots & x(\ell+N-2) \\ \vdots & \vdots & \ddots & \vdots \\ x(\ell-N+1) & x(\ell-N+2) & \dots & x(\ell) \end{bmatrix}, \quad (1.14)$$

containing the  $2N - 1$  complex amplitude range cells surrounding (and including) the range cell of interest.

The MMSE cost function for the complex amplitude of the  $\ell^{\text{th}}$  range cell is

$$J(\ell) = E \left[ \left| x(\ell) - \mathbf{w}^H(\ell) \mathbf{y}(\ell) \right|^2 \right], \quad (1.15)$$

where  $\mathbf{w}(\ell)$  is the adaptive pulse compression filter for the  $\ell^{\text{th}}$  range cell,  $(\bullet)^H$  is the complex-conjugate transpose (or Hermitian) operator, and  $E[\bullet]$  is expectation. Minimizing (1.15) with respect to the conjugate (denoted by  $(\bullet)^*$ ) of the adaptive filter  $\mathbf{w}^*(\ell)$  yields

$$\mathbf{w}(\ell) = \left( E[\mathbf{y}(\ell) \mathbf{y}^H(\ell)] \right)^{-1} \left( E[x^*(\ell) \mathbf{y}(\ell)] \right). \quad (1.16)$$

By assuming the range cells are uncorrelated with one another and with the noise, the filter can be expressed as

$$\mathbf{w}(\ell) = \rho(\ell) \mathbf{R}^{-1}(\ell) \mathbf{s}, \quad (1.17)$$

where  $\rho(\ell) = E \left[ |x(\ell)|^2 \right]$  is the expected power at the  $\ell^{\text{th}}$  range cell and  $\mathbf{R}(\ell) = \mathbf{R}_S(\ell) + \mathbf{R}_{\text{NSE}}$  is the sum of the structured signal covariance matrix

$$\mathbf{R}_S(\ell) = \sum_{n=-N+1}^{N-1} \rho(\ell+n) \mathbf{s}_n \mathbf{s}_n^H, \quad (1.18)$$

based upon the signal model (1.13) in which

$$\mathbf{s}_n = \begin{cases} \left[ s_{|n|} \cdots s_{N-1} \mathbf{0}_{1 \times |n|} \right]^T & \text{for } n \leq 0 \\ \left[ \mathbf{0}_{1 \times n} s_0 \cdots s_{N-1-n} \right]^T & \text{for } n > 0 \end{cases}, \quad (1.19)$$

and the noise covariance matrix  $\mathbf{R}_{\text{NSE}} = \sigma_{\text{NSE}}^2 \mathbf{I}_{N \times N}$  under the assumption of white noise (where  $\sigma_{\text{NSE}}^2$  is the noise power) [13].

The signal covariance matrix used to form the pulse compression filters in (1.17) requires a priori knowledge of the target powers (denoted as  $\rho(\ell)$  in (1.18)). These powers can be estimated by first applying the matched filter, then using this estimate to form a unique pulse compression filter for each range cell of interest. Applying the new filters yields an improved estimate of the scattering coefficients in the illuminated scene. The improved estimates are then used to construct a new set of pulse compression filters. This process of alternating estimation and filter formulation has been found to converge in 2-3 adaptive stages. The RISR algorithm, that is presented in the next section, utilizes this same re-iterative structure.

### 1.6.2 RE-ITERATIVE SUPER RESOLUTION

Re-Iterative Super Resoluiton (RISR) was developed as a direction of arrival algorithm [21] but can be applied in the context of radar to array beamforming or Doppler processing. RISR is implemented as follows, let the output at the  $\ell^{\text{th}}$  time sample of an  $M$  element array be denoted as

$$\mathbf{y}(\ell) = [y_0(\ell) \ y_1(\ell) \ \cdots \ y_{M-1}(\ell)]^T \quad (1.20)$$

and

$$\mathbf{V} = \begin{bmatrix} 1 & 1 & \cdots & 1 \\ 1 & e^{j\frac{2\pi}{K}} & \cdots & e^{j\frac{2\pi(K-1)}{K}} \\ \vdots & \vdots & \ddots & \vdots \\ 1 & e^{j\frac{2\pi}{K}(M-1)} & \cdots & e^{j\frac{2\pi(K-1)(M-1)}{K}} \end{bmatrix} \quad (1.21)$$

be a bank of  $K$  spatial steering vectors. The resulting RISR adaptive filter bank is computed as

$$\mathbf{W}(\ell) = (\mathbf{V}\mathbf{P}(\ell)\mathbf{V}^H + \mathbf{R})^{-1} \mathbf{V}\mathbf{P}(\ell), \quad (1.22)$$

where

$$\mathbf{P}(\ell) = \begin{bmatrix} \rho(\ell, 0) & 0 & 0 \\ 0 & \ddots & 0 \\ 0 & 0 & \rho\left(\ell, \frac{2\pi(K-1)}{K}\right) \end{bmatrix}, \quad (1.23)$$

is a diagonal matrix containing the estimated signal power in each spatial bin at the  $\ell^{\text{th}}$  time sample and  $\mathbf{R} = \sigma_{\text{NSE}}^2 \mathbf{I}_{M \times M}$  is the noise covariance matrix (assuming white noise).

RISR is applied in the same fashion as APC by first obtaining the spatial estimates with the deterministic filter bank in (1.21). Using these estimates the RISR filter bank is computed and applied as

$$\hat{\mathbf{x}}_{\text{RISR}}(\ell, \boldsymbol{\theta}) = \mathbf{W}(\ell)^H \mathbf{y}(\ell). \quad (1.24)$$

RISR is iterated up to 15 times to obtain a good estimate [21]. It should be noted that the RISR algorithm requires over-sampling of the spatial angles to account for steering vector mismatch. This over-sampling affects the performance of the algorithm and can over-suppress the noise, yielding similar results to that of the reduced-dimensionality approach to APC entitled Fast APC [22]. The detrimental effects of limited degrees of freedom can be alleviated by adding a unity gain constraint to the MMSE cost function.

In the next chapter the Adaptive Pulse Compression and Fast Adaptive Pulse Compression cost functions will be augmented with a unity gain constraint via a Minimum Variance Distortionless

Response (MVDR) framework. Later, the MVDR result derived for APC and FAPC will be applied to RISR and developed for the new coupled-domain approaches presented in this paper.

## CHAPTER 2      GAIN-CONSTRAINED ADAPTIVE PULSE COMPRESSION AND FAST ADAPTIVE PULSE COMPRESSION

This chapter details the application of an MVDR framework to facilitate inclusion of a unity gain constraint within the previously developed APC [13] and Fast APC (FAPC) [22] cost functions in an effort to mitigate mismatch loss. The APC algorithm exhibits almost no mismatch loss [13] and, as such, the full-dimension algorithm benefits little from the gain constraint. However, FAPC occasionally suppresses small targets in dense scattering environments due to fewer degrees of freedom inherent to reduced-dimensionality processing [22]. The constrained FAPC algorithm preserves gain on small targets consequently improving detection performance.

The matched filter maximizes the signal-to-noise ratio (SNR) for a solitary point target in white noise [1] and is consequently optimal for this scenario. However, the matched filter exhibits range sidelobes, that in the presence of a large scatterer, can mask smaller targets in surrounding range cells. Several estimation techniques such as Least-Squares [14] and mismatch filtering [15] have been developed that reduce range sidelobes, thereby enhancing the ability to recover small masked targets. Although these algorithms mitigate the effect of range sidelobes, they also induce some mismatch loss relative to the matched filter (albeit this loss may be quite small for some methods/waveforms).

The Adaptive Pulse Compression (APC) algorithm has been shown to suppress range sidelobes into the noise by adaptively estimating a unique pulse compression filter for every range cell of interest [13]. These Minimum Mean-Square Error (MMSE) adaptive filters exhibit very little mismatch loss. However, the computational cost of APC limits its use in current real-time

systems. Recently, the Fast Adaptive Pulse Compression (FAPC) algorithm has been shown to reduce the computational cost of APC significantly while maintaining enhanced sensitivity [22]. The FAPC algorithm approximates the full-dimension APC adaptive filter at each range cell via reduced-dimensionality techniques that consequently induce a slightly increased mismatch loss.

The minimum variance distortionless response (MVDR) [23] technique is widely employed in the array processing literature to yield a constrained MMSE solution that preserves unity gain in the direction of interest and suppresses interference elsewhere. In this paper, the MVDR framework will be applied to obtain an APC-like structure with unity gain (*i.e.* no mismatch loss) for the range cell of interest. However, the real benefit of such a formulation is actually realized for the reduced-dimension FAPC algorithm, where the constrained solution provides additional robustness for small masked scatterers.

### 2.1 GAIN-CONSTRAINED APC COST FUNCTION

The APC MMSE cost function in (1.15) is now cast into the MVDR framework [23] by including the linear constraint

$$\mathbf{w}^H(\ell)\mathbf{s} = 1. \quad (2.1)$$

The resulting constrained cost function is denoted

$$J(\ell) = E \left[ \left| x(\ell) - \mathbf{w}^H(\ell) \mathbf{y}(\ell) \right|^2 \right] + \text{Re} \left\{ \lambda (\mathbf{w}^H(\ell) \mathbf{s} - 1) \right\}, \quad (2.2)$$

in which  $\lambda$  is a Lagrange multiplier and  $\text{Re}\{\bullet\}$  is the real part of the argument. Minimizing (2.2)

with respect to the adaptive filter  $\mathbf{w}^*(\ell)$  yields

$$\mathbf{w}(\ell) = \left( E[\mathbf{y}(\ell) \mathbf{y}^H(\ell)] \right)^{-1} \left( E[x^*(\ell) \mathbf{y}(\ell)] - \frac{\lambda}{2} \mathbf{s} \right). \quad (2.3)$$

By assuming the range cells are uncorrelated with one another and with the noise, the filter can be expressed as

$$\mathbf{w}(\ell) = \left( \rho(\ell) - \frac{\lambda}{2} \right) \mathbf{R}^{-1}(\ell) \mathbf{s}, \quad (2.4)$$

where  $\rho(\ell) = E[|x(\ell)|^2]$  is the expected power at the  $\ell^{\text{th}}$  range cell and  $\mathbf{R}(\ell) = \mathbf{R}_s(\ell) + \mathbf{R}_{\text{NSE}}$  is the sum of the structured signal covariance matrix

$$\mathbf{R}_s(\ell) = \sum_{n=-N+1}^{N-1} \rho(\ell+n) \mathbf{s}_n \mathbf{s}_n^H, \quad (2.5)$$

based upon the signal model from (1.13) in which

$$\mathbf{s}_n = \begin{cases} \left[ s_{|n|} \cdots s_{N-1} \mathbf{0}_{1 \times |n|} \right]^T & \text{for } n \leq 0 \\ \left[ \mathbf{0}_{1 \times n} s_0 \cdots s_{N-1-n} \right]^T & \text{for } n > 0 \end{cases}, \quad (2.6)$$

and the noise covariance matrix  $\mathbf{R}_{\text{NSE}} = \sigma_{\text{NSE}}^2 \mathbf{I}_{N \times N}$  under the assumption of white noise (where  $\sigma_{\text{NSE}}^2$  is the noise power) [13].

The constraint for unity gain can now be included by evaluating the inner product

$$\mathbf{w}^H(\ell) \mathbf{s} = \left( \rho(\ell) - \frac{\lambda}{2} \right) \mathbf{s}^H \mathbf{R}^{-1}(\ell) \mathbf{s}, \quad (2.7)$$

that, in combination with (2.1), yields

$$\frac{\lambda}{2} = \rho(\ell) - \frac{1}{\mathbf{s}^H \mathbf{R}^{-1}(\ell) \mathbf{s}}. \quad (2.8)$$

Note that this result for the Lagrange multiplier is slightly different than is normally obtained [23] due to the presence of the  $\rho(\ell)$  term. However, substitution of (2.8) into (2.4) yields the familiar MVDR form

$$\mathbf{w}(\ell) = \frac{\mathbf{R}^{-1}(\ell) \mathbf{s}}{\mathbf{s}^H \mathbf{R}^{-1}(\ell) \mathbf{s}}, \quad (2.9)$$

thus facilitating a gain-constrained implementation of adaptive pulse compression.

## 2.2 FAST APC SIGNAL MODEL AND COST FUNCTION

The contiguously blocked version of Fast APC (FAPC) [22] utilizes an assumed received signal model formed by segmenting the full-dimension model of (1.13) into  $M$  segments of length  $K = N/M$  as shown in Fig. 2.1. The segments of the received signal model are expressed as

$$\tilde{\mathbf{y}}_m(\ell) = \tilde{\mathbf{X}}_m^T(\ell) \mathbf{s} + \tilde{\mathbf{v}}_m(\ell) \quad (2.10)$$

for  $m = 0, 1, \dots, M-1$ , where  $\tilde{\mathbf{X}}_m(\ell)$  is the  $N \times K$  matrix

$$\tilde{\mathbf{X}}_m(\ell) = [\mathbf{x}(\ell + mK) \ \mathbf{x}(\ell + mK + 1) \ \dots \ \mathbf{x}(\ell + mK + K - 1)] \quad (2.11)$$

and  $\tilde{\mathbf{v}}_m(\ell)$  is the  $K \times 1$  vector

$$\tilde{\mathbf{v}}_m(\ell) = [v(\ell + mK) \ v(\ell + mK + 1) \ \dots \ v(\ell + mK + K - 1)]^T \quad (2.12)$$

formed by contiguously blocking the elements of  $\mathbf{X}(\ell)$  and  $\mathbf{v}(\ell)$  from (1.13), respectively.

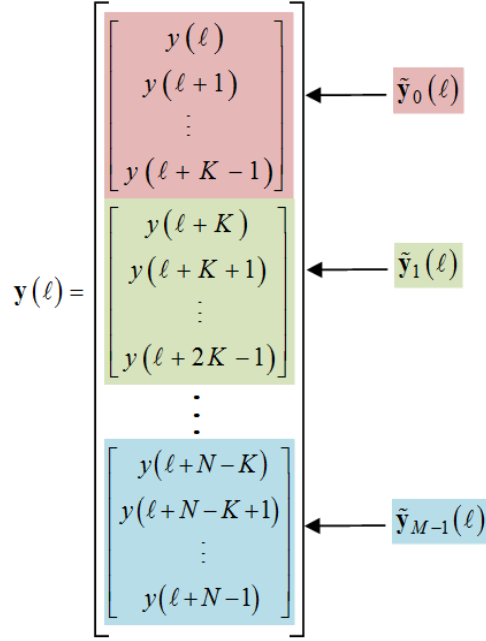


**Figure 2.1** Contiguous blocks of the FAPC signal model

The contiguous FAPC cost function for the complex amplitude of the  $\ell^{\text{th}}$  range cell is an approximation of the full-dimension cost function in (1.15) formulated as

$$\tilde{J}(\ell) = \sum_{m=0}^{M-1} E \left[ \left| \frac{1}{M} x(\ell) - \tilde{\mathbf{w}}_m^H(\ell) \tilde{\mathbf{y}}_m(\ell) \right|^2 \right], \quad (2.13)$$

in which  $\tilde{\mathbf{w}}_m(\ell)$  is the  $m^{\text{th}}$  length- $K$  segment of the  $N$ -length FAPC filter  $\tilde{\mathbf{w}}(\ell)$  that approximates the full-dimension APC filter in (1.17).

### 2.3 GAIN-CONSTRAINED FAST APC

As with the full-dimension case, adding the linear constraint

$$\tilde{\mathbf{w}}^H(\ell) \mathbf{s} = 1 \quad (2.14)$$

to the reduced-dimensionality cost function in (2.13) produces the gain-constrained FAPC cost function

$$\tilde{J}(\ell) = \left[ \sum_{m=0}^{M-1} E \left[ \left| \frac{1}{M} x(\ell) - \tilde{\mathbf{w}}_m^H(\ell) \tilde{\mathbf{y}}_m(\ell) \right|^2 \right] \right] + \text{Re} \left\{ \lambda (\tilde{\mathbf{w}}^H(\ell) \mathbf{s} - 1) \right\}. \quad (2.15)$$

Minimizing the MVDR cost function of (2.15) with respect to the adaptive filter segment  $\tilde{\mathbf{w}}_m(\ell)$  yields

$$\tilde{\mathbf{w}}_m(\ell) = \left( E \left[ \tilde{\mathbf{y}}_m^H(\ell) \tilde{\mathbf{y}}_m(\ell) \right] \right)^{-1} \left[ E \left[ \frac{1}{M} x^*(\ell) \tilde{\mathbf{y}}_m(\ell) \right] - \frac{\lambda}{2} \begin{bmatrix} \mathbf{0}_{M \times mK} & \mathbf{I}_{K \times K} & \mathbf{0}_{M \times N - (m+1)K} \end{bmatrix} \mathbf{s} \right]. \quad (2.16)$$

Again assuming the range cells are uncorrelated with each other and with the noise the FAPC filter segment can be written as

$$\tilde{\mathbf{w}}_m(\ell) = \left( \frac{\rho(\ell)}{M} - \frac{\lambda}{2} \right) \tilde{\mathbf{R}}_m^{-1}(\ell) \tilde{\mathbf{s}}_m, \quad (2.17)$$

where  $\tilde{\mathbf{s}}_m = \left[ s_{mK} \ s_{mK+1} \ \cdots \ s_{(m+1)K-1} \right]^T$  is the  $m^{\text{th}}$  segment of the contiguously blocked waveform and  $\tilde{\mathbf{R}}_m(\ell) = \tilde{\mathbf{R}}_{S,m}(\ell) + \tilde{\mathbf{R}}_{\text{NSE}}$  is the sum of the reduced-dimension structured signal covariance matrix

$$\tilde{\mathbf{R}}_{S,m}(\ell) = \sum_{k=N-1}^{K-1} \rho(\ell + k + mK) \tilde{\mathbf{s}}_k \tilde{\mathbf{s}}_k^H, \quad (2.18)$$

in which

$$\tilde{\mathbf{s}}_k = \left\{ \begin{array}{ll} \left[ s_{|k|} \ \cdots \ s_{N-1} \ \mathbf{0}_{1 \times |k|} \right]^T & \text{for } k < -N + K \\ \left[ s_{|k|} \ s_{|k|+1} \ \cdots \ s_{|k|+K-1} \right]^T & \text{for } -N + K \leq k \leq 0 \\ \left[ \mathbf{0}_{1 \times k} \ s_0 \ \cdots \ s_{K-1-k} \right]^T & \text{for } k > 0 \end{array} \right\}, \quad (2.19)$$

and the reduced-dimension noise covariance matrix  $\tilde{\mathbf{R}}_{\text{NSE}} = \sigma_{\text{NSE}}^2 \mathbf{I}_{K \times K}$  (again assuming white noise) [22]. The full length- $N$  filter is constructed by concatenating the  $M$  filter segments given by (2.17) and is expressed as

$$\tilde{\mathbf{w}}(\ell) = \left( \frac{\rho(\ell)}{M} - \frac{\lambda}{2} \right) \tilde{\mathbf{R}}^{-1} \mathbf{s} \quad (2.20)$$

where

$$\tilde{\mathbf{R}}^{-1}(\ell) = \begin{bmatrix} \tilde{\mathbf{R}}_0^{-1}(\ell) & 0 & \cdots & 0 \\ 0 & \tilde{\mathbf{R}}_1^{-1}(\ell) & \cdots & 0 \\ \vdots & \vdots & \ddots & \vdots \\ 0 & 0 & \cdots & \tilde{\mathbf{R}}_{M-1}^{-1}(\ell) \end{bmatrix}. \quad (2.21)$$

The Lagrange multiplier is found as before resulting in

$$\frac{\lambda}{2} = \frac{\rho(\ell)}{M} - \frac{1}{\mathbf{s}^H \tilde{\mathbf{R}}^{-1} \mathbf{s}}, \quad (2.22)$$

that when substituted into (2.20) yields the familiar gain-constrained form for the FAPC filter as

$$\tilde{\mathbf{w}}(\ell) = \frac{\tilde{\mathbf{R}}^{-1}(\ell) \mathbf{s}}{\mathbf{s}^H \tilde{\mathbf{R}}^{-1}(\ell) \mathbf{s}}. \quad (2.23)$$

The factor of  $1/M$  used to appropriately normalize the  $M$  segments of the approximated cost function in (2.13) does not appear in (2.23) since the MVDR formulation intrinsically provides the necessary normalization factor. In the next section the application of the APC and FAPC filters will be discussed followed by simulation results. It will be shown that the MVDR formulation of the reduced-dimension algorithm achieves superior detection performance when compared to the original MMSE-based FAPC.

## 2.4 IMPLEMENTATION

Both of the constrained filters utilize a re-iterative MMSE structure that relies on prior information obtained from an initial estimate of the complex amplitudes or the estimate from a previous stage. Figure 2.2 illustrates the re-iterative process, described below, used to obtain the gain-constrained APC and FAPC range profile estimates. Initially, the power estimates  $\rho(\ell - N + 1), \rho(\ell - N + 2), \dots, \rho(\ell + N - 1)$  required to form  $\mathbf{R}_s(\ell)$  and  $\tilde{\mathbf{R}}_{s,m}(\ell)$  from (2.5) and (2.18), respectively, are estimated by applying the matched filter. Next, an adaptive filter for each range cell is formed based on (2.9) for Gain-Constrained APC or (2.23) for Gain-Constrained FAPC. A new estimate of the amplitude at the  $\ell^{\text{th}}$  range cell is obtained by applying the unique pulse compression filter for that range cell as

$$\hat{x}(\ell) = \mathbf{w}^H(\ell) \mathbf{y}(\ell). \quad (2.24)$$

The new range cell estimates may be used to recalculate the adaptive filter weights, which are then applied to update each range cell estimate. The algorithm typically converges in 2-3 stages beyond the matched filter initialization. As in [13], a heuristic lower bound has been placed on the range cell estimates to prevent the covariance matrices (that rely on previous estimates) from becoming ill-conditioned. Also, note that efficient implementation strategies were presented in [13] and [22] that are also applicable for the MVDR formulations.

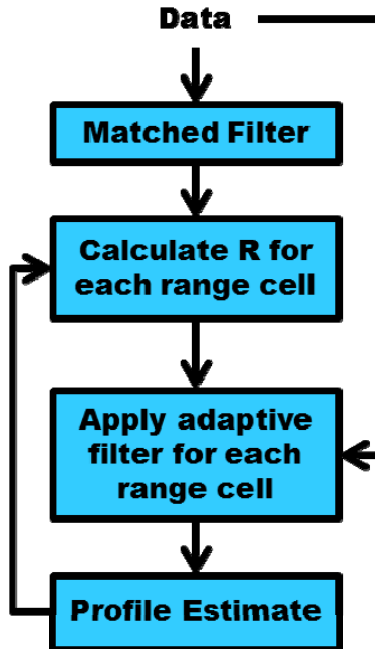


**Figure 2.2** Block diagram of adaptive filter implementation

## 2.5 SIMULATION RESULTS

Two cases are examined, 1) a large scatterer near a small scatterer and 2) a dense range profile. In both cases the transmit waveform is a length  $N = 64$  Lewis-Kretschmer P3 code [8]. The gain-constrained MVDR formulations of APC and FAPC will be compared to the normalized matched filter and a length-256 Least-Squares based mismatch filter in addition to the unconstrained algorithms. FAPC will utilize a segmentation factor of  $M = 4$  which reduces the computational cost of the full-dimension algorithm by a factor of approximately ten in this scenario.

First consider the case of a large scatterer (60 dB SNR after pulse compression) within close proximity to a smaller scatterer (15 dB SNR after pulse compression). In this scenario the sidelobes of the matched filter and, to a lesser degree, the mismatch filter obstruct detection of the small scatterer as seen in Fig. 2.3. In addition, Figure 2.3 compares APC and the gain-constrained

MVDR formulation, both of which suppress the range sidelobes into the noise. Note that little improvement is achieved when the APC algorithm is constrained to unity gain at the match point. However, it is evident from Fig. 2.4 that the unity-gain constraint applied to the contiguous embodiment of the FAPC algorithm alleviates the 1.5 dB of mismatch loss present at the location of the small target (range cell 35). In addition, the MVDR formulation of FAPC eliminates what is essentially an “over-suppression” characteristic (*i.e.* below the noise) of the unconstrained algorithm as observed in Fig. 2.4 and described in [22]. In fact, the MVDR FAPC results in Fig. 2.4 look very much like the full-dimension APC (MMSE or MVDR) observed in Fig. 2.3.

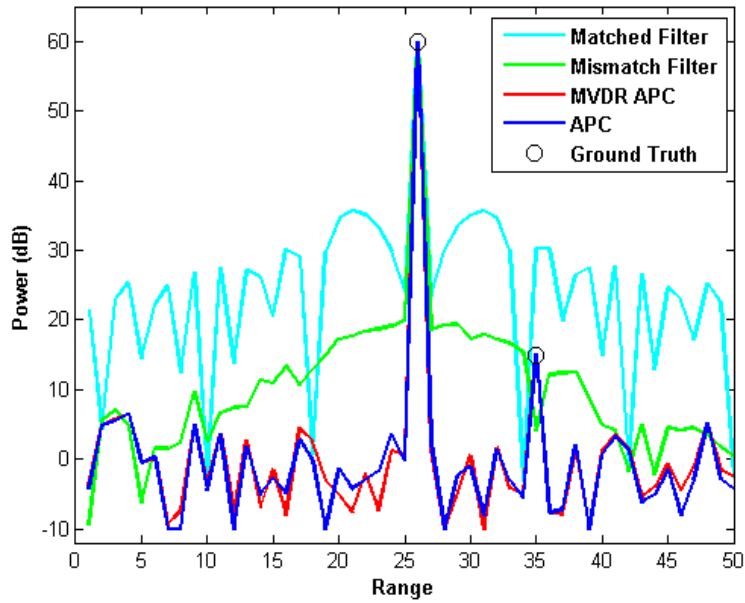


**Figure 2.3** Comparison of APC and Gain-Constrained APC, masked scatter scenario

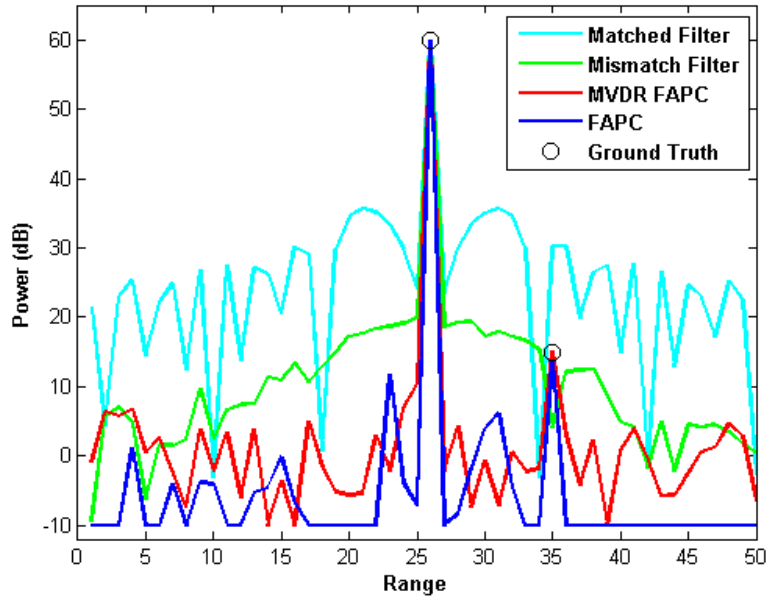


**Figure 2.4** Comparison of FAPC and Gain-Constrained FAPC ( $M = 4$ ), masked scatter scenario

Next we consider the case of a large scatterer (60 dB SNR after pulse compression) surrounded by several smaller scatterers. Figure 2.5 compares APC and the gain-constrained MVDR formulation. Again, neither algorithm suffers from mismatch loss. Fig. 2.6 illustrates the benefit of the Gain-Constrained FAPC algorithm in a dense scattering environment. Here the FAPC algorithm utilizes a limited amount of degrees of freedom to cancel the sidelobes from large scatterers resulting in the suppression of small targets. The addition of the gain-constraint reduces the "over-suppression" of sidelobes thereby enabling the small scatterers at, for example, range indices 4 and 18 to be more easily detected. Note that for the unconstrained adaptive algorithms the severity of the mismatch loss for a particular range cell is dependent upon the relative powers of the scatterers in the surrounding cells.

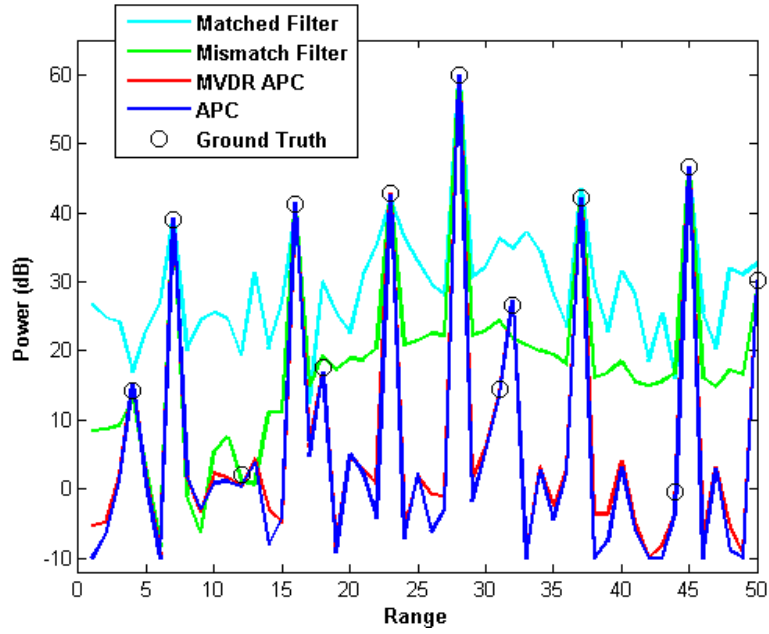


Figure 2.5 Comparison of APC and Gain-Constrained APC, dense scenario

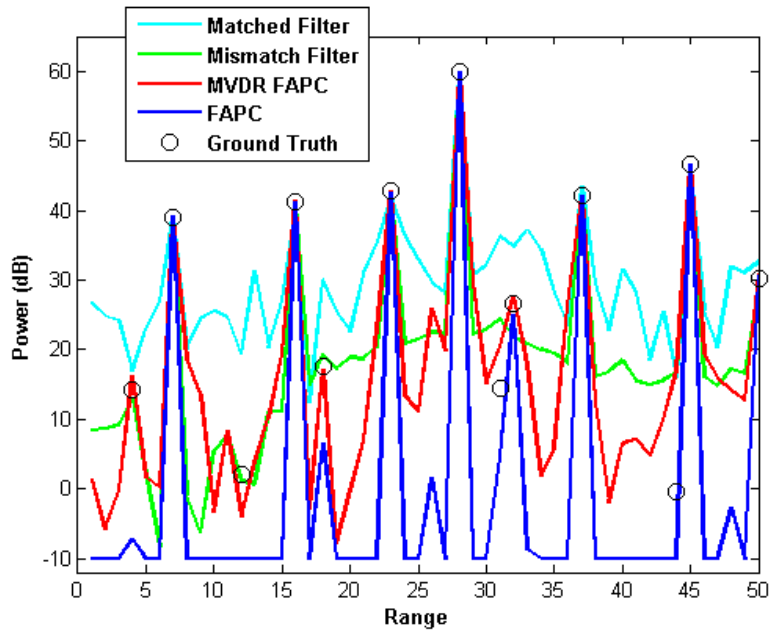


Figure 2.6 Comparison of FAPC and Gain-Constrained FAPC ( $M = 4$ ), dense scenario

## 2.6 CONCLUSIONS

The Adaptive Pulse Compression (APC) algorithm is capable of suppressing the sidelobes into the noise by adaptively estimating a pulse compression filter for each range cell. Currently, APC is limited in real-time applications due to the computational complexity of the algorithm. The recently developed Fast APC (FAPC) algorithm exploits reduced-dimensionality techniques to reduce computational cost while maintaining much of the performance benefit. However, the reduction in degrees of freedom intrinsic of the FAPC formulation introduces a small mismatch loss. In this chapter Gain-Constrained APC and FAPC are constructed by casting the respective MMSE cost functions into an MVDR framework via inclusion of a unity gain-constraint. It is observed that the full-dimension algorithm benefits little from the constraint. However, the reduced dimension algorithm exhibits improved detection performance especially when small scatterers are present.

Re-iterative super resolution (RISR) can also suffer from insufficient degrees of freedom due to the oversampling of the Doppler or spatial frequency space. Hence, RISR benefits from the application of a gain-constraint. Later, the MVDR concept will be used to formulate gain-constraints for multi-dimensional RMMSE algorithms. In the next chapter range-angle coupled beamforming strategies will be examined.

## **CHAPTER 3            ANALYSIS OF RANGE-ANGLE COUPLED BEAMFORMING MIMO ARCHITECTURES**

Traditionally, electronically scanned radar systems apply a fixed (over the duration of a single pulse) inter-element phase shift to the waveforms transmitted from each element of an array. Transmitting different, albeit correlated, waveforms from the elements on an array has been proposed [10-12, 24-27] as a method to effectively broaden the transmit beamwidth, thus alleviating some of the requirements associated with multi-mode radar. For example, surveillance radars may be responsible for searching a large volume thus limiting the duration of the CPI for a particular spatial direction whereas ISAR imaging requires a long CPI in a fixed spatial direction. Beam-spoiling offers the distinct benefit of allowing both long CPI's and a large volume of coverage. In addition to potentially enabling simultaneous multi-mode operation, waveform diversity enhances protection against passive exploitation.

The remainder of this chapter will investigate, in detail, the concept of employing a time-varying (within the duration of a single pulse) inter-element phase shift. These waveforms are a subset of the more general multiple input multiple output (MIMO) radar waveform framework. First, the frequency diverse array (FDA) proposed in [24], which involves applying an incremental frequency shift to the waveforms on each element of the array, will be examined. Specifically, chirp waveforms with slightly different starting frequencies are used to characterize the associated range-dependent beampattern and determine the usefulness of the frequency diverse array architecture in the context of radar. Initially, it is determined that by utilizing this particular waveform structure, the energy transmitted over a pulse duration can be spread in a

practically linear manner within the spatial extent specified by two angles, despite the non-linear relationship between spatial and electrical angles if the set of frequency-diverse chirps are appropriately parameterized. Additionally, a time-varying beam pattern, aggregate beam pattern, and space-range ambiguity diagram is formulated. The properties of the FDA are discussed relative to the traditional case. Finally, a more flexible digital approach entitled the digital waveform diverse array (DWDA) is considered to allow additional freedom in waveform selection and provide greater control over the range-dependent beam pattern. Examples of the ambiguity for two different DWDA approaches will be compared to the FDA and traditional architectures.

### 3.1 *FREQUENCY DIVERSE ARRAY CHIRP STRUCTURE*

The frequency diverse array (FDA) approach involves modulating a single waveform to slightly different center frequencies for each transmit element of the array. The time-varying elemental phase shift induced by the inter-element frequency difference creates a time-varying beam pattern. For an FDA the spatial extent of the range-dependent beam pattern for a given frequency shift and pulse duration is dependent upon the fixed portion of the phase offset across the array (*i.e.* the “traditional” beamforming component) due to the non-linear relationship between the elemental phase shift and spatial angle. A chirp structure is utilized to determine the proper frequency offset so as to provide the desired spatial extent of the beam pattern given the fixed portion inter-element phase shift (that provides the coarse spatial steering). Based on this structure it can be determined how much spatial spreading is possible, for a given coarse steering angle, in order to maintain an approximately linear distribution of energy in space.

Consider the case where the chirp waveform on the  $m^{\text{th}}$  element of an  $M$  element linear array is given by

$$s_m(t) = \cos\left(2\pi(f_0 + m\Delta f)t + \pi\frac{B}{T_p}t^2 - m\psi\right) \quad (3.1)$$

for  $m = 0, \dots, M - 1$  and  $0 \leq t \leq T_p$  where  $f_0$  is the start frequency,  $\Delta f$  is the elemental frequency shift,  $B$  is the bandwidth,  $T_p$  is the pulse duration, and  $\psi$  corresponds to a fixed elemental phase shift (*i.e.* between adjacent antenna elements). The total phase difference between any two adjacent elements is denoted as

$$\Delta\phi(t) = \phi_m(t) - \phi_{m-1}(t) = 2\pi\Delta f t - \psi. \quad (3.2)$$

Using the array geometry in Fig. 2.1, the following relationship can be determined:

$$\phi_{m-1}\left(t - \frac{d \sin(\theta(t))}{c}\right) = \phi_m(t) \quad (3.3)$$

for  $0 \leq t \leq T_p$  where  $\theta(t)$  is the time-varying spatial steering angle corresponding to the angle at which the  $M$  far field phase fronts align at time  $t$ . Substituting the argument of the cosine from (3.1) into (3.3) yields

$$\begin{aligned} 2\pi(f_0 + (m-1)\Delta f)\left(t - \frac{d \sin(\theta(t))}{c}\right) + \pi\frac{B}{T_p}\left(t - \frac{d \sin(\theta(t))}{c}\right)^2 - (m-1)\psi \\ = 2\pi(f_0 + m\Delta f)t + \pi\frac{B}{T_p}t^2 - m\psi. \end{aligned} \quad (3.4)$$

Rearranging (3.4) and substituting from (3.2) then produces

$$\Delta\phi(t) = -2\pi f_0 \frac{d \sin(\theta(t))}{c} - \pi \frac{B}{T_p} \frac{d \sin(\theta(t))}{c} \left( 2t - \frac{d \sin(\theta(t))}{c} \right), \quad (3.5)$$

that upon setting  $d = \frac{\lambda_{\min}}{2} = \frac{c}{2f_{\max}}$ , becomes

$$\Delta\phi(t) = -\pi f_0 \frac{\sin(\theta(t))}{f_{\max}} - \pi \frac{B}{T_p} \frac{\sin(\theta(t))}{f_{\max}} \left( t - \frac{\sin(\theta(t))}{4f_{\max}} \right). \quad (3.6)$$

Assuming  $B \ll f_{\max}$  and  $\frac{1}{T_p} \ll f_{\max}$ , and then solving (3.6) for  $\theta(t)$  results in

$$\theta(t) = \sin^{-1} \left( \frac{-f_{\max} \Delta\phi(t)}{\pi f_0} \right), \quad (3.7)$$

which is similar to the relationship observed between electrical and physical angles for traditional beamforming.

The utility of this relationship is that, for a given set of system parameters, *i.e.*  $f_0$ ,  $B$ ,  $M$ , and  $T_p$ , a range-dependent beam pattern can be formed such that the energy from a single pulse is spread in a practically linear manner between two desired spatial angles. Assuming  $f_{\max} \approx f_0$  in (3.7), the initial angle  $\theta_1$  over which the beam pattern spans is related to the elemental phase shift  $\psi$  as

$$\psi = \pi \sin(\theta_1), \quad (3.8)$$

which is equivalent to traditional beamforming. The elemental frequency shift  $\Delta f$  is then determined by evaluating (3.7) at  $t = T_p$  (again assuming  $f_{\max} \approx f_0$ ) resulting in

$$\Delta f = \frac{1}{2T_p} \left( \frac{\psi}{\pi} - \sin(\theta_2) \right), \quad (3.9)$$

where  $\theta_2$  is the terminal spatial angle.

For example, given the system parameters  $f_0 = 10$  GHz,  $B = 20$  MHz,  $T_p = 1 \mu\text{s}$ , and  $M = 20$ , consider two scenarios. In Case A let  $\theta_1 = 0^\circ$  and  $\theta_2 = -20^\circ$  and in Case B let  $\theta_1 = -40^\circ$  and  $\theta_2 = -60^\circ$ . Note that  $|\theta_2 - \theta_1| = 20^\circ$  change in spatial angle for both cases. The chirp parameters given by (3.8) and (3.9) are found as  $\psi_A = 0^\circ$ ,  $\Delta f_A = 171$  kHz and  $\psi_B = -115.7^\circ$ ,  $\Delta f_B = 111.6$  kHz. The spatial angle as a function of time for Case A is shown in Fig. 3.1 and appears to vary linearly with respect to time. Figure 3.2 displays the resulting spatial angle for Case B as well as the case when  $\Delta f$  is not adjusted to incorporate the linear phase shift  $\psi$ , *i.e.*  $\Delta f = \Delta f_A$ . Both cases in Fig. 3.2 exhibit non-linear behavior when the spatial angle moves farther from boresight as expected from the relationship in (3.7). However, it is evident that the frequency-diverse chirp structure of (3.1) allows for compensation of this non-linear mapping due to the freedom in selecting  $\Delta f$ .

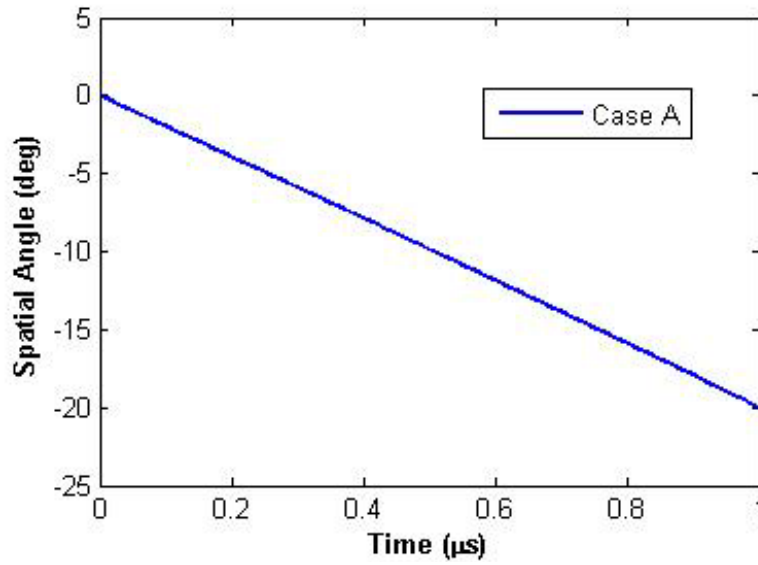


**Figure 3.1** Spatial Angle vs Time for Case A

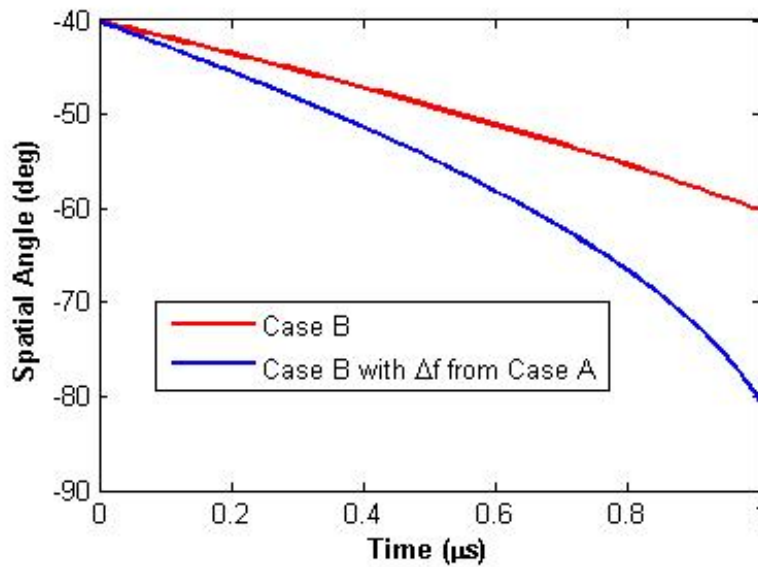


**Figure 3.2** Spatial Angle vs Time for Case B

### 3.1.1 FDA BEAMPATTERN AND AMBIGUITY ANALYSIS

Analysis of the FDA is performed by examining the time-varying beampattern (TVBP), aggregate beampattern, and a space-range ambiguity diagram (SRAD). The definitions of these

three metrics are based on the normalized composite waveform transmitted in the direction specified by the spatial angle  $\theta$ , given by

$$\tilde{s}(t, \theta) = \frac{1}{M} \sum_{m=0}^{M-1} s_m(t) e^{jm\pi \sin \theta}, \quad (3.10)$$

in which  $s_m(t)$  is the waveform transmitted on the  $m^{\text{th}}$  element of a linear array (with  $d = \frac{\lambda}{2}$ ).

The instantaneous features of the range-dependent beampattern created with the FDA can be examined using the normalized TVBP denoted as

$$B_{TV}(\theta) = |\tilde{s}(t, \theta)|^2 \quad (3.11)$$

Integrating over the temporal duration of (3.11) yields the aggregate beampattern denoted as

$$B(\theta) = \frac{1}{T_p} \int_0^{T_p} |\tilde{s}(t, \theta)|^2 dt, \quad (3.12)$$

that is used to quantify the spatial distribution of energy within a single transmit pulse. It should be noted that the aggregate beampattern is normalized to the standard case with no waveform diversity in which  $|\tilde{s}(t, \theta)|^2$  is constant over the entire pulsewidth. The SRAD is constructed as

$$A_{\beta}(\tau, \theta) = \left| \frac{1}{\int_0^{T_p} |\tilde{s}(t, \beta)|^2 dt} \int_0^{T_p} \left[ \frac{1}{M} \sum_{m=0}^{M-1} \tilde{s}(t, \theta) e^{jm\pi \sin \theta} e^{-jm\pi \sin \beta} \right] \tilde{s}^*(t - \tau, \beta) dt \right|^2 \quad (3.13)$$

where  $(\bullet)^*$  denotes the conjugate operation and  $\tau$  is a relative delay. Note that in the SRAD formulation the term  $\tilde{s}(t, \theta) e^{jm\pi \sin \theta}$  is representative of a target return from angle  $\theta$  and delay  $\tau$ .

Additionally, the exponential term  $e^{-jm\pi\sin\beta}$  is associated with the spatial matched filter for angle

$\beta$  and  $\int_0^{T_p} |\tilde{s}(t, \beta)|^2 dt$  is a normalization factor that accounts for transmit beamforming and pulse

compression matched filtering gains. Hence, the ambiguity diagram relates the received energy from angle  $\theta$  at  $t=0$  to the normalized matched filter for angle  $\beta$  and delay  $\tau$ . Reorganizing (3.13), results in the simplified expression for the SRAD

$$A_\beta(\tau, \theta) = \left| \left[ \frac{1}{M} \sum_{m=0}^{M-1} e^{jm\pi(\sin\theta - \sin\beta)} \right] \frac{\int_{-\infty}^{\infty} \tilde{s}(t, \theta) \tilde{s}^*(t - \tau, \beta) dt}{\int_{-\infty}^{\infty} |\tilde{s}(t, \beta)|^2 dt} \right|^2. \quad (3.14)$$

Consider three scenarios based upon the frequency diverse chirp structure in (1). The system parameters for the three cases are  $f_0 = 10$  GHz,  $B = 65$  MHz,  $T_p = 1 \mu\text{s}$ , and  $M = 20$ . The range-dependent beampattern for each case is specified by the initial and final angles as, Case 1:  $\theta_1 = 0^\circ$ ,  $\theta_2 = 0^\circ$  (*i.e.* no frequency diversity), Case 2:  $\theta_1 = -10^\circ$ ,  $\theta_2 = 10^\circ$ , and Case 3:  $\theta_1 = -30^\circ$ ,  $\theta_2 = 30^\circ$ . Figure 3.3 displays the TVBP and aggregate beampatterns for the three cases. It is evident from Fig. 3.3 that the energy in Cases 2 and 3 is spread evenly over the desired spatial extent which is attributed to the method for selecting  $\Delta f$  defined in Section 3.1. The aggregate beampattern illustrates the reduced maximum power that is delivered to a single angle which is a direct consequence of the beamspoiling induced by the FDA.

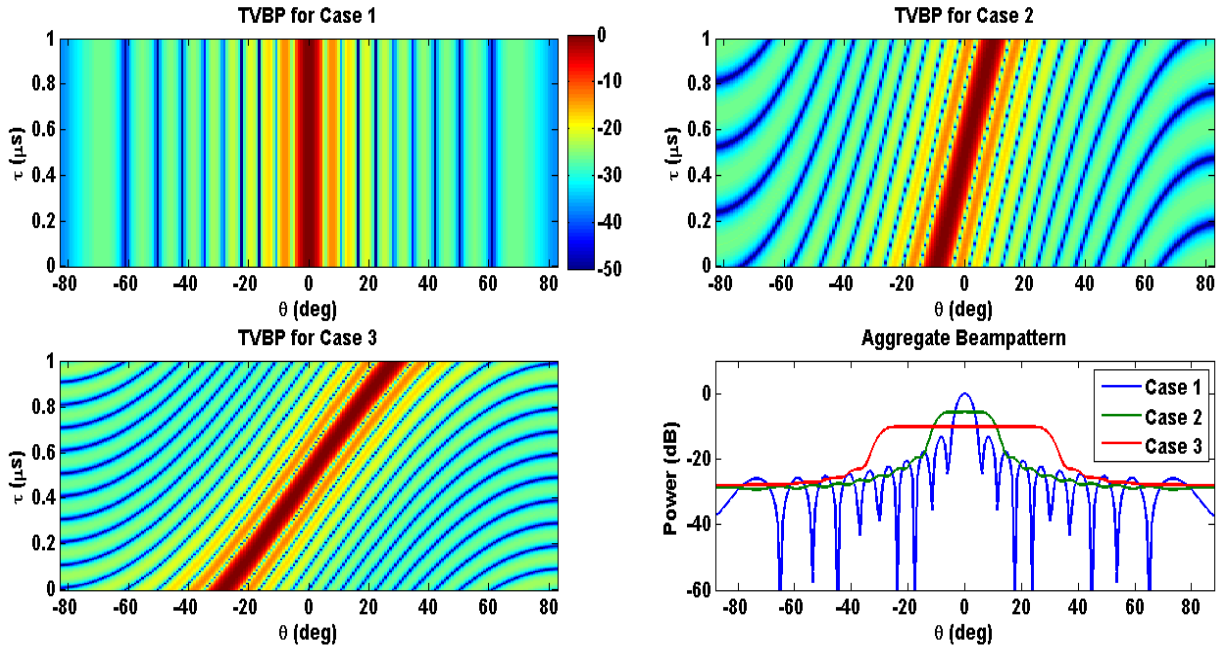


**Figure 3.3** TVBP for FDA Cases 1-3 (in dB) and associated aggregate beampatterns (aggregate beampatterns are normalized to Case 1: no frequency diversity)

Figures 3.4, 3.5, and 3.6 illustrate the space-range ambiguity diagrams, formed by employing (13) with  $\beta = 0^\circ$  for Cases 1, 2, and 3, respectively. Note that the temporal, or range, sidelobes decrease as the transmit beampattern is widened. Also, there is a strong space-range coupling present in Case 3 that can be expected given the TVBP for this case as shown in Fig. 3.3. The FDA technique redistributes the ambiguity such that the spatio-temporal extent of the central peak in the SRAD increases when the energy is distributed over a wider spatial extent as seen in Fig. 3.7. The impact of these properties is an effective loss in temporal resolution when the FDA technique is employed.

The upper portion of Fig. 3.8 shows the  $\theta = 0^\circ$  cut of the normalized boresight ambiguity diagram versus delay for the three scenarios. Notice Cases 2 and 3 exhibit degraded range (temporal) resolution but lower range sidelobes than Case 1. The range-dependent beampatterns

of Cases 2 and 3 have effectively windowed (in time) the composite waveform transmitted in the boresight direction by electronically steering the mainlobe of the array past boresight as the pulse is transmitted. The amplitude weighting imposed on the composite waveform is symmetric at boresight because it lies in the middle of the spatial extent of the beam pattern in all cases. Due to the structure of the chirp waveform this windowing effectively limits the bandwidth of the composite waveform transmitted in a particular spatial direction. The degradation of the range resolution can also be associated with this reduction in bandwidth since range resolution and bandwidth are inversely proportional. What was originally a good radar waveform has now been distributed spatially such that the composite waveform in an individual direction does not retain the desirable properties associated with the original waveform. The lower plot in Fig. 3.8 displays the  $\tau = 0$  cut of the boresight ambiguity diagrams ( $A_0(\tau, \theta)$ ) in Figs. 3.4-3.6 versus spatial angle  $\theta$  for the three cases. Note Case 2 and Case 3 exhibit slightly lower spatial sidelobes than the traditional case. Recall the spatial spreading of the central peak in the SRAD for Cases 2 and 3, and observe that the cut in Fig. 3.8 does not illustrate this feature. This is because the spreading effect is caused by the change in the shape of the spatial component of the ambiguity as you progress through delay (range).

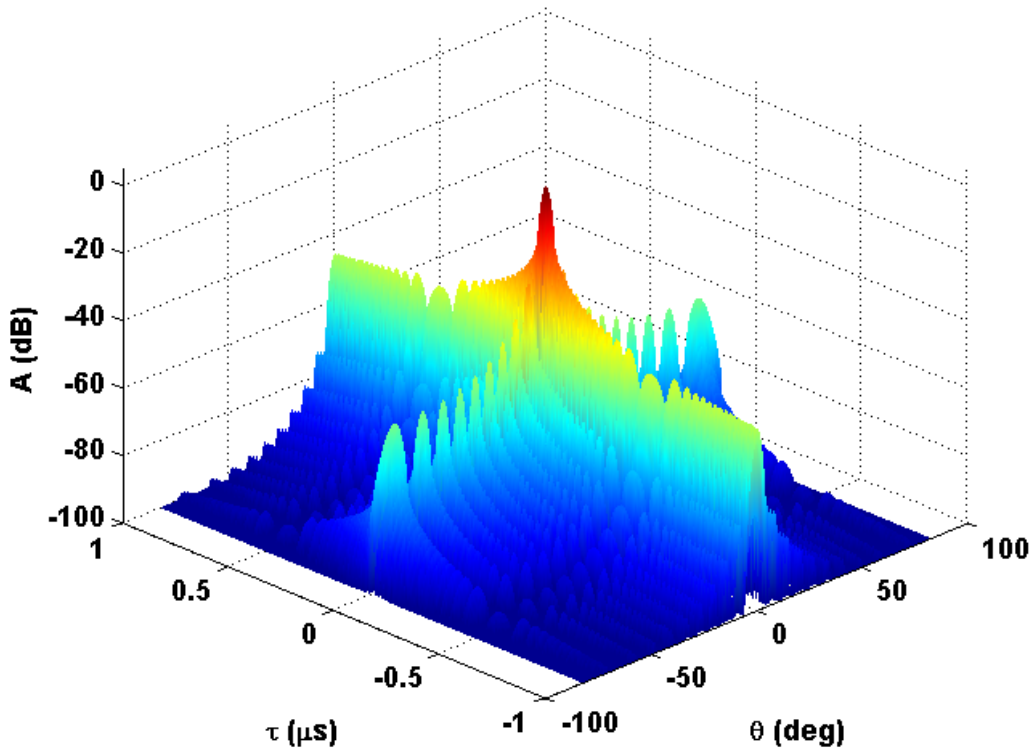


Figure 3.4 SRAD (in dB) for FDA Case 1

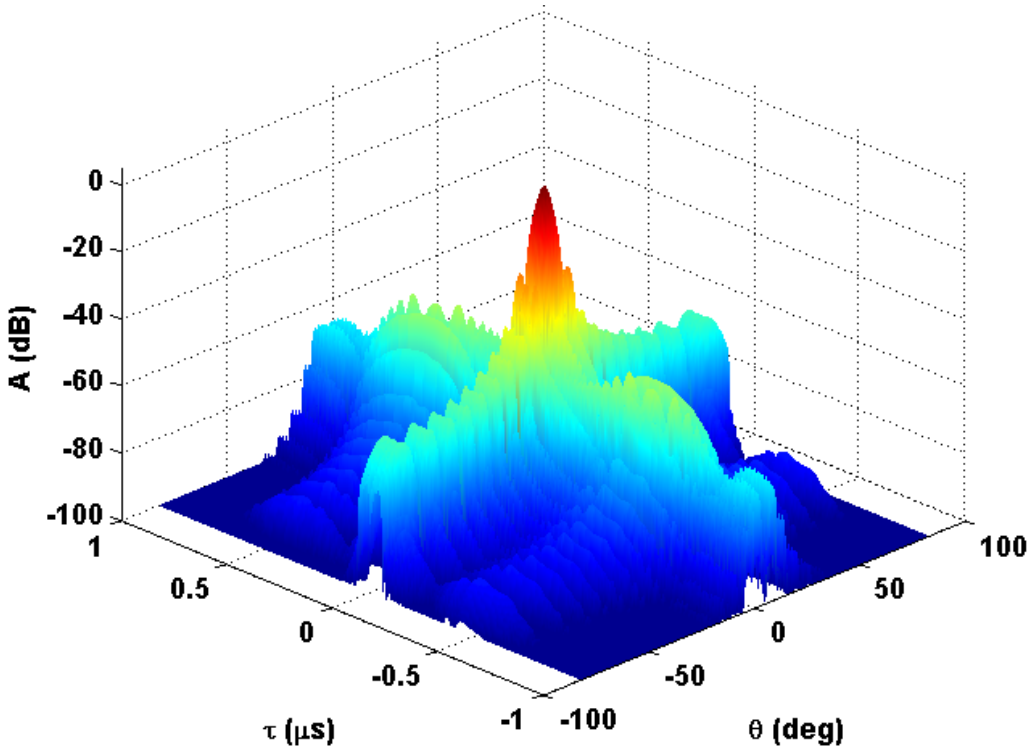


Figure 3.5 SRAD (in dB) for FDA Case 2

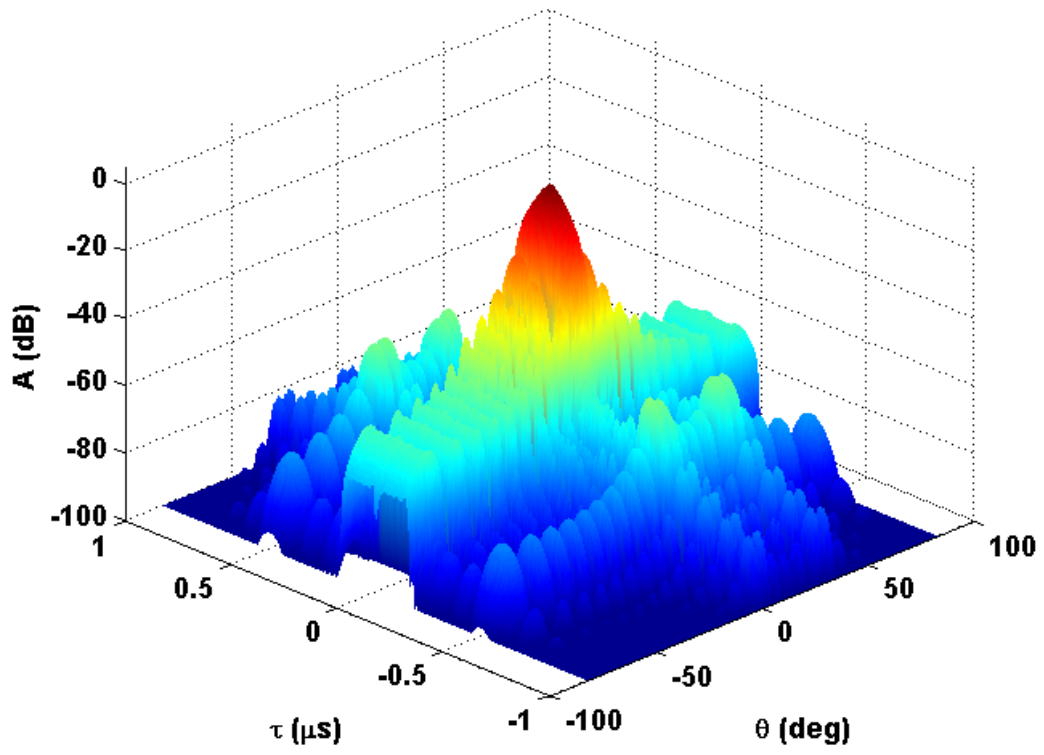
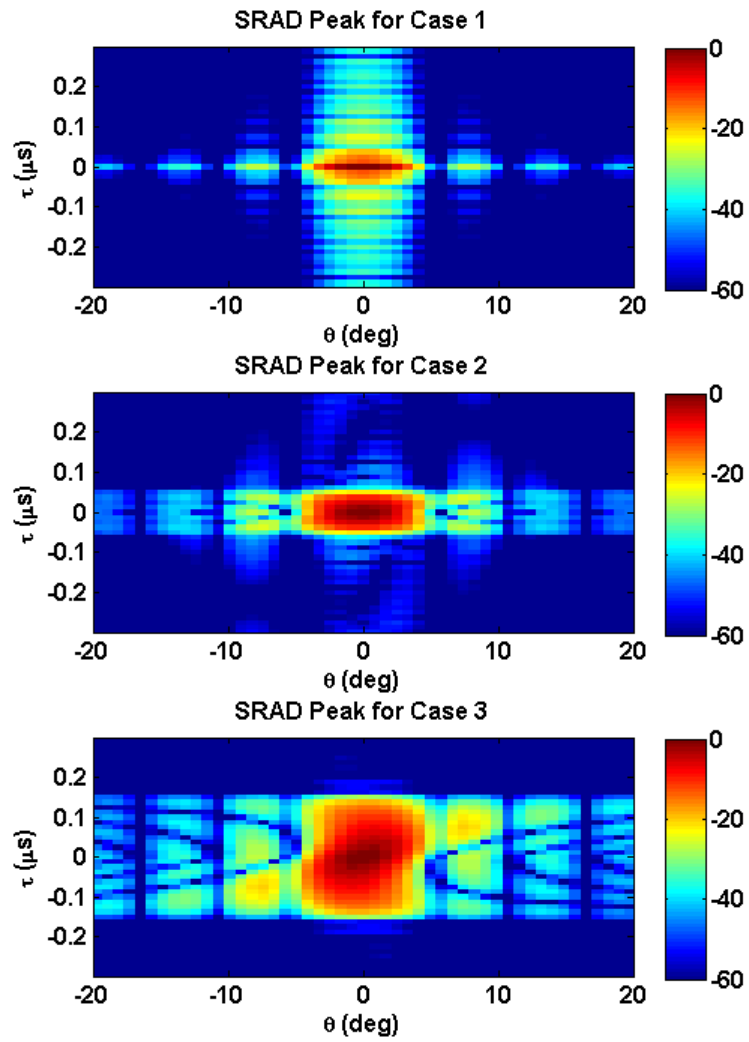
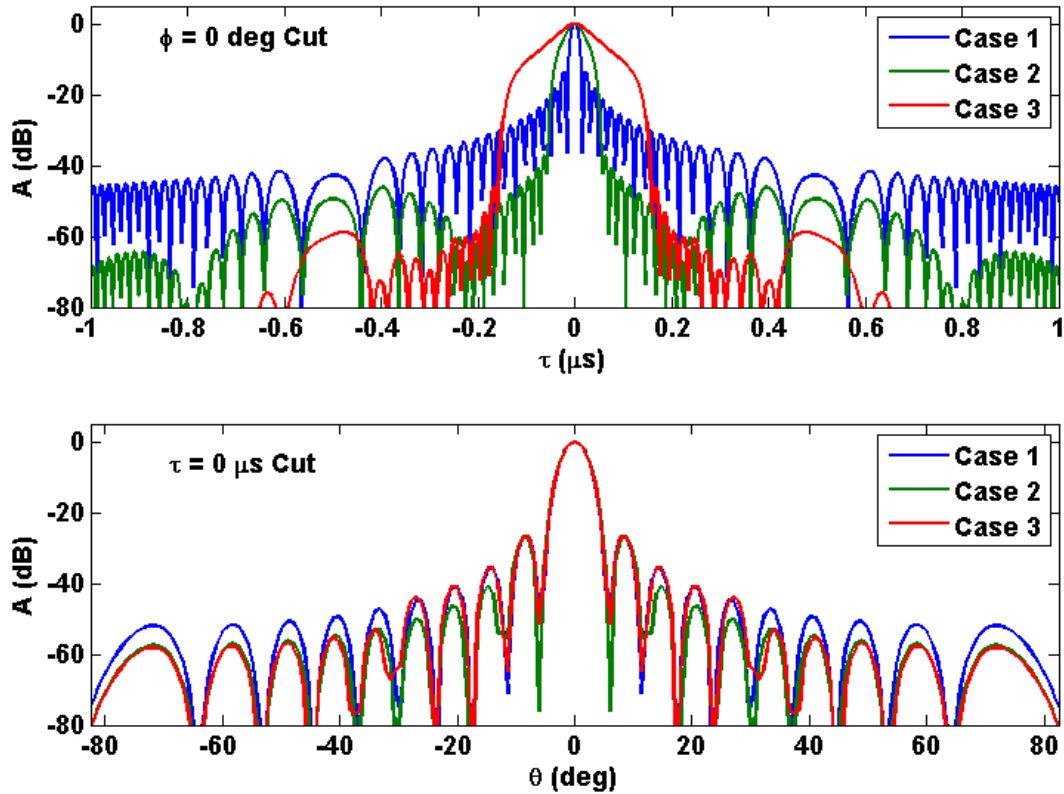


Figure 3.6 SRAD (in dB) for FDA Case 3



**Figure 3.7** Peak of SRAD (in dB) for FDA Cases 1-3



**Figure 3.8** Temporal and spatial cuts of SRAD for FDA Cases 1-3

Although the frequency diverse array offers the potential benefit of beamspooling on transmit, other characteristics, specifically the degradation of range resolution and spatial spreading of the central peak of the SRAD, are not particularly well suited for radar operations. Next, a more general framework for forming range-dependent beampatterns entitled the digital waveform diverse array is examined.

### 3.2 DIGITAL WAVEFORM DIVERSE ARRAY

The digital waveform diverse array (DWDA) concept employs a digital arbitrary waveform generator behind each element of an antenna array. This independent element level waveform control can be utilized to embed an intra-pulse steering by creating a time varying phase shift between the waveforms transmitted from each element. This allows a greater freedom in

waveform selection resulting in the ability to create numerous range-dependent beampatterns. Unlike the LFM waveforms employed in the previous section, the phase coded waveforms implemented within the DWDA use discrete phase values that are fixed for some duration before transitioning to the next value. As a result, the instantaneous bandwidth of phase coded waveforms is dictated by the length (temporal duration) of each discrete phase value, or chip, as well as the slope of the transition region between chips. This feature plays an important role on the shape of the central peak of the SRAD for the DWDA.

Several techniques have been proposed for achieving a desired beampattern [10-12] using phase only coefficients across the elements of a digital array. Here a simple yet effective approach is used to design the transmitted waveforms such that a desired beam pattern is realized. First, a set of  $Z$  desired spatial angles  $\theta_0, \theta_1, \dots, \theta_{Z-1}$  will be assigned  $Z$  length- $N/Z$  discretized waveforms  $\mathbf{s}_0, \mathbf{s}_1, \dots, \mathbf{s}_{Z-1}$ . These waveforms will be then be interleaved in a time-division multiple access (TDMA) fashion to create a single length- $N$  waveform that is repeated for each array element expressed as

$$\tilde{\mathbf{S}} = \text{vec} \left( \begin{array}{c} \left[ \begin{array}{c} \mathbf{s}_0^T \\ \mathbf{s}_1^T \\ \vdots \\ \mathbf{s}_{Z-1}^T \end{array} \right]_{Z \times \frac{N}{Z}} \\ \left[ 1 \ 1 \ \dots \ 1 \right]_{1 \times M} \end{array} \right) \quad (3.15)$$

Finally, the spatial steering associated with each waveform will be applied by imposing the corresponding elemental phase shift to each of the interleaved pieces of the waveforms as

$$\mathbf{S} = \tilde{\mathbf{S}}_{N \times M} \odot \exp \left( j \left( \begin{bmatrix} \mathbf{I}_{Z \times Z} \\ \mathbf{I}_{Z \times Z} \\ \vdots \\ \mathbf{I}_{Z \times Z} \end{bmatrix}_{N \times K} \begin{bmatrix} \pi \sin \theta_0 \\ \pi \sin \theta_1 \\ \vdots \\ \pi \sin \theta_{Z-1} \end{bmatrix}_{Z \times 1} [0 \ 1 \ \dots \ M-1]_{1 \times M} \right) \right). \quad (3.16)$$

This particular method produces a sawtooth raster scan but the order can be augmented by reorganizing the rows of  $\mathbf{S}$ . Note in (3.16) that each temporal sample of an underlying waveform  $\mathbf{s}_z$  is transmitted in the same direction. Traditionally the elemental phase shift is applied over the duration of an entire transmit pulse whereas in (3.16) the phase shift is altered several times within a pulse to steer different portions of the temporal waveform to different spatial locations. In addition to the added benefits of beamspooling on transmit the DWDA enables the ability to transmit different waveforms, for example, search, track, and imaging waveforms, to different spatial locations within a single pulse duration. As was shown for the FDA in the previous section, these advantages come at a significant cost in radar sensitivity. The next section utilizes the SRAD to determine the effects of this transmit strategy on radar performance.

### 3.2.1 DWDA BEAMPATTERN AND AMBIGUITY ANALYSIS

As an example consider the three cases given in Table 3.1. Note that pulse width, time-bandwidth product, number of elements, spatial coverage used here are similar to those used in the FDA examples from Section 3.1. The parameters in the table will be used for two different waveform configurations; in Scenario A all underlying waveforms ( $\mathbf{s}_z$ ) are the same and in Scenario B all underlying waveforms are different. First, Scenario A will be discussed in which a P3 polyphase coded [8] waveform is used as the underlying waveform.

**Table 3.1** Parameters for WDA Cases 1-3

	$M$	$N/Z$	$T_p$	$Z$	$\theta_0, \theta_1, \dots, \theta_z, \dots, \theta_{Z-1}$
Case 1	20	65	1 $\mu$ s	1	0°
Case 2	20	13	1 $\mu$ s	5	-10°, -5°, 0°, 5°, 10°
Case 3	20	5	1 $\mu$ s	13	-25°, -21°, -17°, -12.5°, -8°, -4°, 0°, 4°, 8°, 12.5°, 17°, 21°, 25°

The TVBP and aggregate beampatterns associated with Scenario A are shown in Fig. 3.9. Note that in each desired spatial angle the associated waveform is transmitted with temporal gaps between the chips of the phase code corresponding to the interval assigned to another waveform/direction pair. For Case 1 a 65-chip P3 code is transmitted to a single spatial direction but for Cases 2 and 3 shorter P3 codes are transmitted to multiple different spatial angles. The autocorrelation properties suffer as the number of the chips in the waveform is reduced, hence a degradation in the sidelobe levels for the shortened codes is expected. The aggregate beampatterns for this scenario are similar to the previous examples (from Section 3.1).

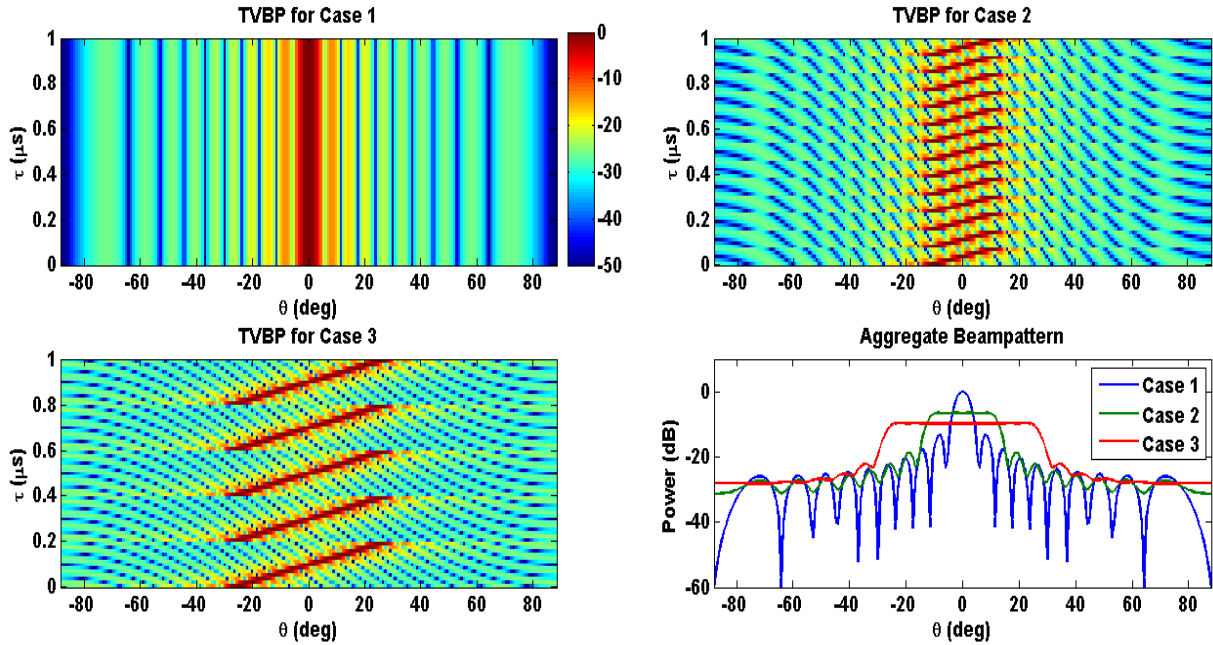


**Figure 3.9** TVBP and aggregate beampatterns (in dB) for the DWDA parameters in Table 4.1

The SRAD diagrams for Scenario A are shown in Figs. 3.10-3.12. It is immediately evident that the ambiguity created by the DWDA transmit construct differs greatly from that associated with the FDA. The SRAD for Case 2, and to a greater extent Case 3, appear to be somewhat “spiky” in the range (time) dimension. This structure is attributed to the particular scanning pattern chosen in (3.16). Unlike the SRAD for the FDA (Figs. 3.4-3.6) the DWDA does not centralize the energy near the peak but distributes the spatio-temporal ambiguity throughout the surface. Upon closer inspection of the peak of the SRAD (Fig. 3.13) for the three cases, the range resolution does not appear to degrade as before. This preservation of resolution is expected due to the aforementioned bandwidth properties of phase coded waveforms. However, the range sidelobe properties degrade as seen in the  $\theta = 0^\circ$  cut shown in the top portion of Fig. 3.14.

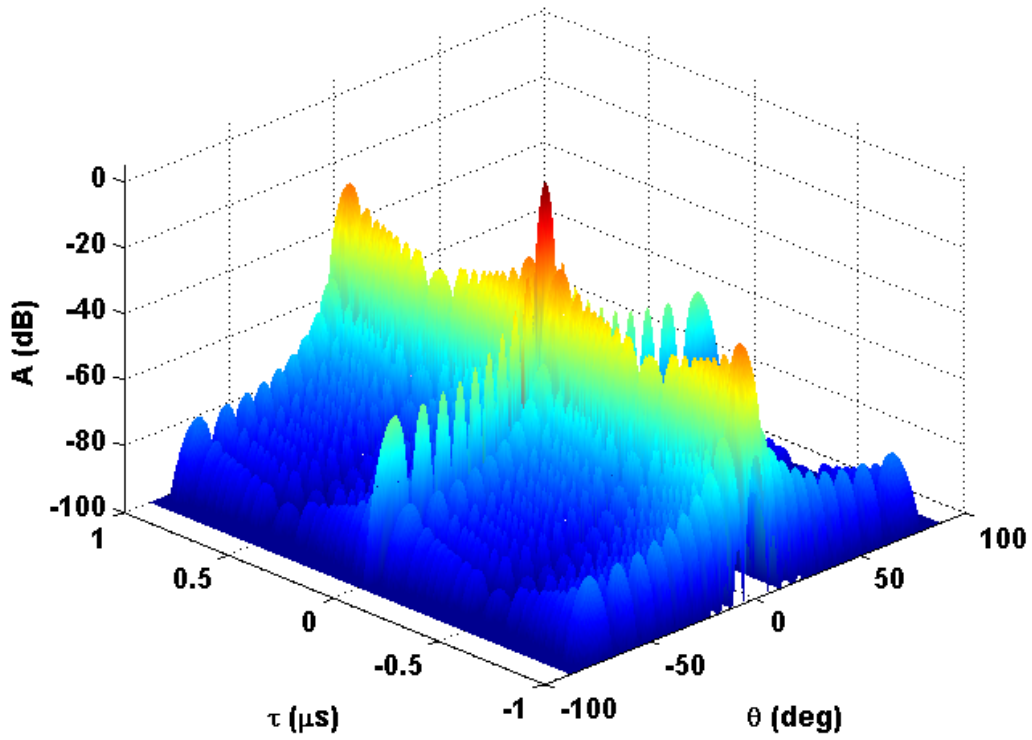


Figure 3.10 SRAD (in dB) for WDA Scenario A, Case 1

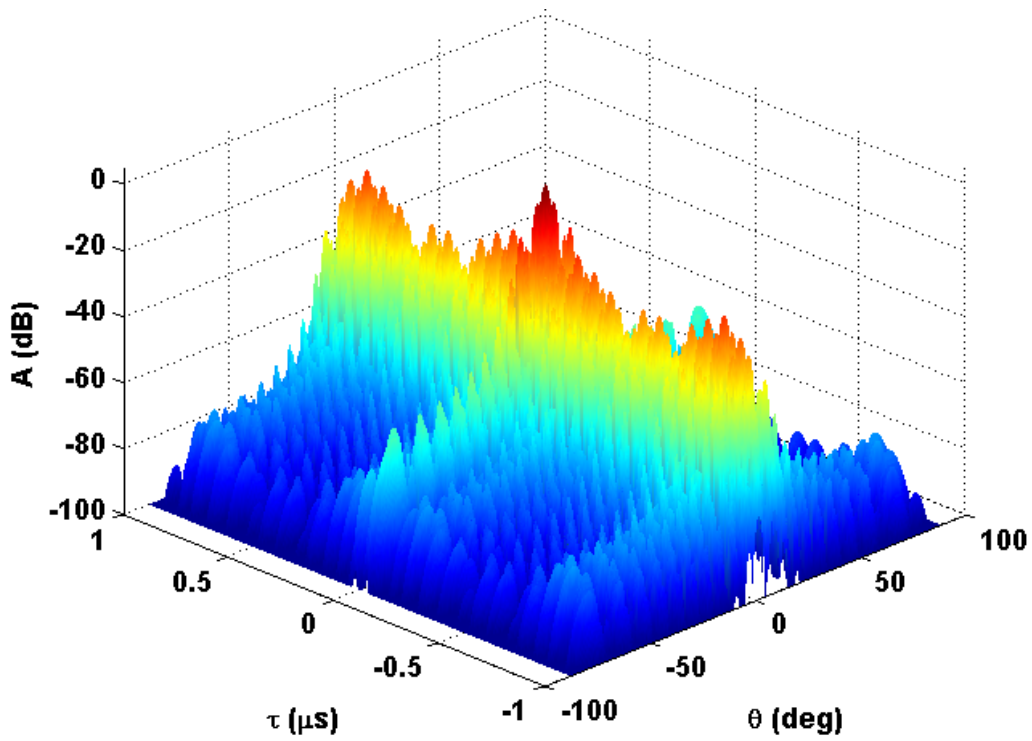


Figure 3.11 SRAD (in dB) for WDA Scenario A, Case 2

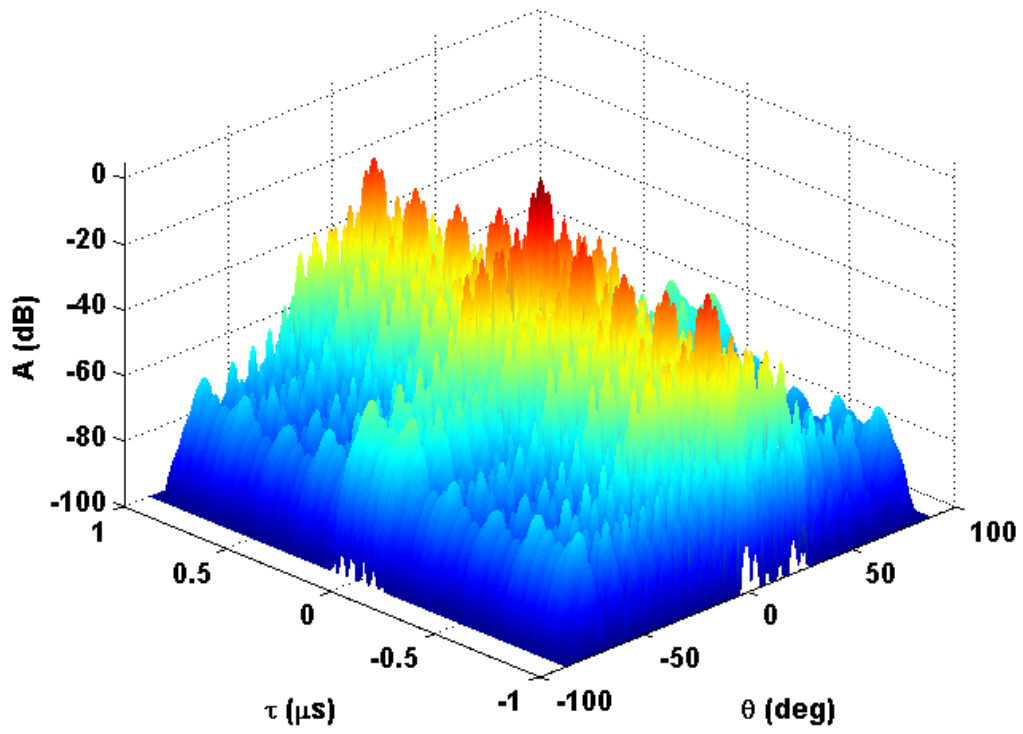


Figure 3.12 SRAD (in dB) for WDA Scenario A, Case 3

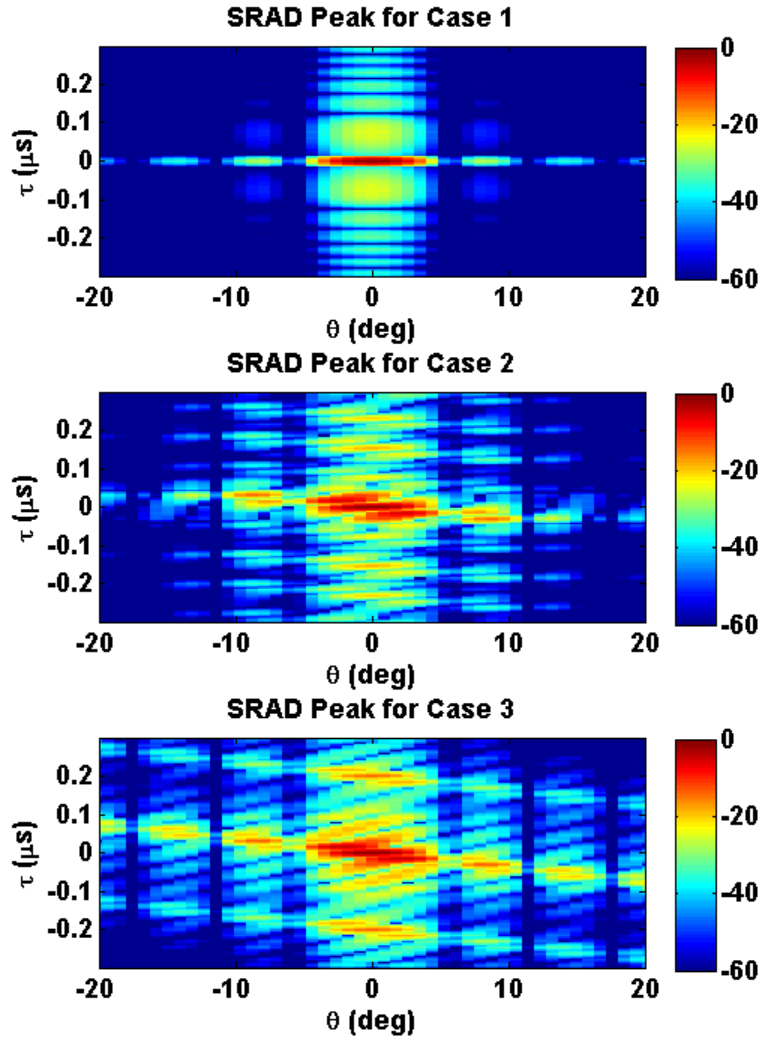


Figure 3.13 SRAD Peak (in dB) for WDA Cases 1-3 (Scenario A)

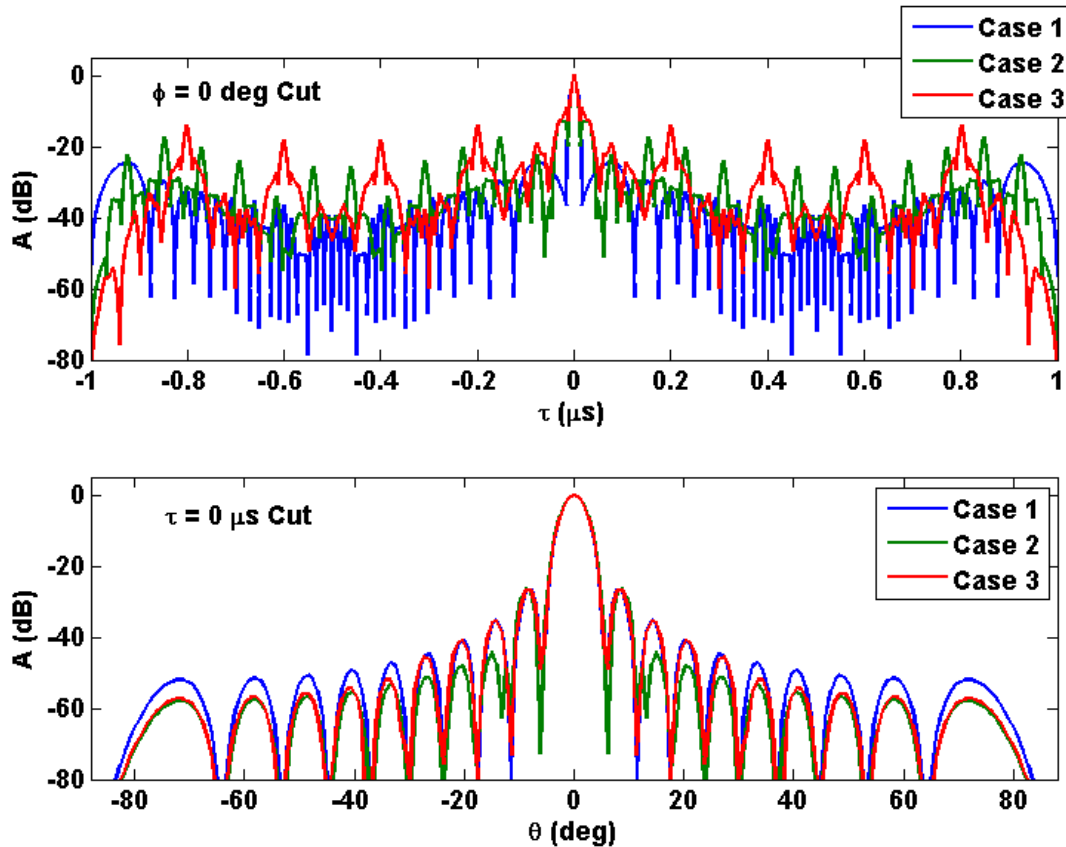
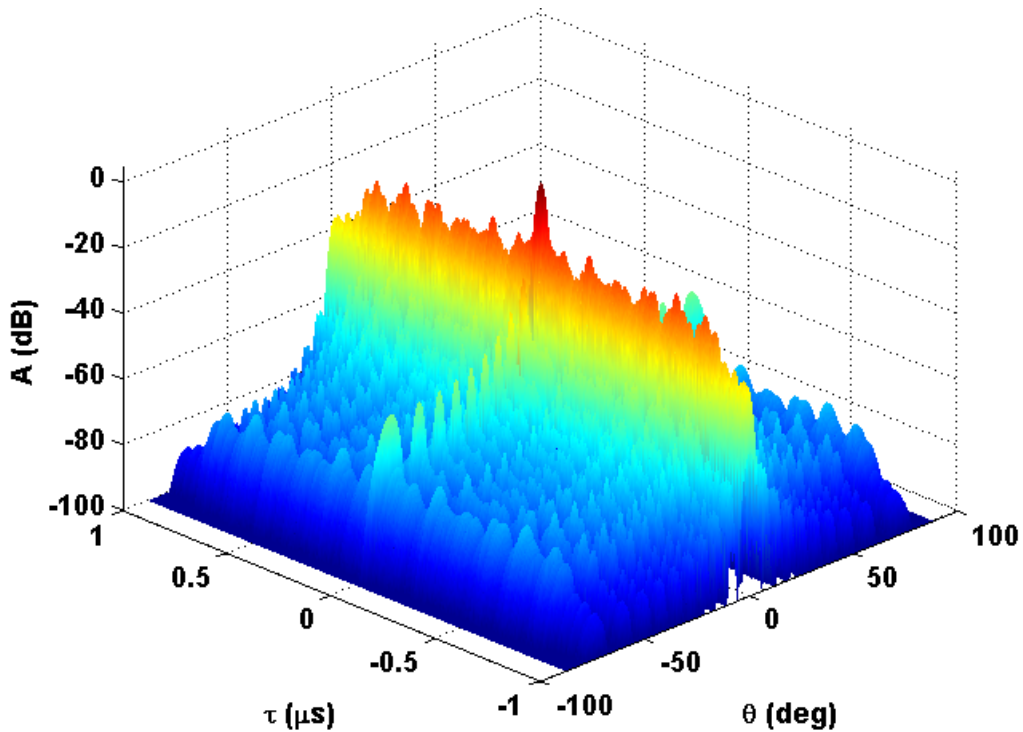


Figure 3.14 Spatial and Temporal Cuts for WDA Scenario A

Consider an alternative strategy where instead of transmitting the same underlying waveform to the discrete angles specified by  $\theta_0, \dots, \theta_{Z-1}$  a different waveform is transmitted to each desired spatial direction. This strategy (Scenario B) employs random polyphase coded waveforms (PN codes) as the underlying waveforms. In general, PN codes exhibit poor sidelobe levels but the ability to have different waveforms should reduce the spatial ambiguity peaks of the SRAD by a factor related to the cross-correlations of the underlying waveforms. The SRAD for Cases 1-3 are shown in Figs. 3.15-3.17, a closer view of the peak of the SRAD is shown in Fig. 3.18, and the central cuts are shown in Fig. 3.19. Relative to Scenario A, the range sidelobes have increased and the spatial sidelobes have decreased. The increase in range sidelobe levels is attributed to the

poor autocorrelation properties of the PN codes and the spatial ambiguity has been reduced due to the reduced cross correlation between the waveforms transmitted in different spatial directions. Note that as the code length increases, the sidelobe and cross-correlation properties improve. The PN coded waveforms used here are sub-optimal and the ambiguity diagram may improve dramatically when waveforms with better auto/cross-correlation properties (such as those in [36-37]) are employed.



**Figure 3.15** SRAD (in dB) for WDA Scenario B, Case 1

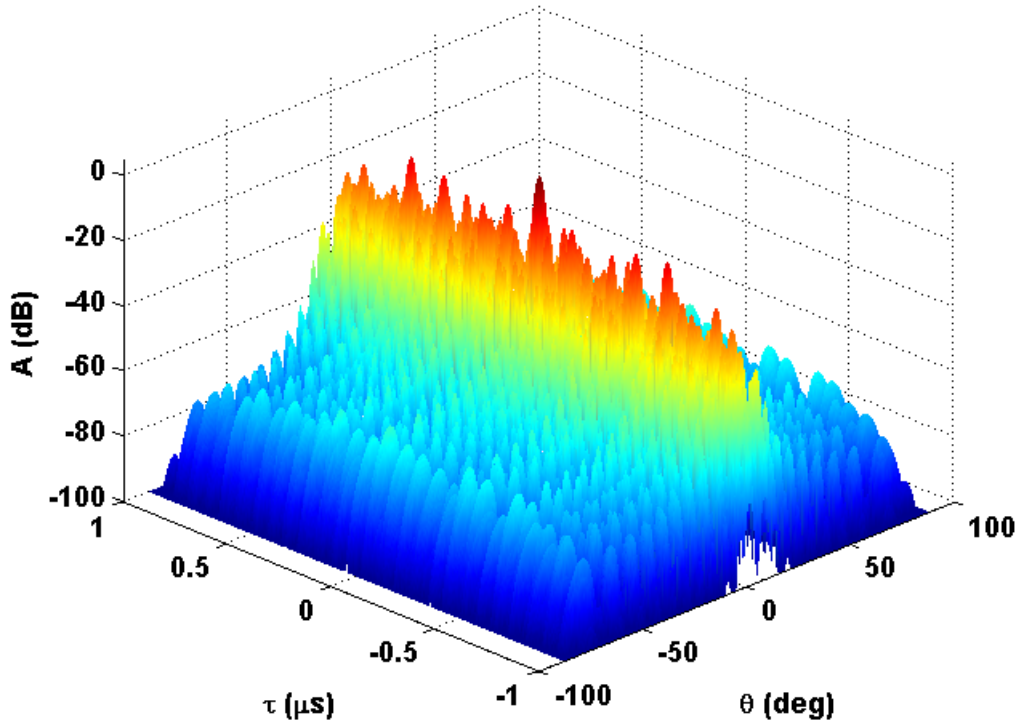


Figure 3.16 SRAD (in dB) for WDA Scenario B, Case 2

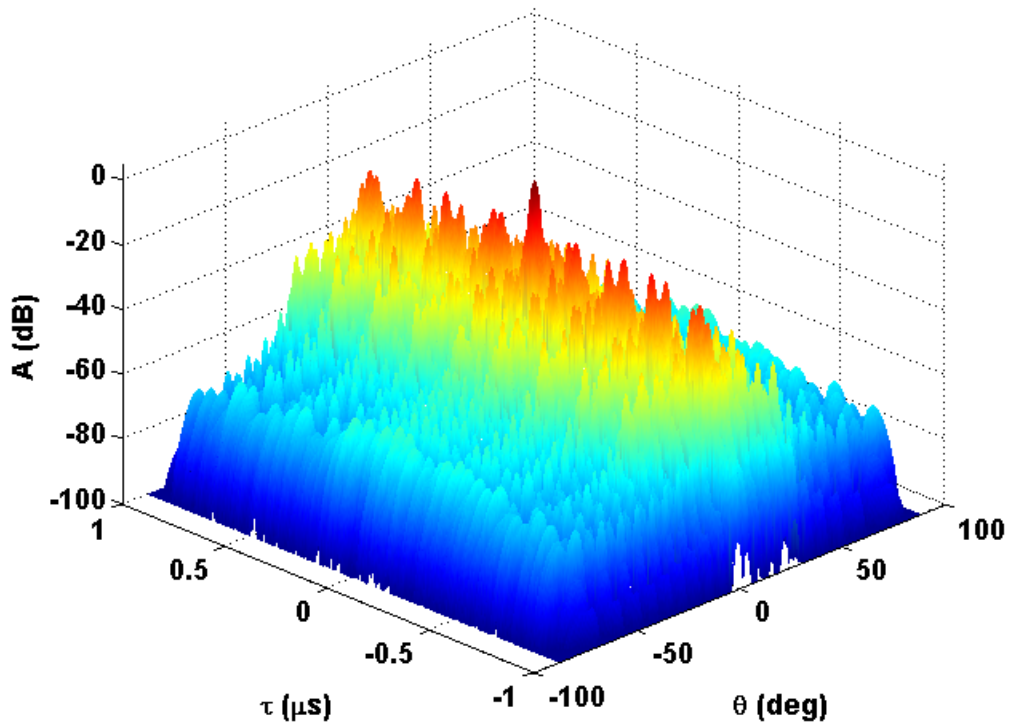
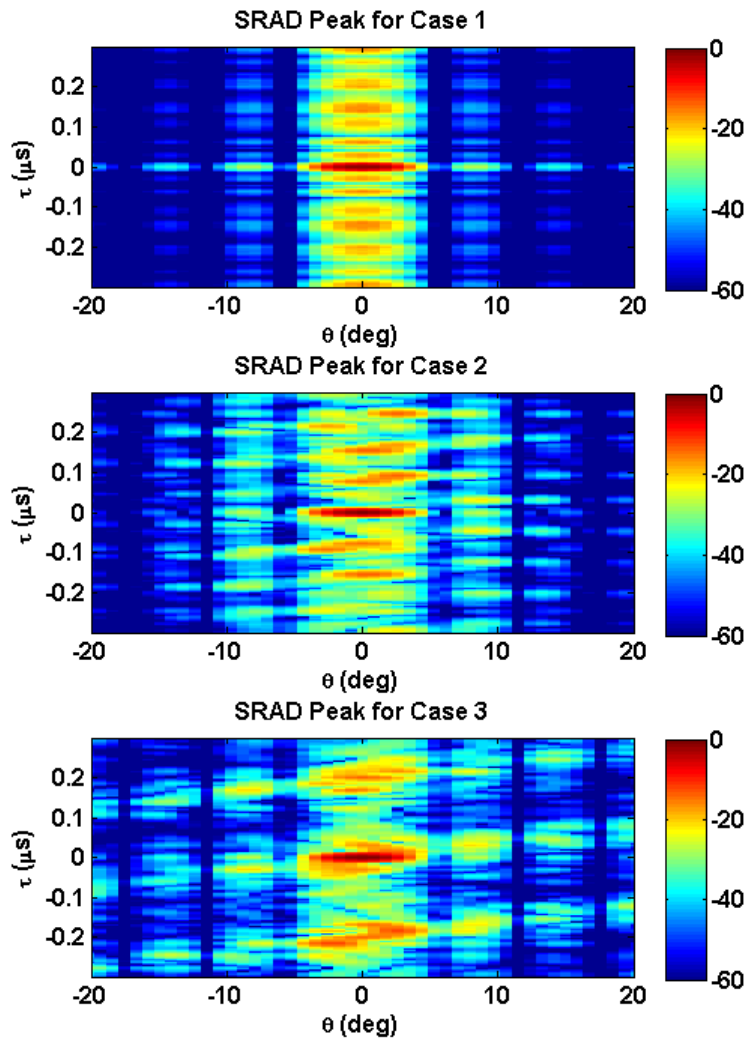


Figure 3.17 SRAD (in dB) for WDA Scenario B, Case 3



**Figure 3.18** SRAD Peak (in dB) for DWDA Scenario B

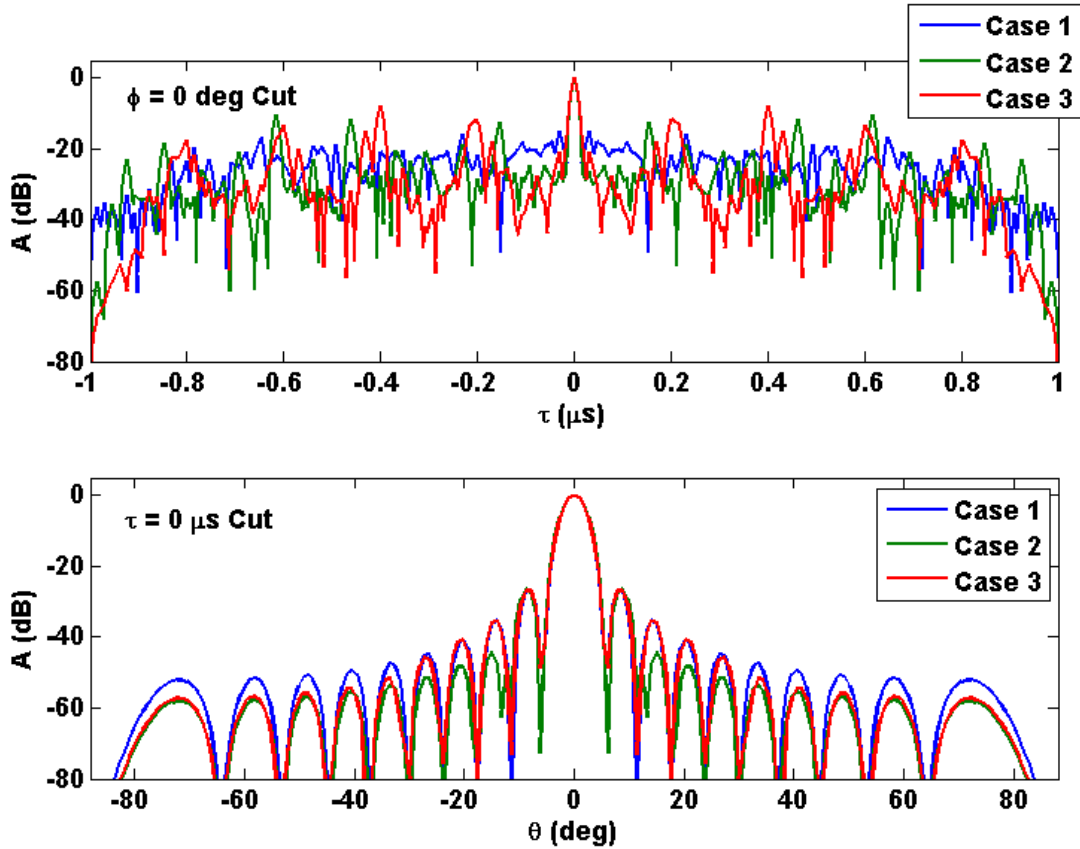


Figure 3.19 Spatial and Temporal Cuts for Scenario B

### 3.3 CONCLUSIONS

The frequency diverse array (FDA) concept is summarized and discussed in the context of chirp radar waveforms. Within this construct a method to compensate for the non-linear relationship between spatial and electrical angles is discussed such that a nearly linear distribution of energy can be achieved over a desired spatial extent regardless of the coarse steering angle. A time-varying beampattern (TVBP), aggregate beampattern, and space-range ambiguity diagram (SRAD) are presented as useful tools to analyze range-dependent beamforming strategies. The FDA is shown to exhibit reduced range sidelobes at the cost of degraded resolution. Finally, a more flexible approach entitled the digital waveform diverse array (DWDA) is discussed. The DWDA does not suffer from the loss in resolution associated with the FDA, however, the DWDA

approaches have high range sidelobes especially when the underlying waveforms are different. The next chapter will introduce a space-range coupled adaptive processing scheme that is capable of simultaneously suppressing spatial and range sidelobes thus enabling radar operations to be performed with the DWDA.

## CHAPTER 4      SPACE-RANGE ADAPTIVE PROCESSING

In the previous chapter, the concept of distributing energy from a single radar pulse over a desired spatial extent was shown to have significant effects on radar sensitivity. In this chapter a new receiver design entitled Space-Range Adaptive Processing (SRAP) is formulated to achieve the necessary radar sensitivity when waveform diversity is employed. SRAP extends the RMMSE methodology utilized by RISR and APC to a joint space-range framework in which a unique receive filter for each range-angle cell is adaptively formed.

Space-range coupled processing for a MIMO imaging modality was considered in [18-20] by means of a weighted least-squares formulation, referred to as the IAA-R algorithm, for the purpose of achieving finer resolution in angle and fast-time Doppler. The IAA-R approach performs quite well, albeit the computational cost of the algorithm in [18-20] is quite large making it difficult to simulate on current personal computing platforms. The new SRAP algorithm developed in this chapter has a significantly lower computational cost than the IAA-R approach, thus offering a distinct benefit in reduced implementation complexity.

First, a space-range coupled signal model is presented that addresses the degrees of freedom necessary to simultaneously adapt in the spatial and range dimensions. This model is used as the basis for deriving a minimum mean-square error cost function. Minimization of this cost function results in the SRAP receive filters. Space-Range Adaptive Processing is initialized with the matched filter estimate followed by alternating profile and filter estimation. An efficient implementation strategy is presented for which the computational complexity is discussed.

Adaptivity in the spatial and range domains independently has been conceived and was summarized in Section 1.6. Later in this chapter the sequential application of these approaches is discussed for the DWDA. Issues associated with sequential adaptation are discussed. Analysis of the adaptive filters formed by different adaptive approaches for a given example is performed to assess the benefits of simultaneous multi-dimensional adaptive processing. Finally, the robustness of SRAP is assessed via simulation of multiple scenarios.

#### 4.1 SPACE-RANGE SIGNAL MODEL

The waveforms transmitted from an  $M$  element uniform linear array can be represented as the  $N \times M$  matrix  $\mathbf{S}$  of which the  $m^{\text{th}}$  column contains the length- $N$  discretized waveform transmitted from the  $m^{\text{th}}$  element of the array. Note that in the standard case the columns of  $\mathbf{S}$  are identical aside from the traditional elemental phase shift used for pulse-to-pulse transmit beamforming.

The discretized model for the received signal from the  $\ell^{\text{th}}$  range cell and  $\theta$  direction (relative to boresight) on the  $M$  elements of a waveform-diverse uniform linear array can be denoted as the length- $M$  vector

$$\mathbf{y}(\ell) = \left[ \sum_{\theta} \mathbf{x}^T(\ell, \theta) \mathbf{S} \mathbf{v}_{\theta} \mathbf{v}_{\theta}^T \right] + \mathbf{n}(\ell), \quad (4.1)$$

in which  $(\bullet)^T$  is the transpose operator,  $\mathbf{x}(\ell, \theta) = [x(\ell, \theta) \ x(\ell-1, \theta) \ \dots \ x(\ell-N+1, \theta)]^T$  is a collection of the complex scattering coefficients associated with the scatterers in the range profile corresponding to the angle  $\theta$ , with which the  $M$  waveforms convolve at delay  $\ell$ ,

$\mathbf{v}_\theta = [1 \ e^{j\pi \sin \theta} \ e^{j2\pi \sin \theta} \ \dots \ e^{j(M-1)\pi \sin \theta}]^T$  is the steering vector associated with the spatial angle  $\theta$ ,

and  $\mathbf{n}(\ell)$  is  $1 \times M$  a vector of additive noise samples.

The collection of  $N$  temporal snapshots of (4.1) can be expressed as

$$\mathbf{Y}(\ell) = \left[ \sum_{\theta} \mathbf{X}(\ell, \theta) \mathbf{S} \mathbf{v}_\theta \mathbf{v}_\theta^T \right] + \mathbf{N}(\ell), \quad (4.2)$$

where

$$\mathbf{X}(\ell, \theta) = \begin{bmatrix} x(\ell, \theta) & x(\ell-1, \theta) & \dots & x(\ell-N+1, \theta) \\ x(\ell+1, \theta) & x(\ell, \theta) & \dots & x(\ell-N+2, \theta) \\ \vdots & \vdots & \ddots & \vdots \\ x(\ell+N-1, \theta) & x(\ell+N-2, \theta) & \dots & x(\ell, \theta) \end{bmatrix} \quad (4.3)$$

is a matrix containing the complex amplitudes within  $2N-1$  range cells of  $x(\ell, \theta)$ . The matched

filter and SRAP signal model is a reorganized version of (4.2) and is expressed as the  $NM \times 1$

vector

$$\tilde{\mathbf{y}}(\ell) = \left[ \sum_{\theta} \mathbf{X}(\ell, \theta) \mathbf{S} \mathbf{v}_\theta \otimes \mathbf{v}_\theta \right] + \tilde{\mathbf{n}}(\ell), \quad (4.4)$$

where  $\otimes$  denotes the Kronecker product and  $\tilde{\mathbf{n}}(\ell) = \text{vec}(\mathbf{N}^T(\ell))$ . A normalized matched filter

can be applied to (4.4) as

$$\hat{x}_{\text{NMF}}(\ell, \theta) = \frac{(\mathbf{S} \mathbf{v}_\theta \otimes \mathbf{v}_\theta)^H}{(\mathbf{S} \mathbf{v}_\theta \otimes \mathbf{v}_\theta)^H (\mathbf{S} \mathbf{v}_\theta \otimes \mathbf{v}_\theta)} \tilde{\mathbf{y}}(\ell), \quad (4.5)$$

in which  $(\bullet)^H$  denotes the complex-conjugate transpose (or Hermitian) operator. Note that the value of the estimate in (4.5) is representative of the complex scattering coefficients resulting in an undesired weighting, with respect to spatial angle, of the output noise floor. The range-angle estimates can be scaled such that the noise power is the same in each spatial bin by applying an angle-dependent weighting that is proportional to the aggregate beampattern in (3.12) as

$$\hat{x}_{MF}(\ell, \theta) = \sqrt{\frac{(\mathbf{S}\mathbf{v}_\theta)(\mathbf{S}\mathbf{v}_\theta)}{G}} \hat{x}_{NMF}(\ell, \theta) = \sqrt{\frac{(\mathbf{S}\mathbf{v}_\theta)(\mathbf{S}\mathbf{v}_\theta)}{G}} \frac{(\mathbf{S}\mathbf{v}_\theta \otimes \mathbf{v}_\theta)^H}{(\mathbf{S}\mathbf{v}_\theta \otimes \mathbf{v}_\theta)^H (\mathbf{S}\mathbf{v}_\theta \otimes \mathbf{v}_\theta)} \tilde{\mathbf{y}}(\ell), \quad (4.6)$$

where  $G = \max_\theta [(\mathbf{S}\mathbf{v}_\theta)^H (\mathbf{S}\mathbf{v}_\theta)]$  is chosen such that the areas of interest, corresponding to the maximums of the aggregate beampattern, have a unity weighting. This weighting in (4.6) results in a uniform noise floor yielding an output that is amenable to a constant false alarm rate detection stage. Likewise, the SRAP estimate is obtained as

$$\hat{x}_{SRAP}(\ell, \theta) = \sqrt{\frac{(\mathbf{S}\mathbf{v}_\theta)(\mathbf{S}\mathbf{v}_\theta)}{G}} \mathbf{w}(\ell, \theta)^H \tilde{\mathbf{y}}(\ell), \quad (4.7)$$

where  $\mathbf{w}(\ell, \theta)$  is an adaptive filter that is derived in the following section.

#### 4.2 SPACE-RANGE ADAPTIVE PROCESSING

The MMSE cost function for the complex amplitude in the range-angle cell corresponding to delay  $\ell$  and spatial angle  $\theta$  is given as

$$J(\ell, \theta) = E \left[ |x(\ell, \theta) - \mathbf{w}^H(\ell, \theta) \tilde{\mathbf{y}}(\ell)|^2 \right], \quad (4.8)$$

where  $E[\bullet]$  is the expectation operator and  $\mathbf{w}(\ell, \theta)$  is the adaptive filter for the  $(\ell, \theta)$  range-angle cell. A unity gain constraint

$$\mathbf{w}^H(\ell, \theta)(\mathbf{S}\mathbf{v}_\theta \otimes \mathbf{v}_\theta) = 1 \quad (4.9)$$

is enforced by adding a Lagrange multiplier to the cost function in (4.8) as

$$J(\ell, \theta) = E\left[|x(\ell, \theta) - \mathbf{w}^H(\ell, \theta)\tilde{\mathbf{y}}(\ell)|^2\right] + \text{Re}\left\{\lambda(\mathbf{w}^H(\ell, \theta)(\mathbf{S}\mathbf{v}_\theta \otimes \mathbf{v}_\theta) - 1)\right\} \quad (4.10)$$

where  $\lambda$  is the Lagrange multiplier and  $\text{Re}\{\bullet\}$  denotes the real part of the argument.

Minimization of (4.10) with respect to  $\mathbf{w}^*(\ell, \theta)$  yields

$$\mathbf{w}(\ell, \theta) = \left(E[\tilde{\mathbf{y}}(\ell)\tilde{\mathbf{y}}^H(\ell)]\right)^{-1} \left(E[x^*(\ell, \theta)\tilde{\mathbf{y}}(\ell)] - \frac{\lambda}{2}(\mathbf{S}\mathbf{v}_\theta \otimes \mathbf{v}_\theta)\right), \quad (4.11)$$

in which  $(\bullet)^*$  denotes the complex conjugate.

Assuming the range-angle cells are uncorrelated with each other and with the noise, the filter in (4.11) can be expressed as

$$\mathbf{w}(\ell, \theta) = \left(\sum_{\phi} (\mathbf{T}(\ell, \phi) \otimes \mathbf{v}_\phi \mathbf{v}_\phi^H) + \mathbf{R}_{\text{NSE}}(\ell)\right)^{-1} \left(\rho(\ell, \theta) - \frac{\lambda}{2}\right)(\mathbf{S}\mathbf{v}_\theta \otimes \mathbf{v}_\theta) \quad (4.12)$$

where  $\rho(\ell, \theta) = E\left[|x(\ell, \theta)|^2\right]$  is the power in the range-angle cell corresponding to delay  $\ell$  and

spatial angle  $\theta$ ,  $\mathbf{R}_{\text{NSE}}(\ell) = \sigma_{\text{NSE}}^2 \mathbf{I}_{NM \times NM}$  is the noise covariance matrix under the assumption of white noise (where  $\sigma_{\text{NSE}}^2$  is the noise power),

$$\mathbf{T}(\ell, \phi) = \sum_{n=-N+1}^{N-1} \rho(\ell+n, \phi) \mathbf{t}_{\phi, n} \mathbf{t}_{\phi, n}^H, \quad (4.13)$$

where

$$\mathbf{t}_{\phi,n} = \begin{cases} \left[ t_{\phi}(|n|) \cdots t_{\phi}(N-1) \mathbf{0}_{1 \times |n|} \right]^T & \text{for } n \leq 0 \\ \left[ \mathbf{0}_{1 \times n} \ t_{\phi}(0) \cdots t_{\phi}(N-1-n) \right]^T & \text{for } n > 0 \end{cases} \quad (4.14)$$

consists of shifted (and zero-padded) versions of the composite waveform transmitted in the  $\phi$  direction given by the product  $\mathbf{Sv}_{\phi}$ . Note that due to the inherent transmit coupling of space and range when time-varying beampatterns are induced, the composite waveform (which possesses a temporal modulation structure) is different for different spatial transmit directions. The Lagrange multiplier is found by evaluating the inner product

$$\mathbf{w}^H(\ell, \theta) (\mathbf{Sv}_{\theta} \otimes \mathbf{v}_{\theta}) = \left( \rho(\ell) - \frac{\lambda}{2} \right) (\mathbf{Sv}_{\theta} \otimes \mathbf{v}_{\theta})^H \left( \sum_{\phi} (\mathbf{T}(\ell, \theta) \otimes \mathbf{v}_{\phi} \mathbf{v}_{\phi}^H) + \mathbf{R}_{\text{NSE}}(\ell) \right)^{-1} (\mathbf{Sv}_{\theta} \otimes \mathbf{v}_{\theta}) \quad (4.15)$$

and solving for  $\lambda$  resulting in

$$\frac{\lambda}{2} = \rho(\ell, \theta) - \frac{1}{(\mathbf{Sv}_{\theta} \otimes \mathbf{v}_{\theta})^H \left( \sum_{\phi} (\mathbf{T}(\ell, \theta) \otimes \mathbf{v}_{\phi} \mathbf{v}_{\phi}^H) + \mathbf{R}_{\text{NSE}}(\ell) \right)^{-1} (\mathbf{Sv}_{\theta} \otimes \mathbf{v}_{\theta})}. \quad (4.16)$$

The SRAP filter now takes the familiar MVDR-like form

$$\mathbf{w}(\ell, \theta) = \frac{\left( \sum_{\phi} (\mathbf{T}(\ell, \theta) \otimes \mathbf{v}_{\phi} \mathbf{v}_{\phi}^H) + \mathbf{R}_{\text{NSE}}(\ell) \right)^{-1} (\mathbf{Sv}_{\theta} \otimes \mathbf{v}_{\theta})}{(\mathbf{Sv}_{\theta} \otimes \mathbf{v}_{\theta})^H \left( \sum_{\phi} (\mathbf{T}(\ell, \theta) \otimes \mathbf{v}_{\phi} \mathbf{v}_{\phi}^H) + \mathbf{R}_{\text{NSE}}(\ell) \right)^{-1} (\mathbf{Sv}_{\theta} \otimes \mathbf{v}_{\theta})}, \quad (4.17)$$

albeit with a structured covariance matrix instead of a sample covariance matrix [23].

#### 4.2.1 IMPLEMENTATION

SRAP utilizes the reiterative MMSE structure to alternate between estimating range-angle specific filters and the range-angle scattering coefficients of the illuminated area. A block diagram depicting the implementation of the SRAP algorithm is shown in Fig. 4.1. The matched filter from (4.5) can be used to obtain an initial estimate of the scattering coefficients that are then used to construct the covariance matrix in (4.13) for each cell needed to form the corresponding adaptive filter. The new estimates obtained by applying these unique range-angle filters can be utilized to update the signal covariance matrix after which a new set of filters can be computed and applied. The algorithm generally converges after three or four adaptive stages.

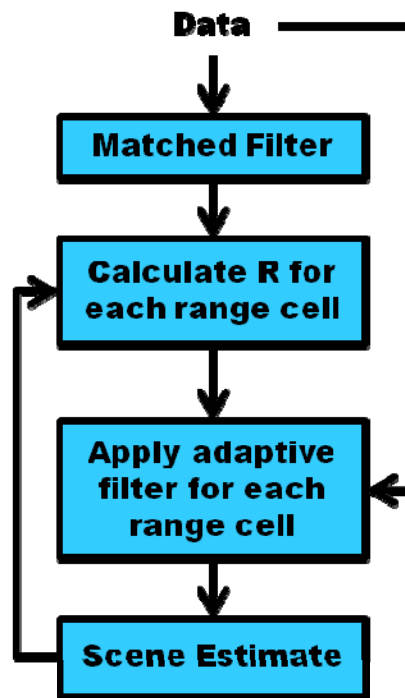


**Figure 4.1** Block diagram of SRAP implementation

#### 4.2.2 FAST MATRIX UPDATE

The computational burden of inverting the  $NM \times NM$  matrix in (4.12) can be alleviated by employing a fast matrix update strategy based on the matrix inversion lemma [29]. The update formulation is analogous to that described for APC in [13]. It is evident upon examining (4.12) - (4.14) that a large portion of the covariance matrix

$$\mathbf{R}(\ell) = \sum_{\phi} (\mathbf{T}(\ell, \phi) \otimes \mathbf{v}_{\phi} \mathbf{v}_{\phi}^H) + \mathbf{R}_{\text{NSE}}(\ell) \quad (4.18)$$

required to form the MMSE filter at the  $\ell^{\text{th}}$  range cell can be obtained from the covariance matrix at the previous range cell. The elements of  $\mathbf{R}(\ell-1)$  and  $\mathbf{R}(\ell)$  can be divided into sub-matrices denoted as

$$\mathbf{R}(\ell-1) = \begin{bmatrix} \mathbf{B}_{M \times M} & \mathbf{A}_{M \times (NM-M)}^H \\ \mathbf{A}_{(NM-M) \times M} & \mathbf{C}_{(NM-M) \times (NM-M)} \end{bmatrix} \quad \mathbf{R}(\ell) = \begin{bmatrix} \mathbf{C}_{(NM-M) \times (NM-M)} & \mathbf{D}_{(NM-M) \times M} \\ \mathbf{D}_{M \times (NM-M)}^H & \mathbf{H}_{M \times M} \end{bmatrix} \quad (4.19)$$

where the  $(NM-M) \times (NM-M)$  matrix  $\mathbf{C}$  represents the portion of the structured covariance matrix that is present in adjacent range cells. The relationship in (4.19) allows the matrix inversion lemma [29] to be applied, significantly reducing the computational cost of SRAP. The update equation is denoted as

$$(\mathbf{R} + \mathbf{ULV})^{-1} = \mathbf{R}^{-1} - \mathbf{R}^{-1} \mathbf{U} (\mathbf{L}^{-1} + \mathbf{VR}^{-1} \mathbf{U})^{-1} \mathbf{VR}^{-1}, \quad (4.20)$$

where

$$\mathbf{R} = \mathbf{P} \mathbf{R}(\ell-1) \mathbf{P}^T = \begin{bmatrix} \mathbf{C}_{(NM-M) \times (NM-M)} & \mathbf{A}_{(NM-M) \times M} \\ \mathbf{A}_{M \times (NM-M)}^H & \mathbf{B}_{M \times M} \end{bmatrix}, \quad (4.21)$$

is computed by applying a permutation matrix to  $\mathbf{R}(\ell-1)$ ,  $\mathbf{U}$  and  $\mathbf{V}$  are expressed as

$$\mathbf{U} = \begin{bmatrix} \mathbf{G}_{(NM-M) \times M} & \mathbf{0}_{(NM-M) \times M} \\ \mathbf{F}_{M \times M} & \mathbf{I}_{M \times M} \end{bmatrix}, \quad \mathbf{V} = \begin{bmatrix} \mathbf{0}_{M \times (NM-M)} & \mathbf{I}_{M \times M} \\ \mathbf{G}^H_{M \times (NM-M)} & \mathbf{0}_{M \times M} \end{bmatrix}, \quad (4.22)$$

in which  $\mathbf{L} = \mathbf{I}_{2M \times 2M}$  is an identity matrix,  $\mathbf{G} = \mathbf{D} - \mathbf{A}$ , and  $\mathbf{F} = \mathbf{H} - \mathbf{B}$ . The sub-matrices  $\mathbf{B}$  and  $\mathbf{A}$  can be computed as

$$\begin{bmatrix} \mathbf{B} \\ \mathbf{A} \end{bmatrix} = \sum_{\phi} (\mathbf{T}_1(\phi) \boldsymbol{\rho}_1(\ell-1, \phi) \otimes \mathbf{v}_{\phi} \mathbf{v}_{\phi}^H), \quad (4.23)$$

where

$$\mathbf{T}_1(\phi) = \begin{bmatrix} \mathbf{t}_{\phi, -(N-1)} & \mathbf{t}_{\phi, -(N-2)} & \cdots & \mathbf{t}_{\phi, 0} \end{bmatrix} \begin{bmatrix} t_{\phi}^*(N-1) & 0 & \cdots & 0 \\ 0 & t_{\phi}^*(N-2) & 0 & \vdots \\ \vdots & 0 & \ddots & 0 \\ 0 & \cdots & 0 & t_{\phi}^*(0) \end{bmatrix} \quad (4.24)$$

and  $\boldsymbol{\rho}_1(\ell, \phi) = [\rho(\ell-N+1, \phi) \ \rho(\ell-N+2, \phi) \ \cdots \ \rho(\ell, \phi)]^T$ . In a similar fashion, the sub-matrices  $\mathbf{D}$  and  $\mathbf{H}$  can be computed as

$$\begin{bmatrix} \mathbf{D} \\ \mathbf{H} \end{bmatrix} = \sum_{\phi} (\mathbf{T}_2(\phi) \boldsymbol{\rho}_2(\ell, \phi) \otimes \mathbf{v}_{\phi} \mathbf{v}_{\phi}^H), \quad (4.25)$$

where

$$\mathbf{T}_2(\phi) = \begin{bmatrix} \mathbf{t}_{\phi, 0} & \mathbf{t}_{\phi, 1} & \cdots & \mathbf{t}_{\phi, N-1} \end{bmatrix} \begin{bmatrix} t_{\phi}^*(N-1) & 0 & \cdots & 0 \\ 0 & t_{\phi}^*(N-2) & 0 & \vdots \\ \vdots & 0 & \ddots & 0 \\ 0 & \cdots & 0 & t_{\phi}^*(0) \end{bmatrix} \quad (4.26)$$

and  $\mathbf{p}_2(\ell, \phi) = [\rho(\ell, \phi) \rho(\ell+1, \phi) \cdots \rho(\ell+N-1, \phi)]^T$ . Note  $\mathbf{T}_1(\phi)$ ,  $\mathbf{T}_2(\phi)$ , and  $\mathbf{v}_\phi \mathbf{v}_\phi^H$  are deterministic and can be computed offline.

### 4.3 REDUCED DIMENSIONALITY SRAP

SRAP employs a large number of degrees of freedom, perhaps more than are necessary for many applications. In this section a reduced-dimensionality approach in the spirit of [22] is presented to further reduce computation. This reduction is achieved by sub-dividing the array elements, corresponding to the receive steering vector, from the signal model in (4.2) into  $K$  contiguous blocks as

$$\tilde{\mathbf{Y}}_k(\ell) = \left[ \sum_{\theta} \mathbf{X}(\ell, \theta) \mathbf{S} \mathbf{v}_\theta \tilde{\mathbf{v}}_{k,\theta}^T \right] + \tilde{\mathbf{N}}_k(\ell) \quad (4.27)$$

where  $\tilde{\mathbf{v}}_{k,\theta} = \left[ v_\theta \left( \frac{M}{K} k \right) \ v_\theta \left( \frac{M}{K} k + 1 \right) \ \cdots \ v_\theta \left( \frac{M}{K} (k+1) - 1 \right) \right]^T$  is a vector containing  $M/K$  contiguous samples of the spatial steering vector  $\mathbf{v}_\theta$  and  $\tilde{\mathbf{N}}_k(\ell) = \left[ \mathbf{n}_{\frac{M}{K}k} \ \mathbf{n}_{\frac{M}{K}k+1} \ \cdots \ \mathbf{n}_{\frac{M}{K}(k+1)-1} \right]^T$  is a matrix containing  $M/K$  columns of  $\mathbf{N}(\ell)$ . As before, the received signal model is reorganized and the reduced dimensionality SRAP (RD-SRAP) model is denoted as

$$\tilde{\mathbf{y}}_k(\ell) = \left[ \sum_{\theta} \mathbf{X}(\ell, \theta) \mathbf{S} \mathbf{v}_\theta \otimes \tilde{\mathbf{v}}_{k,\theta} \right] + \tilde{\mathbf{n}}_k(\ell), \quad (4.28)$$

where the term in front of the Kronecker product is the same as the full-dimensional signal model in (4.4). The reduced dimensionality cost function is expressed as

$$\tilde{J}(\ell, \boldsymbol{\theta}) = \sum_k E \left\{ \left| \frac{1}{K} x(\ell, \boldsymbol{\theta}) - \tilde{\mathbf{w}}_k^H(\ell, \boldsymbol{\theta}) \tilde{\mathbf{y}}_k(\ell) \right|^2 \right\} + \text{Re} \left\{ \lambda \left( \tilde{\mathbf{w}}^H(\ell, \boldsymbol{\theta}) (\mathbf{S} \mathbf{v}_\theta \otimes \mathbf{v}_\theta) - 1 \right) \right\}, \quad (4.29)$$

where  $\tilde{\mathbf{w}}_k(\ell)$  is a length- $NM/K$  filter segment of the length- $NM$  filter  $\tilde{\mathbf{w}}(\ell, \boldsymbol{\theta})$  that approximates the full-dimensional SRAP filter in (4.17), and  $\lambda$  is a Lagrange multiplier. It is more convenient to express (4.29) as

$$\tilde{J}(\ell, \boldsymbol{\theta}) = \sum_k E \left\{ \left| \frac{1}{K} x(\ell, \boldsymbol{\theta}) - \tilde{\mathbf{w}}_k^H(\ell, \boldsymbol{\theta}) \tilde{\mathbf{y}}_k(\ell) \right|^2 \right\} + \text{Re} \left\{ \lambda \left( \sum_{k=0}^{K-1} \tilde{\mathbf{w}}_k^H(\ell, \boldsymbol{\theta}) (\mathbf{S} \mathbf{v}_\theta \otimes \tilde{\mathbf{v}}_{k,\theta}) - 1 \right) \right\}, \quad (4.30)$$

such that minimizing (4.30) yields

$$\tilde{\mathbf{w}}_k(\ell) = \left( E \left\{ \tilde{\mathbf{y}}_k(\ell) \tilde{\mathbf{y}}_k(\ell)^H \right\} \right)^{-1} \left[ E \left\{ \frac{1}{K} x^*(\ell, \boldsymbol{\theta}) \tilde{\mathbf{y}}_k(\ell) \right\} - \frac{\lambda}{2} (\mathbf{S} \mathbf{v} \otimes \tilde{\mathbf{v}}_k) \right]. \quad (4.31)$$

Again, assuming the range-angle cells are uncorrelated with each other and with the noise, the RD-SRAP filter becomes

$$\tilde{\mathbf{w}}_k(\ell, \boldsymbol{\theta}) = \left( \frac{\rho(\ell, \boldsymbol{\theta})}{K} - \frac{\lambda}{2} \right) \left( \sum_{\phi} (\mathbf{T}(\ell, \phi) \otimes \tilde{\mathbf{v}}_{\phi,k} \tilde{\mathbf{v}}_{\phi,k}^H) + \tilde{\mathbf{R}}_{\text{NSE},k}(\ell) \right)^{-1} (\mathbf{S} \mathbf{v}_\theta \otimes \tilde{\mathbf{v}}_{k,\theta}) \quad (4.32)$$

Note that in the presence of white noise the reduced dimensionality covariance matrices

$$\tilde{\mathbf{R}}_k(\ell) = \sum_{\phi} (\mathbf{T}(\ell, \phi) \otimes \tilde{\mathbf{v}}_{k,\phi} \tilde{\mathbf{v}}_{k,\phi}^H) + \tilde{\mathbf{R}}_{\text{NSE},k}(\ell) \quad (4.33)$$

are the same for all  $k$ , i.e.,

$$\tilde{\mathbf{v}}_{i,\phi} \tilde{\mathbf{v}}_{i,\phi}^H = \tilde{\mathbf{v}}_{j,\phi} \tilde{\mathbf{v}}_{j,\phi}^H \quad \forall 0 \leq i \leq (K-1), 0 \leq j \leq (K-1). \quad (4.34)$$

Hence, only a single reduced dimensionality covariance matrix must be computed for each range cell. Combining the filter segments from (4.32) appropriately yields

$$\tilde{\mathbf{w}}(\ell, \boldsymbol{\theta}) = \text{vec} \left( \left[ \begin{array}{ccc|ccc|ccc} \tilde{\mathbf{W}}_{0,0} & \cdots & \tilde{\mathbf{W}}_{0,\frac{M}{K}-1} & \tilde{\mathbf{W}}_{1,0} & \cdots & \tilde{\mathbf{W}}_{1,\frac{M}{K}-1} & \cdots & \tilde{\mathbf{W}}_{K-1,0} & \cdots & \tilde{\mathbf{W}}_{K-1,\frac{M}{K}-1} \\ \tilde{\mathbf{W}}_{0,\frac{M}{K}} & \cdots & \tilde{\mathbf{W}}_{0,\frac{2M}{K}-1} & \tilde{\mathbf{W}}_{1,\frac{M}{K}} & \cdots & \tilde{\mathbf{W}}_{1,\frac{2M}{K}-1} & \cdots & \tilde{\mathbf{W}}_{K-1,\frac{M}{K}} & \cdots & \tilde{\mathbf{W}}_{K-1,\frac{2M}{K}-1} \\ \vdots & \vdots & \vdots & \vdots & \vdots & \vdots & \cdots & \vdots & \vdots & \vdots \\ \tilde{\mathbf{W}}_{0,\frac{(N-1)M}{K}} & \cdots & \tilde{\mathbf{W}}_{0,\frac{NM}{K}-1} & \tilde{\mathbf{W}}_{1,\frac{(N-1)M}{K}} & \cdots & \tilde{\mathbf{W}}_{1,\frac{NM}{K}-1} & \cdots & \tilde{\mathbf{W}}_{K-1,\frac{(N-1)M}{K}} & \cdots & \tilde{\mathbf{W}}_{K-1,\frac{NM}{K}-1} \end{array} \right]^T \right), \quad (4.35)$$

where  $\text{vec}(\bullet)$  is the vectorization operation,  $\tilde{w}_{k,i}$  is the  $i^{\text{th}}$  element of the vector  $\tilde{\mathbf{w}}_k(\ell, \boldsymbol{\theta})$ , and the partition lines indicate the portions of the larger matrix that contain elements from an individual filter segment.

To determine the Lagrange multiplier, the term  $\left( \frac{\rho(\ell, \boldsymbol{\theta})}{K} - \frac{\lambda}{2} \right)$  is factored out of

(4.35) resulting in

$$\tilde{\mathbf{w}}(\ell, \boldsymbol{\theta}) = \left( \frac{\rho(\ell, \boldsymbol{\theta})}{K} - \frac{\lambda}{2} \right) \bar{\mathbf{w}}(\ell, \boldsymbol{\theta}), \quad (4.36)$$

in which

$$\bar{\mathbf{w}}(\ell, \boldsymbol{\theta}) = \text{vec} \left( \left[ \begin{array}{ccc|ccc|ccc} \bar{\mathbf{W}}_{0,0} & \cdots & \bar{\mathbf{W}}_{0,\frac{M}{K}-1} & \bar{\mathbf{W}}_{1,0} & \cdots & \bar{\mathbf{W}}_{1,\frac{M}{K}-1} & \cdots & \bar{\mathbf{W}}_{K-1,0} & \cdots & \bar{\mathbf{W}}_{K-1,\frac{M}{K}-1} \\ \bar{\mathbf{W}}_{0,\frac{M}{K}} & \cdots & \bar{\mathbf{W}}_{0,\frac{2M}{K}-1} & \bar{\mathbf{W}}_{1,\frac{M}{K}} & \cdots & \bar{\mathbf{W}}_{1,\frac{2M}{K}-1} & \cdots & \bar{\mathbf{W}}_{K-1,\frac{M}{K}} & \cdots & \bar{\mathbf{W}}_{K-1,\frac{2M}{K}-1} \\ \vdots & \vdots & \vdots & \vdots & \vdots & \vdots & \cdots & \vdots & \vdots & \vdots \\ \bar{\mathbf{W}}_{0,\frac{(N-1)M}{K}} & \cdots & \bar{\mathbf{W}}_{0,\frac{NM}{K}-1} & \bar{\mathbf{W}}_{1,\frac{(N-1)M}{K}} & \cdots & \bar{\mathbf{W}}_{1,\frac{NM}{K}-1} & \cdots & \bar{\mathbf{W}}_{K-1,\frac{(N-1)M}{K}} & \cdots & \bar{\mathbf{W}}_{K-1,\frac{NM}{K}-1} \end{array} \right]^T \right), \quad (4.37)$$

where  $\bar{w}_{k,i}$  is now the  $i^{\text{th}}$  element of the filter segment given by

$$\bar{\mathbf{w}}_k(\ell, \boldsymbol{\theta}) = \left( \tilde{\mathbf{R}}_k(\ell) \right)^{-1} \left( \mathbf{S} \mathbf{v}_\theta \otimes \tilde{\mathbf{v}}_{k,\theta} \right). \quad (4.38)$$

The Lagrange multiplier can now be found by taking the conjugate transpose of (4.36) and post-multiplying both sides by  $(\mathbf{S} \mathbf{v}_\theta \otimes \mathbf{v}_\theta)$  resulting in

$$\tilde{\mathbf{w}}^H(\ell, \theta)(\mathbf{S}\mathbf{v}_\theta \otimes \mathbf{v}_\theta) = \left( \frac{\rho(\ell, \theta)}{K} - \frac{\lambda}{2} \right) \bar{\mathbf{w}}^H(\ell, \theta)(\mathbf{S}\mathbf{v}_\theta \otimes \mathbf{v}_\theta). \quad (4.39)$$

To enforce the unity gain constraint the left hand side of (4.39) is set to unity yielding

$$\frac{\lambda}{2} = \frac{\rho(\ell, \theta)}{K} - \frac{1}{\bar{\mathbf{w}}^H(\ell, \theta)(\mathbf{S}\mathbf{v}_\theta \otimes \mathbf{v}_\theta)}. \quad (4.40)$$

Combining (4.36) and (4.40) we arrive at the RD-SRAP filter for the  $(\ell, \theta)$  range-angle cell

$$\tilde{\mathbf{w}}(\ell, \theta) = \frac{\bar{\mathbf{w}}(\ell, \theta)}{\bar{\mathbf{w}}^H(\ell, \theta)(\mathbf{S}\mathbf{v}_\theta \otimes \mathbf{v}_\theta)}, \quad (4.41)$$

which is applied to the full-dimensional data vector  $\tilde{\mathbf{y}}(\ell)$  from (4.4) to obtain an estimate.

#### 4.3.1 FAST MATRIX UPDATE FOR RD-SRAP

The fast update strategy can also be used to compute the reduced dimension inverse. The reduced dimensionality covariance matrix from (4.32) for adjacent range cells can be expressed as

$$\tilde{\mathbf{R}}_k(\ell-1) = \begin{bmatrix} \tilde{\mathbf{B}}_{\frac{M \times M}{K \times K}} & \tilde{\mathbf{A}}_{\frac{M \times (NM-M)}{K \times K}}^H \\ \tilde{\mathbf{A}}_{\frac{(NM-M) \times M}{K \times K}} & \tilde{\mathbf{C}}_{\frac{(NM-M) \times (NM-M)}{K \times K}} \end{bmatrix} \quad \tilde{\mathbf{R}}_k(\ell) = \begin{bmatrix} \tilde{\mathbf{C}}_{\frac{(NM-M) \times (NM-M)}{K \times K}} & \tilde{\mathbf{D}}_{\frac{(NM-M) \times M}{K \times K}} \\ \tilde{\mathbf{D}}_{\frac{M \times (NM-M)}{K \times K}}^H & \tilde{\mathbf{H}}_{\frac{M \times M}{K \times K}} \end{bmatrix}. \quad (4.42)$$

The reduced-dimensionality update equation is denoted as

$$(\tilde{\mathbf{R}} + \tilde{\mathbf{U}}\tilde{\mathbf{L}}\tilde{\mathbf{V}})^{-1} = \tilde{\mathbf{R}}^{-1} - \tilde{\mathbf{R}}^{-1}\tilde{\mathbf{U}}(\tilde{\mathbf{L}}^{-1} + \tilde{\mathbf{V}}\tilde{\mathbf{R}}^{-1}\tilde{\mathbf{U}})^{-1}\tilde{\mathbf{V}}\tilde{\mathbf{R}}^{-1}, \quad (4.43)$$

where

$$\tilde{\mathbf{R}} = \tilde{\mathbf{P}} \tilde{\mathbf{R}}_k(\ell-1) \tilde{\mathbf{P}}^T = \begin{bmatrix} \tilde{\mathbf{C}}_{\frac{(NM-M)}{K} \times \frac{(NM-M)}{K}} & \tilde{\mathbf{A}}_{\frac{(NM-M)}{K} \times \frac{M}{K}} \\ \tilde{\mathbf{A}}_{\frac{M}{K} \times \frac{(NM-M)}{K}}^H & \tilde{\mathbf{B}}_{\frac{M}{K} \times \frac{M}{K}} \end{bmatrix}, \quad (4.44)$$

is a permutation of  $\tilde{\mathbf{R}}_k(\ell-1)$ ,  $\tilde{\mathbf{U}}$  and  $\tilde{\mathbf{V}}$  are expressed as

$$\tilde{\mathbf{U}} = \begin{bmatrix} \tilde{\mathbf{G}}_{\frac{(NM-M)}{K} \times \frac{M}{K}} & \mathbf{0}_{\frac{(NM-M)}{K} \times \frac{M}{K}} \\ \tilde{\mathbf{F}}_{\frac{M}{K} \times \frac{M}{K}} & \mathbf{I}_{\frac{M}{K} \times \frac{M}{K}} \end{bmatrix}, \quad \tilde{\mathbf{V}} = \begin{bmatrix} \mathbf{0}_{\frac{M}{K} \times \frac{(NM-M)}{K}} & \mathbf{I}_{\frac{M}{K} \times \frac{M}{K}} \\ \tilde{\mathbf{G}}_{\frac{M}{K} \times \frac{(NM-M)}{K}}^H & \mathbf{0}_{\frac{M}{K} \times \frac{M}{K}} \end{bmatrix}, \quad (4.45)$$

in which  $\tilde{\mathbf{L}} = \mathbf{I}_{\frac{2M}{K} \times \frac{2M}{K}}$  is an identity matrix,  $\tilde{\mathbf{G}} = \tilde{\mathbf{D}} - \tilde{\mathbf{A}}$ , and  $\tilde{\mathbf{F}} = \tilde{\mathbf{H}} - \tilde{\mathbf{B}}$ . The reduced-dimensionality sub-matrices  $\tilde{\mathbf{B}}$ ,  $\tilde{\mathbf{A}}$ ,  $\tilde{\mathbf{D}}$ , and  $\tilde{\mathbf{H}}$  can be computed as

$$\begin{bmatrix} \tilde{\mathbf{B}} \\ \tilde{\mathbf{A}} \end{bmatrix} = \sum_{\phi} (\mathbf{T}_1(\phi) \boldsymbol{\rho}_1(\ell-1, \phi) \otimes \tilde{\mathbf{v}}_{k,\phi} \tilde{\mathbf{v}}_{k,\phi}^H) \quad (4.46)$$

and

$$\begin{bmatrix} \tilde{\mathbf{D}} \\ \tilde{\mathbf{H}} \end{bmatrix} = \sum_{\phi} (\mathbf{T}_2(\phi) \boldsymbol{\rho}_2(\ell, \phi) \otimes \tilde{\mathbf{v}}_{k,\phi} \tilde{\mathbf{v}}_{k,\phi}^H). \quad (4.47)$$

#### 4.4 COMPUTATIONAL COMPLEXITY

The Adaptive Pulse Compression (APC) [13] and Re-Iterative Super-Resolution (RISR) [21] algorithms were realizations of the RMMSE approach applied to radar pulse compression and adaptive beamforming, respectively. As such, they provide a convenient benchmark to assess the computational complexity of the joint range-angle approach developed here.

The computational cost of APC in terms of complex multiplies (per range cell, per iteration) was previously shown to be approximately  $C_{\text{APC}} = 6N^2 + 13N + 27$  (where  $N$  is the length of the radar

waveform) . RISR incurs a (per range cell, per iteration) cost of approximately  $C_{\text{RISR}}=M^3+2QM^2+3QM$  complex multiplies where  $M$  is the number of antenna elements and  $Q$  is the number of spatial bins used for processing. Thus, the combined cost of sequential RISR-APC per range cell is  $C_{\text{RA}}=I_{\text{RISR}}C_{\text{RISR}}+ QI_{\text{APC}}C_{\text{APC}}$ , where  $I_{\text{RISR}}$  and  $I_{\text{APC}}$  are the number of iterations employed by RISR and APC, respectively.

The computational complexity of SRAP is determined by assessing the number of complex multiplies required to compute the filter for a single range-angle cell for a single iteration when the fast matrix update derived in the previous section is employed. First consider the components of the update equation from (4.20), restated here with matrix dimensionalities included:

$$(\bar{\mathbf{R}} + \mathbf{U}\mathbf{L}\mathbf{V})^{-1} = \bar{\mathbf{R}}^{-1}_{NM \times NM} - [\bar{\mathbf{R}}^{-1}\mathbf{U}]_{NM \times 2M} \left[ (\mathbf{L}^{-1} + \mathbf{V}\bar{\mathbf{R}}^{-1}\mathbf{U})^{-1} \right]_{2M \times 2M} [\mathbf{V}\bar{\mathbf{R}}^{-1}]_{2M \times NM}. \quad (4.48)$$

For this analysis, multiplication by a “1” or “0” is not counted, thus the product  $\bar{\mathbf{R}}^{-1}\mathbf{U}$  requires  $M(NM)^2$  multiplies. The computation of  $\mathbf{V}\bar{\mathbf{R}}^{-1}\mathbf{U}$  only requires  $2M^2(NM-M)$  since  $\bar{\mathbf{R}}^{-1}\mathbf{U}$  has already been computed. The component  $\mathbf{V}\bar{\mathbf{R}}^{-1}$  requires  $NM^2(NM-M)$ . Inversion of  $(\mathbf{L}^{-1} + \mathbf{V}\bar{\mathbf{R}}^{-1}\mathbf{U})^{-1}$  requires  $(2M)^3$  multiplies. The final product needed to compute (4.48) is

$$[\bar{\mathbf{R}}^{-1}\mathbf{U}]_{NM \times 2M} \left[ (\mathbf{L}^{-1} + \mathbf{V}\bar{\mathbf{R}}^{-1}\mathbf{U})^{-1} \right]_{2M \times 2M} [\mathbf{V}\bar{\mathbf{R}}^{-1}]_{2M \times NM} \text{ which incurs a cost of } 4NM^3 + 2M(NM)^2$$

complex multiplies. It is evident from (4.23) and (4.25) that the computation of  $[\mathbf{B} \ \mathbf{A}]^T$  and  $[\mathbf{D} \ \mathbf{H}]^T$  requires  $QN^2 + QN(M)^2$  multiplies where  $Q$  is the number of spatial bins used for processing. Constructing and applying the filters requires  $Q(NM)^2 + 2QNM$ . Thus, the total computational cost of SRAP per range cell, per iteration is

$$C_{\text{SRAP}} = Q \left[ (NM)^2 + NM^2 + 2NM + N^2 \right] + NM \left[ 4NM^2 + 5M^2 \right] + 6M^3. \quad (4.49)$$

Figure 4.2 displays the computational cost of SRAP and sequential RISR-APC as well as the ratio of computations for different values of  $N$  and  $M$ . In this case, the number of spatial bins used for processing was chosen to be  $5M$ , APC and SRAP employ 3 adaptive iterations, and RISR performs 5 adaptive iterations. Notice that when  $N$  and  $M$  are large the additional cost of SRAP, relative to independent adaptation, can be significant.

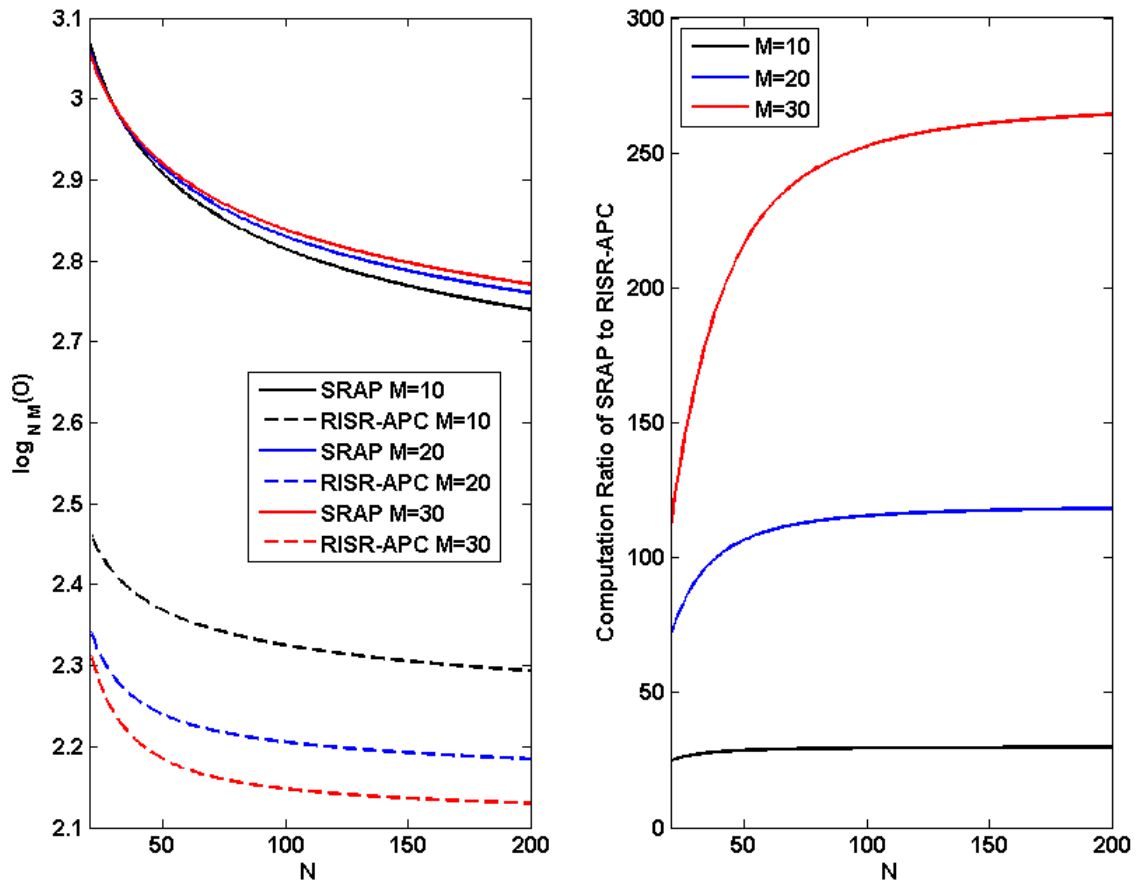


**Figure 4.2** Computational complexity of SRAP and Sequential RISR-APC (per range cell)

In a similar fashion, the computational complexity of the RD-SRAP algorithm is found to be

$$C_{\text{RD-SRAP}} = Q \left[ K \left( N \frac{M}{K} \right)^2 + N \left( \frac{M}{K} \right)^2 + 2NM + N^2 \right] + \frac{NM}{K^3} [4NM^2 + 5M^2] + 6 \left( \frac{M}{K} \right)^3. \quad (4.50)$$

Figure 4.3 shows the computational cost of RD-SRAP compared to independent adaptations under the same assumptions used to generate Fig. 4.2. In this case, the blocking factor is set to  $K=5$ . The computation of the reduced dimensionality SRAP algorithm is now less severe relative to separate adaptation in range and angle. The following sections will compare the performance of SRAP, RD-SRAP, and RISR-APC.

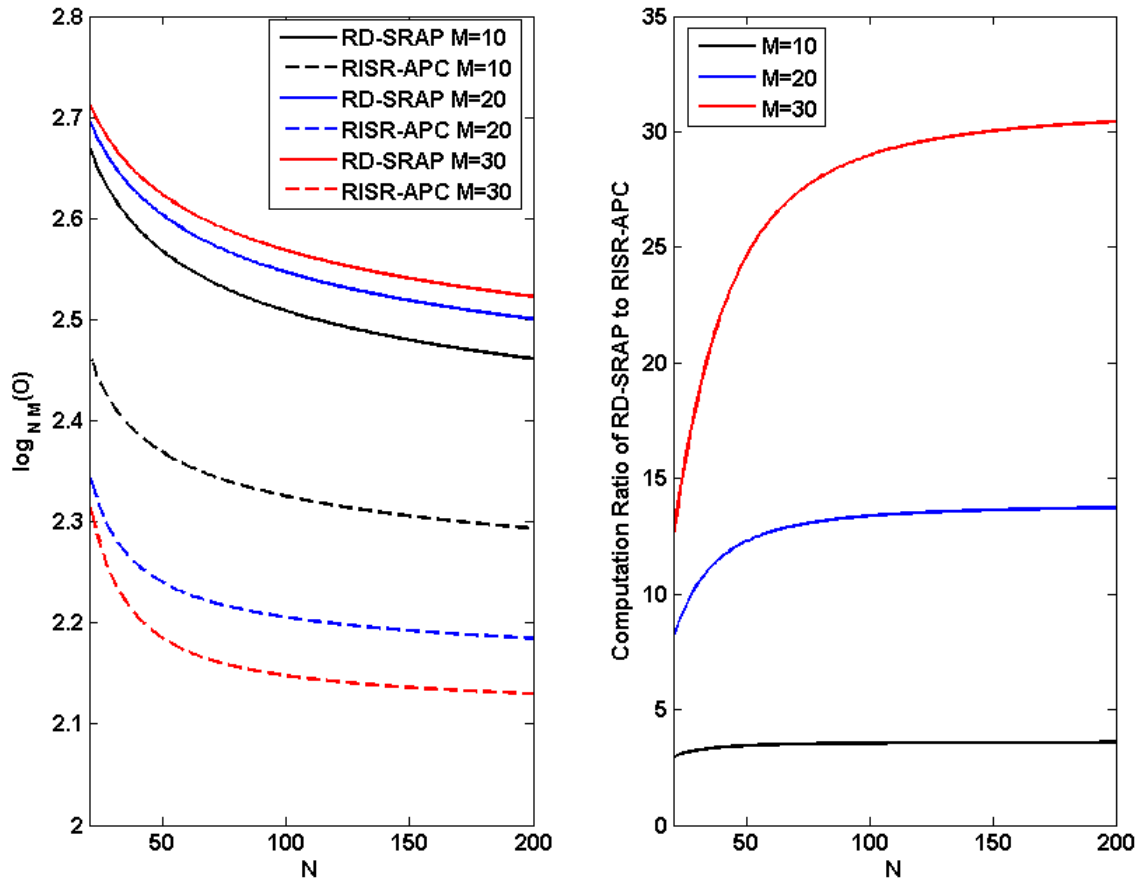


**Figure 4.3** Computational complexity of RD-SRAP (with  $K=5$ ) and Sequential RISR-APC (per range cell)

#### 4.5 ASSESSMENT OF JOINT ADAPTIVE PROCESSING

The "one size fits all" approach of deterministic filtering attempts to construct a filter that is appropriate for all scenarios, typically by minimizing the peak or average sidelobe level. In contrast, adaptive filter structures allow a unique filter to be designed for each signal of interest based upon estimation of the environment, thereby making the most out of the available filter degrees of freedom. This approach alleviates the constraints on the filter by requiring only enhanced performance for the particular scenario corresponding to each filter's location. The adaptive filter typically achieves superior performance by constructing a weight vector that is orthogonal only to undesired signals that are present in the subset of the received data used to estimate the desired quantity.

To ascertain the benefit of applying adaptive processing jointly in range and angle, it is instructive to first assess the performance of adaptive processing in the range and angle domains separately. Consider the application of both adaptive spatial processing and adaptive range processing to perform spatial beamforming and pulse compression, respectively, for DWDA emissions. The proposed DWDA transmit strategy results in a transmitted waveform that possesses a different temporal modulation in each direction. Hence, in the following analysis adaptive spatial processing is applied first to separate the angle-dependent waveforms into their respective spatial bins. Consequently, pulse compression within each spatial bin must only consider an individual angle-dependent waveform.

Consider the sequential application of RISR and APC to perform spatial beamforming and pulse compression, respectively. If RISR is applied to the received data before pulse compression, it will be subject to multiple overlapped pulses from different spatial angles (targets

separated by less than a pulse width in range, regardless of angle, will have temporally overlapping returns). However, if it is possible to perform APC first the pulses would ideally be localized to individual range cells, thus reducing the extent of the overlap. Albeit, without the spatial isolation provided by RISR, the degrees of freedom inherent to APC can become overwhelmed by returns from spatially distributed targets. Hence, from a theoretical standpoint it is unclear in which order the independent approaches should be applied. Note that whichever algorithm is applied first does not account for the processing gain that will be achieved in the second stage. When the same waveform is transmitted from each element of an array either algorithm can be applied first, but for the case of the DWDA, in which different waveforms are transmitted to different spatial angles, spatial processing should be performed first.

#### 4.5.1 SEQUENTIAL ANGLE-RANGE ADAPTIVE PROCESSING

The implementation of independent adaptation in angle and range is, in general, executed as follows. The data received on an array is down-converted, digitized, converted to the complex analytical representation, and collected into a matrix denoted as

$$\mathbf{Y} = [\mathbf{y}_0 \ \mathbf{y}_1 \ \cdots \ \mathbf{y}_{M-1}], \quad (4.51)$$

where the  $m^{\text{th}}$  column  $\mathbf{y}_m = [y_m(0) \ y_m(1) \ \cdots \ y_m(L-1)]^T$  contains  $L$  complex samples from the  $m^{\text{th}}$  antenna element. First, an adaptive spatial weight vector of the form  $\mathbf{w}_\zeta(\ell, \theta) = \mu_\zeta \mathbf{R}_\zeta^{-1}(\ell) \mathbf{v}_\theta$  is constructed, where  $\mu_\zeta$  is a scale factor based on the particular choice of adaptive beamformer,  $\mathbf{R}_\zeta(\ell)$  is an  $M \times M$  spatial covariance matrix for the  $\ell^{\text{th}}$  range cell, and  $\mathbf{v}_\theta$  is a spatial steering vector. The adaptive filters are applied to the data matrix from (4.51) as

$$\hat{\mathbf{x}}_{\zeta}(\ell, \boldsymbol{\theta}) = \mathbf{w}_{\zeta}^H(\ell, \boldsymbol{\theta}) [y_0(\ell) \ y_1(\ell) \ \cdots \ y_{M-1}(\ell)]^T. \quad (4.52)$$

The output of (4.52) is organized into the matrix

$$\hat{\mathbf{X}}_{\zeta}(\ell, \boldsymbol{\theta}) = \begin{bmatrix} \hat{x}_{\zeta}(0, \boldsymbol{\theta}_0) & \hat{x}_{\zeta}(0, \boldsymbol{\theta}_1) & \cdots & \hat{x}_{\zeta}(0, \boldsymbol{\theta}_{Q-1}) \\ \hat{x}_{\zeta}(1, \boldsymbol{\theta}_0) & \hat{x}_{\zeta}(1, \boldsymbol{\theta}_1) & \cdots & \hat{x}_{\zeta}(1, \boldsymbol{\theta}_{Q-1}) \\ \vdots & \vdots & \ddots & \vdots \\ \hat{x}_{\zeta}(L-1, \boldsymbol{\theta}_0) & \hat{x}_{\zeta}(L-1, \boldsymbol{\theta}_1) & \cdots & \hat{x}_{\zeta}(L-1, \boldsymbol{\theta}_{Q-1}) \end{bmatrix}, \quad (4.53)$$

where  $Q$  is the number of spatial bins and each column contains the fast time data for an individual spatial bin. Finally, adaptive range processing is applied to each column of  $\hat{\mathbf{X}}_{\zeta}(\ell, \boldsymbol{\theta})$ .

The range-adaptive weight vector for spatial angle  $\boldsymbol{\theta}$  and range cell  $\ell$  is chosen to be the length of the discretized transmit waveform and takes the form  $\mathbf{w}_R(\ell, \boldsymbol{\theta}) = \mu_R \mathbf{R}_R^{-1}(\ell, \boldsymbol{\theta}) \mathbf{s}_{\boldsymbol{\theta}}$ , where  $\mu_R$  is again a scale factor based on the choice of processing scheme,  $\mathbf{R}_R(\ell, \boldsymbol{\theta})$  is an  $N \times N$  covariance matrix, and  $\mathbf{s}_{\boldsymbol{\theta}}$  is a steering vector based on the transmitted waveform and spatial angle  $\boldsymbol{\theta}$ . The space-range estimates are obtained by applying the range-adaptive filter to the adaptive beamformer outputs as

$$\hat{\mathbf{x}}_{\text{SEQ}}(\ell, \boldsymbol{\theta}) = \mathbf{w}_R^H(\ell, \boldsymbol{\theta}) [\hat{x}_{\zeta}(\ell, \boldsymbol{\theta}) \ \hat{x}_{\zeta}(\ell+1, \boldsymbol{\theta}) \ \cdots \ \hat{x}_{\zeta}(\ell+N-1, \boldsymbol{\theta})]^T. \quad (4.54)$$

The methodology discussed above is now used to formulate a filter response for each component of independent adaptation as well as a sequential filter response.

#### 4.5.2 FILTER RESPONSE

In this section general filter responses for adaptivity in angle, range, sequential angle-range, and joint angle-range are assessed. These responses are used to evaluate how the available

adaptive degrees of freedom impact performance within this paradigm of range-angle coupled emissions. Specifically, the filter response illustrates the effect that surrounding scatterers will have upon the estimation of a particular range-angle cell.

The filter response for adaptation in the angle domain is computed as

$$\chi_{\angle}^{\phi}(\ell, \theta) = \mathbf{w}_{\angle}^H(\ell, \phi) \mathbf{v}_{\theta}, \quad (4.55)$$

where  $\mathbf{w}_{\angle}(\ell, \phi)$  is the filter formed within an adaptive beamforming algorithm for spatial angle  $\phi$  at the  $\ell^{\text{th}}$  range cell of  $\mathbf{Y}(\ell)$  and  $\mathbf{v}_{\theta}$  is a spatial steering vector. The range-adaptive filter response is denoted as

$$\chi_{\text{R}}^{\phi}(\ell + n, \theta) = \mathbf{w}_{\text{R}}^H(\ell, \phi) \mathbf{t}_{\theta, n}, \quad (4.56)$$

for  $n = -N + 1, \dots, N - 1$ , in which  $\mathbf{w}_{\text{R}}(\ell, \phi)$  is the range-adaptive filter for the  $\ell^{\text{th}}$  range cell in the spatial bin corresponding to angle  $\phi$  and  $\mathbf{t}_{\theta, n}$  is given by (4.14). The combined space-range filter response for sequential adaptive processing is expressed as

$$\chi_{\text{SEQ}}^{\phi}(\ell + n, \theta) = \mathbf{w}_{\text{R}}^H(\ell, \phi) \left[ \left( \begin{bmatrix} \mathbf{w}_{\angle}^H(\ell, \phi) \\ \mathbf{w}_{\angle}^H(\ell + 1, \phi) \\ \vdots \\ \mathbf{w}_{\angle}^H(\ell + N - 1, \phi) \end{bmatrix} \mathbf{v}_{\theta} \right) \odot \mathbf{t}_{\theta, n} \right]. \quad (4.57)$$

Finally, the SRAP filter response is obtained as

$$\chi_{\text{SRAP}}^{\phi}(\ell + n, \theta) = \mathbf{w}_{\text{SRAP}}^H(\ell, \phi) (\mathbf{t}_{\theta, n} \otimes \mathbf{v}_{\theta}) \quad (4.58)$$

for  $n = -N + 1, \dots, N - 1$ , where  $\mathbf{t}_{\theta, n}$  is given in (4.14).

### 4.5.3 SEQUENTIAL RISR-APC

The filter responses described in the previous section can be used to assess the performance of independent adaptation in angle and range. In the next section, the RISR and APC algorithms are chosen as the specific realizations of independent sequential adaptive processing techniques. RISR can be employed initially to isolate the returns from different spatial angles thus separating the different waveforms associated with different directions. After the RISR estimate is obtained APC is applied to the output of each of the spatial filter banks. A different waveform is used within the APC framework for each spatial bin. The following details the sequential application of RISR and APC.

The data received on the array is down-converted, digitized, converted to the complex analytical representation, and collected into a matrix denoted as

$$\mathbf{Y}(\ell) = [\mathbf{y}_0(\ell) \ \mathbf{y}_1(\ell) \ \cdots \ \mathbf{y}_{M-1}(\ell)], \quad (4.59)$$

where the  $m^{\text{th}}$  column contains the complex samples from the  $m^{\text{th}}$  antenna element. First, the RISR filter (derived in Section 1.6.2) is computed and applied to the data received on the array as

$$\hat{\mathbf{x}}_{\text{RISR}}(\ell) = \mathbf{W}_{\text{RISR}}^H(\ell) \mathbf{y}^T(\ell). \quad (4.60)$$

The data in  $\hat{\mathbf{x}}_{\text{RISR}}(\ell)$  contains an estimate for each spatial bin at the  $\ell^{\text{th}}$  time sample. Next, the output after 3-10 iterations of RISR is organized into a matrix

$$\hat{\mathbf{X}}_{\text{RISR}} = \left[ \hat{\mathbf{x}}_{\text{RISR}}^T(0) \ \hat{\mathbf{x}}_{\text{RISR}}^T(1) \ \cdots \ \hat{\mathbf{x}}_{\text{RISR}}^T(L+N-1) \right]^T, \quad (4.61)$$

where each column contains the fast time data for an individual spatial bin. Finally, APC (derived in Section 1.6.1) is applied to each column of  $\hat{\mathbf{X}}_{\text{RISR}}$ . The APC estimate output for a particular spatial bin is obtained as

$$\hat{\mathbf{x}}(\ell, \theta)_{\text{RISR-APC}} = (\mathbf{R}_S(\ell, \theta) + \mathbf{R}_{\text{NSE}})^{-1} \mathbf{s}_\theta, \quad (4.62)$$

where  $\mathbf{s}_\theta = \mathbf{S}\mathbf{v}_\theta$  is the product of the waveform matrix and spatial steering vector associated with the particular spatial bin and the signal covariance matrix

$$\mathbf{R}_S(\ell, \theta) = \sum_{n=-N+1}^{N-1} \rho(\ell+n) \mathbf{s}_{\theta,n} \mathbf{s}_{\theta,n}^H, \quad (4.63)$$

in which

$$\mathbf{s}_{\theta,n} = \begin{cases} \left[ \begin{array}{ccc} s_{\theta,|n|} & \cdots & s_{\theta,N-1} & \mathbf{0}_{1 \times |n|} \end{array} \right]^T & \text{for } n \leq 0 \\ \left[ \begin{array}{ccc} \mathbf{0}_{1 \times n} & s_{\theta,0} & \cdots & s_{\theta,N-1-n} \end{array} \right]^T & \text{for } n > 0 \end{cases}. \quad (4.64)$$

and the noise covariance matrix  $\mathbf{R}_{\text{NSE}} = \sigma_{\text{NSE}}^2 \mathbf{I}_{N \times N}$  under the assumption of white noise (where  $\sigma_{\text{NSE}}^2$  is the noise power). The output of the filter in (4.62) is used to construct the estimate of the illuminated scene. Note that the spatial weighting developed in (4.6) for the space-range matched filter is also applied to the sequential estimate as well.

#### 4.5.4 FILTER RESPONSE SIMULATION ANALYSIS

The properties of the receive filter structure for SRAP, RISR, and APC will be examined by simulating a digital waveform diverse array (DWDA) radar scenario and then examining the space-range responses for each particular filter. The DWDA parameters used for this analysis are:  $M=10$  antenna elements,  $N=100$  samples in the transmitted pulse, and  $Z=5$  sub-waveforms

transmitted to 5 distinct spatial angles. The underlying waveforms are chosen to be random polyphase codes of the form

$$\mathbf{s}_z = e^{j2\pi\boldsymbol{\eta}_z} \quad (4.65)$$

where  $\boldsymbol{\eta}_z$  is a  $N/Z$ -length vector of independent samples drawn from a uniform distribution (between 0 and 1). The time-varying and aggregate beampatterns are shown in Fig. 4.4 and 4.5, respectively, and the space-range ambiguity diagram (SRAD) is displayed in Fig. 4.6.

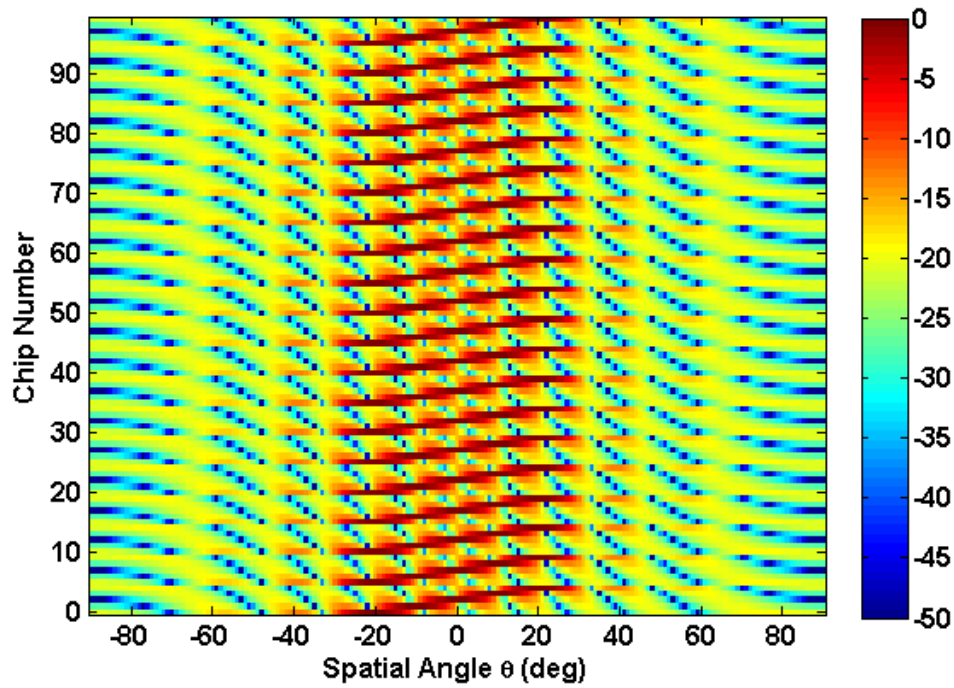


**Figure 4.4** Time-varying beampattern for filter analysis case

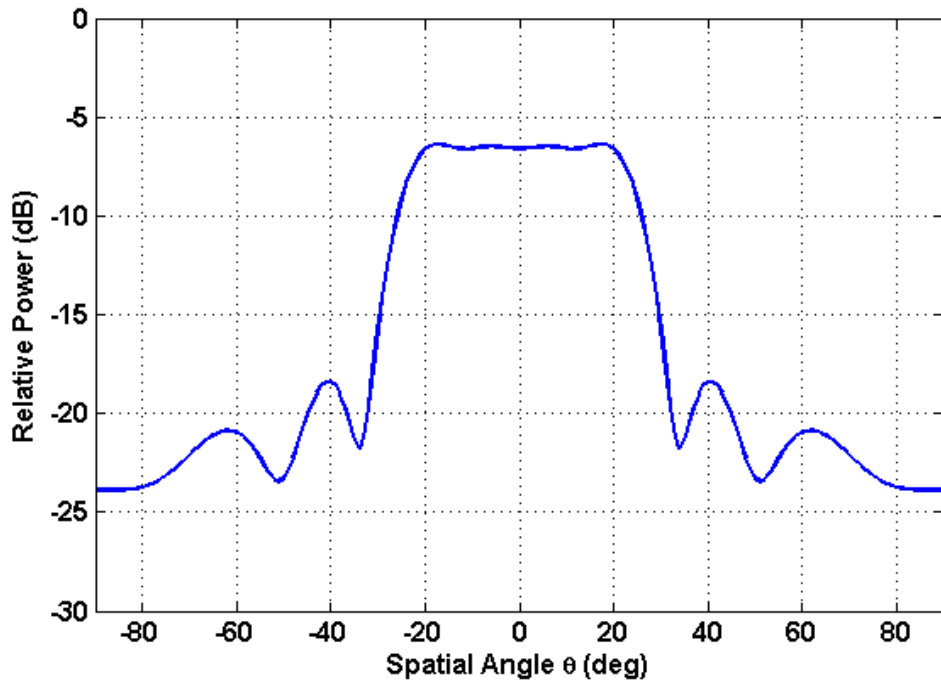


Figure 4.5 Aggregate beampattern for filter analysis case

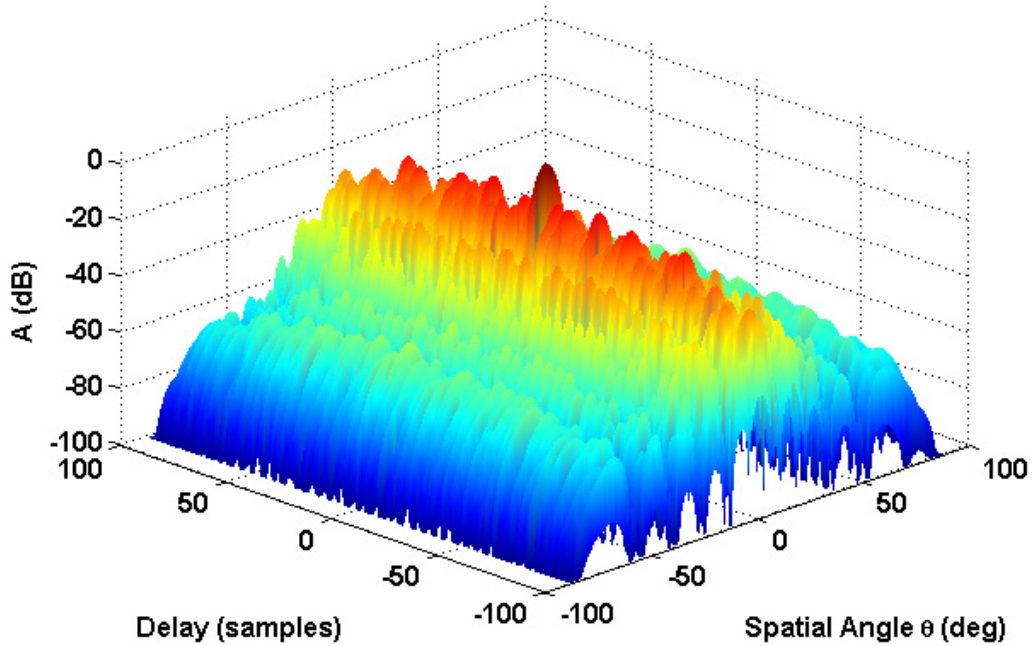
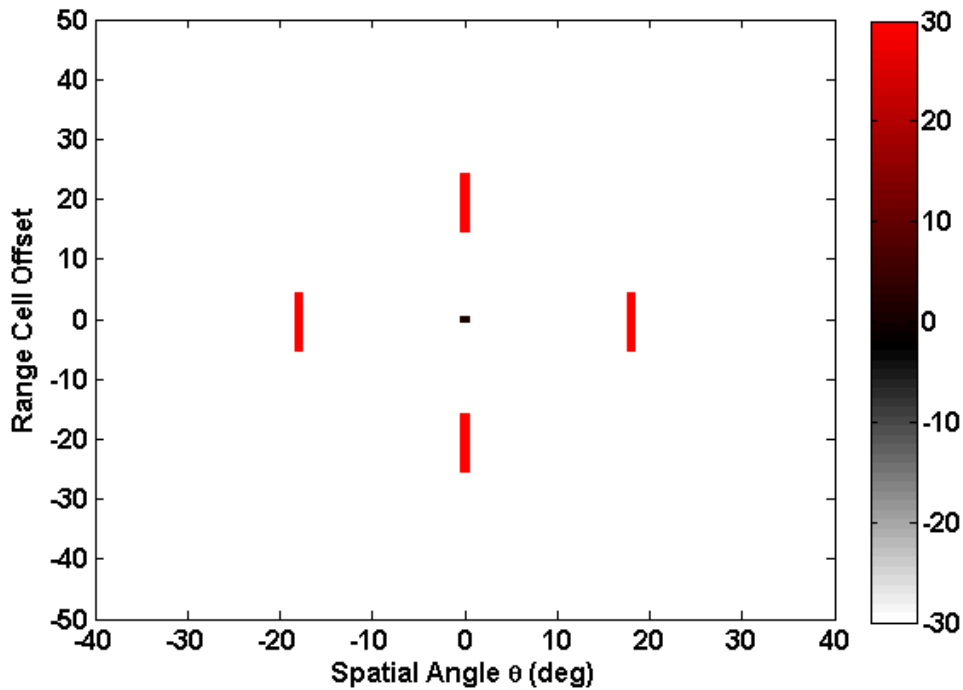


Figure 4.6 SRAD for filter analysis case

The ground truth for this simplified example (Fig. 4.7) consists of a central point scatterer surrounded by 4 clusters of large point scatterers in the absence of clutter and with very low noise. For reference the central target is located at range cell 200 but in Fig. 4.7 the y-axis is relative to the central target. This example is only used to assess the filter responses and not receiver performance. For the remainder of this chapter the illuminated scenes are constructed using 181 spatial bins distributed evenly between  $\pm 90^\circ$  relative to boresight. For this case the matched filter, RISR, and SRAP will use 51 spatial bins for processing and RISR, APC, and SRAP employ 7, 2, and 3 iterations, respectively.



**Figure 4.7** Ground truth for filter analysis simulation

The results after the matched filter, sequential RISR-APC, and SRAP are applied are shown in Figs. 4.8-4.10. The matched filter result is plagued with spatial and range sidelobes as suggested

by the SRAD in Fig. 4.6. Sequential RISR-APC suppresses some of the spatial and range sidelobes and SRAP suppresses nearly all of the range sidelobes and most of the spatial sidelobes.

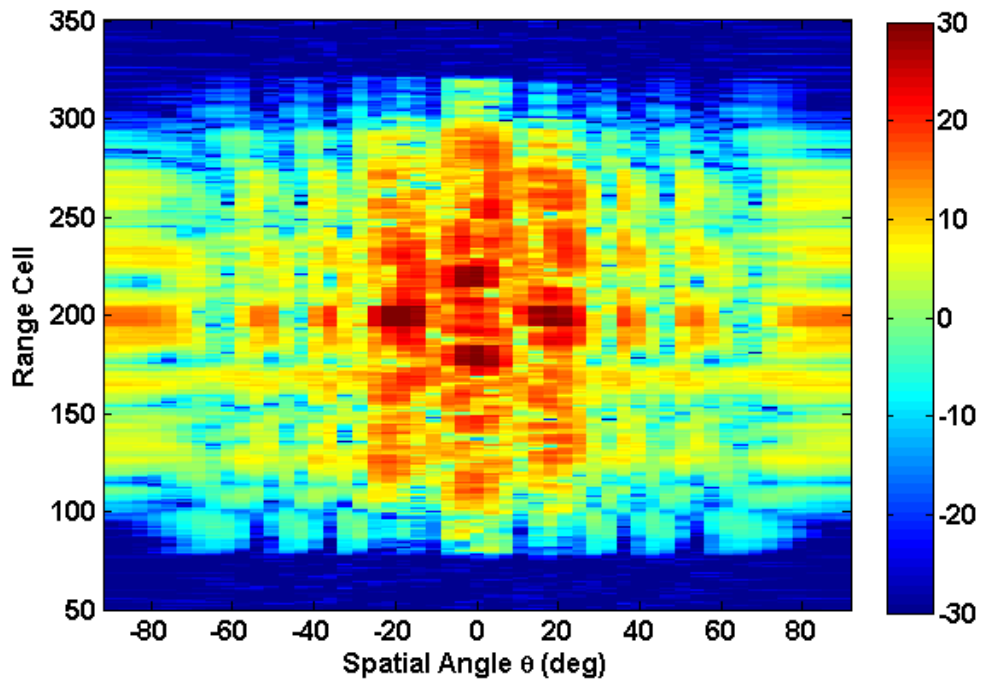


**Figure 4.8** Matched filter output for the filter analysis case

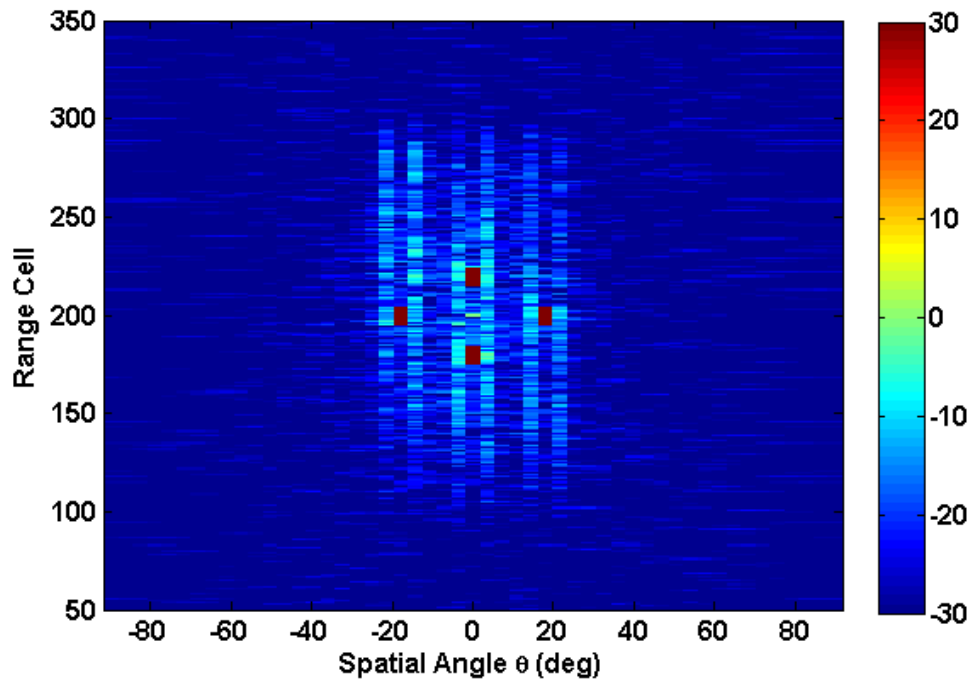


**Figure 4.9** Sequential RISR-APC output for the filter analysis case

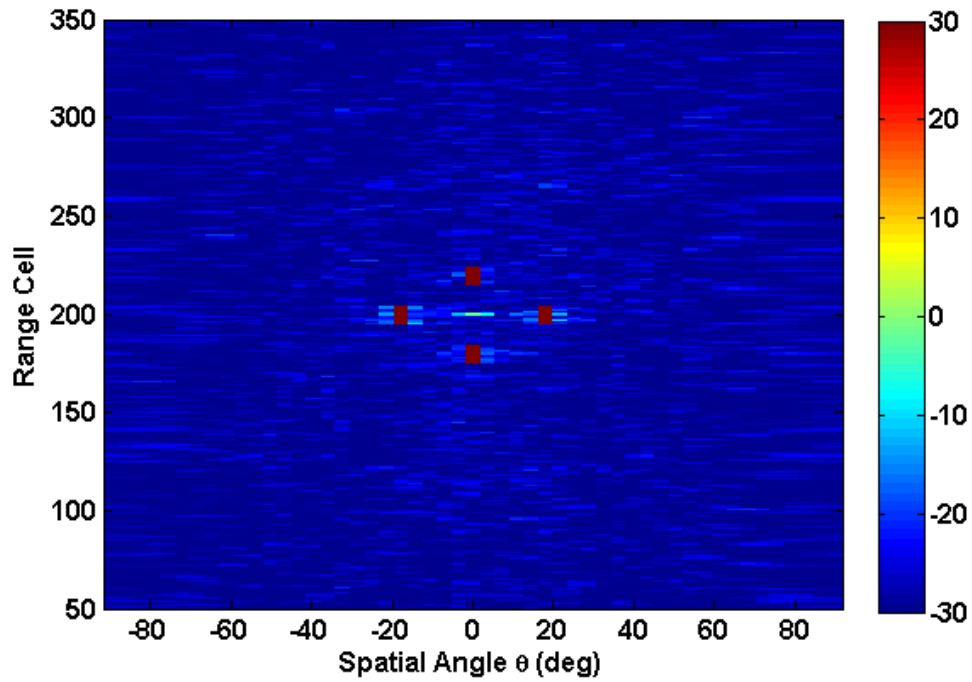


**Figure 4.10** SRAP output for the filter analysis case

The attributes of RISR, APC, and SRAP are examined by investigating the filter response for the adaptive filters associated with the central target (located at range cell 200, spatial angle  $0^\circ$ ) in Fig. 4.7. The filter response for RISR given by (4.55) is displayed in Fig. 4.11 wherein the white boxes denote the nulls created by the adaptive RISR filter structure to mitigate the spatial interference from the target groups at  $\pm 18^\circ$  degrees. Note the depth of the indicated nulls only account for the array processing gain and not the pulse compression gain that will be achieved when RISR is followed by APC. The APC filter response for the adaptive filters from the boresight spatial bin for range cells 100 to 300 is shown in Fig. 4.12. For a given filter range cell index deep nulls appear at the range offset corresponding to the target clusters seen in Fig. 4.13 at ranges 175-184 and 215-224 in the boresight spatial bin. The APC filter response does not indicate the error that is caused by residual spatial sidelobes that spread into the boresight spatial bin. The sequential RISR-APC filter response (Fig. 4.13) incorporates the effects of both algorithms. In Fig. 4.13 the black boxes indicate the locations of the nulls formed by both RISR and APC; note the nulls in range are isolated to the range cells that contain targets but the spatial nulls extend beyond the locations of the off-boresight target groups. Conversely, the SRAP filter response exhibits very precise space-range nulls indicated by the black boxes in Fig. 4.14, which appear at spatial and range offsets corresponding to the surrounding target groups, thus demonstrating the ability of SRAP to manipulate the available degrees of freedom to reduce contributions from range/spatial sidelobes where appropriate. Note that the filter response still contains sidelobe levels near that of the matched filter response. However, the SRAP filter's sidelobes reside in locations that correspond to regions of the scene that do not contain any large scatterers and thus do not impact performance.

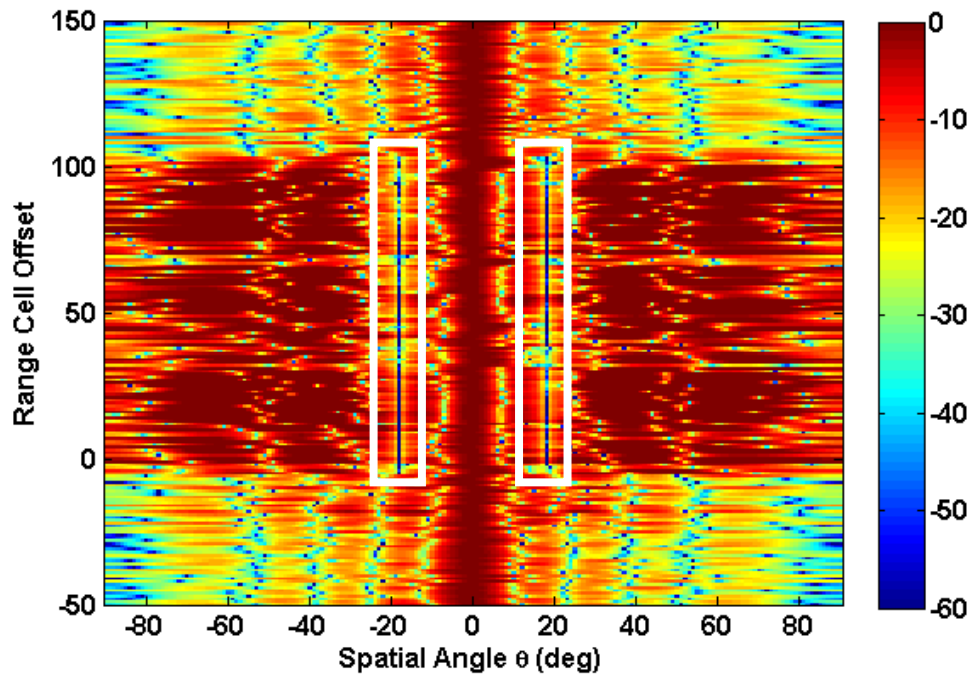


Figure 4.11 RISR filter response

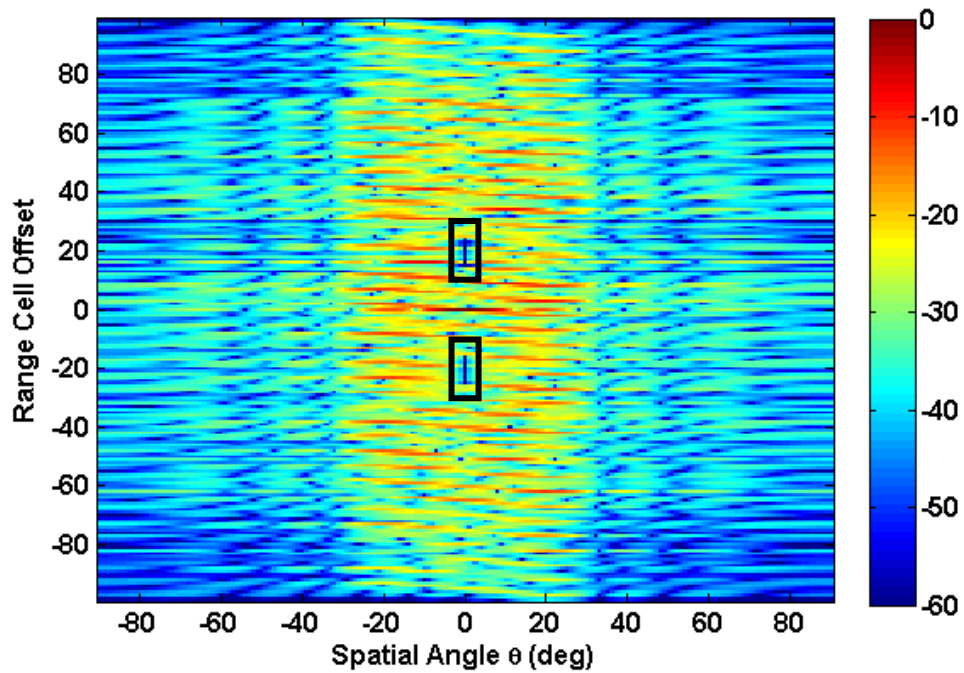


Figure 4.12 APC filter response

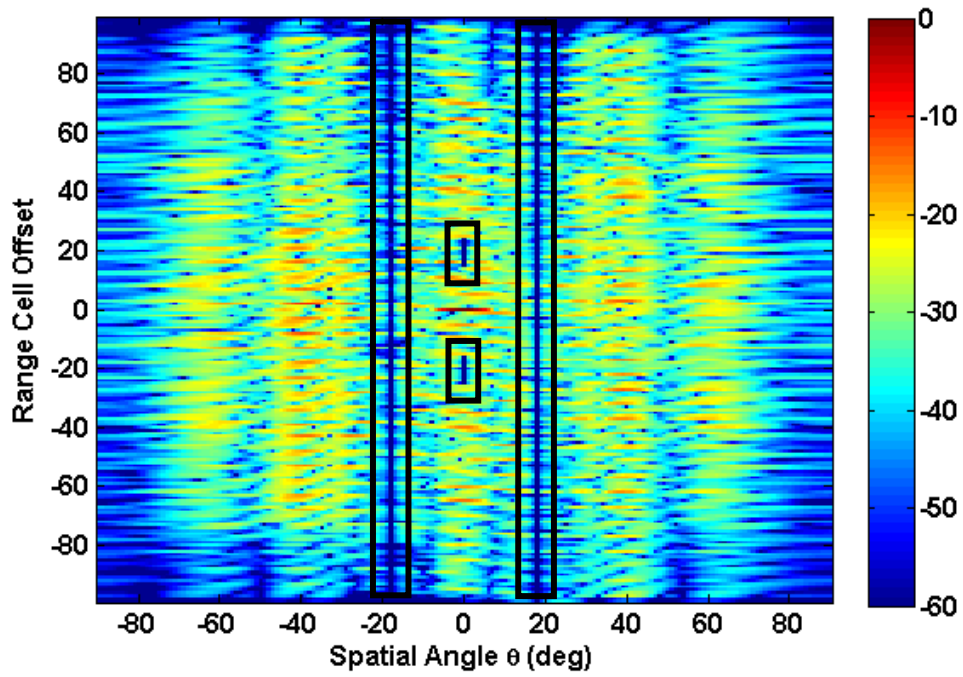


Figure 4.13 Sequential RISR-APC filter response

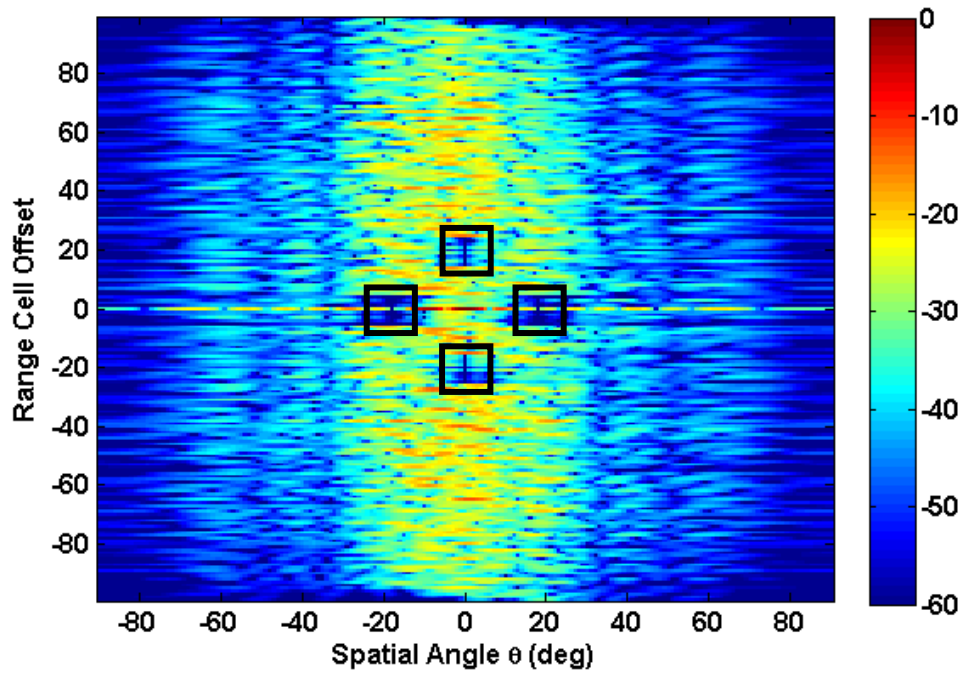


Figure 4.14 SRAP filter response

## 4.6 SIMULATION RESULTS

The performance of SRAP in three different scenarios will be assessed via simulation. First an imaging scenario will be examined followed by a surveillance example and finally this section will conclude with a moving target indication (MTI) simulation. Each simulation consists of point targets in complex additive white Gaussian noise. The performance of SRAP will be compared to standard matched filtering in range and angle as well as sequential adaptive processing achieved by first applying the RISR algorithm followed by APC.

### 4.6.1 IMAGING SCENARIO

The following simulation assumes an  $M = 20$  element uniform linear array with half-wavelength spacing. In this scenario, the transmitted waveform parameters are  $N=200$  and  $Z=10$ , where the underlying waveforms are again composed of random polyphase codes. The time-varying beampattern, aggregate beampattern, and SRAD for the waveforms used in this section are shown in Figs. 4.15, 4.16, and 4.17, respectively. This particular mode enables wide area coverage for a sustained period of time, thus allowing for inverse synthetic aperture imaging to be accomplished at the same time as detection and tracking operations. It should be also noted that different types of waveforms, e.g., track, search, and imaging, can be transmitted simultaneously using the transmission scheme presented in Chapter 3. In the following, 101 spatial bins are used for processing and RISR, APC, SRAP, and RD-SRAP employ 5, 3, 3, and 3 adaptive iterations, respectively.

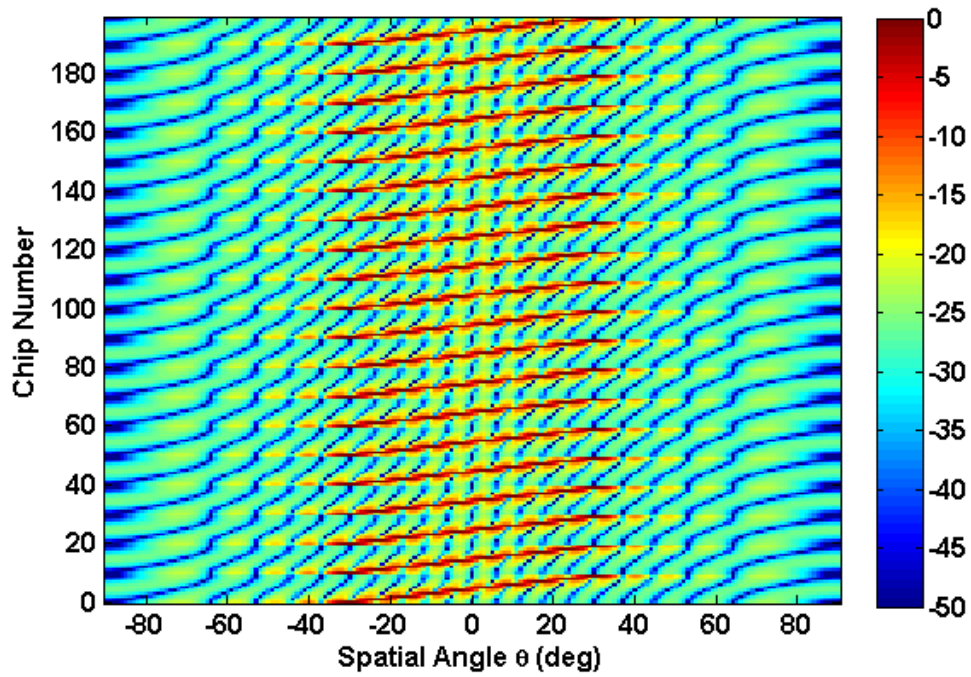


Figure 4.15 Time-varying beam pattern for simulation results

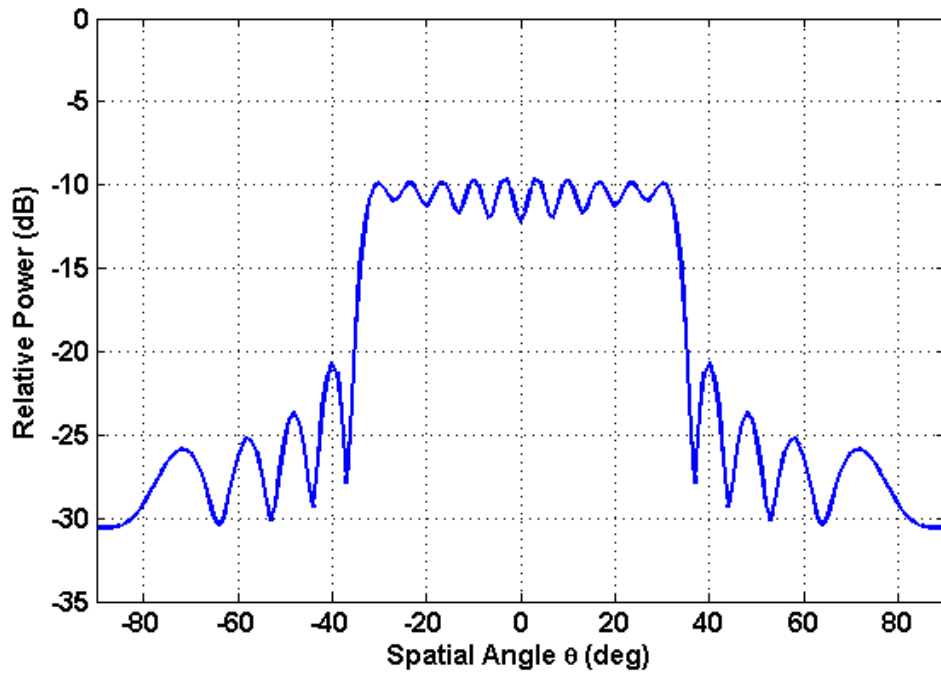
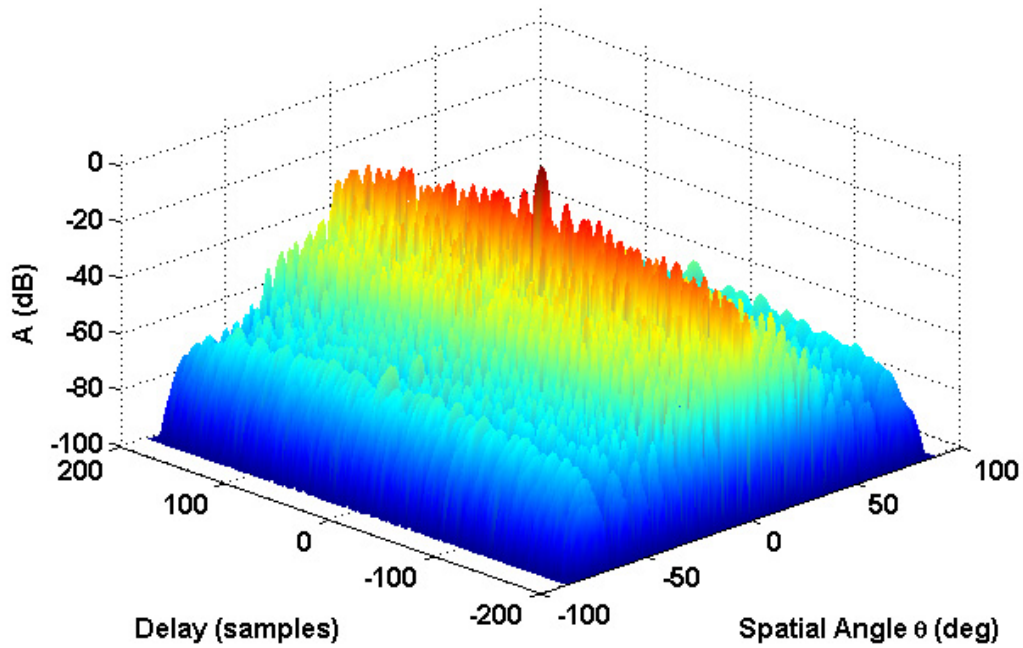


Figure 4.16 Aggregate beam pattern for imaging scenario



**Figure 4.17** SRAD (in dB) for imaging scenario

Figure 4.18 displays the ground truth for the imaging case which consists of several closely spaced shapes. Before processing the SNR of the shapes range from  $-12$  dB to  $0$  dB where the total processing gain is  $26$  dB. The matched filter output in Fig. 4.19 is plagued with space-range sidelobes, as expected, resulting in a very poor image. Sequential RISR-APC outperforms the matched filter as evidenced by Fig. 4.20, albeit some sidelobes remain. Fig. 4.21 displays the SRAP output that has suppressed nearly all of the space-range sidelobes to the level of the noise and Fig. 4.22 illustrates that RD-SRAP with  $K=4$  has performed nearly as well as the full dimension version.

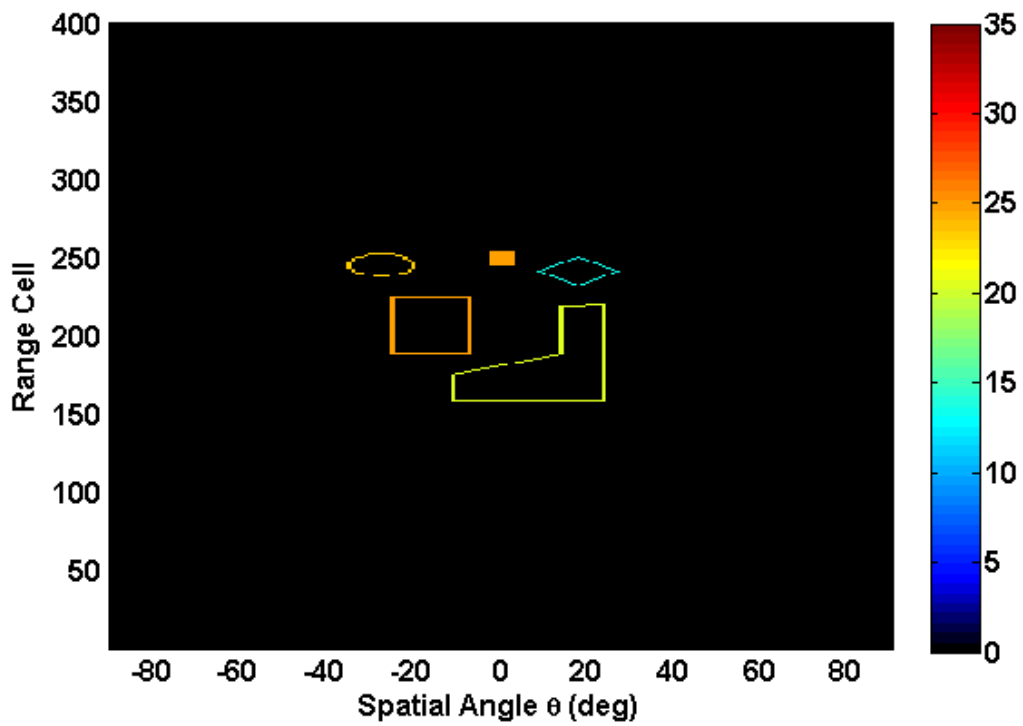


Figure 4.18 Ground truth (in dB) for imaging scenario

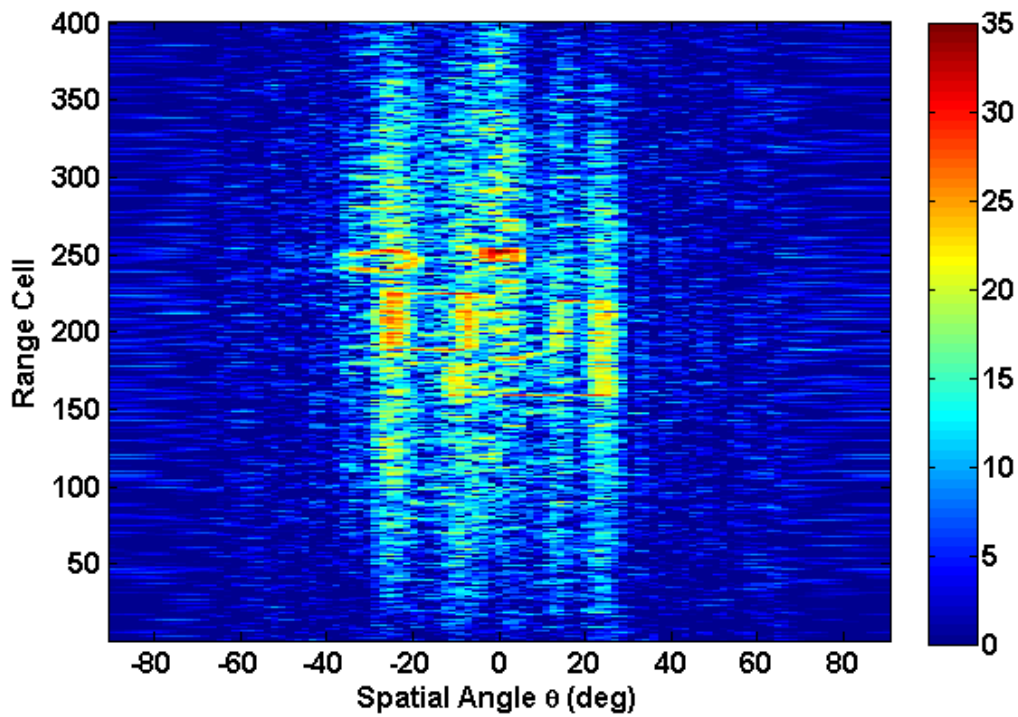


Figure 4.19 Matched filter estimate (in dB) for imaging scenario

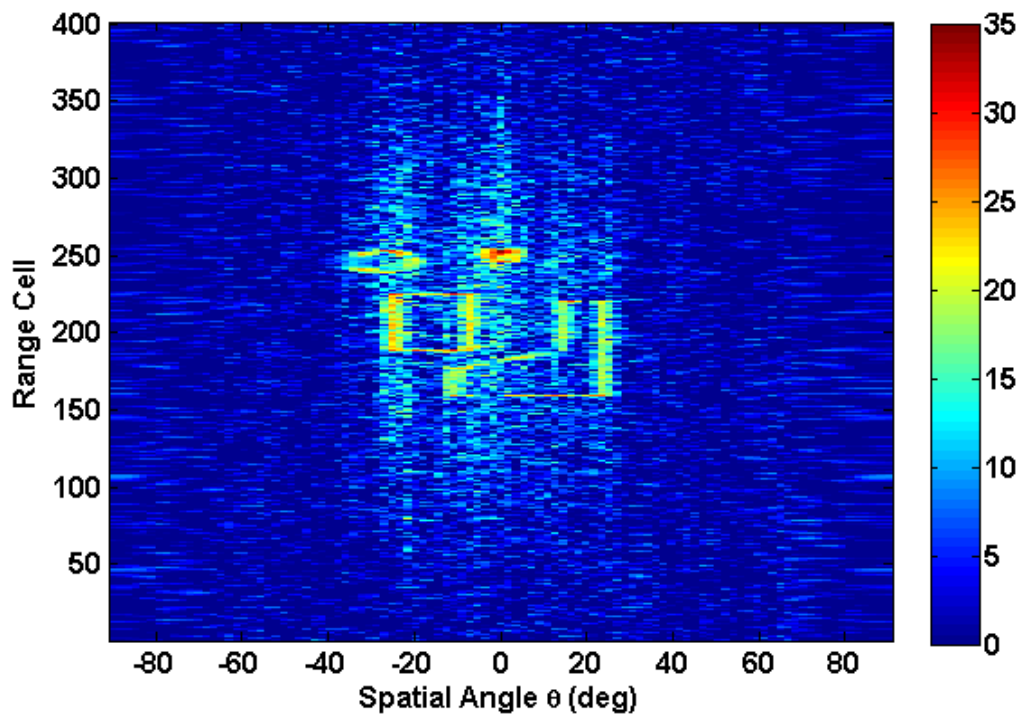


Figure 4.20 Sequential RISR-APC estimate (in dB) for imaging scenario

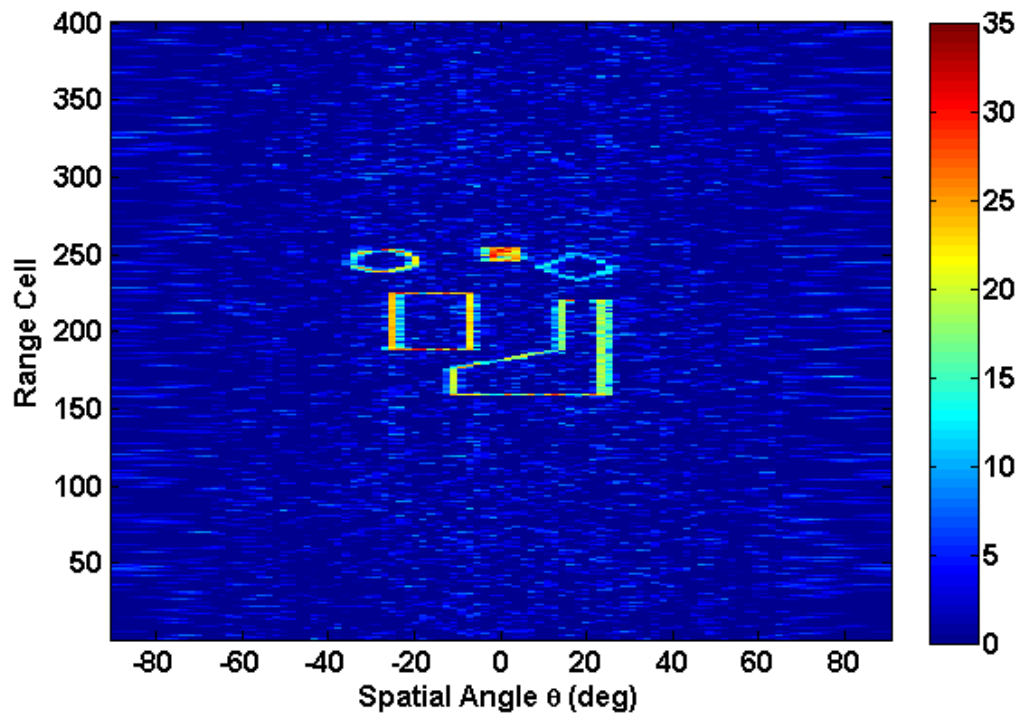
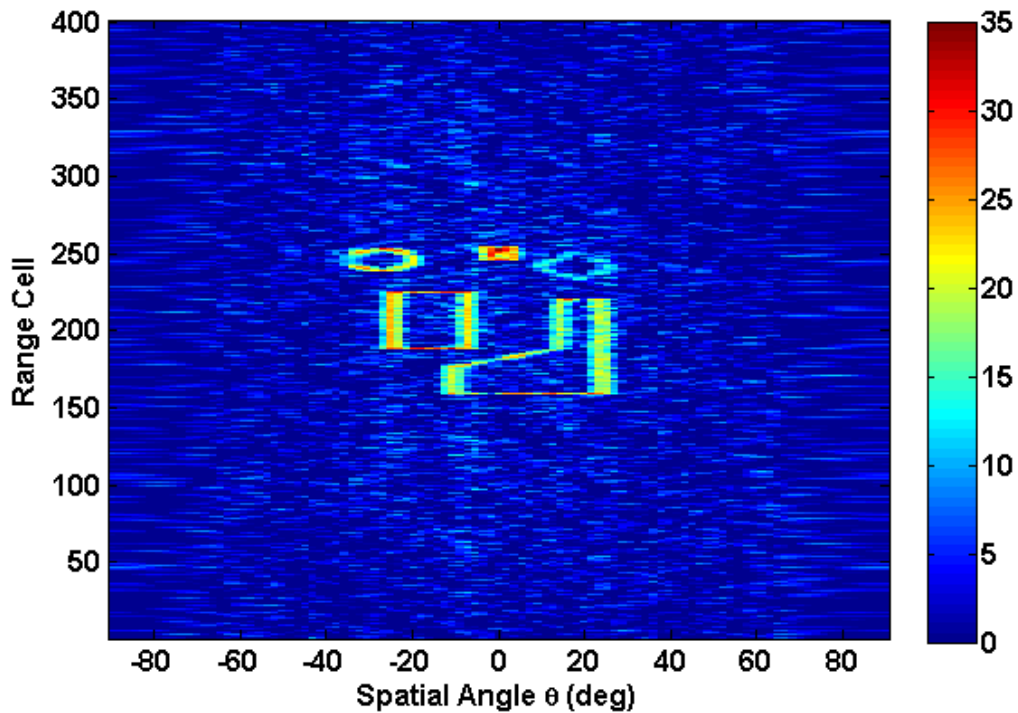


Figure 4.21 SRAP estimate (in dB) for imaging scenario



**Figure 4.22** RD-SRAP ( $K=4$ ) estimate (in dB) for imaging scenario

#### 4.6.2 SURVEILLANCE SCENARIO

The radar parameters for the second scenario are the same as Section 4.5.4 ( $N=100$ ,  $Z=5$ , and  $M=10$ ) and the illuminated scene now contains 12 distributed targets between range cells 183 and 225 and angles  $-12^\circ$  and  $+15^\circ$  as described in Table 1 (stated SNR values are before processing). The SNR of the largest target is 40 dB after a processing gain of 23.6 dB. Similar to the previous case the matched filter results in limited sensitivity as illustrated in Fig. 4.23, in which it is difficult to separate the targets, whose locations are denoted by the white circles, from the sidelobes. In this case, sequential adaptation (Fig. 4.24) exhibits some improvement. Figure 4.25 displays the result after two adaptive stages of SRAP resulting in complete sidelobe mitigation thus revealing all 12 targets. Fig. 4.26 depicts the output of RD-SRAP with  $K=5$ , in which the reduced dimensionality version has performed nearly as well as SRAP.

**Table 4.2** Target Description for Surveillance Scenario

Range Cell $\ell$	Angle $\theta$	SNR (dB)
183	$10^\circ$	11.4
190	$-10^\circ$	16.4
191	$5^\circ$	6.4
197	$15^\circ$	-8.6
201	$-6^\circ$	-9.6
203	$-12^\circ$	-2.6
205	$-5^\circ$	-8.6
208	$-9^\circ$	-5.6
210	$-10^\circ$	16.4
222	$0^\circ$	-3.6
224	$14^\circ$	9.4
225	$8^\circ$	-10.6

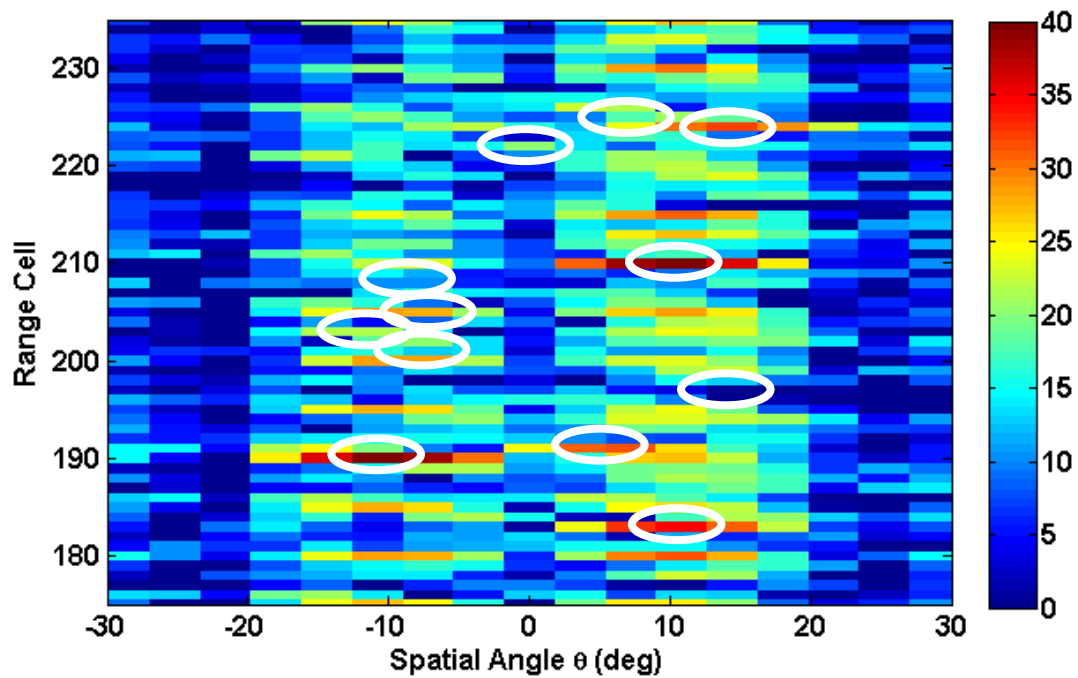


**Figure 4.23** Matched filter estimate (in dB) for surveillance scenario

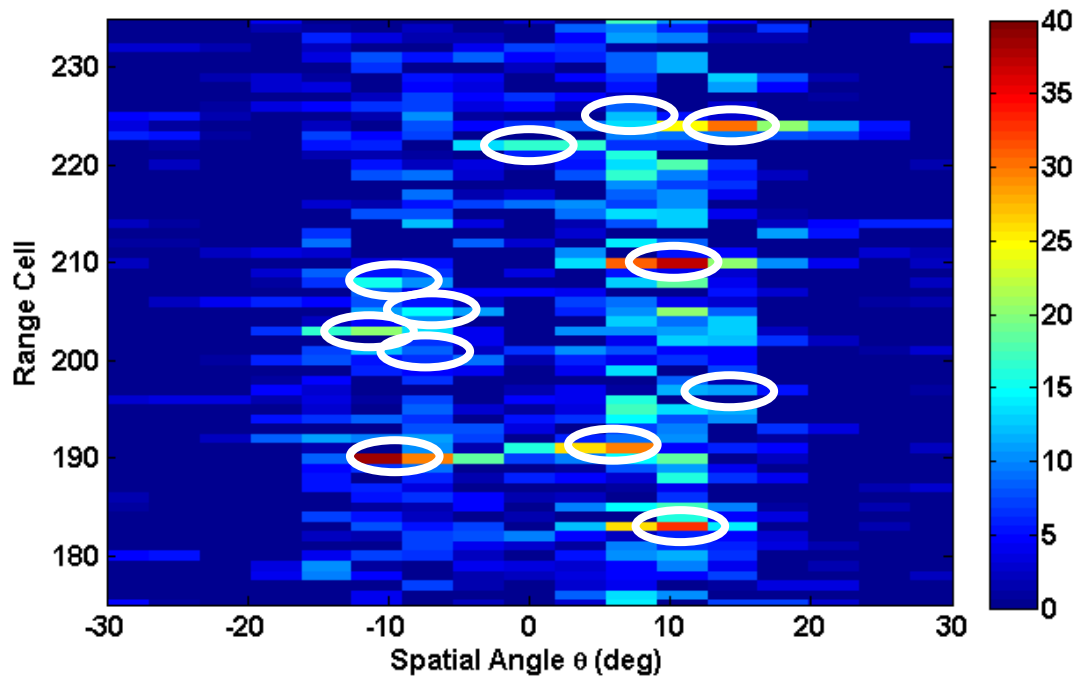


Figure 4.24 Sequential RISR-APC estimate (in dB) for surveillance scenario

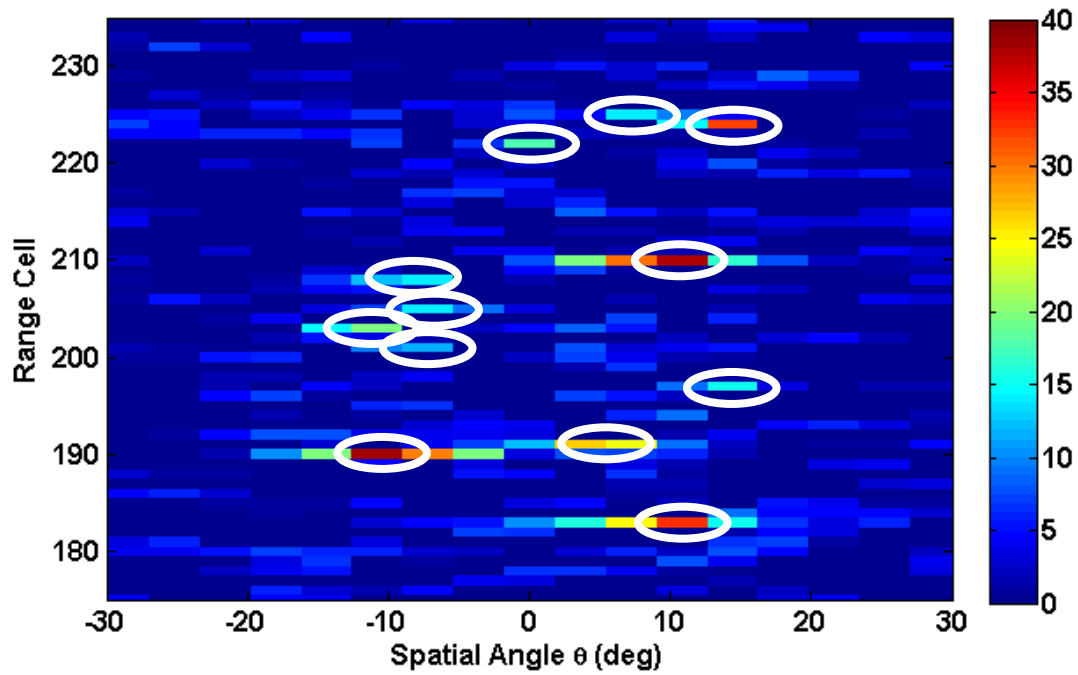
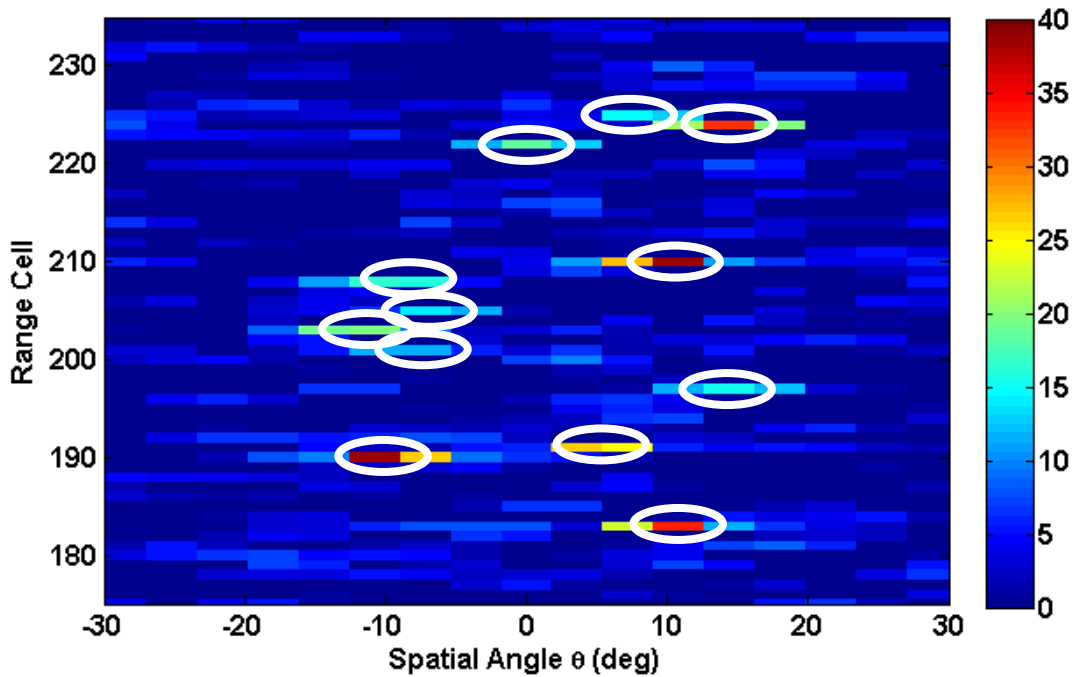


Figure 4.25 SRAP estimate (in dB) for surveillance scenario



**Figure 4.26** RD-SRAP ( $K=5$ ) estimate (in dB) for surveillance scenario

#### 4.6.3 *MTI SCENARIO*

A moving target indication scenario (MTI) will be simulated to assess the performance of SRAP when proceeding clutter cancellation. In this case the radar is located on a stationary platform such that low velocity ground clutter is present. The moving targets are modeled as point targets in additive white Gaussian noise. The clutter is independent and identically distributed in range and angle where the real and imaginary components are zero mean Gaussian random variables each with a variance of half the clutter power. The clutter Doppler phase is distributed uniformly between  $-2^\circ$  and  $2^\circ$  and the average clutter to noise ratio 70 dB (after coherent processing gain). An  $M=10$  element uniform linear array with half-wavelength spacing is used. The transmitted waveform parameters are again identical to those in Section

4.5.4. The radar CPI consists of 64 pulses and Doppler processing is performed using a 128-point FFT in conjunction with a Chebychev window.

In the following, RD-SRAP is used with a blocking factor of  $K = 5$ , 51 spatial bins are used for processing, and SRAP employs 3 adaptive iterations. Note that the RD-SRAP algorithm is applied only to the first pulse of the received data to determine each range-angle filter, after which the filters are stored and used to process the remainder of pulses in the CPI. The illuminated scene contains 10 distributed targets between range cells 176 and 223 and angles  $-7^\circ$  and  $+16^\circ$  as described in Table 2 (stated SNR values are before a coherent processing gain of 41 dB).

For each processing methodology, the received data is first processed by applying clutter cancellation via the projection

$$\mathbf{W}_{cc} = (\mathbf{C}\mathbf{C}^H + \delta\mathbf{I})^{-1}, \quad (4.66)$$

where

$$\mathbf{C} = [\mathbf{c}_0 \ \mathbf{c}_1 \ \dots \ \mathbf{c}_{p-1}] \quad (4.67)$$

is composed of a set of Doppler steering vectors

$$\mathbf{c}_p = \left[ 1 \ e^{j\frac{2\pi f_p}{f_{PRF}}} \ \dots \ e^{j\frac{2\pi f_p}{f_{PRF}}(M-1)} \right]^T \quad (4.68)$$

parameterized by the Doppler frequencies  $f_p$  at which a notch in the Doppler spectrum is desired and the radar PRF  $f_{PRF}$ . Furthermore, the term  $\delta$  is a diagonal loading term to prevent the matrix in (4.66) from becoming ill-conditioned; for the following simulation  $\delta = 10^{-8}$ . The clutter cancellation filter is applied to the pulses received at each element and range sample.

**Table 2** Target Description for Surveillance Scenario

Target Number	Range Cell $\ell$	Angle $\theta$	Doppler Phase	SNR (dB)
1	176	10°	90°	1
2	193	-4°	45°	2
3	195	13°	-90°	-1
4	213	-7°	-45°	4
5	198	16°	30°	3
6	181	-3°	-30°	-6
7	202	13°	135°	-11
8	187	-1°	-135°	-16
9	223	4°	150°	-11
10	208	12°	-150°	-16

Figure 4.27 displays the matched filtering results (simple coherent integration in range and angle) when the scattering estimates are compressed (summed incoherently) in Doppler (top plot) and spatial angle (bottom plot). Figures 4.28-4.30 depict the compressed estimates for sequential adaptive processing, SRAP, and RD-SRAP (with  $K=5$ ), respectively. It is evident that SRAP and RD-SRAP have suppressed most of the range and spatial sidelobes such that the targets are readily identifiable. In contrast, sequential adaptive processing and to a greater degree the matched filter outputs possess sidelobes, making it difficult to identify the moving targets. Figures 4.31-4.36 show various range cuts in which SRAP and RD-SRAP outperform the matched filter and sequential adaptation.

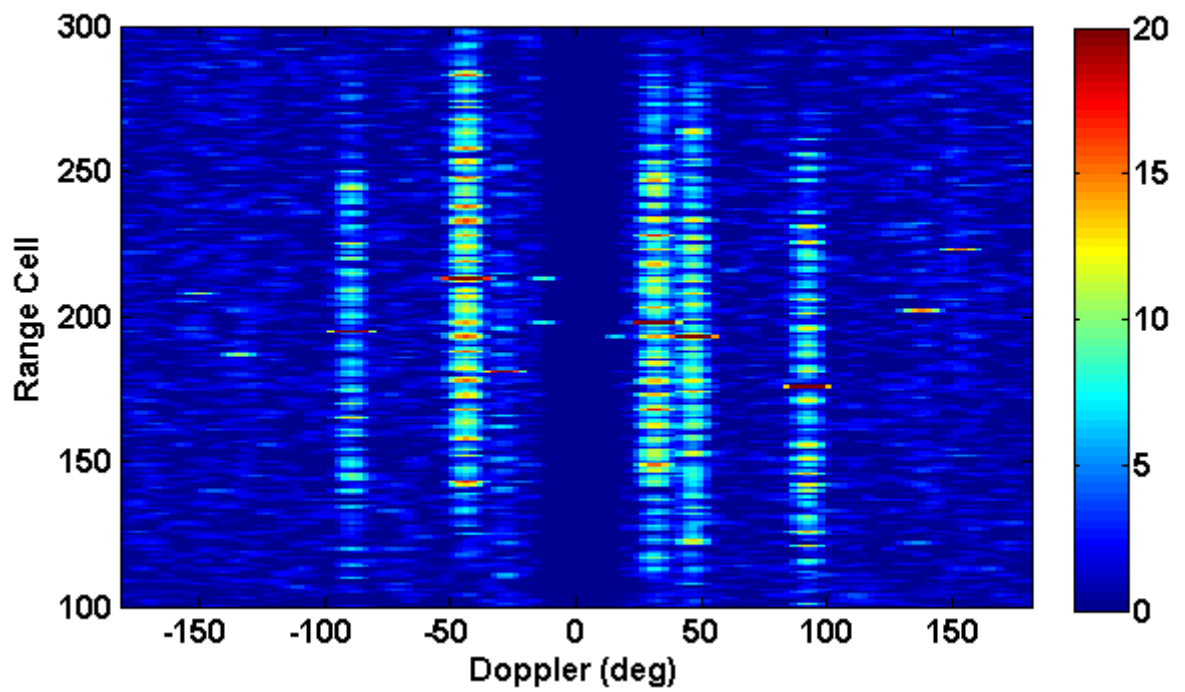
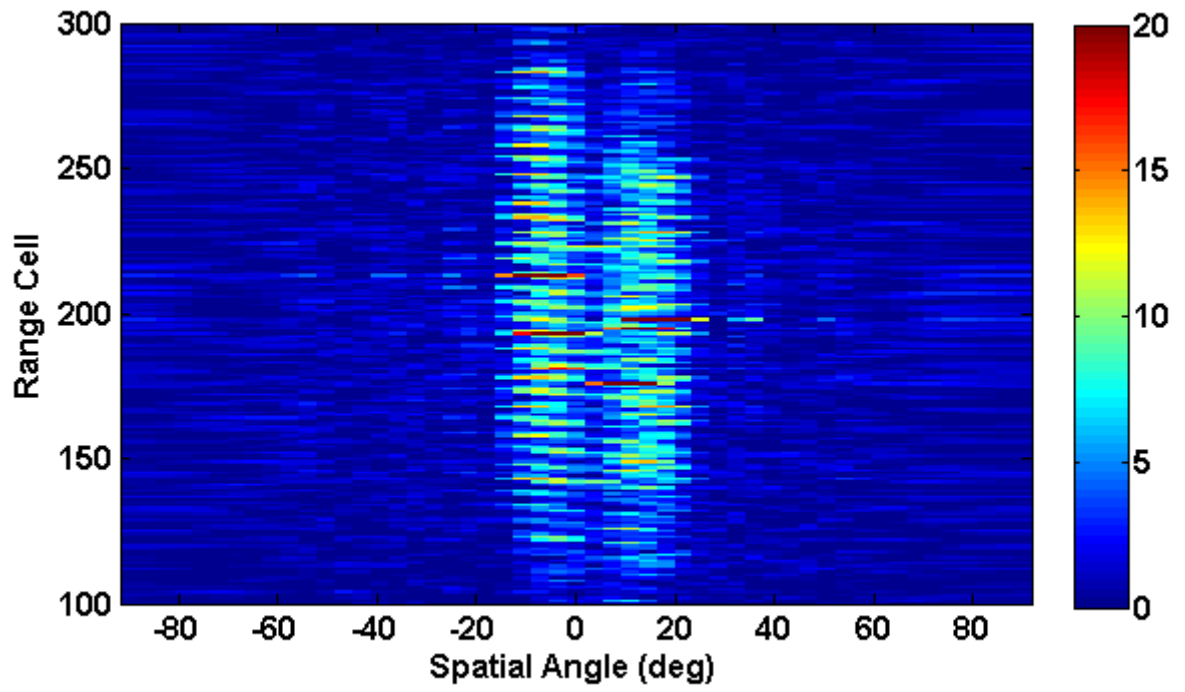


**Figure 4.27** Matched filter output (in dB) compressed in Doppler (top) and spatial angle (bottom)

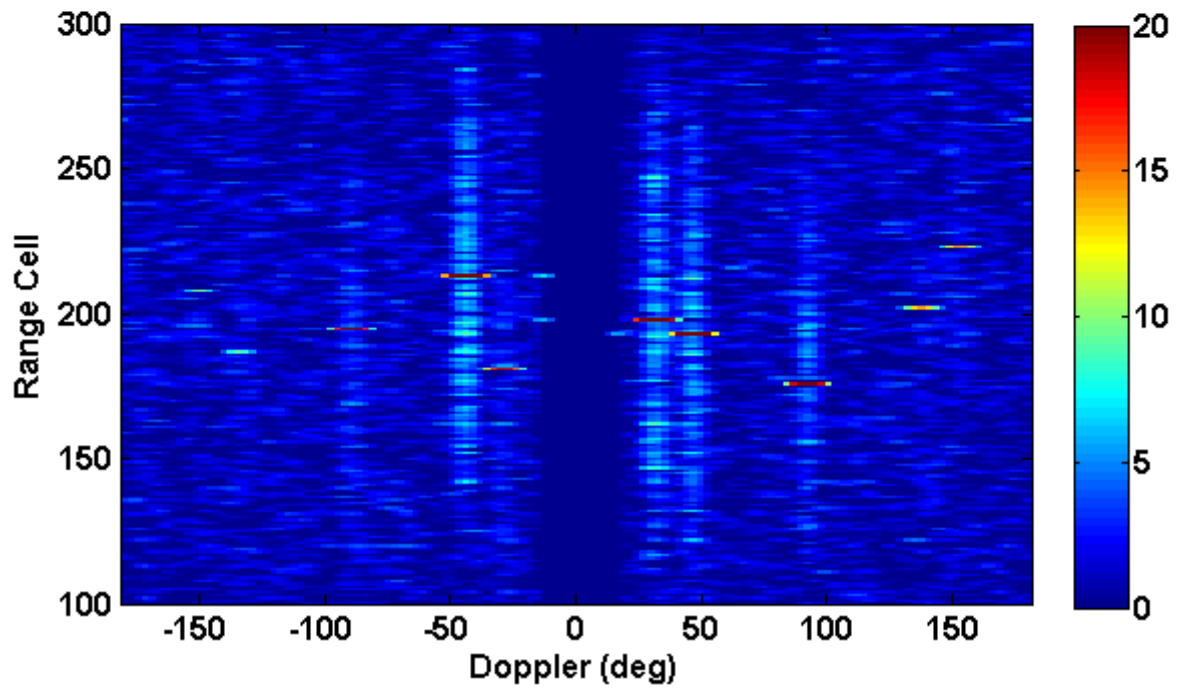
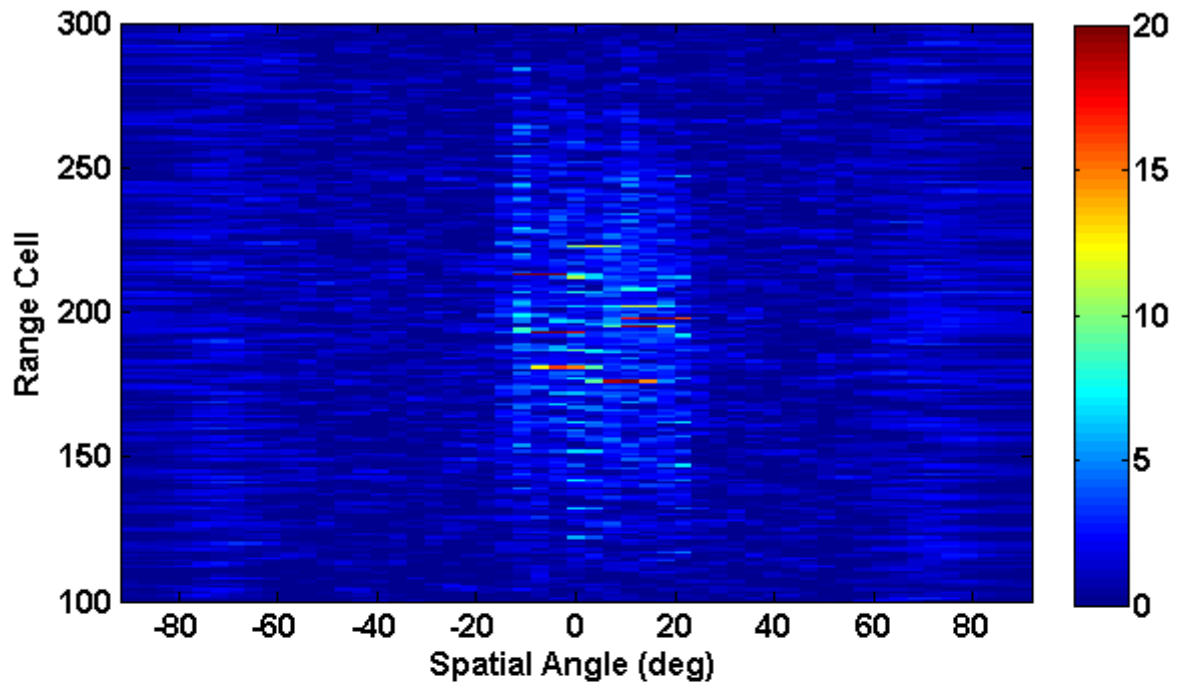


**Figure 4.28** Sequential adaptive processing output (in dB) compressed in Doppler (top) and spatial angle (bottom)

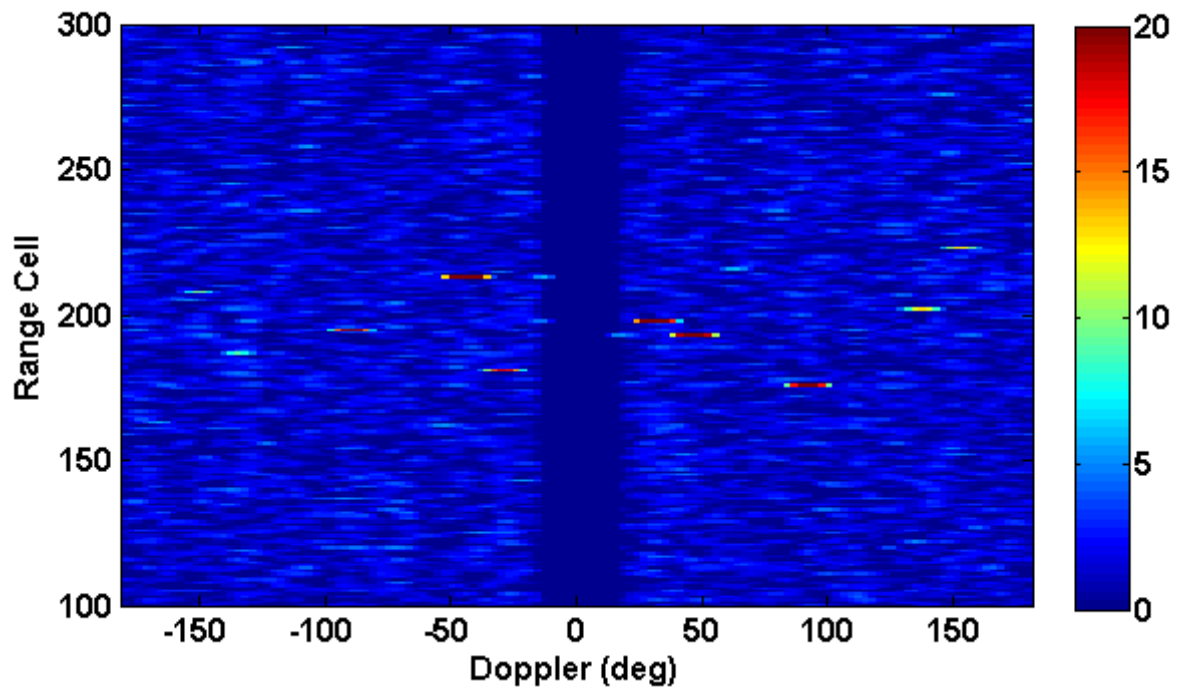
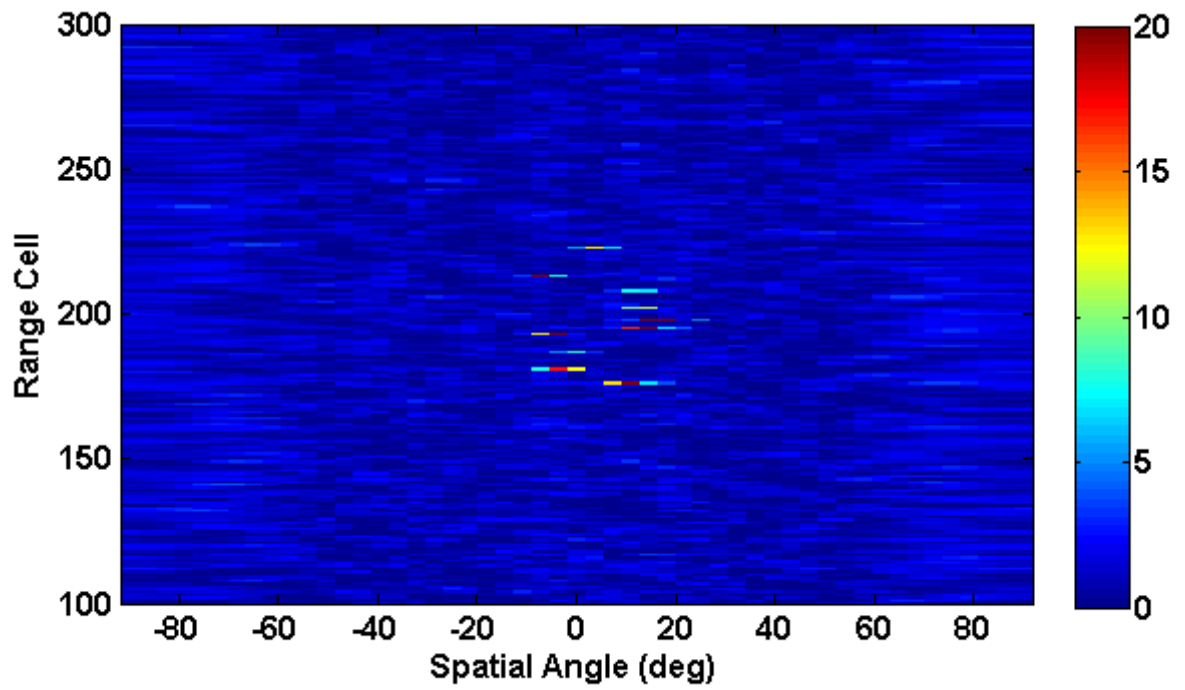


**Figure 4.29** SRAP output (in dB) compressed in Doppler (top) and spatial angle (bottom)

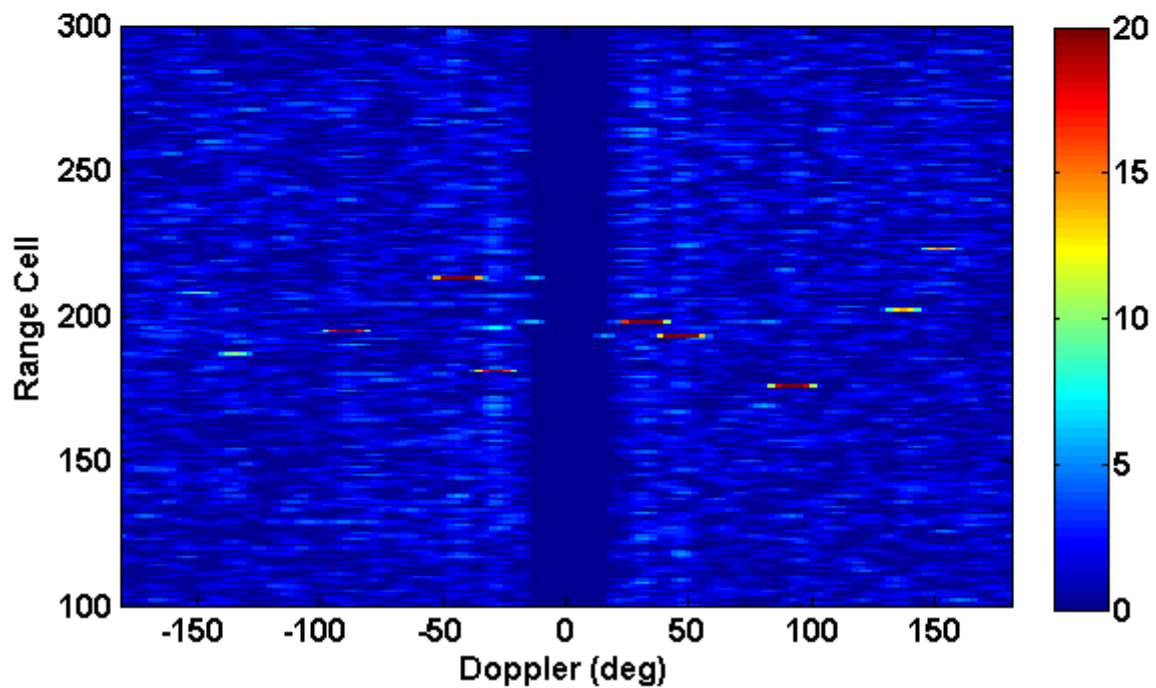
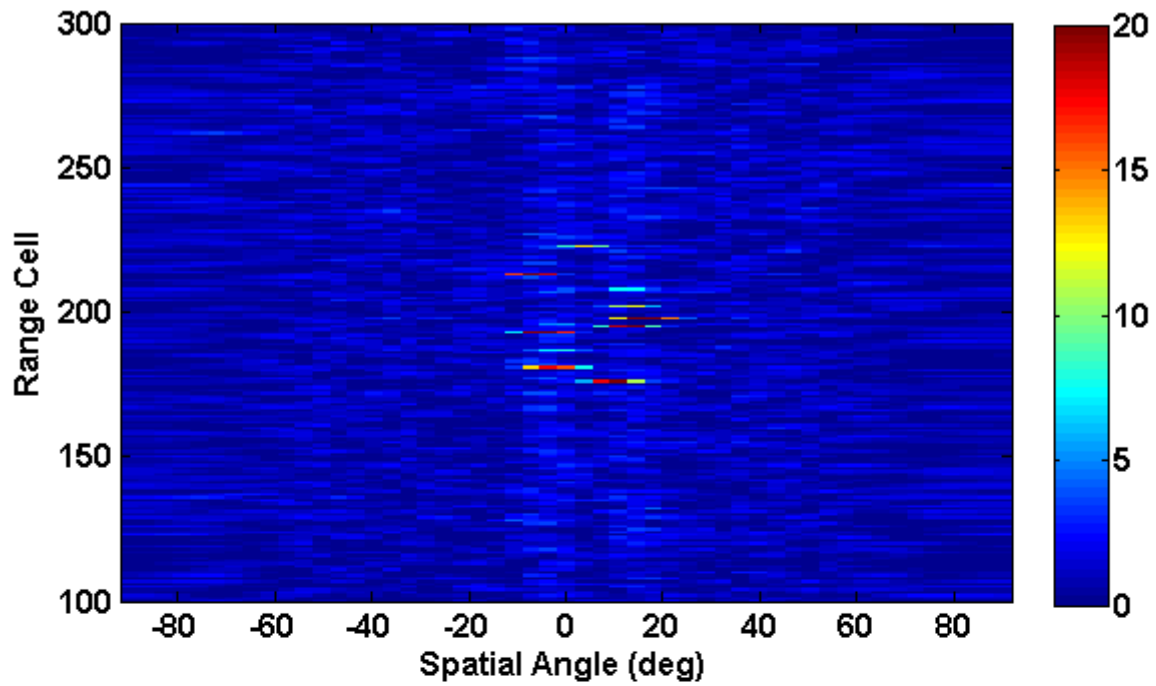


**Figure 4.30** RD-SRAP ( $K=5$ ) output (in dB) compressed in Doppler (top) and spatial angle (bottom)

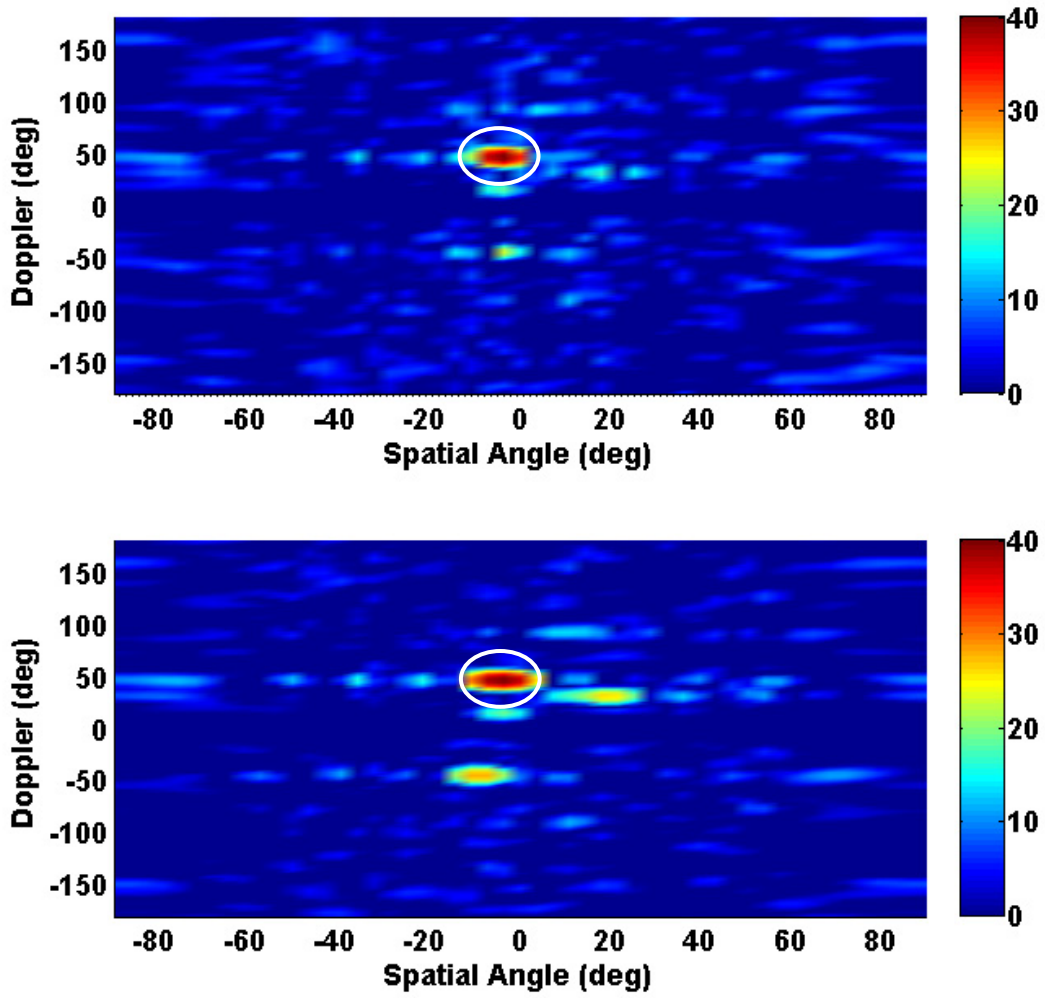


**Figure 4.31** Sequential adaptive processing (top) and matched filter (bottom) outputs in dB for range cell 193, Target 2 is denoted by the white circle

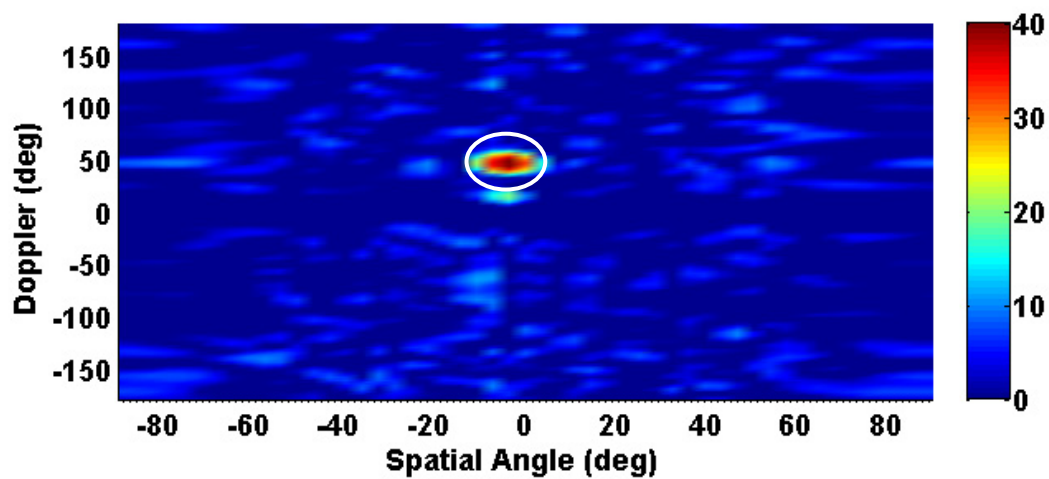
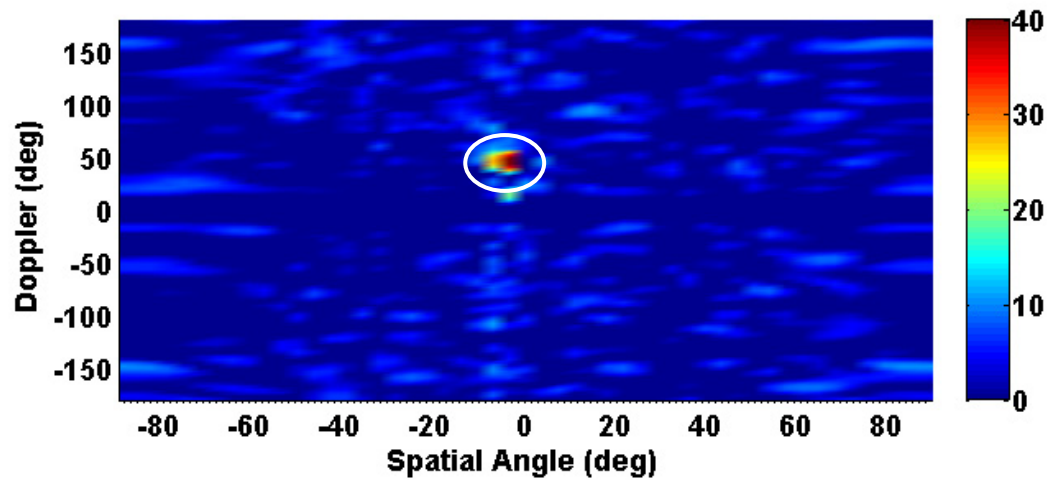
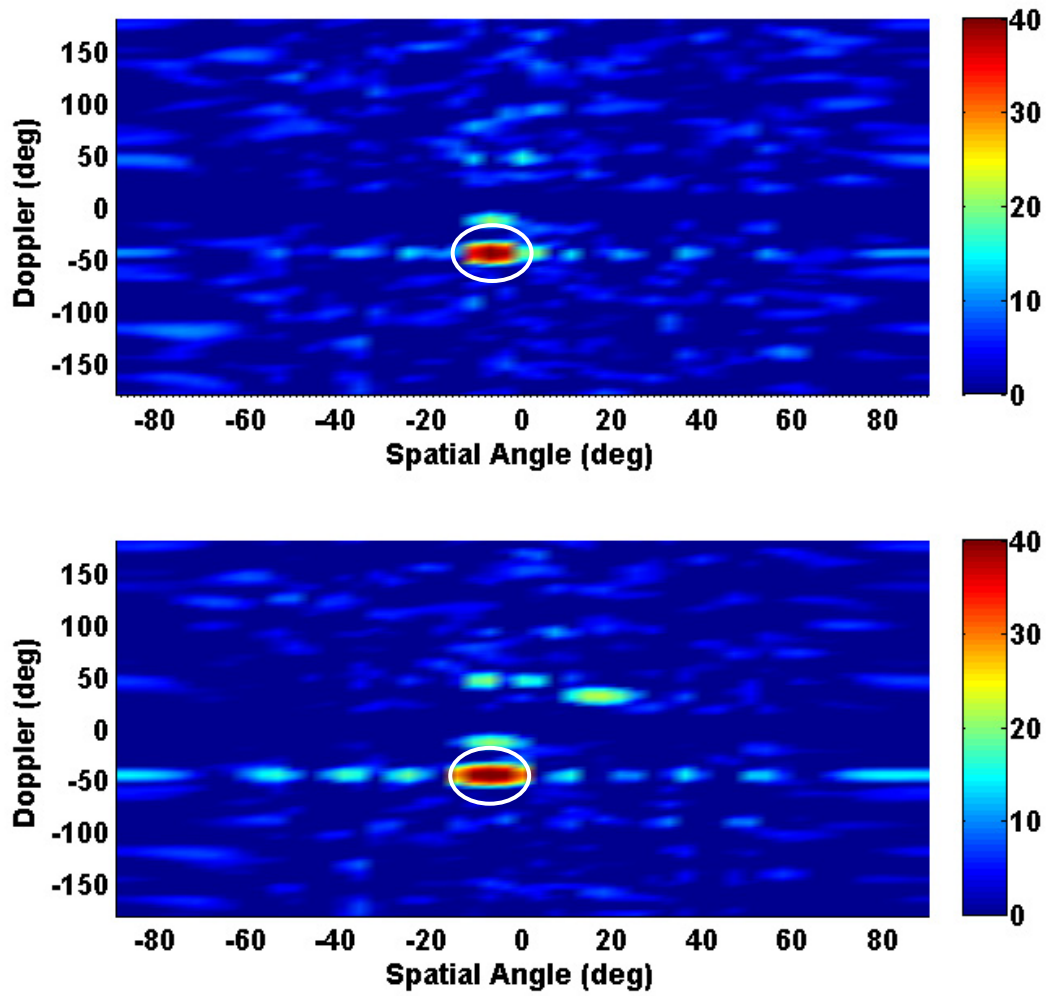
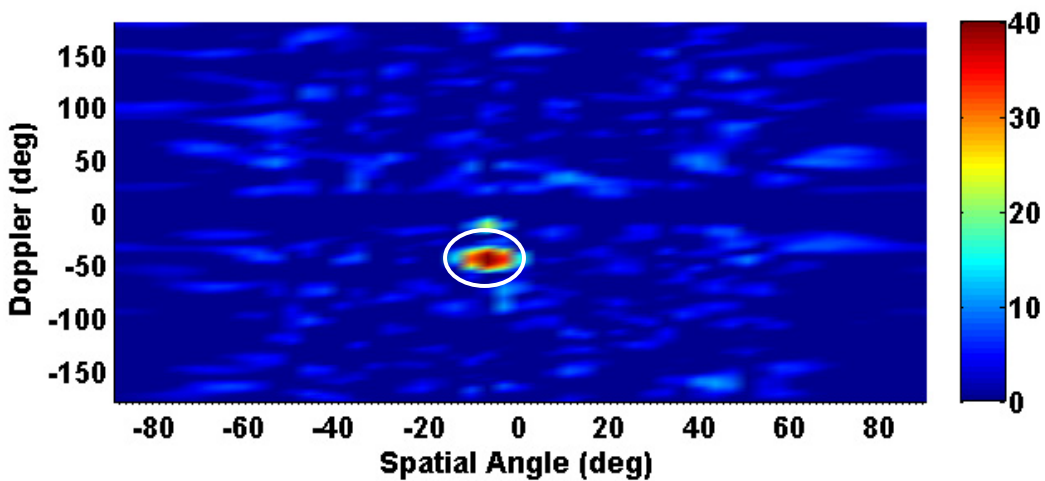
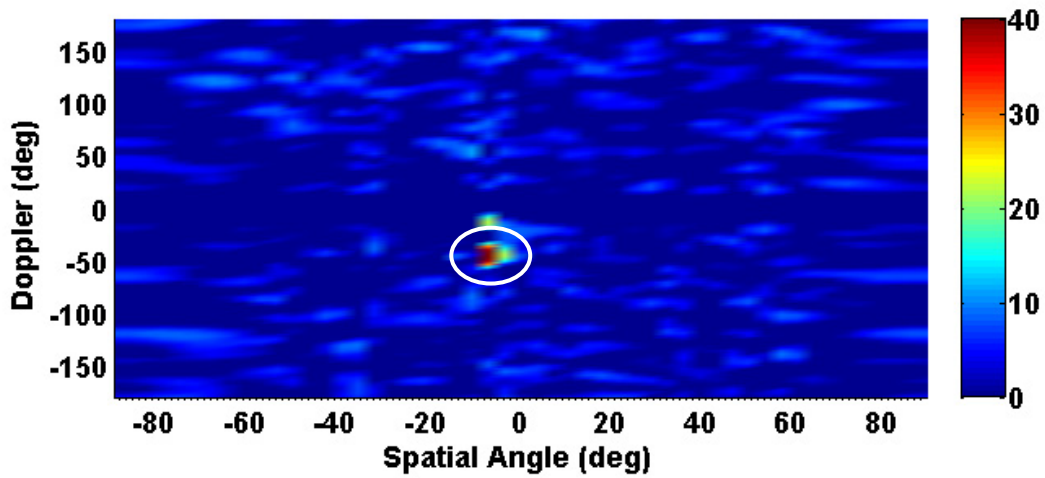


Figure 4.32 SRAP (top) and RD-SRAP (bottom) outputs in dB for range cell 193, Target 2 is denoted by the white circle



**Figure 4.33** Sequential adaptive processing (top) and matched filter (bottom) outputs in dB for range cell 213, Target 4 is denoted by the white circle



**Figure 4.34** SRAP (top) and RD-SRAP (bottom) outputs in dB for range cell 213, Target 4 is denoted by the white circle

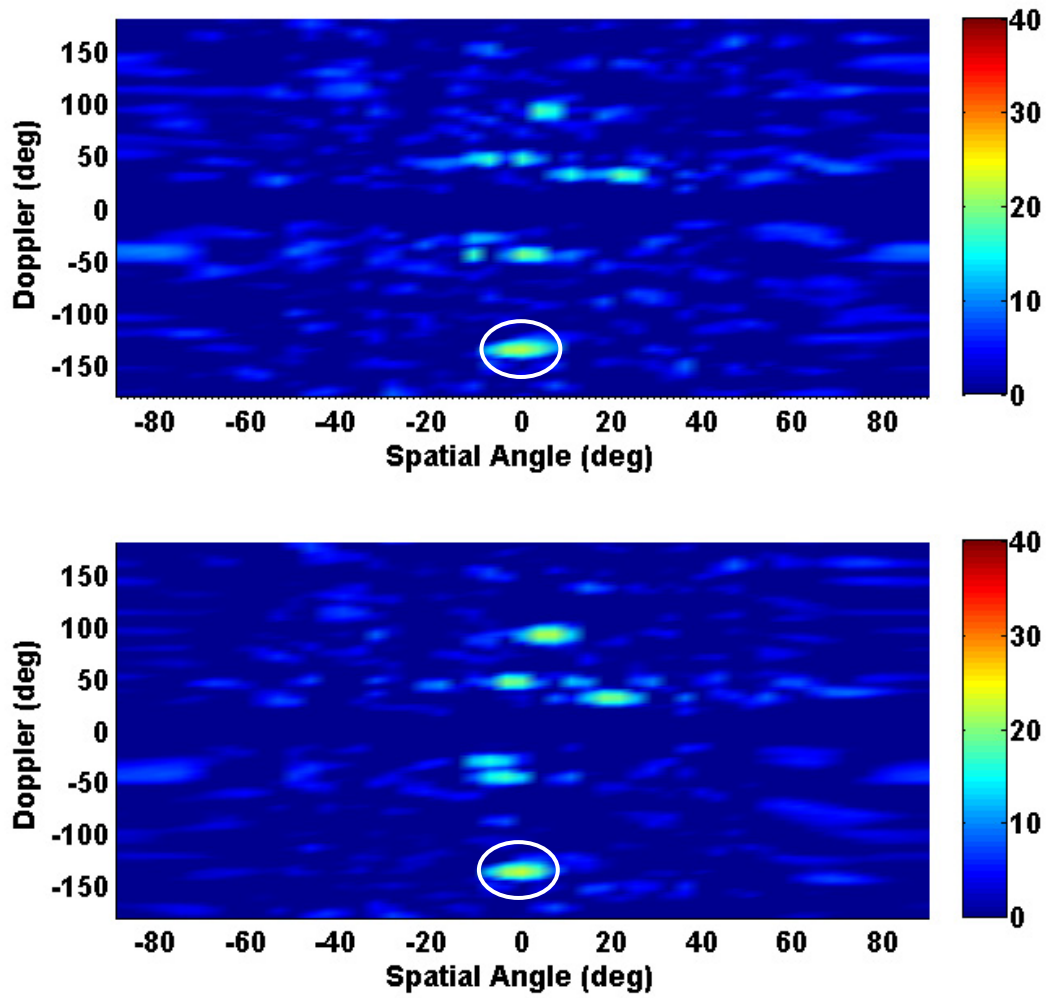


**Figure 4.35** Sequential adaptive processing (top) and matched filter (bottom) outputs in dB for range cell 187, Target 8 is denoted by the white circle

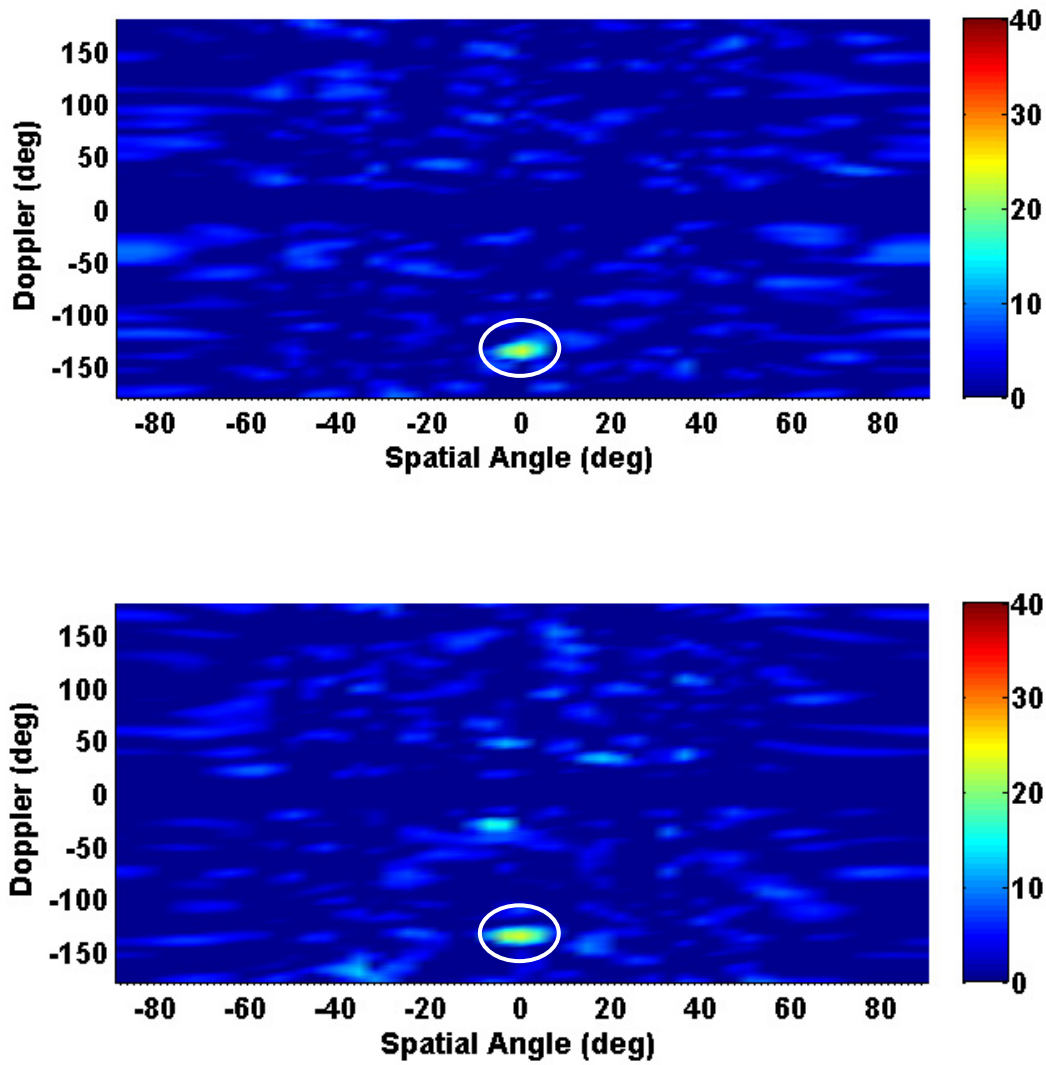


Figure 4.36 SRAP (top) and RD-SRAP (bottom) outputs in dB for range cell 187, Target 8 is denoted by the white circle

#### 4.7 CONCLUSIONS

Range-angle coupled radar emissions have a dramatic impact on radar sensitivity. A simple strategy for designing practical range-angle coupled waveforms is to select a set of waveforms to be transmitted to a corresponding set of desired spatial angles, then transmit the waveforms via time-multiplexing. The resulting angle-range matched filter sidelobes are significantly degraded

relative to those associated with a traditional radar waveform (with the same time-bandwidth product). A new minimum mean squared error (MMSE) based technique, Space-Range Adaptive Processing (SRAP), is proposed that is capable of mitigating the joint space-range sidelobes inherent to waveform-diverse arrays. In the spirit of the well known STAP formulation, SRAP utilizes a range-angle coupled signal model allowing for simultaneous adaptation in the spatial and range dimensions. SRAP is shown to exhibit enhanced sensitivity when compared to the matched filter and adaptation in angle and range separately. Simulation results of a moving target indication radar illustrate that the digital waveform diverse array transmit strategy can be effective when SRAP is employed in conjunction with clutter cancellation. In combination with the transmission scheme presented here, SRAP facilitates the potential realization of some forms of simultaneous multi-mode operation. The reduced dimensionality SRAP (RD-SRAP) algorithm performs nearly as well as its full dimensional counterpart but with a significant reduction in computational cost.

In the next chapter the coupled-domain RMMSE framework will be extended to the analogous case of slow-time (Doppler) and range. It is important to understand that in this chapter the transmitted waveforms combine to form composite waveforms for each spatial angle while in the next chapter each waveform will be truly independent as it is transmitted at a different time.

## CHAPTER 5      TIME-RANGE ADAPTIVE PROCESSING

Traditionally, pulse Doppler radar systems repeat the same waveform to allow efficient pulse compression and Doppler processing techniques to be used. However, some radars transmit waveforms that change on a pulse-to-pulse basis; in this context the vast amount of degrees of freedom provided by coupled domain processing may be useful. The SRAP algorithm can be augmented by replacing spatial frequency with Doppler frequency such that a new algorithm denoted Time-Range Adaptive Processing (TRAP), that adapts simultaneously in slow-time and range, can be formulated.

Low cost, high speed radio frequency circuitry will enable future radar systems to change waveforms in real-time; this technique is referred to as pulse agility in the remainder of this document. Pulse-to-pulse waveform changes can facilitate range disambiguation with a single PRF [30], radar-embedded communications [31], and high range resolution (HRR) imaging [32-33]. However, waveform and frequency agility requires more complex processing on receive to achieve the sensitivity of traditional pulse-Doppler radar. In particular, pulse agility greatly complicates clutter cancellation, especially when multiple range intervals of clutter are present. In the next chapter a deterministic technique for clutter cancellation based on the following is presented.

In this chapter, a new method is proposed that simultaneously estimates the range and Doppler of illuminated scatterers. This approach, entitled Time-Range Adaptive Processing (TRAP), employs a minimum mean-squared error (MMSE) framework and is capable of suppressing range and Doppler sidelobes in a pulse agile regime, thus achieving the sensitivity associated with

standard pulse-Doppler radar. TRAP is particularly useful when range-Doppler coupling is inherent to the transmitted pulse train, such as with stepped frequency waveforms [33].

The pulse compression matched filter in conjunction with traditional Doppler processing performs poorly when pulse agility is employed, due to the pulse-to-pulse variations of each waveform pulse compression output. Hence, a cascaded approach of APC and RISR will be used as an additional metric for comparison. This approach adapts separately in range and Doppler while TRAP offers a simultaneous approach. TRAP, APC, and RISR are all formed using the same mathematical framework, thus the comparison between TRAP and the APC-RISR combination should highlight the benefits of the coupled domain approach.

### 5.1 TIME-RANGE SIGNAL MODEL

Typically a medium to high PRF radar will transmit a number of fill pulses, or pulses transmitted before the receiver begins to record the received data, to ensure that the clutter from all range intervals is present in each of the recorded pulses that will be used for processing. Fill pulses are beneficial because clutter cancellation techniques are greatly simplified when the clutter from each range interval is present in each received pulse. Fill pulses are used in the following derivation without loss of generality. The radar will transmit  $M + R - 1$  pulses where  $R$  is the number of range intervals (including the first range unambiguous interval) and  $M$  is the number of pulses recorded in a single coherent processing interval (CPI). The transmitted waveforms can be represented as the  $N \times M + R - 1$  matrix  $\mathbf{S}$  where the  $m^{\text{th}}$  column contains the  $m^{\text{th}}$  length- $N$  discretized waveform. The waveforms in  $\mathbf{S}$  may have a different coding, center frequency, or both. The received signal from the  $\ell^{\text{th}}$  range cell in the  $r^{\text{th}}$  range interval and  $(R - 1 - r + m)^{\text{th}}$  modulated pulse  $\mathbf{s}_{R-1-r+m}$  can be denoted as

$$y_m(\ell) = \left[ \sum_{r=0}^{R-1} \sum_{\theta} \mathbf{x}_r^T(\ell, \theta) \mathbf{s}_{R-1-r+m} e^{jm\theta} \right] + n(\ell), \quad (5.1)$$

for  $m=0, 1, \dots, M-1$ , in which  $\mathbf{x}_r(\ell, \theta) = [x_r(\ell, \theta) \ x_r(\ell-1, \theta) \ \dots \ x_r(\ell-N+1, \theta)]^T$  is a collection of the complex scattering coefficients associated with the scatterers in the range profile of the  $r^{\text{th}}$  interval corresponding to Doppler phase shift  $\theta$  with which  $\mathbf{s}_{R-1-r+m}$  convolves at delay  $\ell$ ,  $n(\ell)$  is a sample of additive noise, and  $(\bullet)^T$  is the transpose operator.

The collection of  $N$  fast-time (range) snapshots for the  $M$  pulses described by (5.1) can be expressed as

$$\mathbf{Y}(\ell) = \left[ \sum_{r=0}^{R-1} \sum_{\theta} \mathbf{X}(\ell, \theta) (\mathbf{S}_r \odot \mathbf{V}_{\theta}) \right] + \mathbf{N}(\ell), \quad (5.2)$$

where

$$\mathbf{V}_{\theta} = \begin{bmatrix} 1 \\ 1 \\ \vdots \\ 1 \end{bmatrix} \begin{bmatrix} 1 & e^{j\theta} & \dots & e^{j\theta(M-1)} \end{bmatrix} \quad (5.3)$$

is  $N \times M$ ,

$$\mathbf{X}_r(\ell, \theta) = \begin{bmatrix} x_r(\ell, \theta) & x_r(\ell-1, \theta) & \dots & x_r(\ell-N+1, \theta) \\ x_r(\ell+1, \theta) & x_r(\ell, \theta) & \dots & x_r(\ell-N+2, \theta) \\ \vdots & \vdots & \ddots & \vdots \\ x_r(\ell+N-1, \theta) & x_r(\ell+N-2, \theta) & \dots & x_r(\ell, \theta) \end{bmatrix} \quad (5.4)$$

is an  $N \times N$  matrix containing the scatterer complex amplitudes within  $2N-1$  range cells of  $x_r(\ell, \theta)$ ,

$$\mathbf{S}_r = [\mathbf{s}_{R-1-r} \ \mathbf{s}_{R-1-r+1} \ \cdots \ \mathbf{s}_{R-1-r+M-1}], \quad (5.5)$$

and  $\odot$  denotes the Hadamard product. The matched filter and TRAP signal model is a reorganized version of (5.2) and is expressed as the  $NM \times 1$  vector

$$\tilde{\mathbf{y}}(\ell) = \text{vec}(\mathbf{Y}^T(\ell)) = \text{vec} \left( \left[ \sum_{r=0}^{R-1} \sum_{\theta} \mathbf{X}_r(\ell, \theta) \mathbf{S}_r \odot \mathbf{V}_\theta \right]^T \right) + \tilde{\mathbf{n}}(\ell), \quad (5.6)$$

where  $\tilde{\mathbf{n}}(\ell) = \text{vec}(\mathbf{N}^T(\ell))$ . A joint range-Doppler normalized matched filter can be applied to (5.6) as

$$\hat{x}_{\text{NMF}}(\ell, \theta, r) = \frac{1}{NM} \left[ \text{vec}([\mathbf{S}_r \odot \mathbf{V}_\theta]^T) \right]^H \tilde{\mathbf{y}}(\ell), \quad (5.7)$$

in which  $(\bullet)^H$  denotes the complex-conjugate transpose (or Hermitian) operator. The TRAP estimate is obtained as

$$\hat{x}_{\text{TRAP}}(\ell, \theta, r) = \mathbf{w}^H(\ell, \theta, r) \tilde{\mathbf{y}}(\ell), \quad (5.8)$$

where  $\mathbf{w}(\ell, \theta, r)$  is an adaptive filter that is derived in the following section.

## 5.2 TIME-RANGE ADAPTIVE PROCESSING

The MVDR cost function, which includes the unity gain constraint analogous to that used in Section 4.2, for the complex amplitude  $x_r(\ell, \theta)$  in the range-Doppler cell corresponding to delay  $\ell$  and Doppler shift  $\theta$  in the  $r^{\text{th}}$  interval is given as

$$J(\ell, \theta, r) = E \left[ \left| x_r(\ell, \theta) - \mathbf{w}^H(\ell, \theta, r) \tilde{\mathbf{y}}(\ell) \right|^2 \right] + \text{Re} \left\{ \lambda \left( \mathbf{w}^H(\ell, \theta, r) \text{vec}([\mathbf{S} \odot \mathbf{V}_\theta]^T) - 1 \right) \right\}, \quad (5.9)$$

where  $E[\bullet]$  is the expectation operator,  $\mathbf{w}(\ell, \theta, r)$  is the adaptive filter for the  $(\ell, \theta)$  range-Doppler cell in the  $r^{\text{th}}$  interval, and  $\lambda$  is a Lagrange multiplier. Minimization of (5.9) with respect to  $\mathbf{w}^*(\ell, \theta, r)$  yields the standard MVDR solution

$$\mathbf{w}(\ell, \theta, r) = \left( E[\tilde{\mathbf{y}}(\ell) \tilde{\mathbf{y}}^H(\ell)] \right)^{-1} \left( E[x_r^*(\ell, \theta) \tilde{\mathbf{y}}(\ell)] - \frac{\lambda}{2} \text{vec}([\mathbf{S} \odot \mathbf{V}_\theta]^T) \right), \quad (5.10)$$

in which  $(\bullet)^*$  denotes complex conjugation.

Assuming the range-angle cells are uncorrelated with one another and with the noise, the filter in (5.10) can be expressed as

$$\mathbf{w}(\ell, \theta, r) = \left( \left[ \sum_r \sum_\phi (\mathbf{R}_r(\ell, \phi)) \right] + \mathbf{R}_{\text{NSE}}(\ell) \right)^{-1} \left( \rho_r(\ell, \theta) - \frac{\lambda}{2} \right) \text{vec}([\mathbf{S}_r \odot \mathbf{V}_\theta]^T), \quad (5.11)$$

where  $\rho_r(\ell, \theta) = E[|x_r(\ell, \theta)|^2]$  is the power for the  $r^{\text{th}}$  interval in the range-Doppler cell at delay  $\ell$  and Doppler shift  $\theta$ ,  $\mathbf{R}_{\text{NSE}}(\ell) = \sigma_{\text{NSE}}^2 \mathbf{I}_{NM \times NM}$  is the range-Doppler noise covariance matrix assuming white noise with noise power  $\sigma_{\text{NSE}}^2$ , and

$$\mathbf{R}_r(\ell, \phi) = \sum_{n=-N+1}^{N-1} \rho_r(\ell+n, \phi) \mathbf{t}_{r, \phi, nM} \mathbf{t}_{r, \phi, nM}^H, \quad (5.12)$$

where

$$\mathbf{t}_{r, \phi, nM} = \begin{cases} \left[ t_{r, \phi}(|nM|) \cdots t_{r, \phi}(NM-1) \mathbf{0}_{1 \times |nM|} \right]^T & \text{for } n \leq 0 \\ \left[ \mathbf{0}_{1 \times nM} \ t_{r, \phi}(0) \cdots t_{r, \phi}(NM-1-nM) \right]^T & \text{for } n > 0 \end{cases} \quad (5.13)$$

consists of Doppler shifted versions of the vectorized transmit matrix  $\mathbf{S}_r$  expressed as

$$\mathbf{t}_{r,\phi} = [t_{r,\phi}(0) \ t_{r,\phi}(1) \ \cdots \ t_{r,\phi}(NM-1)]^T = \text{vec}([\mathbf{S}_r \odot \mathbf{V}_\theta]^T), \quad (5.14)$$

which corresponds to  $\mathbf{t}_{r,\phi,nM}$  with  $n = 0$ . The Lagrange multiplier is found to be

$$\frac{\lambda}{2} = \rho_r(\ell, \theta) - \frac{1}{\left[ \text{vec}([\mathbf{S}_r \odot \mathbf{V}_\theta]^T) \right]^H \left( \left[ \sum_r \sum_\phi (\mathbf{R}_r(\ell, \phi)) \right] + \mathbf{R}_{\text{NSE}}(\ell) \right)^{-1} \text{vec}([\mathbf{S}_r \odot \mathbf{V}_\theta]^T)}, \quad (5.15)$$

resulting in the MVDR filter

$$\mathbf{w}(\ell, \theta, r) = \frac{\left( \left[ \sum_r \sum_\phi (\mathbf{R}_r(\ell, \phi)) \right] + \mathbf{R}_{\text{NSE}}(\ell) \right)^{-1} \text{vec}([\mathbf{S}_r \odot \mathbf{V}_\theta]^T)}{\left[ \text{vec}([\mathbf{S}_r \odot \mathbf{V}_\theta]^T) \right]^H \left( \left[ \sum_r \sum_\phi (\mathbf{R}_r(\ell, \phi)) \right] + \mathbf{R}_{\text{NSE}}(\ell) \right)^{-1} \text{vec}([\mathbf{S}_r \odot \mathbf{V}_\theta]^T)}. \quad (5.16)$$

### 5.2.1 IMPLEMENTATION

TRAP recursively alternates between estimation of the illuminated scene and estimation of the range-Doppler specific adaptive filters in (5.16). The implementation of TRAP is analogous to that of SRAP discussed in Section 4.2.2. The power estimates in (5.12) required to compute the adaptive filter weights can be estimated by first applying the matched filter from (5.7). After constructing an adaptive filter for each range-Doppler cell the filters are applied to the received signal to obtain an enhanced estimate of the scene. A new set of adaptive filters can be computed based on the enhanced estimate. TRAP alternates between filter and scene estimation until the spectral and range sidelobes are suppressed. The algorithm generally converges after three or four adaptive stages.

### 5.2.2 FAST MATRIX UPDATE

The computational complexity of TRAP can be alleviated by applying the fast matrix update used for SRAP in Section 4.2.2 with covariance update matrices based on (5.12)-(5.14). The details of the fast update matrix for TRAP are provided below for completeness.

The TRAP covariance matrices

$$\tilde{\mathbf{R}}(\ell) = \sum_r \sum_{\phi} \sum_{n=-N+1}^{N-1} \rho_r(\ell+n, \phi) \mathbf{t}_{r, \phi, nM} \mathbf{t}_{r, \phi, nM}^H, \quad (5.17)$$

required to form the MVDR filter at the  $\ell^{\text{th}}$  range cell are related to the covariance matrix at the previous range cell. The elements of  $\tilde{\mathbf{R}}(\ell-1)$  and  $\tilde{\mathbf{R}}(\ell)$  can be divided into sub-matrices denoted as

$$\tilde{\mathbf{R}}(\ell-1) = \begin{bmatrix} \mathbf{B}_{M \times M} & \mathbf{A}_{M \times (NM-M)}^H \\ \mathbf{A}_{(NM-M) \times M} & \mathbf{C}_{(NM-M) \times (NM-M)} \end{bmatrix}, \quad \tilde{\mathbf{R}}(\ell) = \begin{bmatrix} \mathbf{C}_{(NM-M) \times (NM-M)} & \mathbf{D}_{(NM-M) \times M} \\ \mathbf{D}_{M \times (NM-M)}^H & \mathbf{H}_{M \times M} \end{bmatrix}, \quad (5.18)$$

where the  $(NM-M) \times (NM-M)$  matrix  $\mathbf{C}$  represents the portion of the structured covariance matrix that is present in adjacent range cells. The relationship in (5.18) allows the matrix inversion lemma [29] to be applied significantly reducing the computational cost of TRAP. The update equation is denoted as

$$(\bar{\mathbf{R}} + \mathbf{U}\mathbf{L}\mathbf{V})^{-1} = \bar{\mathbf{R}}^{-1} - \bar{\mathbf{R}}^{-1}\mathbf{U}(\mathbf{L}^{-1} + \mathbf{V}\bar{\mathbf{R}}^{-1}\mathbf{U})^{-1}\mathbf{V}\bar{\mathbf{R}}^{-1}, \quad (5.19)$$

where

$$\bar{\mathbf{R}} = \mathbf{P} \tilde{\mathbf{R}}(\ell-1) \mathbf{P}^T = \begin{bmatrix} \mathbf{C}_{(NM-M) \times (NM-M)} & \mathbf{A}_{(NM-M) \times M} \\ \mathbf{A}_{M \times (NM-M)}^H & \mathbf{B}_{M \times M} \end{bmatrix}, \quad (5.20)$$

is computed by applying a permutation matrix to  $\tilde{\mathbf{R}}(\ell-1)$ ,  $\mathbf{U}$  and  $\mathbf{V}$  are expressed as

$$\mathbf{U} = \begin{bmatrix} \mathbf{G}_{(NM-M) \times M} & \mathbf{0}_{(NM-M) \times M} \\ \mathbf{F}_{M \times M} & \mathbf{I}_{M \times M} \end{bmatrix}, \quad \mathbf{V} = \begin{bmatrix} \mathbf{0}_{M \times (NM-M)} & \mathbf{I}_{M \times M} \\ \mathbf{G}_{M \times (NM-M)}^H & \mathbf{0}_{M \times M} \end{bmatrix}, \quad (5.21)$$

in which  $\mathbf{L} = \mathbf{I}_{2M \times 2M}$  is an identity matrix,  $\mathbf{G} = \mathbf{D} - \mathbf{A}$ , and  $\mathbf{F} = \mathbf{H} - \mathbf{B}$ . The sub-matrices  $\mathbf{B}$  and  $\mathbf{A}$  can be computed as

$$\begin{bmatrix} \mathbf{B} \\ \mathbf{A} \end{bmatrix} = \sum_r \sum_\phi \left[ \sum_{n=-N+1}^0 \rho_r(\ell+n-1, \phi) \mathbf{t}_{r, \phi, nM} \underline{\mathbf{t}}_{r, \phi, nM}^H \right], \quad (5.22)$$

where

$$\underline{\mathbf{t}}_{r, \phi, nM} = \left[ t_{r, \phi}(|nM|) \cdots t_{r, \phi}(|nM| + M - 1) \right]^T, \quad (5.23)$$

and  $\mathbf{t}_{r, \phi, nM}$  and  $\mathbf{t}_{r, \phi}$  are defined in (5.13) and (5.14), respectively. In a similar fashion, the sub-matrices  $\mathbf{D}$  and  $\mathbf{H}$  can be computed as

$$\begin{bmatrix} \mathbf{D} \\ \mathbf{H} \end{bmatrix} = \sum_r \sum_\phi \left[ \sum_{n=0}^{N-1} \rho_r(\ell+n, \phi) \mathbf{t}_{r, \phi, nM} \bar{\mathbf{t}}_{r, \phi, nM}^H \right], \quad (5.24)$$

where

$$\bar{\mathbf{t}}_{r, \phi, nM} = \left[ t_{r, \phi}(NM - nM - M) \cdots t_{r, \phi}(NM - 1 - nM) \right]^T. \quad (5.25)$$

Note the products  $\mathbf{t}_{r, \phi, nM} \underline{\mathbf{t}}_{r, \phi, nM}^H$  and  $\mathbf{t}_{r, \phi, nM} \bar{\mathbf{t}}_{r, \phi, nM}^H$  are deterministic and can be computed offline.

This formulation differs from the SRAP fast matrix update (Section 4.2.2) in that (5.22) and (5.24) consider multiple range intervals. Additionally, Kronecker products are not used to allow for independent waveform selection on each transmitted pulse.

### 5.3 REDUCED DIMENSIONALITY TRAP

The computational burden of TRAP can be reduced using the same methodology that led to RD-SRAP in the previous chapter. The pulses from the signal model in (5.2) are sub-divided into  $K$  contiguous blocks as

$$\tilde{\mathbf{Y}}_k(\ell) = \sum_{r=0}^{R-1} \left[ \sum_{\theta} \mathbf{X}_r(\ell, \theta) (\tilde{\mathbf{S}}_{k,r} \odot \tilde{\mathbf{V}}_{k,\theta}) \right] + \tilde{\mathbf{N}}_k(\ell), \quad (5.26)$$

where  $\tilde{\mathbf{S}}_{k,r} = \begin{bmatrix} \mathbf{s}_{k\frac{M}{K}+R-r-1} & \mathbf{s}_{k\frac{M}{K}+1+R-r-1} & \cdots & \mathbf{s}_{(k+1)\frac{M}{K}+R-r-2} \end{bmatrix}$ ,  $\tilde{\mathbf{N}}_k(\ell) = \begin{bmatrix} \mathbf{n}_{k\frac{M}{K}} & \mathbf{n}_{k\frac{M}{K}+1} & \cdots & \mathbf{n}_{(k+1)\frac{M}{K}-1} \end{bmatrix}$ , and

$$\tilde{\mathbf{V}}_{k,\theta} = \begin{bmatrix} 1 \\ 1 \\ \vdots \\ 1 \end{bmatrix} \begin{bmatrix} e^{j\theta k\frac{M}{K}} & e^{j\theta(k\frac{M}{K}+1)} & \cdots & e^{j\theta((k+1)\frac{M}{K}-1)} \end{bmatrix}. \quad (5.27)$$

The RD-TRAP signal model is formed by vectorizing (5.26) as

$$\tilde{\mathbf{y}}_k(\ell) = \text{vec}(\tilde{\mathbf{Y}}_k^T(\ell)) = \text{vec} \left( \sum_{r=0}^{R-1} \left[ \sum_{\theta} \mathbf{X}_r(\ell, \theta) (\tilde{\mathbf{S}}_{k,r} \odot \tilde{\mathbf{V}}_{k,\theta}) \right]^T \right) + \tilde{\mathbf{n}}_k(\ell), \quad (5.28)$$

where  $\tilde{\mathbf{n}}_k(\ell) = \text{vec}(\tilde{\mathbf{N}}_k^T(\ell))$ . The MVDR cost function for RD-TRAP is denoted as

$$\tilde{J}(\ell, \theta) = \left[ \sum_k E \left\{ \left| \frac{1}{K} x_r(\ell, \theta) - \tilde{\mathbf{w}}_k^H(\ell, \theta, r) \tilde{\mathbf{y}}_k(\ell) \right|^2 \right\} \right] + \text{Re} \left\{ \lambda (\tilde{\mathbf{w}}^H(\ell, \theta, r) \text{vec}(\mathbf{S}_r \odot \mathbf{V}_\theta) - 1) \right\}, \quad (5.29)$$

where  $\tilde{\mathbf{w}}_k(\ell, \theta, r)$  is a length- $\frac{NM}{K}$  filter segment of the length- $NM$  filter  $\tilde{\mathbf{w}}(\ell, \theta, r)$  that approximates the full-dimensional TRAP filter in (5.10) and  $\lambda$  is a Lagrange multiplier. Note that (5.29) can be rewritten in the form

$$\tilde{J}(\ell, \boldsymbol{\theta}) = \left[ \sum_k E \left\{ \left| \frac{1}{K} x_r(\ell, \boldsymbol{\theta}) - \tilde{\mathbf{w}}_k^H(\ell, \boldsymbol{\theta}, r) \tilde{\mathbf{y}}_k(\ell) \right|^2 \right\} \right] + \text{Re} \left\{ \lambda \left( \left[ \sum_{k=0}^{K-1} \tilde{\mathbf{w}}_k^H(\ell, \boldsymbol{\theta}, r) \text{vec}(\tilde{\mathbf{S}}_{k,r} \odot \tilde{\mathbf{V}}_{k,\boldsymbol{\theta}}) \right] - 1 \right) \right\}. \quad (5.30)$$

The cost function in (5.30) is minimized to determine the filter segments as

$$\tilde{\mathbf{w}}_k(\ell, \boldsymbol{\theta}, r) = \left( E \left\{ \tilde{\mathbf{y}}_k(\ell) \tilde{\mathbf{y}}_k^H(\ell) \right\} \right)^{-1} \left[ E \left\{ \frac{1}{K} x_r^*(\ell, \boldsymbol{\theta}) \tilde{\mathbf{y}}_k(\ell) \right\} - \frac{\lambda}{2} \text{vec}(\tilde{\mathbf{S}}_{k,r} \odot \tilde{\mathbf{V}}_{k,\boldsymbol{\theta}}) \right]. \quad (5.31)$$

As before, assuming the range-Doppler cells are uncorrelated with each other as well as with the noise, the filter segment is denoted

$$\tilde{\mathbf{w}}_k(\ell, \boldsymbol{\theta}, r) = \left( \frac{\rho_r(\ell, \boldsymbol{\theta})}{K} - \frac{\lambda}{2} \right) \tilde{\mathbf{R}}_k^{-1}(\ell) \text{vec}(\tilde{\mathbf{S}}_{k,r} \odot \tilde{\mathbf{V}}_{k,\boldsymbol{\theta}}), \quad (5.32)$$

in which

$$\tilde{\mathbf{R}}_k(\ell) = \sum_r \sum_{\phi} \sum_{n=-N+1}^{N-1} \left[ \rho_r(\ell+n) \tilde{\mathbf{t}}_{k,r,\phi, \frac{nM}{K}} \tilde{\mathbf{t}}_{k,r,\phi, \frac{nM}{K}}^H \right] + \tilde{\mathbf{R}}_{\text{NSE},k}(\ell), \quad (5.33)$$

where

$$\tilde{\mathbf{t}}_{k,r,\phi, \frac{nM}{K}} = \begin{cases} \left[ \tilde{t}_{k,r,\phi} \left( \frac{|nM|}{K} \right) \cdots \tilde{t}_{k,r,\phi} \left( \frac{NM}{K} - 1 \right) \mathbf{0}_{1 \times \frac{|nM|}{K}} \right]^T & \text{for } n \leq 0 \\ \left[ \mathbf{0}_{1 \times \frac{nM}{K}} \tilde{t}_{k,r,\phi}(0) \cdots \tilde{t}_{k,r,\phi} \left( \frac{NM}{K} - 1 - \frac{nM}{K} \right) \right]^T & \text{for } n > 0 \end{cases} \quad (5.34)$$

consists of Doppler shifted versions of the vectorized block of transmit waveforms  $\tilde{\mathbf{S}}_{k,r}$  denoted as

$$\tilde{\mathbf{t}}_{k,r,\phi} = \left[ \tilde{t}_{k,r,\phi}(0) \tilde{t}_{k,r,\phi}(1) \cdots \tilde{t}_{k,r,\phi}\left(\frac{NM}{K}-1\right) \right]^T = \text{vec} \left( \left[ \tilde{\mathbf{S}}_{k,r} \odot \tilde{\mathbf{V}}_{k,\phi} \right]^T \right), \quad (5.35)$$

where  $\tilde{\mathbf{t}}_{k,r,\phi}$  corresponds to  $\tilde{\mathbf{t}}_{k,r,\phi,\frac{nM}{K}}$  with  $n=0$ . The matrix  $\tilde{\mathbf{R}}_{\text{NSE},k}(\ell)$  in (5.33) is the reduced dimensionality noise covariance matrix  $\sigma_{\text{NSE}}^2 \mathbf{I}_{\frac{NM}{K} \times \frac{NM}{K}}$ , under the assumption of white noise. The

filter segments from (5.32) can be combined to form the length- $NM$  filter  $\tilde{\mathbf{w}}(\ell, \theta, r)$  in (5.29) expressed as

$$\tilde{\mathbf{w}}(\ell, \theta, r) = \text{vec} \left( \left[ \begin{array}{ccc|ccc|ccc} \tilde{w}_{0,0} & \cdots & \tilde{w}_{0,\frac{M}{K}-1} & \tilde{w}_{1,0} & \cdots & \tilde{w}_{1,\frac{M}{K}-1} & \cdots & \tilde{w}_{K-1,0} & \cdots & \tilde{w}_{K-1,\frac{M}{K}-1} \\ \tilde{w}_{0,\frac{M}{K}} & \cdots & \tilde{w}_{0,\frac{2M}{K}-1} & \tilde{w}_{1,\frac{M}{K}} & \cdots & \tilde{w}_{1,\frac{2M}{K}-1} & \cdots & \tilde{w}_{K-1,\frac{M}{K}} & \cdots & \tilde{w}_{K-1,\frac{2M}{K}-1} \\ \vdots & \vdots & \vdots & \vdots & \vdots & \vdots & \cdots & \vdots & \vdots & \vdots \\ \tilde{w}_{0,\frac{(N-1)M}{K}} & \cdots & \tilde{w}_{0,\frac{NM}{K}-1} & \tilde{w}_{1,\frac{(N-1)M}{K}} & \cdots & \tilde{w}_{1,\frac{NM}{K}-1} & \cdots & \tilde{w}_{K-1,\frac{(N-1)M}{K}} & \cdots & \tilde{w}_{K-1,\frac{NM}{K}-1} \end{array} \right]^T \right), \quad (5.36)$$

where  $\tilde{w}_{k,i}$  is the  $i^{\text{th}}$  element of  $\tilde{\mathbf{w}}_k(\ell, \theta, r)$  and the partition lines indicate the portions of the larger matrix that contain elements from an individual filter segment. The term  $\left( \frac{\rho_r(\ell, \theta)}{K} - \frac{\lambda}{2} \right)$  is common to all filter segments allowing the full-dimension filter formed from the segments to be written as

$$\tilde{\mathbf{w}}(\ell, \theta, r) = \left( \frac{\rho_r(\ell, \theta)}{K} - \frac{\lambda}{2} \right) \bar{\mathbf{w}}(\ell, \theta, r), \quad (5.37)$$

in which

$$\bar{\mathbf{w}}(\ell, \boldsymbol{\theta}, r) = \text{vec} \left( \left[ \begin{array}{c|c|c|c} \bar{w}_{0,0} & \cdots & \bar{w}_{0,\frac{M}{K}-1} & \bar{w}_{1,0} & \cdots & \bar{w}_{1,\frac{M}{K}-1} & \cdots & \bar{w}_{K-1,0} & \cdots & \bar{w}_{K-1,\frac{M}{K}-1} \\ \bar{w}_{0,\frac{M}{K}} & \cdots & \bar{w}_{0,\frac{2M}{K}-1} & \bar{w}_{1,\frac{M}{K}} & \cdots & \bar{w}_{1,\frac{2M}{K}-1} & \cdots & \bar{w}_{K-1,\frac{M}{K}} & \cdots & \bar{w}_{K-1,\frac{2M}{K}-1} \\ \vdots & \vdots & \vdots & \vdots & \vdots & \vdots & \cdots & \vdots & \vdots & \vdots \\ \bar{w}_{0,\frac{(N-1)M}{K}} & \cdots & \bar{w}_{0,\frac{NM}{K}-1} & \bar{w}_{1,\frac{(N-1)M}{K}} & \cdots & \bar{w}_{1,\frac{NM}{K}-1} & \cdots & \bar{w}_{K-1,\frac{(N-1)M}{K}} & \cdots & \bar{w}_{K-1,\frac{NM}{K}-1} \end{array} \right]^T \right), \quad (5.38)$$

where  $\bar{w}_{k,i}$  is the  $i^{\text{th}}$  element of the modified filter segment

$$\bar{w}_k(\ell, \boldsymbol{\theta}, r) = \tilde{\mathbf{R}}_k^{-1}(\ell) \text{vec}(\tilde{\mathbf{S}}_{k,r} \odot \tilde{\mathbf{V}}_{k,\boldsymbol{\theta}}). \quad (5.39)$$

The unity gain constraint can now be applied to (5.37) resulting in

$$1 = \left( \frac{\rho_r(\ell, \boldsymbol{\theta})}{K} - \frac{\lambda}{2} \right) \bar{\mathbf{w}}^H(\ell, \boldsymbol{\theta}, r) \text{vec}(\mathbf{S}_r \odot \mathbf{V}_\theta), \quad (5.40)$$

which after rearranging yields

$$\frac{\lambda}{2} = \frac{\rho_r(\ell, \boldsymbol{\theta})}{K} - \frac{1}{\bar{\mathbf{w}}^H(\ell, \boldsymbol{\theta}, r) \text{vec}(\mathbf{S}_r \odot \mathbf{V}_\theta)}. \quad (5.41)$$

Finally, using (5.37) and (5.41), the RD-SRAP filter for a given range cell, Doppler phase, and interval can be written as

$$\tilde{\mathbf{w}}(\ell, \boldsymbol{\theta}, r) = \frac{\bar{\mathbf{w}}^H(\ell, \boldsymbol{\theta}, r)}{\bar{\mathbf{w}}^H(\ell, \boldsymbol{\theta}, r) \text{vec}(\tilde{\mathbf{S}}_{k,r} \odot \tilde{\mathbf{V}}_{k,\boldsymbol{\theta}})}. \quad (5.42)$$

The estimates are obtained by applying the filters to the blocks of received data as

$$\hat{x}_{\text{RD-TRAP}}(\ell, \boldsymbol{\theta}, r) = \tilde{\mathbf{w}}^H(\ell, \boldsymbol{\theta}, r) \tilde{\mathbf{y}}(\ell), \quad (5.43)$$

where  $\tilde{\mathbf{y}}(\ell)$  is given by (5.6).

### 5.3.1 FAST MATRIX UPDATE FOR RD-TRAP

The structure of the fast matrix update for the RD-TRAP algorithm is similar to that for RD-SRAP in Section 4.3.1, much of which is repeated here for completeness. Begin by examining the relationship between the reduced dimensionality covariance matrices from (5.33) for adjacent range cells

$$\tilde{\mathbf{R}}_k(\ell-1) = \begin{bmatrix} \tilde{\mathbf{B}}_{\frac{M}{K} \times \frac{M}{K}} & \tilde{\mathbf{A}}_{\frac{M}{K} \times \frac{(NM-M)}{K}}^H \\ \tilde{\mathbf{A}}_{\frac{(NM-M)}{K} \times \frac{M}{K}} & \tilde{\mathbf{C}}_{\frac{(NM-M)}{K} \times \frac{(NM-M)}{K}} \end{bmatrix} \quad \tilde{\mathbf{R}}_k(\ell) = \begin{bmatrix} \tilde{\mathbf{C}}_{\frac{(NM-M)}{K} \times \frac{(NM-M)}{K}} & \tilde{\mathbf{D}}_{\frac{(NM-M)}{K} \times \frac{M}{K}} \\ \tilde{\mathbf{D}}_{\frac{M}{K} \times \frac{(NM-M)}{K}}^H & \tilde{\mathbf{H}}_{\frac{M}{K} \times \frac{M}{K}} \end{bmatrix}. \quad (5.44)$$

The reduced-dimensionality update equation, based on the matrix inversion lemma [29], is denoted as

$$(\tilde{\mathbf{R}} + \tilde{\mathbf{U}}\tilde{\mathbf{L}}\tilde{\mathbf{V}})^{-1} = \tilde{\mathbf{R}}^{-1} - \tilde{\mathbf{R}}^{-1}\tilde{\mathbf{U}}(\tilde{\mathbf{L}}^{-1} + \tilde{\mathbf{V}}\tilde{\mathbf{R}}^{-1}\tilde{\mathbf{U}})^{-1}\tilde{\mathbf{V}}\tilde{\mathbf{R}}^{-1}, \quad (5.45)$$

where

$$\tilde{\mathbf{R}} = \tilde{\mathbf{P}} \tilde{\mathbf{R}}_k(\ell-1) \tilde{\mathbf{P}}^T = \begin{bmatrix} \tilde{\mathbf{C}}_{\frac{(NM-M)}{K} \times \frac{(NM-M)}{K}} & \tilde{\mathbf{A}}_{\frac{(NM-M)}{K} \times \frac{M}{K}} \\ \tilde{\mathbf{A}}_{\frac{M}{K} \times \frac{(NM-M)}{K}}^H & \tilde{\mathbf{B}}_{\frac{M}{K} \times \frac{M}{K}} \end{bmatrix}, \quad (5.46)$$

is a permutation of  $\tilde{\mathbf{R}}_k(\ell-1)$ ,  $\tilde{\mathbf{U}}$  and  $\tilde{\mathbf{V}}$  are expressed as

$$\tilde{\mathbf{U}} = \begin{bmatrix} \tilde{\mathbf{G}}_{\frac{(NM-M)}{K} \times \frac{M}{K}} & \mathbf{0}_{\frac{(NM-M)}{K} \times \frac{M}{K}} \\ \tilde{\mathbf{F}}_{\frac{M}{K} \times \frac{M}{K}} & \mathbf{I}_{\frac{M}{K} \times \frac{M}{K}} \end{bmatrix}, \quad \tilde{\mathbf{V}} = \begin{bmatrix} \mathbf{0}_{\frac{M}{K} \times \frac{(NM-M)}{K}} & \mathbf{I}_{\frac{M}{K} \times \frac{M}{K}} \\ \tilde{\mathbf{G}}_{\frac{M}{K} \times \frac{(NM-M)}{K}}^H & \mathbf{0}_{\frac{M}{K} \times \frac{M}{K}} \end{bmatrix}, \quad (5.47)$$

in which  $\tilde{\mathbf{L}} = \mathbf{I}_{\frac{2M}{K} \times \frac{2M}{K}}$  is an identity matrix,  $\tilde{\mathbf{G}} = \tilde{\mathbf{D}} - \tilde{\mathbf{A}}$ , and  $\tilde{\mathbf{F}} = \tilde{\mathbf{H}} - \tilde{\mathbf{B}}$ . The reduced-

dimensionality sub-matrices  $\tilde{\mathbf{B}}$ ,  $\tilde{\mathbf{A}}$ ,  $\tilde{\mathbf{D}}$ , and  $\tilde{\mathbf{H}}$  can computed as

$$\begin{bmatrix} \tilde{\mathbf{B}} \\ \tilde{\mathbf{A}} \end{bmatrix} = \sum_r \sum_\phi \left[ \sum_{n=-N+1}^0 \rho_r(\ell+n-1) \tilde{\mathbf{t}}_{k,r,\phi,\frac{nM}{K}} \tilde{\mathbf{t}}_{k,r,\phi,\frac{nM}{K}}^H \right], \quad (5.48)$$

where

$$\tilde{\mathbf{t}}_{k,r,\phi,\frac{nM}{K}} = \left[ t_{k,r,\phi} \left( \left\lfloor \frac{nM}{K} \right\rfloor \right) \cdots t_{k,r,\phi} \left( \left\lfloor \frac{nM}{K} \right\rfloor + \frac{M}{K} - 1 \right) \right]^T \quad (5.49)$$

and

$$\begin{bmatrix} \tilde{\mathbf{D}} \\ \tilde{\mathbf{H}} \end{bmatrix} = \sum_r \sum_\phi \left[ \sum_{n=0}^{N+1} \rho_r(\ell+n) \tilde{\mathbf{t}}_{k,r,\phi,\frac{nM}{K}} \tilde{\mathbf{t}}_{k,r,\phi,\frac{nM}{K}}^H \right], \quad (5.50)$$

where

$$\tilde{\mathbf{t}}_{k,r,\phi,\frac{nM}{K}} = \left[ \left[ t_{k,r,\phi} \left( \frac{NM}{K} - \frac{nM}{K} - \frac{M}{K} \right) \cdots t_{k,r,\phi} \left( \frac{NM}{K} - \frac{nM}{K} - 1 \right) \right]^T \right]^T. \quad (5.51)$$

#### 5.4 ECLIPSING REPAIR

In practice, many pulse-Doppler radar systems employ a technique referred to as blanking to protect sensitive electronics in the radar receiver from the high power transmitter when a common antenna is used for both transmitting and receiving signals. Blanking is implemented with a high speed switch that connects the antenna to either the radar transmitter or receiver, depending upon the state of the switch. When the radar is transmitting, the receiver is disconnected from the antenna and does not receive any reflected echoes throughout the transmit pulse duration. After transmission of the radar pulse, the switch is flipped and the receiver is able to capture target returns until the next pulse is transmitted. Blanking results in some target echoes being only partially captured by the receiver as depicted in Fig. 5.1. When only a partial return is captured

the target is said to be eclipsed and the portions of the range profile that contain these targets is referred to as the eclipsed region.

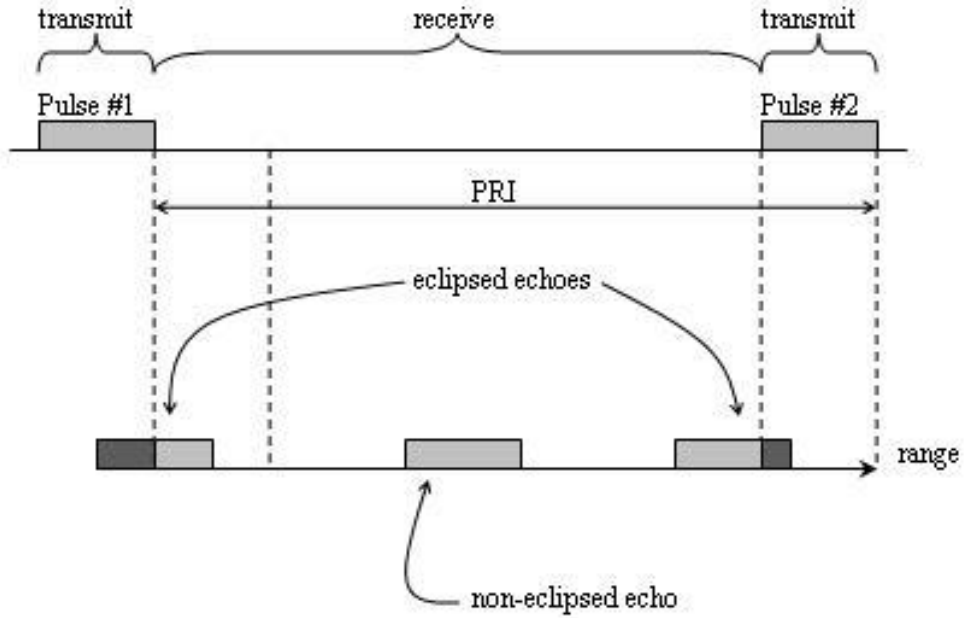


**Figure 5.1** Illustration of eclipsed targets due to receiver blanking

In the context of the TRAP algorithm, assume the received data for a given pulse  $y_m(\ell)$  has length  $L$ , i.e.,  $\ell = 0, 1, \dots, L-1$ . Then the covariance matrix  $\mathbf{R}_r(\ell, \theta)$  in (5.12) can only be computed for  $\ell = N-1, N, \dots, L-N$  due to the dependence of  $\mathbf{R}_r(\ell, \theta)$  on  $\rho_r(\ell-N+1), \dots, \rho_r(\ell+N-1)$ . However, the methodology used to extend the adaptive pulse compression estimate into the eclipsed region of the range profile [35] can be applied to TRAP as well. The resulting filter used to estimate the eclipsed region at the beginning of the range profile corresponding to  $\ell = 0, 1, \dots, N-2$  is denoted as

$$\mathbf{w}(\ell, \boldsymbol{\theta}, r) = \frac{\left( \left[ \sum_r \sum_{\phi} (\mathbf{R}_r(N-1, \phi)) \right] + \mathbf{R}_{\text{NSE}}(N-1) \right)^{-1} \mathbf{t}_{r, \boldsymbol{\theta}, (\ell-N+1)M}}{\mathbf{t}_{r, \boldsymbol{\theta}, (\ell-N+1)M}^H \left( \left[ \sum_r \sum_{\phi} (\mathbf{R}_r(N-1, \phi)) \right] + \mathbf{R}_{\text{NSE}}(N-1) \right)^{-1} \mathbf{t}_{r, \boldsymbol{\theta}, (\ell-N+1)M}}, \quad (5.52)$$

where

$$\mathbf{t}_{r, \boldsymbol{\theta}, (\ell-N+1)M} = \left[ t_{r, \boldsymbol{\theta}}(|(\ell-N+1)M|) \cdots t_{r, \boldsymbol{\theta}}(NM-1) \mathbf{0}_{1 \times |(\ell-N+1)M|} \right]^T. \quad (5.53)$$

Note that in (5.52) the covariance matrix  $\left[ \sum_r \sum_{\phi} (\mathbf{R}_r(N-1, \phi)) \right] + \mathbf{R}_{\text{NSE}}(N-1)$  from the  $\ell = N-1$  range cell is used to compute all the filters for the eclipsed region at the beginning of the range profile. In a similar fashion, the adaptive filters for the eclipsed region at the end of the range profile ( $\ell = L-N+1, L-N+2, \dots, L-1$ ) are expressed as

$$\mathbf{w}(\ell, \boldsymbol{\theta}, r) = \frac{\left( \left[ \sum_r \sum_{\phi} (\mathbf{R}_r(L-N, \phi)) \right] + \mathbf{R}_{\text{NSE}}(L-N) \right)^{-1} \mathbf{t}_{r, \boldsymbol{\theta}, (\ell-L+N)M}}{\mathbf{t}_{r, \boldsymbol{\theta}, (\ell-L+N)M}^H \left( \left[ \sum_r \sum_{\phi} (\mathbf{R}_r(L-N, \phi)) \right] + \mathbf{R}_{\text{NSE}}(L-N) \right)^{-1} \mathbf{t}_{r, \boldsymbol{\theta}, (\ell-L+N)M}}, \quad (5.54)$$

where

$$\mathbf{t}_{r, \boldsymbol{\theta}, (\ell-L+N)M} = \left[ \mathbf{0}_{1 \times (\ell-L+N)M} \ t_{r, \boldsymbol{\theta}}(0) \cdots t_{r, \boldsymbol{\theta}}(NM-1-(\ell-L+N)M) \right]^T. \quad (5.55)$$

Similarly note that in (5.54) the covariance matrix  $\left[ \sum_r \sum_{\phi} (\mathbf{R}_r(L-N, \phi)) \right] + \mathbf{R}_{\text{NSE}}(L-N)$  from the  $\ell = L-N$  range cell is used to compute all the filters for the eclipsed region at the end of the range profile. Eclipsing repair can be applied to RD-TRAP by modifying (5.39) and (5.42) as

$$\bar{\mathbf{w}}_k(\ell, \theta, r) = \tilde{\mathbf{R}}_k^{-1}(\ell) \tilde{\mathbf{t}}_{k,r,\phi, \frac{(\ell-N+1)M}{K}} \quad (5.56)$$

and

$$\tilde{\mathbf{w}}(\ell, \theta, r) = \frac{\bar{\mathbf{w}}^H(\ell, \theta, r)}{\bar{\mathbf{w}}^H(\ell, \theta, r) \tilde{\mathbf{t}}_{k,r,\phi, \frac{(\ell-N+1)M}{K}}}, \quad (5.57)$$

respectively, for first eclipsed region corresponding to  $\ell = 0, 1, \dots, N-2$  where

$$\tilde{\mathbf{t}}_{k,r,\phi, \frac{nM}{K}} = \begin{cases} \left[ \tilde{t}_{k,r,\phi} \left( \frac{|nM|}{K} \right) \cdots \tilde{t}_{k,r,\phi} \left( \frac{NM}{K} - 1 \right) \mathbf{0}_{1 \times \frac{|nM|}{K}} \right]^T & \text{for } n \leq 0 \\ \left[ \mathbf{0}_{1 \times \frac{nM}{K}} \tilde{t}_{k,r,\phi}(0) \cdots \tilde{t}_{k,r,\phi} \left( \frac{NM}{K} - 1 - \frac{nM}{K} \right) \right]^T & \text{for } n > 0 \end{cases}. \quad (5.58)$$

For the latter eclipsed region corresponding to  $\ell = L-N+1, L-N+2, \dots, L-1$  the RD-TRAP filter is based on

$$\bar{\mathbf{w}}_k(\ell, \theta, r) = \tilde{\mathbf{R}}_k^{-1}(\ell) \tilde{\mathbf{t}}_{k,r,\phi, \frac{(\ell-L+N)M}{K}} \quad (5.59)$$

and

$$\tilde{\mathbf{w}}(\ell, \theta, r) = \frac{\bar{\mathbf{w}}^H(\ell, \theta, r)}{\bar{\mathbf{w}}^H(\ell, \theta, r) \tilde{\mathbf{t}}_{k,r,\phi, \frac{(\ell-L+N)M}{K}}}. \quad (5.60)$$

The Space-Range Adaptive Processing (SRAP) algorithm in the previous chapter can be extended in a similar fashion to account for targets in the eclipsed region.

## 5.5 SEQUENTIAL APC-RISR

Adaptive Pulse Compression (APC) [13], detailed in Section 1.6.1, for range sidelobe suppression and the Re-Iterative Super Resolution (RISR) algorithm [21] for spectral sidelobe suppression are implemented sequentially for comparison to TRAP. RISR was originally conceived as a means to perform direction of arrival estimation (see Section 1.6.2). Interestingly, in the digital waveform diverse array scenario RISR was performed first followed by APC but in this scenario pulse compression must be performed before Doppler processing. APC is valid for the range unambiguous case however, the multistatic APC (MAPC) [28] can be employed to account for multiple waveforms in a single pulse of received data. The application of MAPC to extend sequential adaptation to multiple range intervals is left as future work. The application of RISR for velocity estimation in a pulse-Doppler regime is outlined below.

The pulse compressed output at the  $\ell^{\text{th}}$  range cell of  $M$  pulses, after employing APC, can be denoted as

$$\bar{\mathbf{x}}(\ell) = [\bar{x}_0(\ell) \ \bar{x}_1(\ell) \ \cdots \ \bar{x}_{M-1}(\ell)]^T. \quad (5.61)$$

Let

$$\bar{\mathbf{V}} = \begin{bmatrix} 1 & 1 & \cdots & 1 \\ 1 & e^{j\frac{2\pi}{K}} & \cdots & e^{j\frac{2\pi(K-1)}{K}} \\ \vdots & \vdots & \vdots & \cdots \\ 1 & e^{j\frac{2\pi}{K}(M-1)} & \cdots & e^{j\frac{2\pi(K-1)}{K}(M-1)} \end{bmatrix} \quad (5.62)$$

be a bank of  $K$  Doppler steering vectors, as opposed to spatial steering vectors. The resulting RISR adaptive filter bank is computed as

$$\bar{\mathbf{W}}(\ell) = (\bar{\mathbf{V}}\bar{\mathbf{P}}(\ell)\bar{\mathbf{V}} + \bar{\mathbf{R}})^{-1} \bar{\mathbf{V}}\bar{\mathbf{P}}(\ell), \quad (5.63)$$

where

$$\bar{\mathbf{P}}(\ell) = \begin{bmatrix} \rho(\ell, 0) & 0 & 0 \\ 0 & \ddots & 0 \\ 0 & 0 & \rho\left(\ell, \frac{2\pi(K-1)}{K}\right) \end{bmatrix} \quad (5.64)$$

is a diagonal matrix containing the expected target power in each Doppler bin at the  $\ell^{\text{th}}$  range cell and  $\bar{\mathbf{R}} = \sigma_{\text{NSE}}^2 \mathbf{I}_{M \times M}$  is the noise covariance matrix again assuming white noise. A normalization is applied to the adaptive filters as

$$\tilde{\bar{\mathbf{w}}}_q(\ell) = \frac{\bar{\mathbf{w}}_q(\ell)}{\bar{\mathbf{w}}_q^H(\ell)\bar{\mathbf{v}}_q}, \quad (5.65)$$

where  $\bar{\mathbf{w}}_q(\ell)$  and  $\bar{\mathbf{v}}_q$  are the  $q^{\text{th}}$  columns of  $\bar{\mathbf{W}}(\ell)$  and  $\bar{\mathbf{V}}$ , respectively. Thus, the final range-Doppler estimate is obtained as

$$\hat{x}_{\text{APC-RISR}}(\ell, \theta_q) = \tilde{\bar{\mathbf{w}}}_q(\ell)^H \bar{\mathbf{x}}(\ell). \quad (5.66)$$

In the same fashion as TRAP, the initial power estimates in (5.64) can be obtained using the Doppler filter bank in (5.62), after which 3-10 adaptive iterations are performed.

The combination of APC and RISR is expected to perform well when APC is capable of completely mitigating range sidelobes and RISR is only responsible for reducing the Doppler sidelobes associated with the targets. However, when APC is overwhelmed with a large number

of targets at different velocities, the performance will suffer, resulting in some residual range sidelobes. This range sidelobe residue will not be suppressed by the RISR algorithm, which will attempt to suppress the Doppler sidelobes of the targets as well as the Doppler sidelobes of the residue. This lack of degrees of freedom is particularly problematic when pulse agility is employed on transmit due to the resultant range-Doppler coupling.

## 5.6 SIMULATION RESULTS

Simulation results will be presented to illustrate the benefit of coupled processing using TRAP for pulse agile radar systems. TRAP will be compared to standard matched filtering in range and Doppler and, in the first scenario, to the sequential APC-RISR approach described above. Targets are modeled as point scatterers embedded in additive white Gaussian noise. The first simulation considers moving targets without and with ground clutter and will be performed using a stepped-frequency phase-coded waveform. The second simulation consists of both eclipsed and non-eclipsed moving targets throughout multiple range intervals and unambiguous ranging is achieved via transmission of a unique random polyphase code on each pulse.

### 5.6.1 SYNTHETIC WIDEBAND SCENARIO

Stepped-frequency waveforms offer the distinct benefit of providing enhanced range resolution by synthesizing a wide bandwidth using several frequency shifted narrowband waveforms. Coherent processing must be used to realize the range resolution improvement. The stepped frequency pulse train consists of  $M = 30$  pulses where the normalized center frequency of the  $m^{\text{th}}$  pulse is given by

$$f_m = \frac{m}{M-1} \left( 1 - \frac{1}{G} \right) = m \frac{3}{116}, \quad (5.67)$$

for  $m = 0, 1, \dots, M - 1$ , where  $G = 4$  is the ratio of the total pulse train bandwidth to the single pulse bandwidth. The total bandwidth is 4 times greater than that of a single pulse, yielding a commensurate increase in range resolution when coherent processing is performed. Each pulse consists of a 15 chip P4 code [8] that is oversampled by 4 for processing ( $N = 60$ ). Figure 5.2 shows the spectrum of each pulse. Observe that the bandwidth from pulse-to-pulse has approximately 90% overlap. Additionally, the waveforms have been bandpass filtered to emulate the narrow instantaneous bandwidth associated with stepped-frequency radar systems. If the waveforms are not bandlimited, the adaptive algorithms will take advantage of the extraneous bandwidth produced by the phase coded waveform, though this bandwidth is not available in reality. Note the filtered waveforms are used as the reference waveforms for processing in all algorithms.

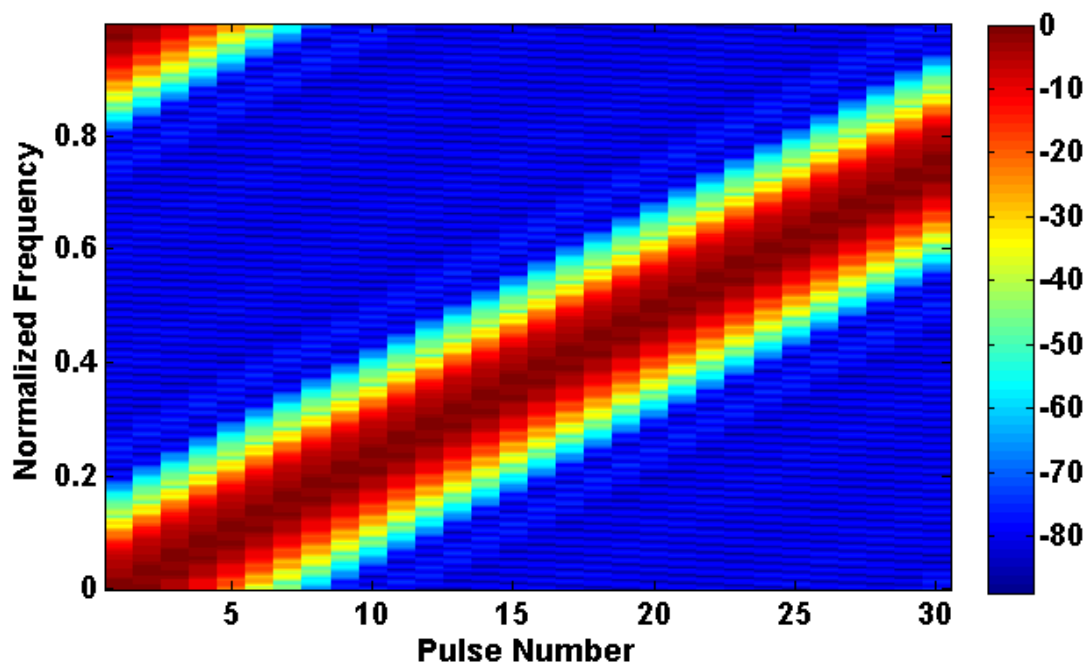


**Figure 5.2** Spectral content as a function of pulse number for stepped-frequency waveforms

The simulation scenario consists of six moving targets for both clutter-free and ground clutter environments. The location, Doppler phase, and SNR of the targets are provided in Table 5.1. Stated SNR values are before a coherent processing gain of 26.5 dB. Both TRAP and RISR employ 91 Doppler bins distributed evenly between phase angles of  $\pm 180^\circ$  for processing, resulting in some steering vector mismatch for the targets in Table 5.1.

**Table 5.1** Target Parameters for Synthetic Wideband Scenario

Range Cell $\ell$	Doppler Phase $\theta$	SNR (dB)
177	$-100^\circ$	-6.5
180	$75^\circ$	3.5
183	$150^\circ$	-3.5
186	$-130^\circ$	-1.5
189	$50^\circ$	-11.5
192	$-120^\circ$	-8.5

First, the clutter free scenario will be examined. Figure 5.3 displays the standard matched filter (range and Doppler) result in which the target locations are denoted with white circles. The range-Doppler coupling of the stepped-frequency waveform is evidenced by the spreading of the pulse compression mainlobe near the target locations. Also, range sidelobes appear throughout the image and can be confused with target returns. Figure 5.4 displays the sequential APC-RISR output that has suppressed the range and Doppler sidelobes and alleviated much of the coupling. Note that an oversampled version of APC [34] is employed here to enhance the range resolution, *i.e.*, reduce the width of the pulse compression mainlobe, that is responsible for the reduction in range-Doppler coupling. This approach performs well here due to the small number of degrees of freedom required to estimate the illuminated scene. The result after TRAP is applied is shown in

Fig. 5.5. TRAP marginally outperforms the sequential APC-RISR approach as evidenced by the reduction of the range-Doppler sidelobes into the noise floor.

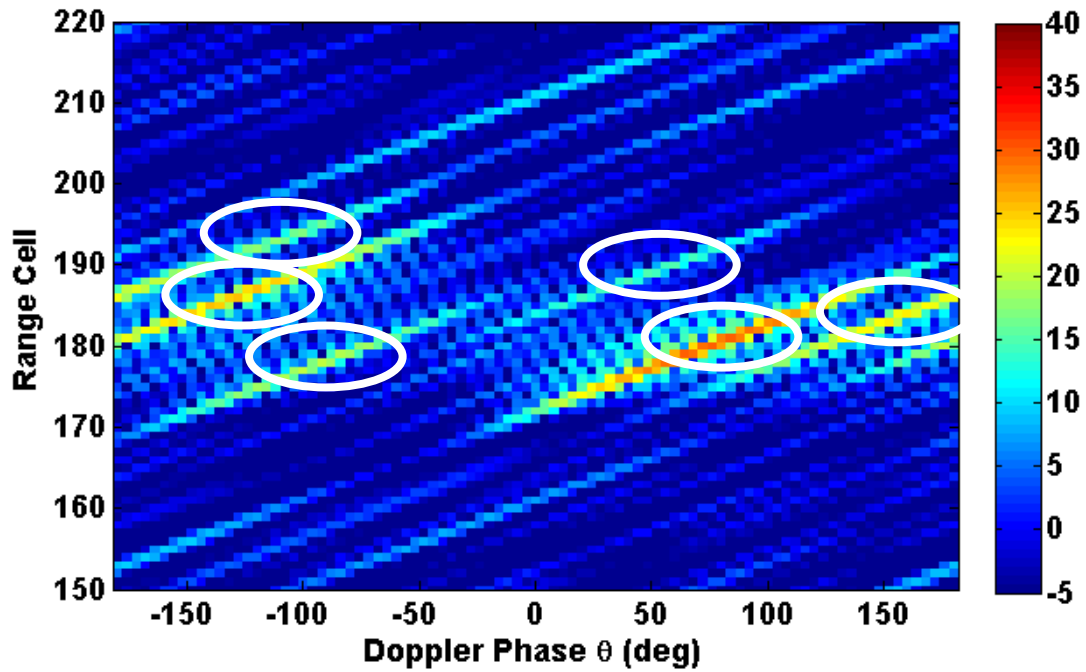


Figure 5.3 Matched filter range-Doppler map (in dB), moving targets are obscured by Doppler and range sidelobes

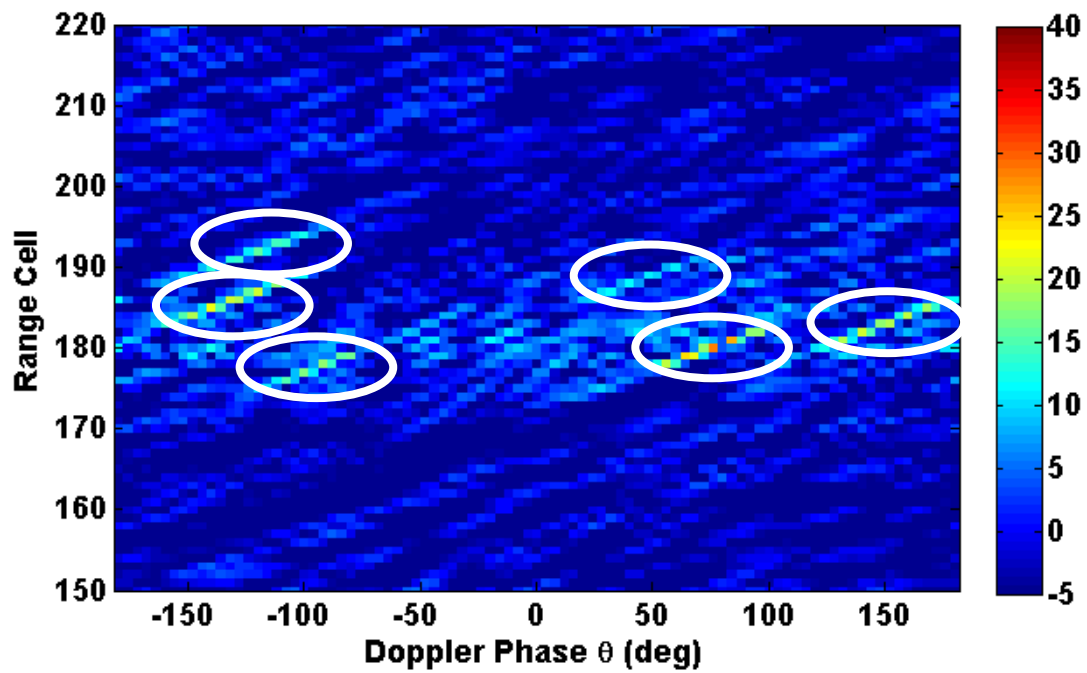


Figure 5.4 Sequential APC-RISR range-Doppler map (in dB), moving targets at locations indicated by the white circles

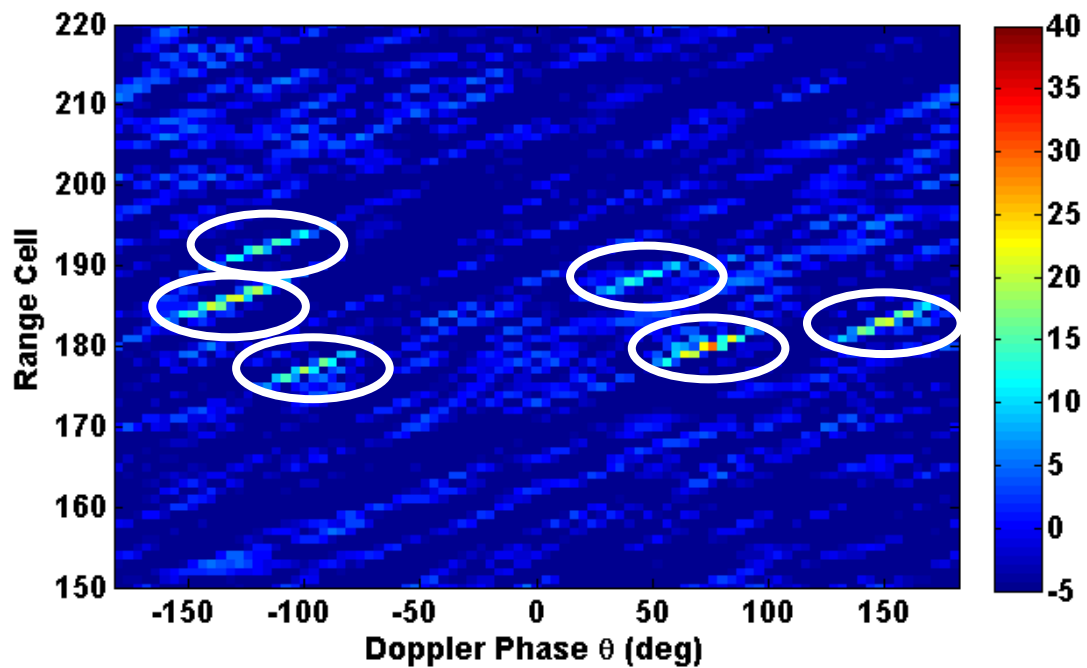
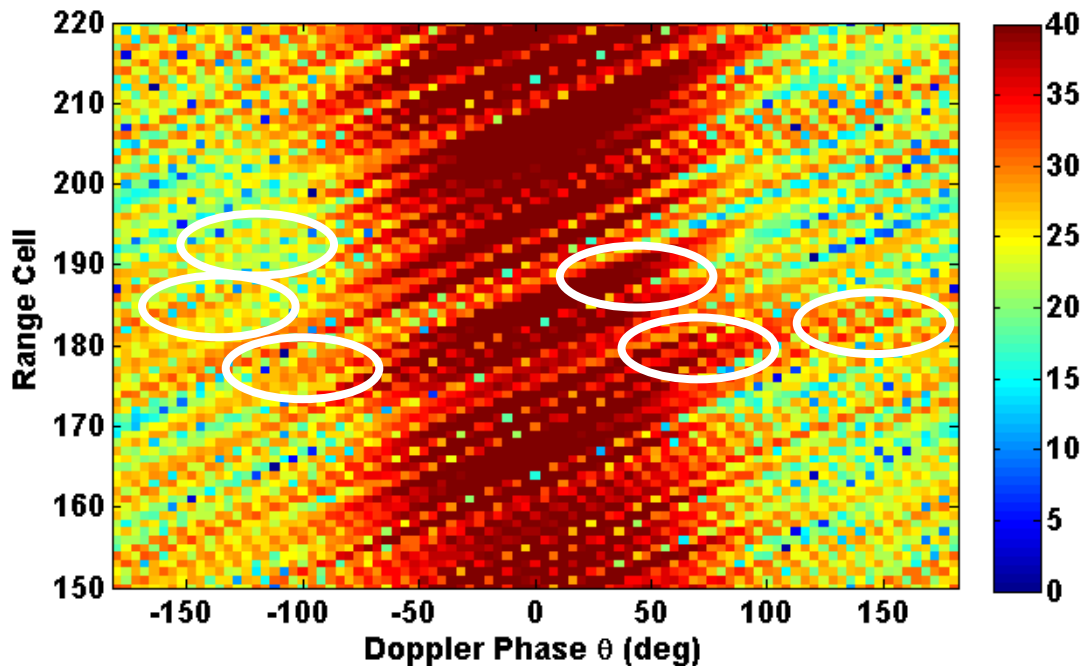


Figure 5.5 TRAP range-Doppler map (in dB), moving targets at locations indicated by the white circles

Now consider the previous example with the addition of stationary ground clutter in range cells 130 to 290 where the average clutter-to-noise ratio is 40 dB after processing. Note that clutter cancellation, which would be complicated by the pulse-to-pulse frequency agility, is not performed here. The matched filter performs poorly in this scenario, as seen in Fig. 5.6 where none of the moving targets are visible. The sequential APC-RISR approach (Fig. 5.7) suppresses some of the sidelobes, but even the largest target at range cell 180 and Doppler phase angle  $75^\circ$  is not readily identifiable. This performance degradation is attributed to the limited number of degrees of freedom when adaptation is employed in range and Doppler separately. In Figure 5.8, the TRAP algorithm uncovers all but one of the masked scatterers (at range cell 189 and Doppler phase angle  $50^\circ$ ) by accurately estimating the range-Doppler scene, including the clutter.



**Figure 5.6** Matched filter range-Doppler map (in dB), moving targets are masked by Doppler and range sidelobes

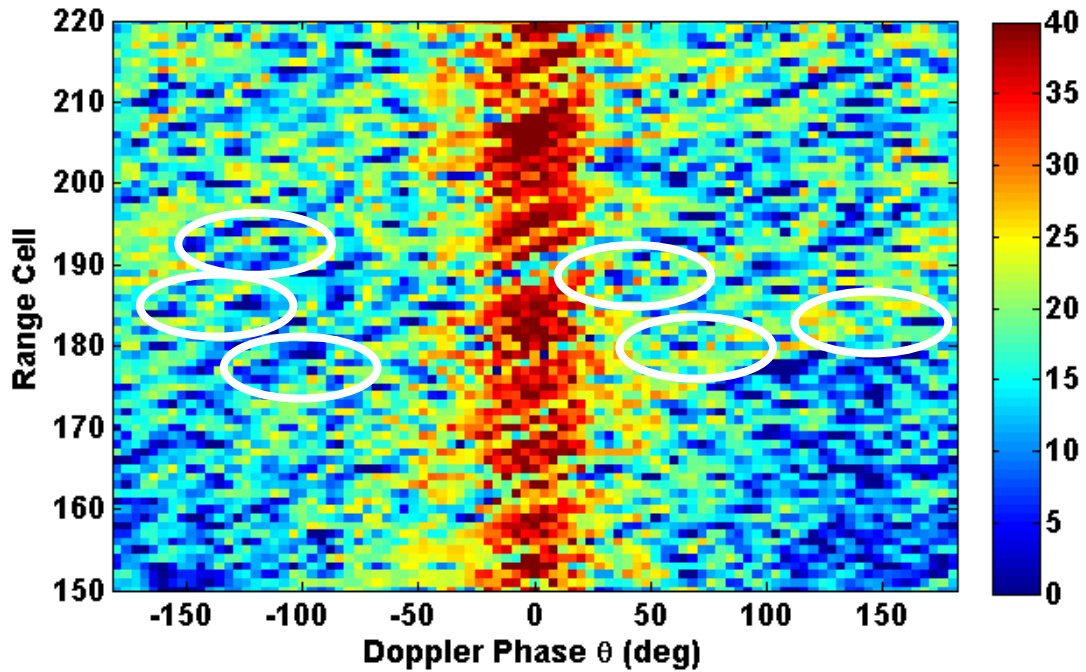


Figure 5.7 Sequential APC-RISR range-Doppler map (in dB), moving targets are masked by Doppler and range sidelobes

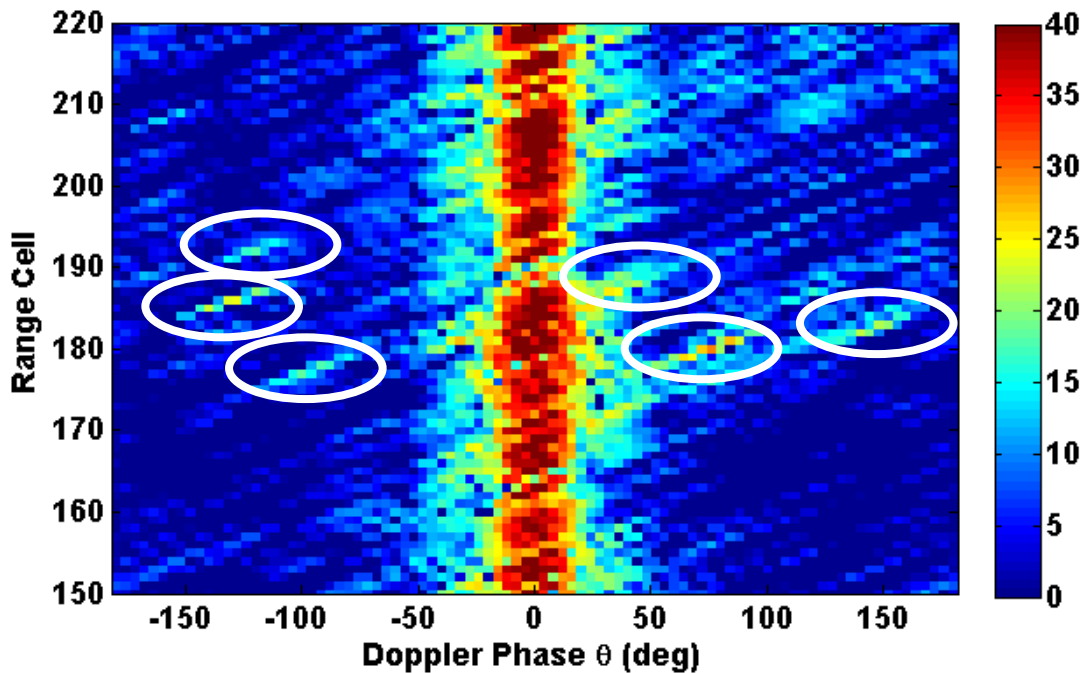


Figure 5.8 TRAP range-Doppler map (in dB), moving targets are revealed at locations indicated by the white circles

Observe the reduction in range-Doppler coupling, indicated by the narrower clutter returns in Figs. 5.7 and 5.8, that occurs when sequential APC-RISR and to a greater degree TRAP are employed. This behavior is expected since the RISR algorithm is capable of achieving resolution enhancement depending on the available SNR [21].

### 5.6.2 ECLIPSING REPAIR SCENARIO

Next consider a scenario with three range intervals ( $R=3$ ), each containing two targets. For this case the transmitted waveforms are length  $N=32$  constant modulus random phase codes and  $M+R-1=22$  pulses are employed, each with a unique phase code. RD-TRAP ( $K=10$ ) with eclipsing repair will be employed. The location and Doppler phase of the six moving targets are provided in Table 5.2. In each interval, Target 1 and Target 2 have an SNR of 20 dB and 40 dB, respectively, after a coherent processing gain of 28 dB. At least one of the targets in each interval is eclipsed. APC-RISR is not considered here due to the presence of multiple waveforms contained in each received pulses data. RD-TRAP uses 51 Doppler bins distributed evenly between phase angles of  $\pm 180^\circ$  for processing and 2 adaptive iterations.

**Table 5.2** Target Description for Pulse Agile Scenario

Range Interval	Range Cell $\ell$ for Target 1	Doppler Phase $\theta$ for Target 1	Range Cell $\ell$ for Target 2	Doppler Phase $\theta$ for Target 2
0	120	$20^\circ$	100	$-30^\circ$
1	15	$-70^\circ$	75	$75^\circ$
2	45	$70^\circ$	20	$-75^\circ$

When different random phase codes are transmitted on each pulse, the range sidelobes associated with each phase code are different and thus do not coherently integrate when Doppler processing is performed. The pulse compression peak benefits from coherent integration gain

associated with Doppler processing although the uncorrelated range sidelobes spread throughout the Doppler spectrum. As a result, the average range sidelobe level will be reduced by approximately  $1/M$ , relative to before Doppler processing. Pulse agility can be beneficial when the waveforms have sufficiently low range sidelobes and a large number of pulses are integrated. Similarly, the set of cross-correlations between each pair of waveforms in the pulse train associated with the range interval of interest and another interval will likewise be incoherent.

Figures 5.9-5.11 display the results for the matched filter and RD-TRAP for the first, second, and third range intervals, respectively. Target locations are denoted by white circles and the eclipsed regions are shown in yellow boxes. In each interval, the matched filter is capable of estimating the larger target, however, the small targets are masked by the aforementioned spectral spreading of range sidelobes or cross-correlation due to large targets in other intervals. In contrast, TRAP-RD ( $K=10$ ) with eclipsing repair is able to suppress range and Doppler sidelobes as well as the interference from targets in other intervals. The TRAP-RD algorithm with eclipsing repair is able to estimate into the eclipsed regions, resulting in the mitigation of sidelobes and cross-correlations due to large targets in these regions. Note that even when  $K$  is large with respect to  $M$ , RD-TRAP performs well due the presence of only a few large targets. Often, pulse-Doppler radars must contend with many range intervals of ground clutter, which will use many of TRAP's degrees of freedom. In the next chapter a non-adaptive algorithm to suppress clutter in a pulse agile regime is presented. Hence, it may be necessary to combine the non-adaptive approach and TRAP to suppress ground clutter and the ambiguity from large moving targets, respectively.

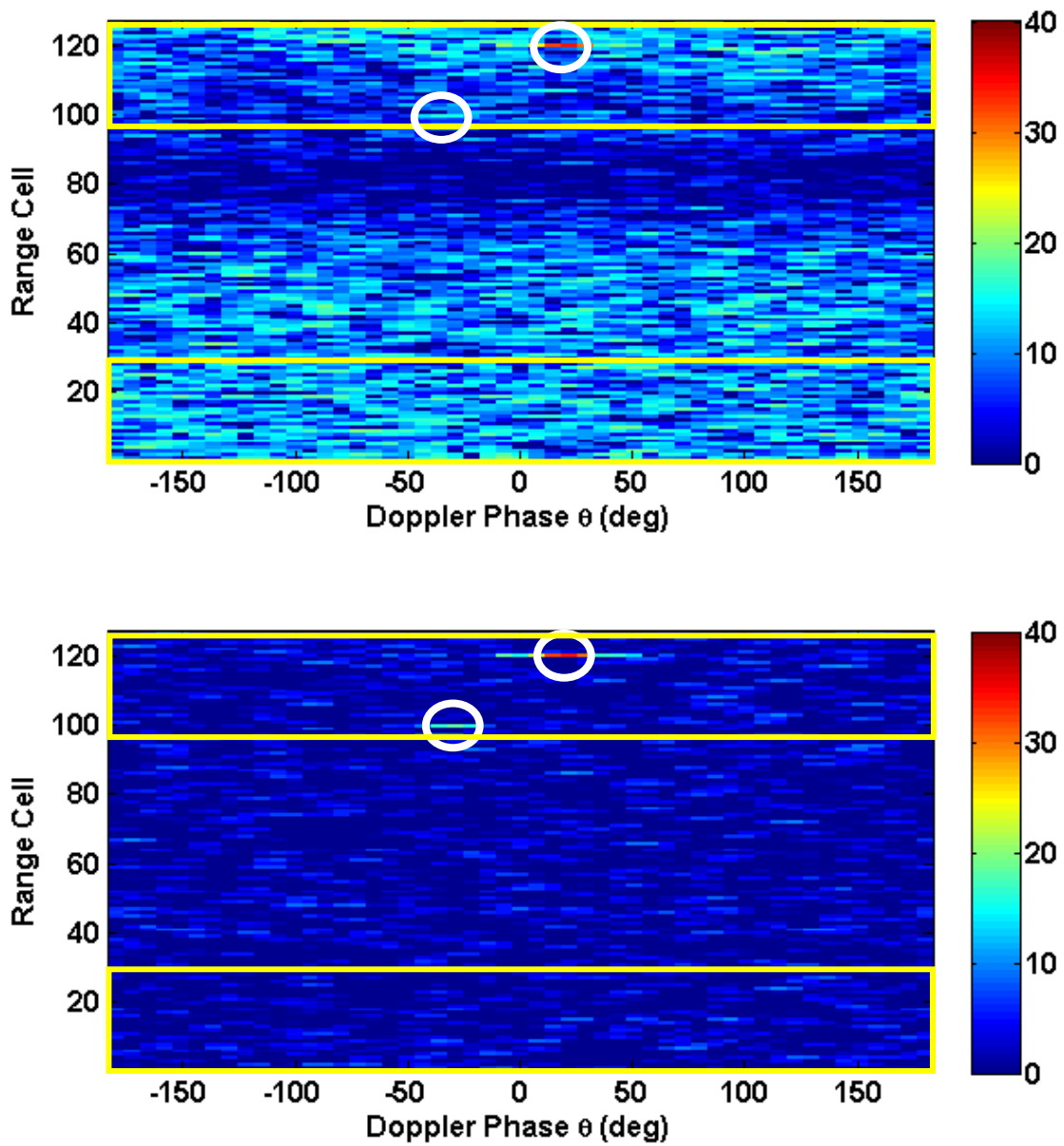


**Figure 5.9** Matched filter (top) and RD-TRAP with  $K=10$  (bottom) output (in dB) for the first range interval, eclipsed regions are denoted by yellow boxes

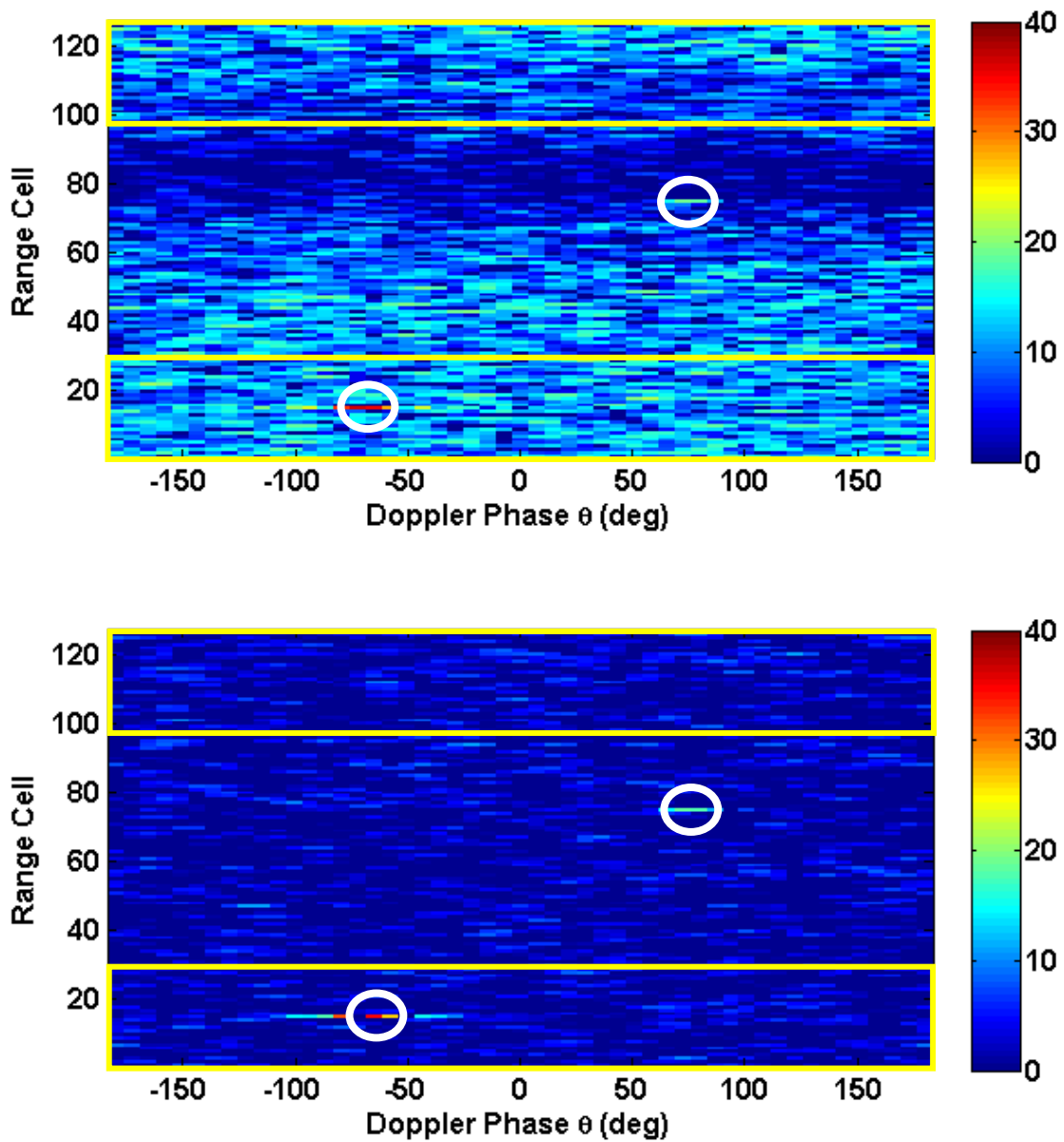


**Figure 5.10** Matched filter (top) and RD-TRAP with  $K=10$  (bottom) output (in dB) for the second range interval, eclipsed regions are denoted by yellow boxes

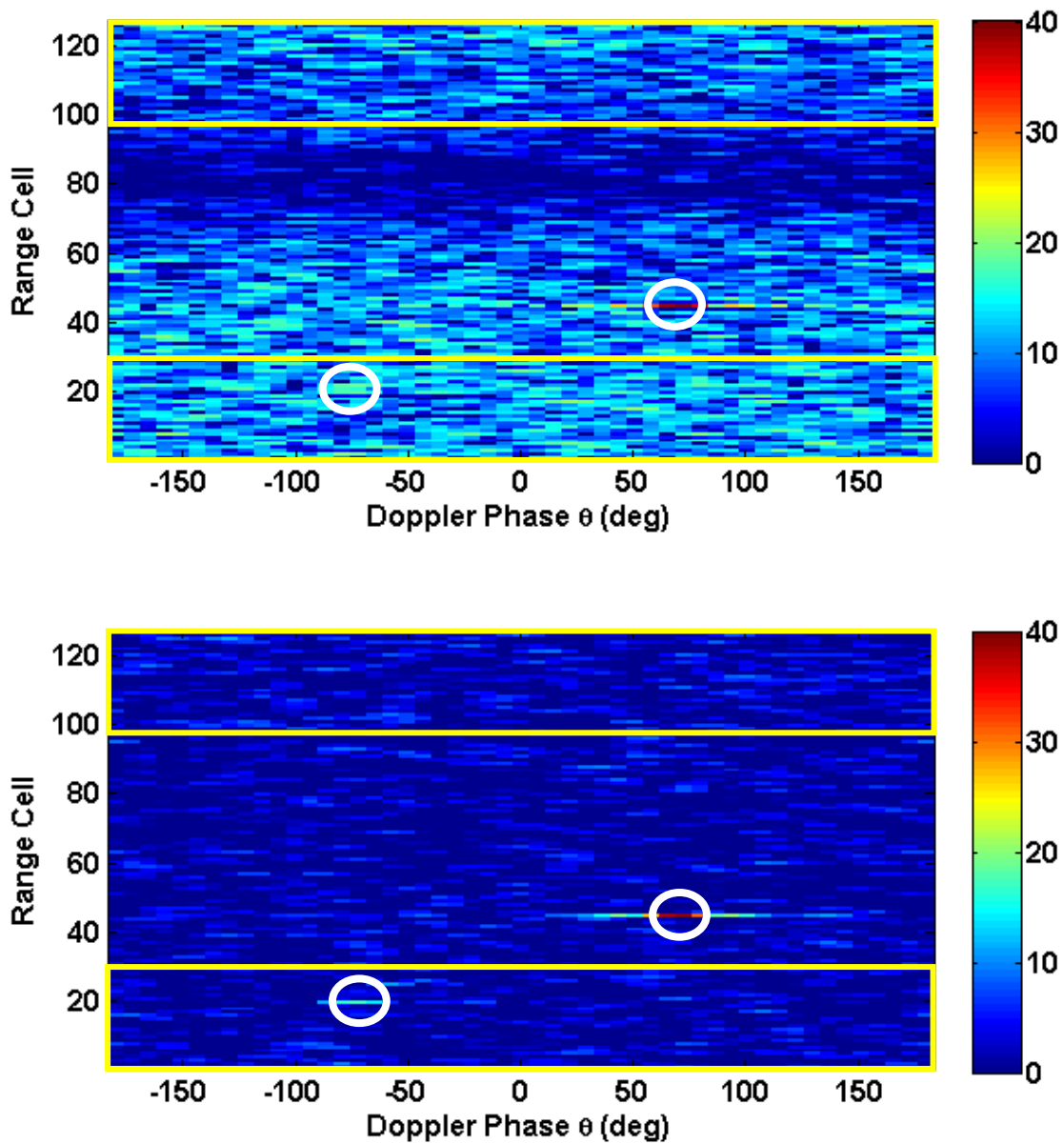


**Figure 5.11** Matched filter (top) and RD-TRAP with  $K=10$  (bottom) output (in dB) for the third range interval, eclipsed regions are denoted by yellow boxes

## 5.7 CONCLUSIONS

Waveform diversity via pulse-to-pulse waveform changes can offer a variety of benefits, e.g., enhanced range resolution or unambiguous ranging. However, pulse-Doppler waveform diversity can have dramatic effects on radar sensitivity. A new joint range-Doppler technique, Time Range Adaptive Processing (TRAP), is proposed that is capable of mitigating range and Doppler sidelobes inherent to pulse-agile radar systems. To alleviate the computational burden of the multi-dimensional TRAP algorithm, a reduced-dimensionality technique is applied to the full-dimension cost function resulting in a more efficient algorithm. The full dimension and reduced-dimension TRAP algorithms are augmented to estimate targets in the eclipsed regions. The new algorithms are shown to exhibit enhanced sensitivity when compared to standard matched filtering (in range and Doppler) and offer more degrees of freedom than sequential adaptivity in range and Doppler. In the next chapter, the time-range signal model presented in this chapter is used to develop a deterministic clutter cancellation technique for pulse agile regimes.

## CHAPTER 6      **NON-IDENTICAL MULTIPLE PULSE COMPRESSION AND CLUTTER CANCELLATION**

Pulse-Doppler radar systems typically employ pulse compression and Doppler processing to achieve sufficient SNR to detect, range, and determine the velocity of moving targets. Additionally, clutter cancellation is used to remove the returns from stationary or slow moving objects, e.g. land and sea clutter. Transmitting an identical waveform on each pulse allows standard clutter cancellation implemented in the pulse or slow-time domain where the available degrees of freedom is dictated by the number of pulses within a coherent-processing interval (CPI). Great care is taken to ensure that there is very little timing error from pulse-to-pulse as any jitter will limit the clutter cancellation ability of the radar system. Note that in this scenario the transmit waveform may have some distortion relative to the ideal waveform, albeit this distortion is nearly identical for each of the transmitted pulses and thus does not affect clutter cancellation. In addition, fill pulses are used to ensure that returns from range ambiguous clutter or multiple time around clutter (MTAC) are present in each pulse and therefore possess the same slow-time structure as unambiguous clutter returns.

Some radars transmit different waveforms on each pulse for various reasons, for example, to synthesize a wider bandwidth or resolve range ambiguities, thus preventing the use of standard non-adaptive clutter cancellation techniques. In this chapter a framework entitled Non-Identical Multiple Pulse Compression (NIMPC) is presented for which the available degrees of freedom for clutter cancellation is significantly higher than traditional techniques. A waveform based clutter cancellation technique is presented within the NIMPC framework and discussed. Simulation

results are presented and discussed for the synthetic wideband scenario where each of the transmitted pulses has a slightly different center frequency. Previously, pulse-to-pulse phase changes have been considered as a means to resolve range ambiguities. In this scenario, clutter cancellation can be performed using a more traditional approach [30] applied in the slow-time (pulse-to-pulse) domain. Both pulse-to-pulse waveform and center frequency changes are addressed herein by utilizing a filter construct that operates simultaneously in the slow and fast time dimensions. A similar approach can be found in [38], which was published shortly after the work detailed in the following.

### 6.1 NON-IDENTICAL MULTIPLE PULSE COMPRESSION

The NIMPC signal model is similar to that for Time-Range Adaptive Processing (TRAP) presented in Chapter 5. However, here we will consider the non-adaptive benefits of this structure, specifically, how it can be used to implement deterministic clutter cancellation techniques.

The waveforms transmitted in a radar CPI can be represented by the  $N \times M$  matrix  $\mathbf{S}$  where the  $m^{\text{th}}$  column  $\mathbf{s}_m$  is the  $m^{\text{th}}$  length- $N$  transmitted waveform. The waveforms in  $\mathbf{S}$  are arbitrary and may change coding, modulation, center frequency, etc., from pulse-to-pulse. The received signal at the  $\ell^{\text{th}}$  range cell (from all  $M$  pulses in the CPI) is expressed as the row vector

$$\mathbf{y}(\ell) = [y_0(\ell) \ y_1(\ell) \ \cdots \ y_m(\ell) \ \cdots \ y_{M-1}(\ell)] \quad (6.1)$$

in which the  $m^{\text{th}}$  pulse is denoted as

$$y_m(\ell) = \sum_{\theta} [\mathbf{x}_{\theta}^T(\ell) \mathbf{s}_m e^{jm\theta}] + n(\ell), \quad (6.2)$$

where  $\mathbf{x}(\ell, \theta) = [x(\ell, \theta) \ x(\ell-1, \theta) \ \dots \ x(\ell-N+1, \theta)]^T$  is a collection of the complex scattering coefficients associated with the scatterers in the range profile corresponding to Doppler phase shift  $\theta$ , with which the  $m^{\text{th}}$  waveform convolves at delay  $\ell$ , and  $n(\ell)$  is a sample of additive noise. Collecting  $N$  fast-time (range) samples of the received signal model in (6.1) can be expressed as

$$\mathbf{Y}(\ell) = \sum_{\theta} [\mathbf{X}_{\theta}(\ell)(\mathbf{S} \odot \mathbf{V}_{\theta})] + \mathbf{N}(\ell), \quad (6.3)$$

where

$$\mathbf{V}_{\theta} = \begin{bmatrix} 1 \\ 1 \\ \vdots \\ 1 \end{bmatrix} [1 \ e^{j\theta} \ \dots \ e^{j\theta(M-1)}], \quad (6.4)$$

and

$$\mathbf{X}(\ell, \theta) = \begin{bmatrix} x(\ell, \theta) & x(\ell-1, \theta) & \dots & x(\ell-N+1, \theta) \\ x(\ell+1, \theta) & x(\ell, \theta) & \dots & x(\ell-N+2, \theta) \\ \vdots & \vdots & \ddots & \vdots \\ x(\ell+N-1, \theta) & x(\ell+N-2, \theta) & \dots & x(\ell, \theta) \end{bmatrix} \quad (6.5)$$

is an  $N \times N$  matrix containing the complex scattering amplitudes within  $2N-1$  range cells of  $x(\ell, \theta)$ , and  $\odot$  denotes the Hadamard product. As in the previous chapter, we reorganize the snapshots into a single length  $NM \times 1$  vector

$$\tilde{\mathbf{y}}(\ell) = \text{vec}(\mathbf{Y}(\ell)) = \text{vec} \left( \left[ \sum_{\theta} \mathbf{X}(\ell, \theta)(\mathbf{S} \odot \mathbf{V}_{\theta}) \right] \right) + \tilde{\mathbf{n}}(\ell), \quad (6.6)$$

in which  $\tilde{\mathbf{n}}(\ell) = \text{vec}(\mathbf{N}(\ell))$ . Based on (6.6), a (normalized) joint range-Doppler steering vector can be expressed as

$$\mathbf{w}_\theta = \frac{1}{NM} \text{vec}(\mathbf{S} \odot \mathbf{V}_\theta), \quad (6.7)$$

which can subsequently be applied to obtain the normalized NIMPC estimate

$$\hat{\mathbf{x}}_{NIMPC}(\ell, \theta) = \mathbf{w}_\theta^H \tilde{\mathbf{y}}(\ell). \quad (6.8)$$

It should be noted that applying the filter in (6.8) yields an identical result to standard range and Doppler processing which are computed separately. However, in the next section the added degrees of freedom in the NIMPC framework will be exploited to achieve non-identical pulse clutter cancellation, which is not easily achieved using separate range and Doppler processing. To process multiple range intervals the matrix  $\mathbf{S}$  in (6.7) can be replaced by  $\mathbf{S}_r$  from (5.5).

### 6.1.1 CLUTTER CANCELLATION

When identical pulses are transmitted, the relative slow-time (pulse-to-pulse) change between clutter returns is constant throughout the entire pulse duration; however, in the non-identical case, the relative pulse-to-pulse phase difference between returns changes as a function of fast time. These waveform changes yield matched filter range sidelobes that are different for each waveform, which is referred to as range sidelobe modulation (RSM). The RSM may be highly correlated, as in the case of synthetic wideband waveforms, or uncorrelated, for example, when random pulse-to-pulse coding is used [31]. Hence, standard clutter cancellation techniques, which are applied in the slow-time domain, do not typically possess the degrees of freedom necessary to cancel all of the different pulse-to-pulse phase progressions associated with RSM.

Clutter cancellation is achieved by deterministically modeling the clutter signal structure from an individual range cell as interference and applying the maximum signal-to-interference and noise ratio (SINR) solution. The interference covariance matrix for clutter at Doppler phase  $\phi$  is constructed as

$$\mathbf{R} = (\mathbf{P}_\phi \mathbf{P}_\phi^H + \varepsilon \mathbf{I}), \quad (6.9)$$

where

$$\mathbf{P}_\phi = [\mathbf{c}_{-(N-1)}^\phi \quad \mathbf{c}_{-(N-1)+1}^\phi \quad \cdots \quad \mathbf{c}_0^\phi \quad \cdots \quad \mathbf{c}_{N-2}^\phi \quad \mathbf{c}_{N-1}^\phi], \quad (6.10)$$

$$\mathbf{c}_n^\phi = \text{vec}(\mathbf{S}_n \odot \mathbf{V}_\phi), \quad (6.11)$$

$$\mathbf{S}_n = [\mathbf{s}_0^n \quad \mathbf{s}_1^n \quad \cdots \quad \mathbf{s}_{M-1}^n], \quad (6.12)$$

and

$$\mathbf{s}_m^n = \begin{cases} [\mathbf{0}_n^T \quad s_m(0) \quad \cdots \quad s_m(N-1-n)]^T & \text{for } 0 \leq n \leq N-1 \\ [s_m(|n|) \quad \cdots \quad s_m(N-1) \quad \mathbf{0}_{|n|}^T]^T & \text{for } -(N-1) \leq n < 0 \end{cases} \quad (6.13)$$

in which  $s_m(n)$  is the  $n^{\text{th}}$  sample of the  $m^{\text{th}}$  pulse and  $\mathbf{0}_n$  is an  $n \times 1$  vector of zeros. In (6.9)  $\varepsilon$  is a diagonal loading factor to prevent ill-conditioning. It has been observed that the receiver noise power is a suitable value for  $\varepsilon$  in most scenarios. The middle column of  $\mathbf{P}_\phi$ ,  $\mathbf{c}_0^\phi$ , corresponds to the contribution of clutter in the desired range cell and the other  $2(N-1)$  columns correspond to contributions from clutter in the surrounding range cells, thus accounting for the RSM. The resulting clutter-cancelled estimate is

$$\hat{x}_{NIMPC-C}(\ell, \theta) = \tilde{\mathbf{w}}_\theta^H \tilde{\mathbf{y}}(\ell), \quad (6.14)$$

where

$$\tilde{\mathbf{w}}_{\theta} = \frac{\mu}{NM} \mathbf{R}^{-1} \text{vec}(\mathbf{S} \odot \mathbf{V}_{\theta}) \quad (6.15)$$

is the clutter-whitened NIMPC filter, and  $\mu$  is an arbitrary scale factor. For range ambiguous operation the matrix  $\mathbf{S}$  in (6.15) is replaced by  $\mathbf{S}_r$  from (5.5) to estimate the  $r^{\text{th}}$  of  $R$  total range intervals. When identical pulses are transmitted, the relative slow-time (pulse-to-pulse) change between clutter returns is constant throughout the entire pulse duration. In the non-identical case, the relative slow-time difference between returns changes as a function of fast-time over the pulse duration.

Extending the clutter notch to account for clutter Doppler-spread can be achieved by placing multiple closely-spaced notches. This is implemented by replacing  $\mathbf{P}_{\phi}$  in (6.9) by  $\tilde{\mathbf{P}} = [\mathbf{P}_{\phi_0} \ \mathbf{P}_{\phi_1} \ \dots \ \mathbf{P}_{\phi_{Q-1}}]$  where  $Q$  is the total number of notches. However, each notch requires  $2N-1$  degrees of freedom and may necessitate the use of additional pulses to increase the available degrees of freedom, which is given by the product  $NM$ . Next, the clutter cancellation techniques in this section are extended to account for multiple time around clutter (MTAC).

### 6.1.2 EXTENSION TO MULTIPLE TIME AROUND CLUTTER

MTAC is present in medium and high PRF surveillance radar systems where the clutter response is measured from distances greater than the unambiguous range

$$r_u = \frac{c}{2\text{PRF}} \quad (6.16)$$

where  $c$  is the speed of light and PRF is pulse repetition frequency. The returns from beyond  $r_u$  will appear to originate from within the primary interval such that several different PRF values are

normally used to decipher the true range of ambiguous targets. Typically, in the range-ambiguous case, the radar will transmit several pulses before the receiver is turned on to ensure that returns from each ambiguous clutter interval will be present when the receiver starts recording the first pulse used for processing. The pulses that are transmitted before the receiver turns on are referred to as fill pulses. When identical waveforms are used, a fill pulse is required for each expected range ambiguous interval, i.e., the number of fill pulses is equal to the number of ambiguous intervals (not counting the primary unambiguous interval).

Although it is not necessary to transmit fill pulses when pulse agility is used since the clutter returns from each interval will inherently be different, the following analysis will consider fill pulses to ensure that the returns from each range interval have uniform energy. For a given interval, targets and clutter from other intervals will not coherently integrate, thus producing interference in addition to the aforementioned effects of RSM. Clutter residue from ambiguous intervals can be addressed by modifying the covariance matrix from (6.9) to include the clutter response from multiple intervals. For  $K$  intervals (including the primary interval), the matrix  $\mathbf{P}_\phi$  in (6.9) is replaced with

$$\mathbf{P}_\phi^K = \begin{bmatrix} \mathbf{P}_{\phi,0} & \mathbf{P}_{\phi,1} & \cdots & \mathbf{P}_{\phi,K-1} \end{bmatrix} \quad (6.17)$$

where

$$\mathbf{P}_{\phi,k} = \begin{bmatrix} \mathbf{c}_{-(N-1),k}^\phi & \mathbf{c}_{-(N-1)+1,k}^\phi & \cdots & \mathbf{c}_{0,k}^\phi & \cdots & \mathbf{c}_{N-2,k}^\phi & \mathbf{c}_{N-1,k}^\phi \end{bmatrix}, \quad (6.18)$$

$$\mathbf{c}_{n,k}^\phi = \text{vec}(\mathbf{S}_{n,k} \odot \mathbf{V}_\phi), \quad (6.19)$$

and

$$\mathbf{S}_{n,k} = \left[ \mathbf{s}_{K-1-k}^n \quad \mathbf{s}_{K-k}^n \quad \cdots \quad \mathbf{s}_{K-1-k+M-1}^n \right]. \quad (6.20)$$

Note that in the range ambiguous case the transmit matrix  $\mathbf{S}$  has dimensionality  $N \times (M + K - 1)$  due to the use of fill pulses.

To account for clutter Doppler spread, multiple notches can be added in the MTAC formulation as well via the same extension previously described, i.e., replacing  $\mathbf{P}_\phi$  in (6.9) with  $\tilde{\mathbf{P}} = \left[ \mathbf{P}_{\phi_0}^K \quad \mathbf{P}_{\phi_1}^K \quad \cdots \quad \mathbf{P}_{\phi_{Q-1}}^K \right]$  (for  $Q$  notches). Note that the DOF used for clutter cancellation is a function of the number of notches at each interval. For  $K$  intervals and  $Q$  notches in each interval, the required DOF is bounded by the number of linearly independent columns in  $\tilde{\mathbf{P}}$ , i.e.,

$$\text{DOF} \leq KQ(2N - 1), \quad (6.21)$$

which should not exceed the available DOF dictated by the product  $MN$ .

### 6.1.3 FAST IMPLEMENTATION

The NIMPC filter in (6.15) can be computationally expensive to apply due to the large dimensionality. However, fast convolution (FFT processing) can be used to efficiently apply the whitened NIMPC filters, which may be computed offline. First, examine the relationship between  $\tilde{\mathbf{y}}(\ell)$  and  $\tilde{\mathbf{y}}(\ell+1)$ :

$$\tilde{\mathbf{y}}(\ell) = \begin{bmatrix} \boxed{\begin{matrix} y_0(\ell) \\ \vdots \\ y_0(\ell+N-1) \end{matrix}} \\ \boxed{\begin{matrix} y_1(\ell) \\ \vdots \\ y_1(\ell+N-1) \end{matrix}} \\ \vdots \\ \boxed{\begin{matrix} y_{M-1}(\ell) \\ \vdots \\ y_{M-1}(\ell+N-1) \end{matrix}} \end{bmatrix}, \quad \tilde{\mathbf{y}}(\ell+1) = \begin{bmatrix} \boxed{\begin{matrix} y_0(\ell+1) \\ \vdots \\ y_0(\ell+N-1+1) \end{matrix}} \\ \boxed{\begin{matrix} y_1(\ell+1) \\ \vdots \\ y_1(\ell+N-1+1) \end{matrix}} \\ \vdots \\ \boxed{\begin{matrix} y_{M-1}(\ell+1) \\ \vdots \\ y_{M-1}(\ell+N-1+1) \end{matrix}} \end{bmatrix}. \quad (6.22)$$

Note that the colored blocks in (6.22) represent the contributions of the individual pulses to the received signal vector. Next, consider the whitened NIMPC filter that can be expressed in contiguously blocked form as

$$\tilde{\mathbf{w}}_{\theta} = \left[ \tilde{\mathbf{w}}_{0,\theta}^T \quad \tilde{\mathbf{w}}_{1,\theta}^T \quad \cdots \quad \tilde{\mathbf{w}}_{M-1,\theta}^T \right]^T, \quad (6.23)$$

in which the filter has been segmented into  $M$  separate  $N$ -length contiguous blocks. The application of the NIMPC filter for a single Doppler bin can be represented as a convolution of the received signal blocks in (6.22) with the corresponding segment of the NIMPC filter from (6.23). This convolutional implementation is expressed as

$$\hat{x}_{NIMPC-C}(\ell, \theta) = \frac{1}{NM} \sum_{m=0}^{M-1} \left[ \sum_{n=0}^{N-1} \tilde{w}_{m,\theta}^* (N-1-n) y_m(\ell+N-1-n) \right], \quad (6.24)$$

for  $\ell = 0, 1, \dots, L-1$  where  $L-1$  is the length of the range profile and  $(\bullet)^*$  denotes complex conjugation. Equation (6.24) can be implemented efficiently using the fast Fourier transform (FFT) as

$$\hat{x}_{NIMPC-C}(\ell, \theta) = \frac{1}{NM} F^{-1} \left\{ \sum_{m=0}^{M-1} \left[ F \{ \tilde{\mathbf{w}}_{m,\theta}^* \} \odot F \{ \mathbf{y}_m \} \right] \right\}, \quad (6.25)$$

in which  $\mathbf{y}_m$  is the received data from the  $m^{\text{th}}$  pulse,  $\tilde{\mathbf{w}}_{m,\theta}^*$  is the time-reversed complex conjugate of  $\tilde{\mathbf{w}}_{m,\theta}$  zero-padded to the length of  $\mathbf{y}_m$ , and  $F$  and  $F^{-1}$  are the FFT and inverse FFT respectively. Note that usually the received vector is padded with zeros before the FFT, however, the formulation in (6.24) does not include the convolutional tails that represent the eclipsed region, thus the additional zero-padding is unnecessary. In fact, the first  $N-1$  samples of the output from (6.25) should be discarded to produce a result equivalent to that produced by (6.24). While the NIMPC formulation naturally accounts for the range sidelobes associated with clutter in the eclipsed region that extend into the leading and trailing edges of the range profile, it does not provide a clutter-free estimate in the eclipsed region. Thus, the convolutional tails associated with the eclipsed regions are discarded.

## 6.2 SIMULATION RESULTS

The performance of NIMPC will be assessed by considering two different scenarios. First, a synthetic wideband waveform, which offers the benefit of increased range resolution is employed in a range ambiguous simulation. Next, pulse-to-pulse phase code changes, which are attractive because of their ability to perform unambiguous ranging with a single PRF, will be considered. In both cases targets will be modeled as point scatterers in additive white Gaussian noise. Ground clutter is modeled as point targets in each range cell with a pulse-to-pulse Doppler phase chosen from a uniform distribution between  $\mp\sigma_\theta$  degrees.

### 6.2.1 SYNTHETIC WIDEBAND SCENARIO

Consider the synthetic wideband scenario for which each column of the matrix  $\mathbf{S}$  is a 40 chip P3 phase-coded waveform [8] over-sampled by a factor of two (to support the total bandwidth of the pulse train) such that  $N = 80$  and each waveform is at a slightly different center frequency [33]. The CPI contains  $M = 50$  and two additional fill pulses, resulting in a total of 52 transmitted waveforms for which the normalized center frequency of the  $m^{\text{th}}$  pulse is given by

$$f_m = \frac{m}{2(M + K - 2)} \quad (6.26)$$

for  $m = 0, 1, \dots, M + K - 2$ , where  $K=3$  is the number of range intervals (1 unambiguous and 2 ambiguous). The resulting bandwidth is twice as large as that of a single pulse and consequently, the range resolution twice as fine. The simulated scene consists of four small moving targets in the fourth interval with the ranges (relative to the range interval that contains the target) and Doppler phases listed in Table 6.1. For an X-band radar with a 10 kHz PRF, the Doppler phases in Table 6.1 are comparable to target velocities ranging from 37 to 65 mph. The moving targets have a signal-to-noise ratio (SNR) of  $-13$  dB, and the average clutter-to-noise ratio (CNR) is 47 dB (stated values are pre-processing) such that the clutter power is 60 dB higher than that of the targets. The clutter extends through the primary interval and two range ambiguous intervals and is present in all eclipsed regions. Clutter Doppler spread is induced by selecting  $\sigma_\theta = 1^\circ$ . The coherent processing gain is 33 dB for the range and Doppler matched filter. For the synthetic wideband waveform described above, the added benefit is enhanced range resolution, and ambiguous ranges will still have to be unwrapped using a multiple staggered PRF scheme.

**Table 6.1** Target Description for Synthetic Wideband Scenario

Range Interval	Range Cell $\ell$	Doppler Phase $\theta$
1	270	65°
2	220	40°
3	170	70°

Figure 6.1 displays the NIMPC estimate for the first (unambiguous) interval when no clutter cancellation is applied, which is equivalent to the standard range-Doppler processor output. The clutter exhibits a range-Doppler coupling due to the structure of the transmitted waveforms and masks the moving targets. In contrast, Figs. 6.2-6.4 shows the result when NIMPC, in conjunction with clutter cancellation, is used to estimate the first, second, and third intervals, respectively. Here the moving targets are clearly visible as indicated by the white circles in Fig 6.2. Note the range cell indices in all figures are relative to the range interval they are displaying. The range ambiguous targets in each interval are also denoted in Figs. 6.2-6.4 which are visible due to the LFM-like ambiguity diagram of the P3 code [1]. The center frequency deviation of returns from surrounding intervals relative to a particular interval causes range ambiguous targets to appear as if they have a fast-time Doppler shift over the length of the received ambiguous return. This frequency deviation results in a range shift of the matched filter peak according to the ambiguity diagram for the P3 code, which in conjunction with the coherent processing of the stepped-frequency transmit scheme results in a range and Doppler shift of the ambiguous targets from surrounding intervals.

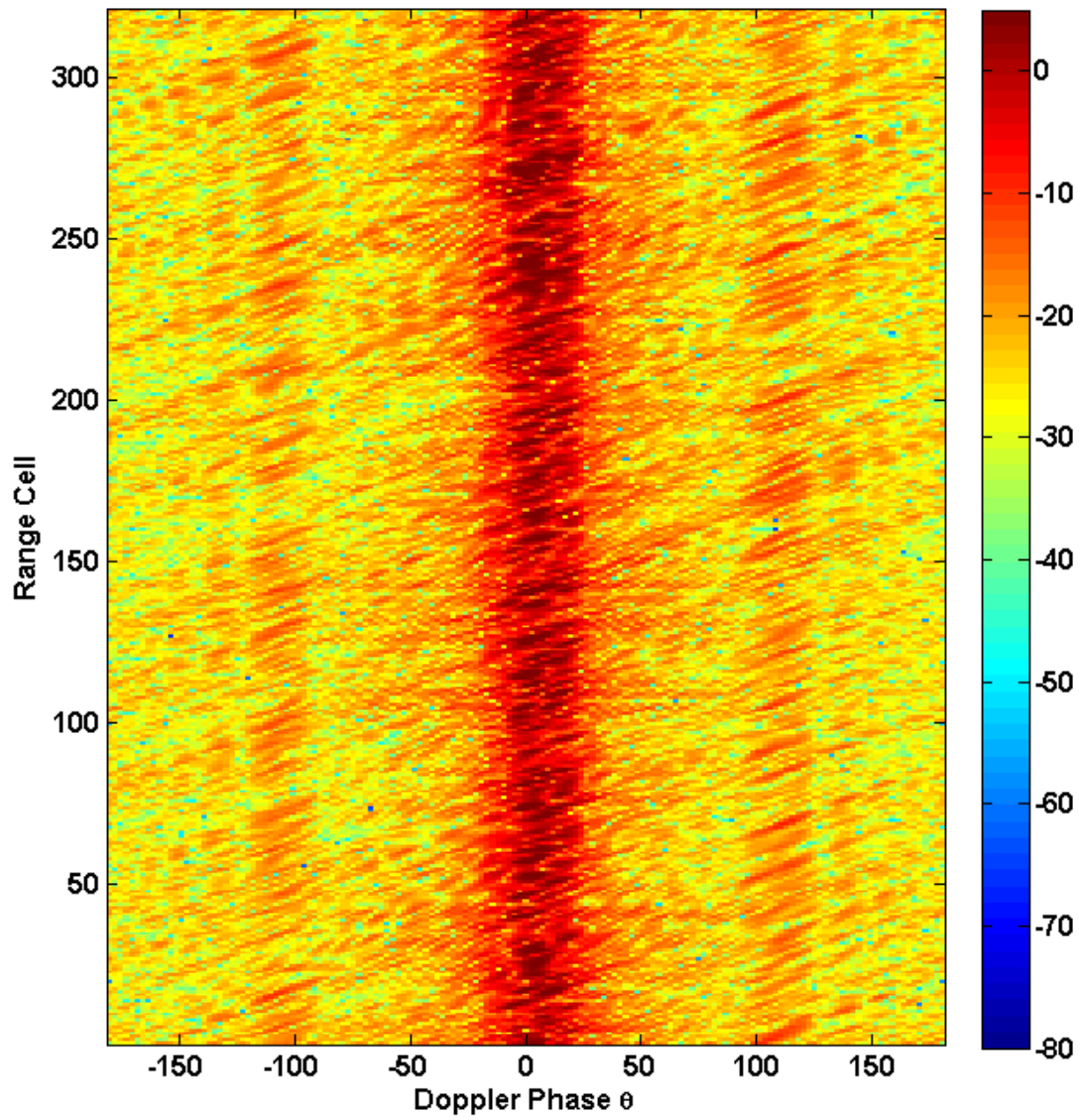


**Figure 6.1** NIMPC estimate (in dB) with no clutter cancellation for the first range interval when the P3 code is used

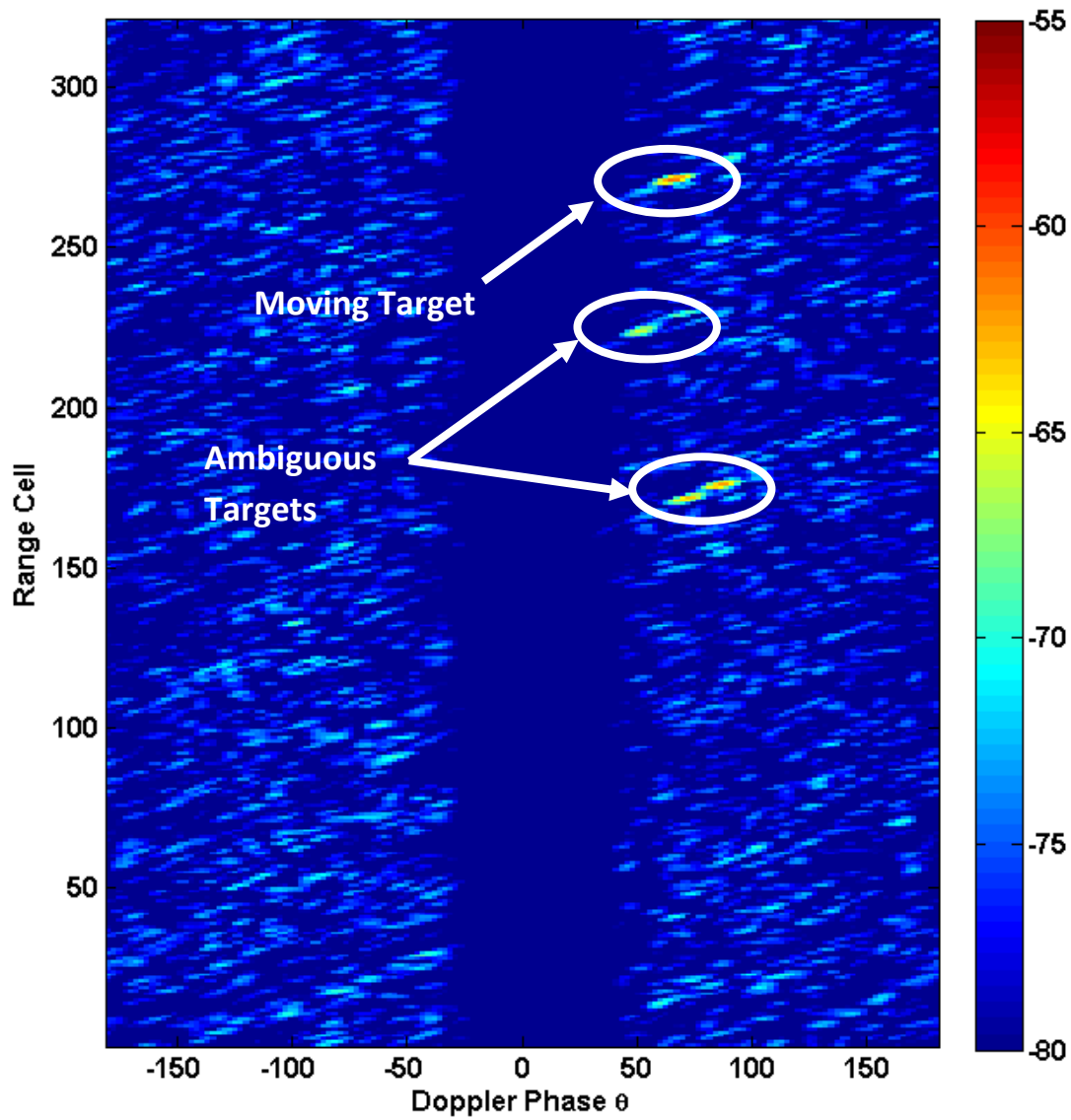


**Figure 6.2** NIMPC estimate (in dB) with clutter cancellation for the first range interval when the P3 code is used

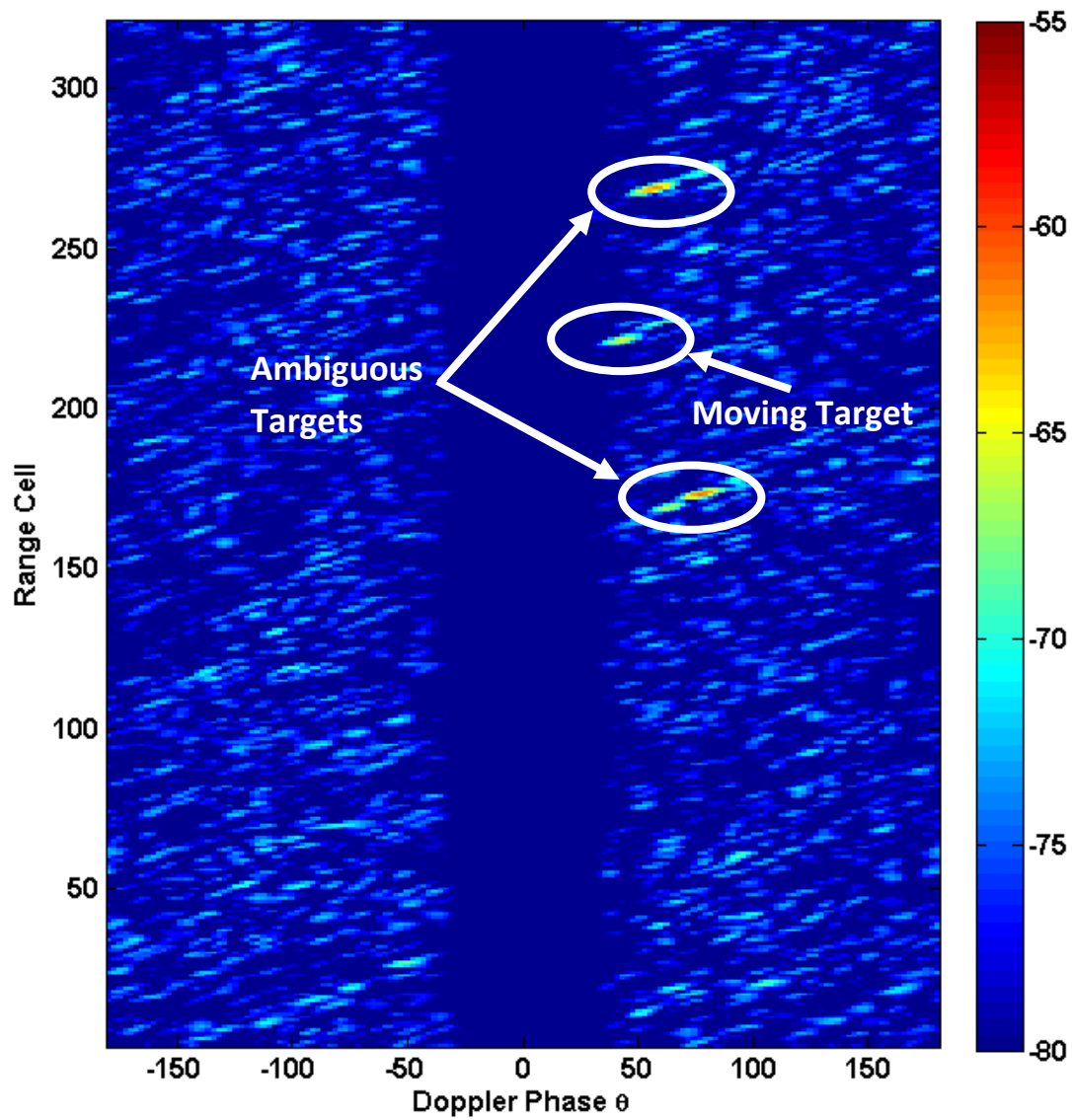


**Figure 6.3** NIMPC estimate (in dB) with clutter cancellation for the second range interval when the P3 code is used

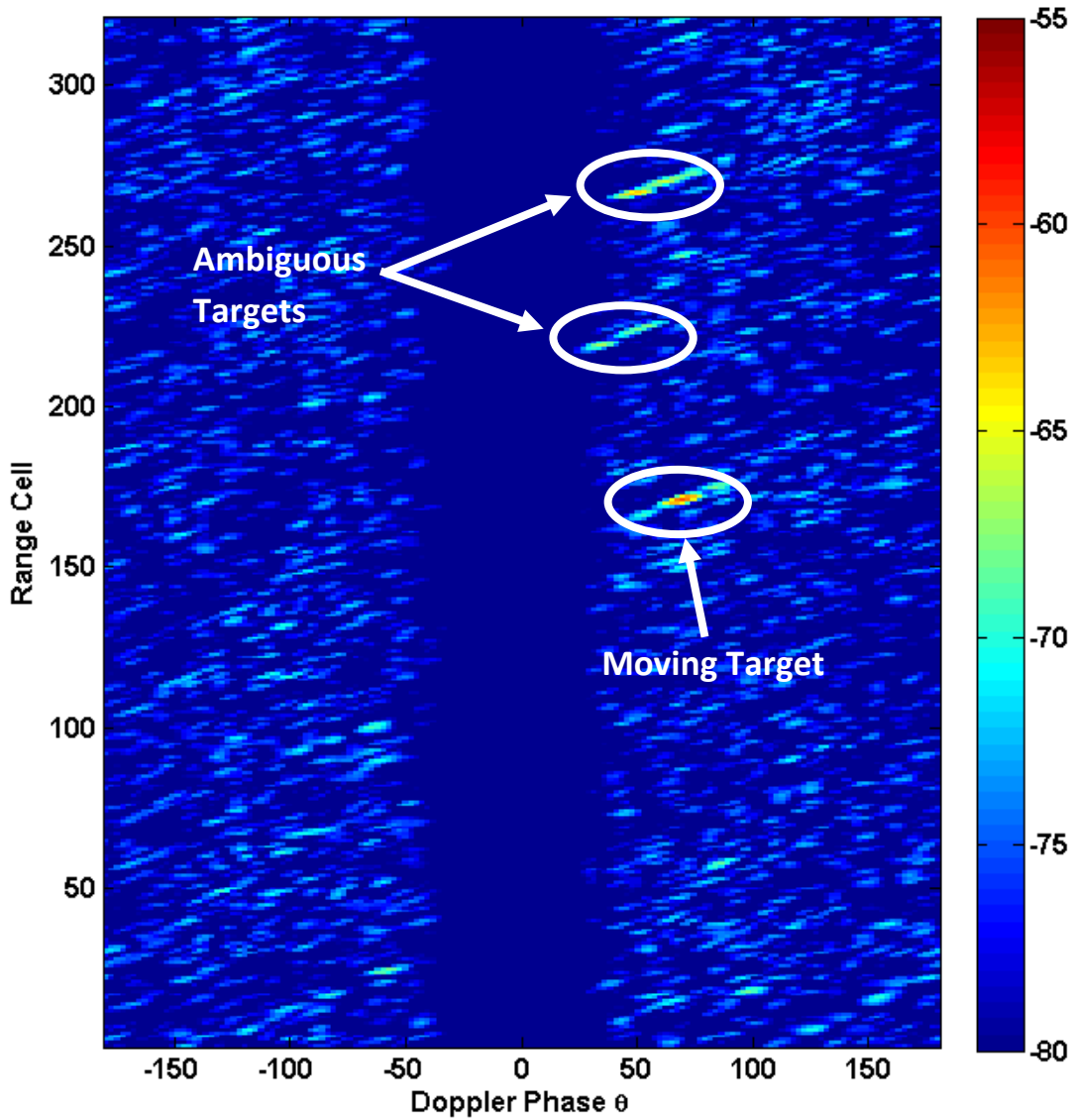


**Figure 6.4** NIMPC estimate (in dB) with clutter cancellation for the third range interval when the P3 code is used

The Doppler view of the range-Doppler map in Fig. 6.4 is displayed in Fig. 6.5, which is formed by taking the maximum value over all of the range cells in each Doppler bin. The clutter has been suppressed by approximately 80 dB. Figure 6.6 shows the NIMPC filter response, defined as

$$\chi(\theta) = \frac{|\tilde{\mathbf{w}}_{\theta}^H \text{vec}(\mathbf{S} \odot \mathbf{V}_{\theta})|^2}{\tilde{\mathbf{w}}_{\theta}^H \tilde{\mathbf{w}}_{\theta} \text{vec}(\mathbf{S} \odot \mathbf{V}_{\theta})^H \text{vec}(\mathbf{S} \odot \mathbf{V}_{\theta})} \quad (6.27)$$

which compares the processing gain of the NIMPC filter with that of the optimal (for a point target in white noise) range-Doppler matched filter. The filter response illustrates that for this scenario there is an SNR loss of 3 to 4 dB, outside of the clutter notch, which is an acceptable trade-off for 80 dB of range ambiguous pulse-agile clutter cancellation.

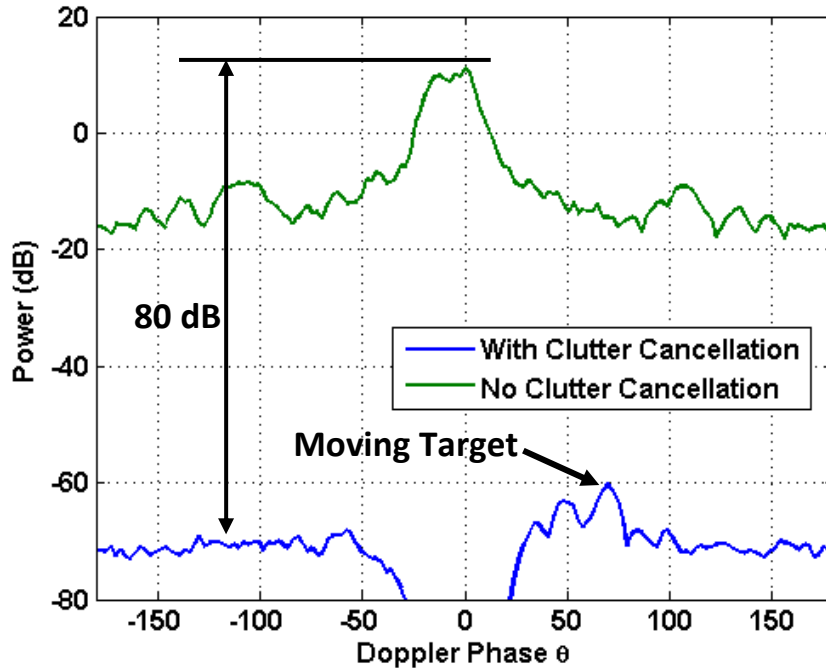


**Figure 6.5** Doppler view of NIMPC estimate with and without clutter cancellation for the third interval when the P3 code is used

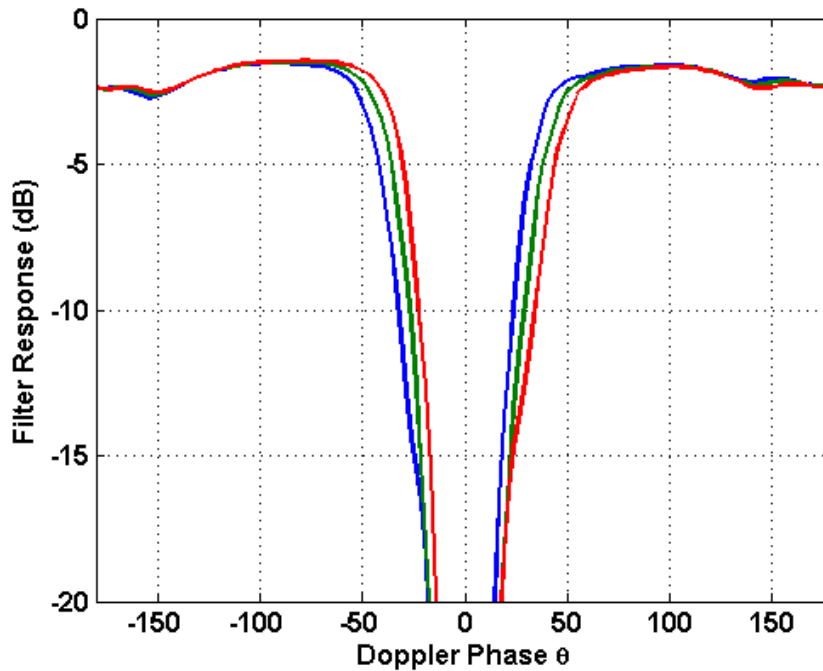


**Figure 6.6** NIMPC filter response for the first (red), second (green), and third (blue) intervals when the P3 code is used

Observe that the clutter response in Fig. 6.1 and corresponding clutter notches in Figs. 6.2-6.4 are offset from zero even though there is very little clutter–Doppler spread. This unexpected spread may result in an undesired suppression of slow moving targets. The asymmetry is caused by the Doppler tolerance of the P3 code in combination with the stepped-frequency waveform present in the ambiguous clutter from the other intervals. The clutter returns from other intervals are composed of pulse trains that are higher or lower in frequency (depending on the interval) than the pulse train used for processing a particular interval. This frequency shift results in either a positive or negative range shift of the matched filter peak (depending on the aforementioned frequency shift), which, in conjunction with the range-Doppler coupling of the stepped-frequency waveform, shifts the peak of the clutter response from the other intervals in the Doppler spectrum resulting in the wide notch seen in the simulation results.

To alleviate the effective Doppler spread associated with the range ambiguous clutter, the P3 code from the previous example is replaced with a single random polyphase code of the same length (40 chips, over-sampled by 2). Although the random phase code suffers from elevated range sidelobes, the Doppler intolerance of this waveform should alleviate the Doppler spreading of the clutter returns from other intervals when examining a particular interval. Figures 6.7 and 6.8 are the simulated outputs from the first interval for NIMPC without and with clutter cancellation, respectively. The effect of the clutter-Doppler spread associated with the P3 code has been reduced to a width commensurate with a single unambiguous interval of clutter illuminated with a stepped-frequency waveform. Also, the elevated range sidelobe levels of the random phase code result in an elevated clutter Doppler sidelobe level as seen in Fig. 6.7. Figures 6.9 and 6.10 display the clutter cancelled outputs for the second and third intervals, respectively. When the random phase code is employed the ambiguous targets are suppressed in the incorrect interval due to the thumbtack like ambiguity diagram of a random phase code. Hence, it may be possible to perform unambiguous ranging with this type of synthetic wideband waveform.

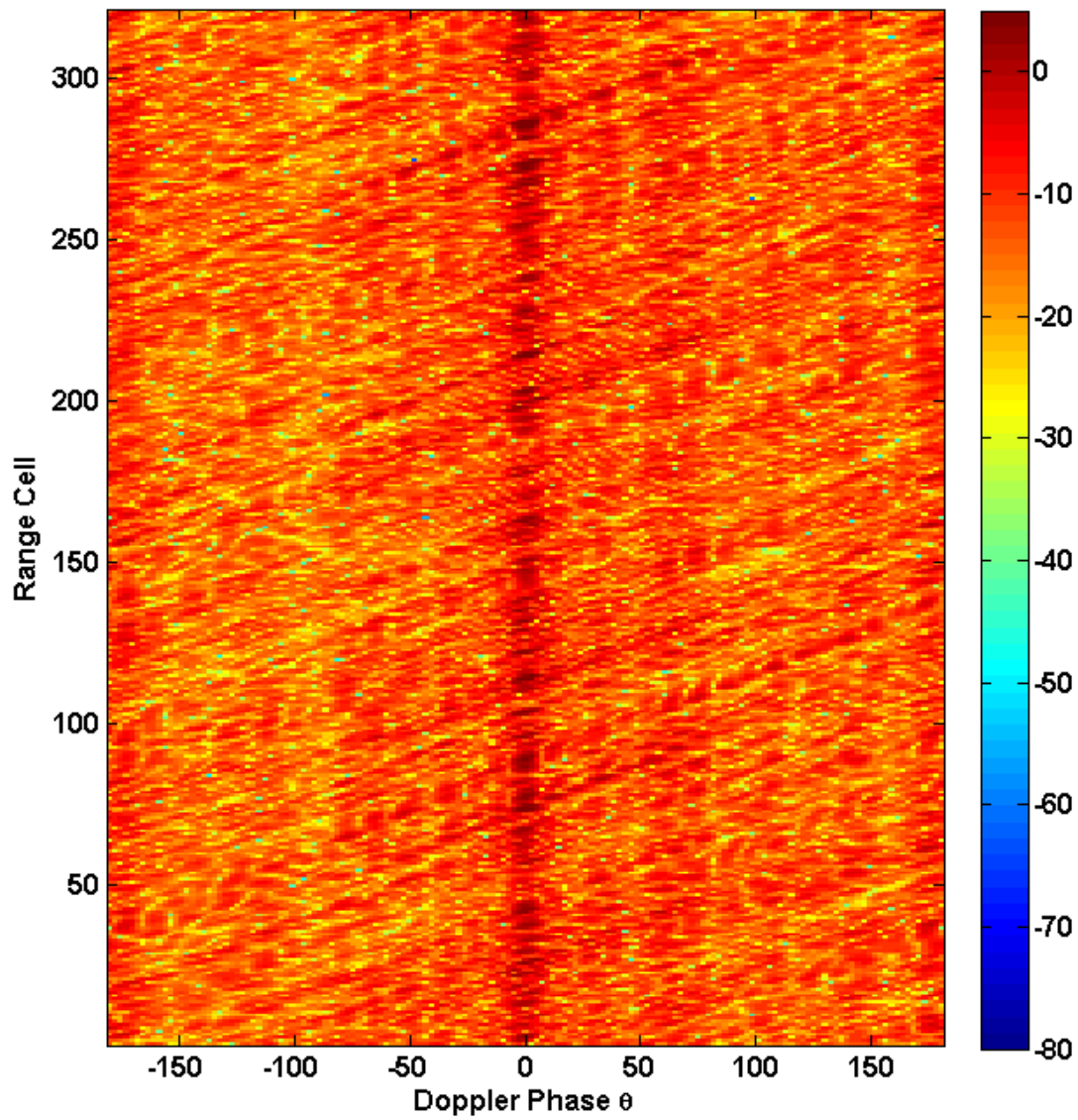


**Figure 6.7** NIMPC estimate (in dB) with no clutter cancellation for the first range interval when the random phase code is used

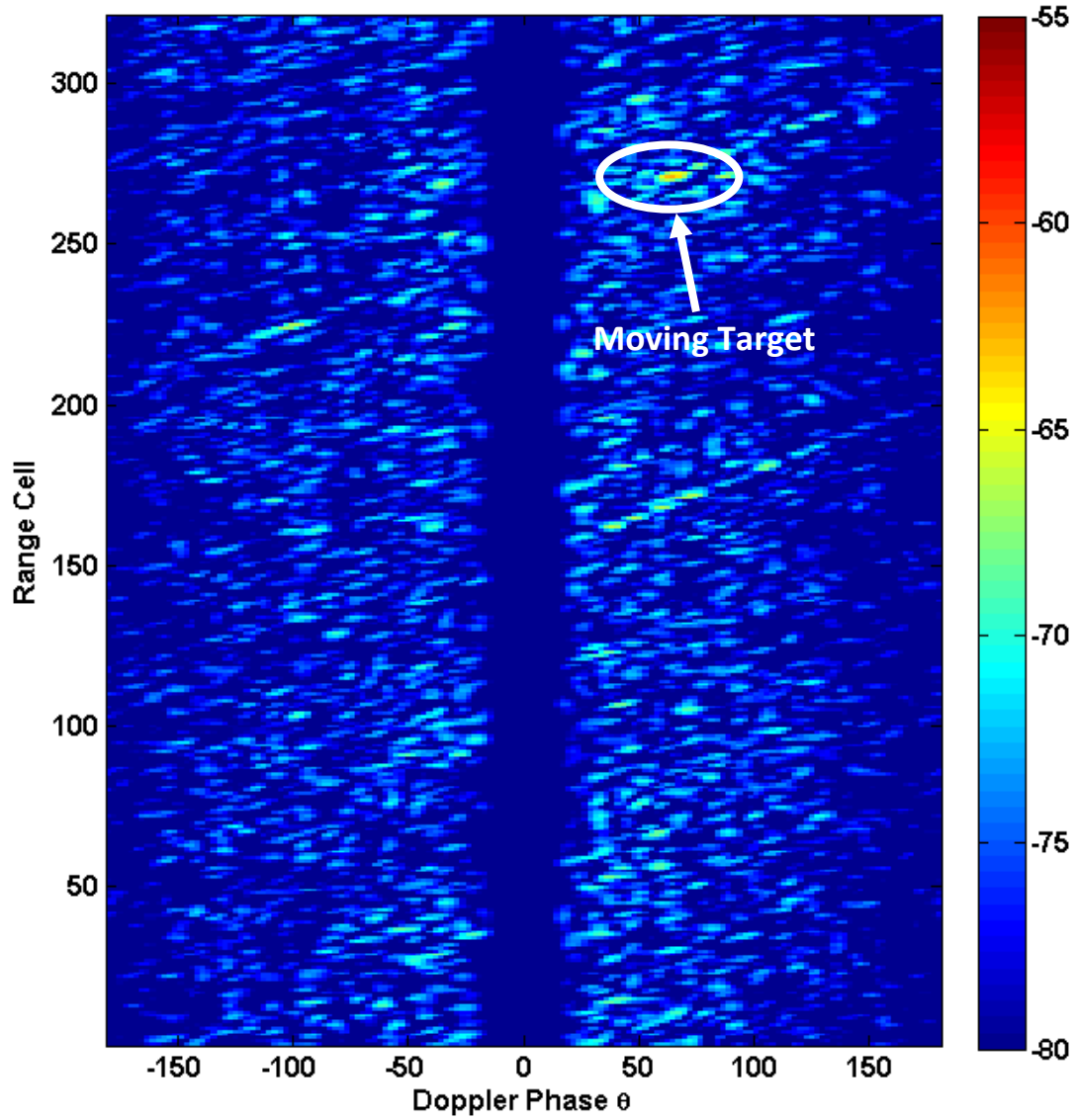


**Figure 6.8** NIMPC estimate (in dB) with clutter cancellation for the first range interval when the random phase code is used

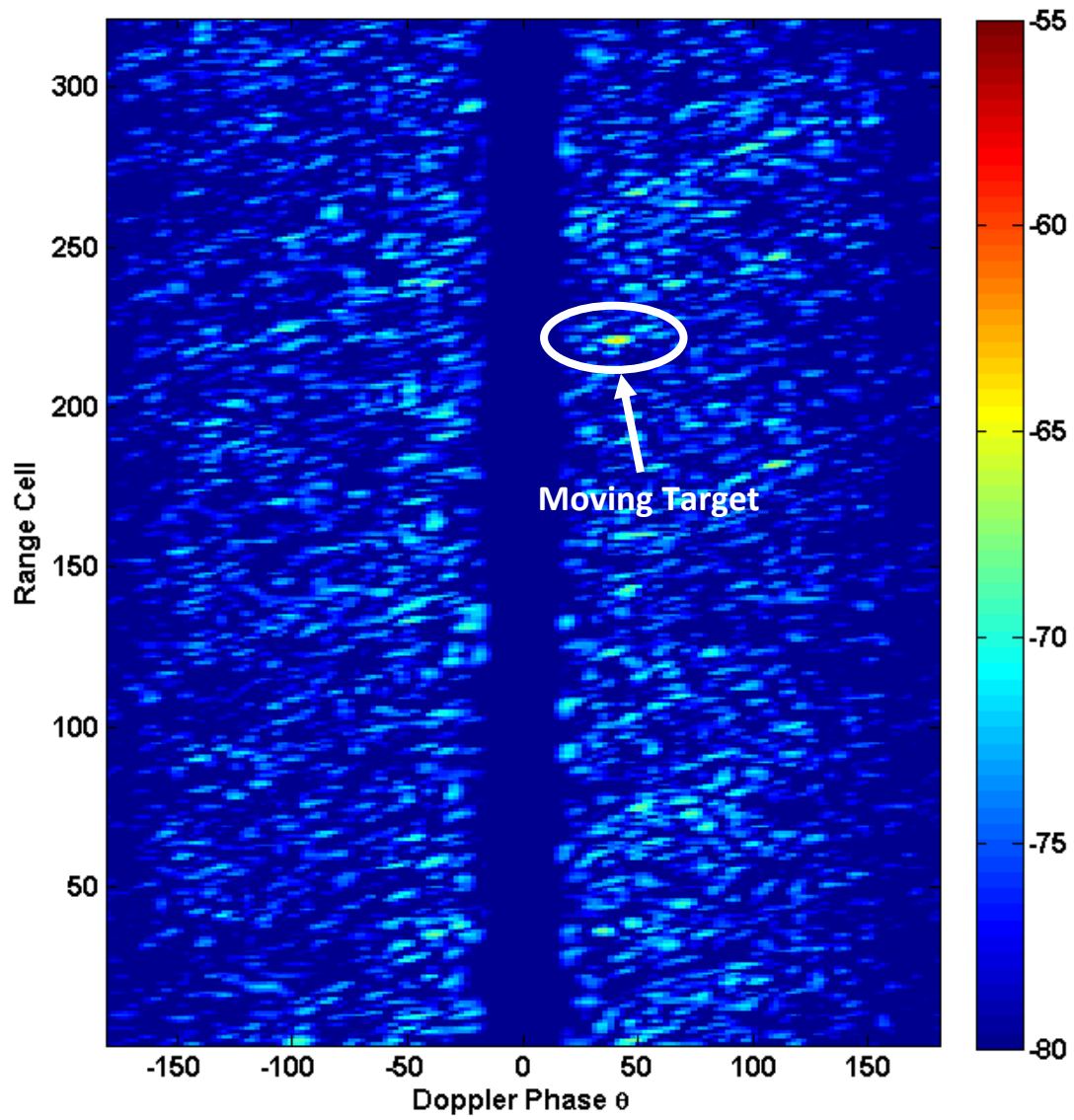


**Figure 6.9** NIMPC estimate (in dB) with clutter cancellation for the second range interval when the random phase code is used

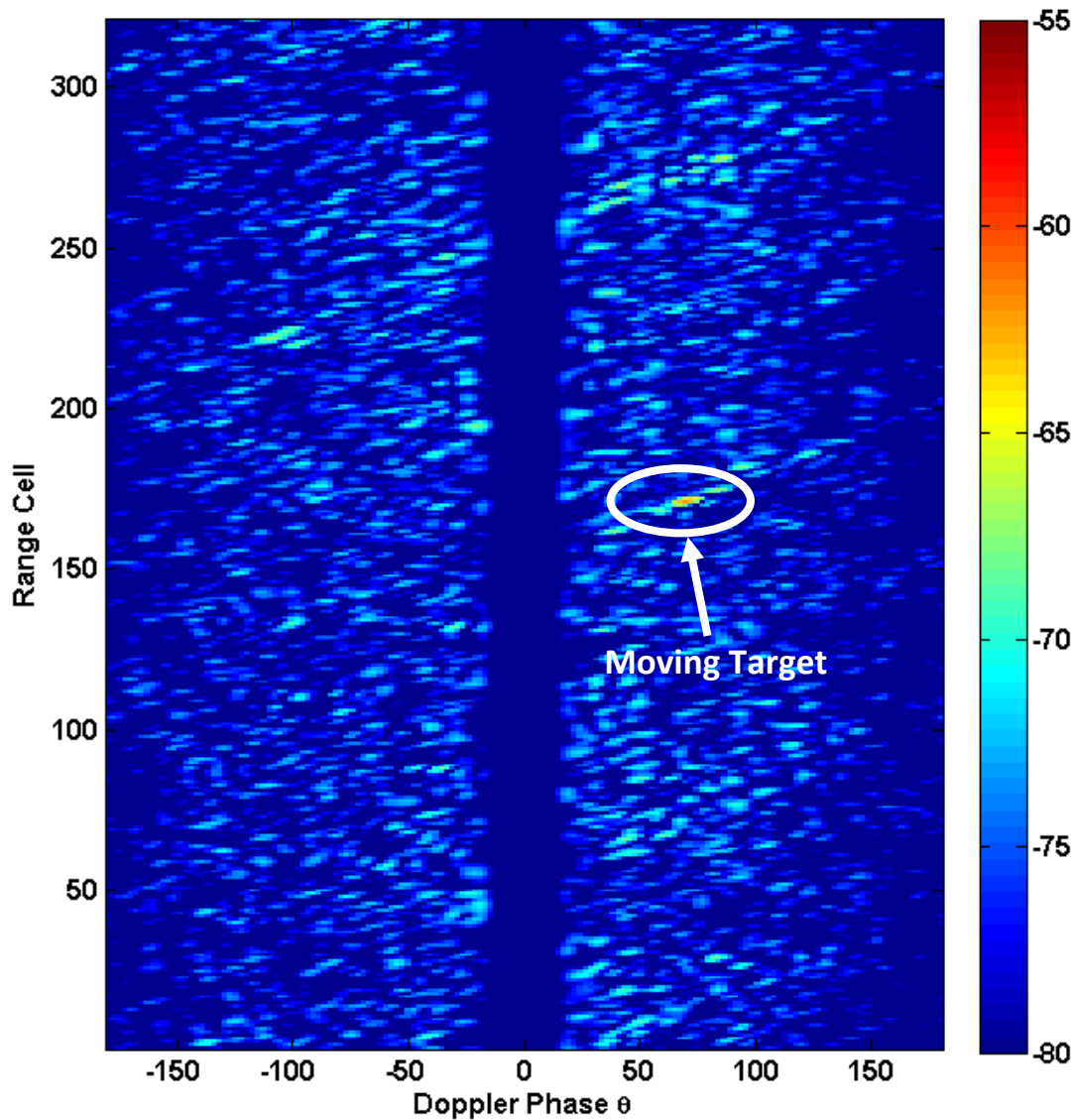


**Figure 6.10** NIMPC estimate (in dB) with clutter cancellation for the third range interval when the random phase code is used

The clutter notch in this case is much narrower as evidenced in the range-Doppler maps (Figs. 6.8-6.10). However, the clutter suppression performance is slightly degraded when compared to the P3 (see Fig. 6.11) and the loss indicated by the NIMPC filter response (Fig. 6.12) has worsened, especially as the magnitude of the Doppler phase increases.

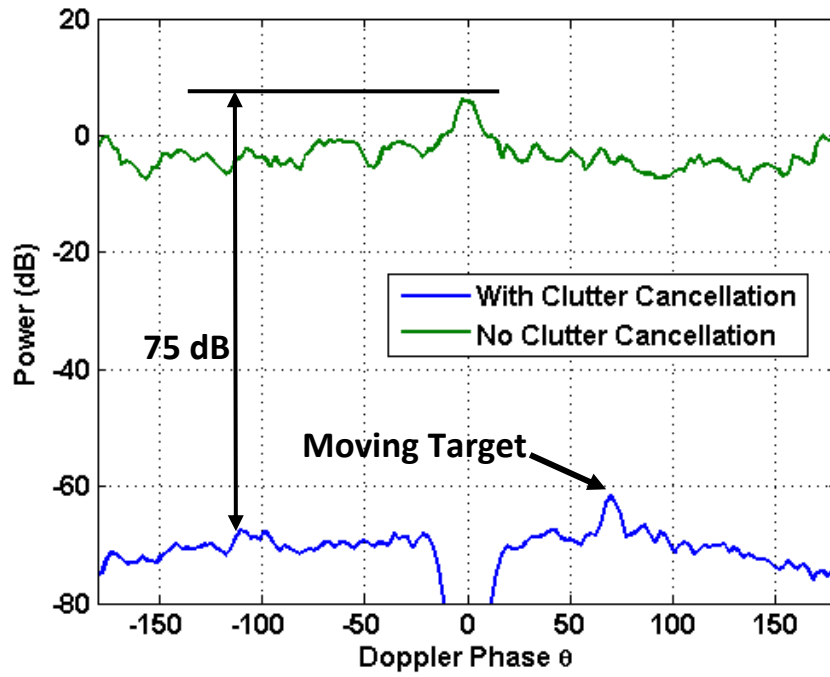


**Figure 6.11** Doppler view of NIMPC estimate with and without clutter cancellation for the third interval when the random phase code is used

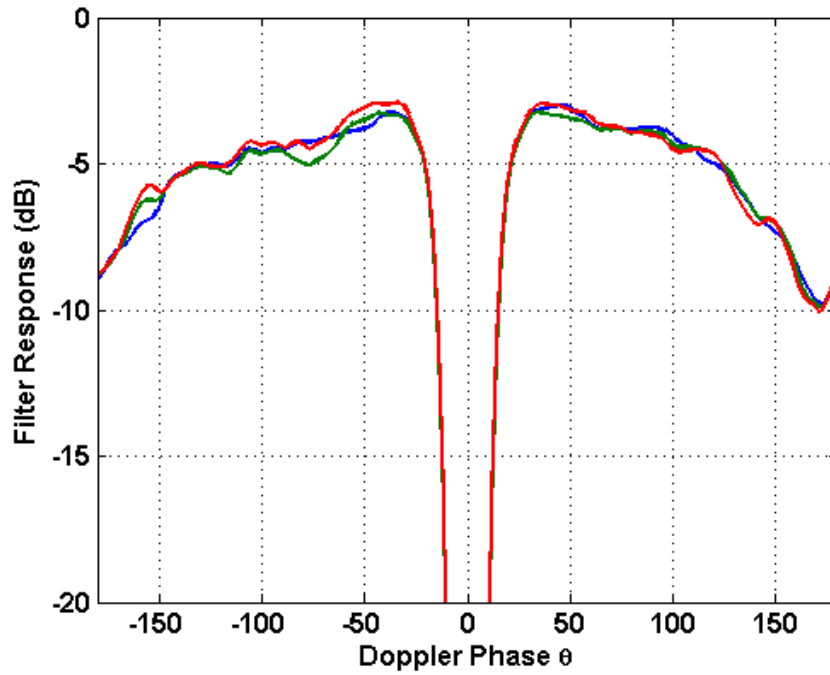


**Figure 6.12** NIMPC filter response for the first (red), second (green), and third (blue) intervals when the random phase code is used

Both of the waveforms discussed above has desirable properties; the chirp-like P3 code yields lower range sidelobe levels and the random phase code results in a narrower Doppler clutter notch. The choice of waveform should be determined by the goal and requirements of a particular radar system. In the next section, the effect of changing the phase coding of the radar waveform on a pulse-to-pulse basis will be examined.

### 6.2.2 PULSE AGILE SCENARIO

As in the previous case, this scenario will consider moving targets in the presence of ground clutter. However, each transmitted pulse is modulated by a unique random polyphase code (with a fixed center frequency). Each waveform contains 32 chips and the CPI consists of 150 pulses (155 pulses are transmitted). Six range intervals are simulated, each of which contains clutter in all range cells as well as the eclipsed regions. The clutter spread factor is  $\sigma_\theta = 2^\circ$  and the average clutter to noise power is 33 dB before processing. There are two moving targets in each interval with a SNR of  $-17$  dB (before a range and Doppler matched filter processing gain of 37 dB). Table 6.2 lists the target range and velocities for each interval (range cell indices are relative to each range interval).

**Table 6.2** Target Description for Pulse Agile Scenario

Range Interval	Range Cell $\ell$ for Target 1	Doppler Phase $\theta$ for Target 1	Range Cell $\ell$ for Target 2	Doppler Phase $\theta$ for Target 2
0	111	$20^\circ$	221	$-20^\circ$
1	116	$80^\circ$	216	$-80^\circ$
2	121	$-40^\circ$	211	$30^\circ$
3	126	$20^\circ$	206	$-30^\circ$
4	131	$-70^\circ$	201	$75^\circ$
5	136	$70^\circ$	196	$-75^\circ$

The NIMPC estimate without clutter cancellation is displayed in Fig. 6.13; the detrimental effects of range sidelobe modulation when ground clutter is present are evident. When clutter cancellation is employed the moving targets (denoted by white circles) are uncovered (Figs. 6.14-6.19) for all six intervals. The clutter is suppressed to near the noise floor in this case, however the SNR loss relative to the matched filter (in a clutter-free environment) is approximately 8 dB according to the NIMPC filter response in Fig. 6.20. This mismatch loss is expected due to the challenging nature of suppressing range ambiguous clutter from multiple intervals when pulse agile waveforms are employed. In each pulse of received data the target returns from different range intervals will consist of different waveforms. Consider the first pulse of received data (recorded immediately after transmission of the sixth pulse), in which target returns from the first interval are delayed and attenuated versions of the sixth transmitted pulse whereas returns from the second interval will be composed of versions of the fifth transmitted pulse due to the round trip time it takes to travel the distance to the second interval and back to the receiver. Hence, when the received data is processed with the pulse train corresponding to a particular interval, targets from other intervals will appear as the cross correlation between the waveform used to process each received pulse and the waveforms associated with returns from each of the other intervals. Only the targets present in each interval are visible due to the low cross correlation (relative to the target SNR) between the random phase codes modulated on each pulse resulting in an unambiguous range estimate (as evidenced by Figs. 6.14-6.19), a distinct benefit of this transmission strategy.

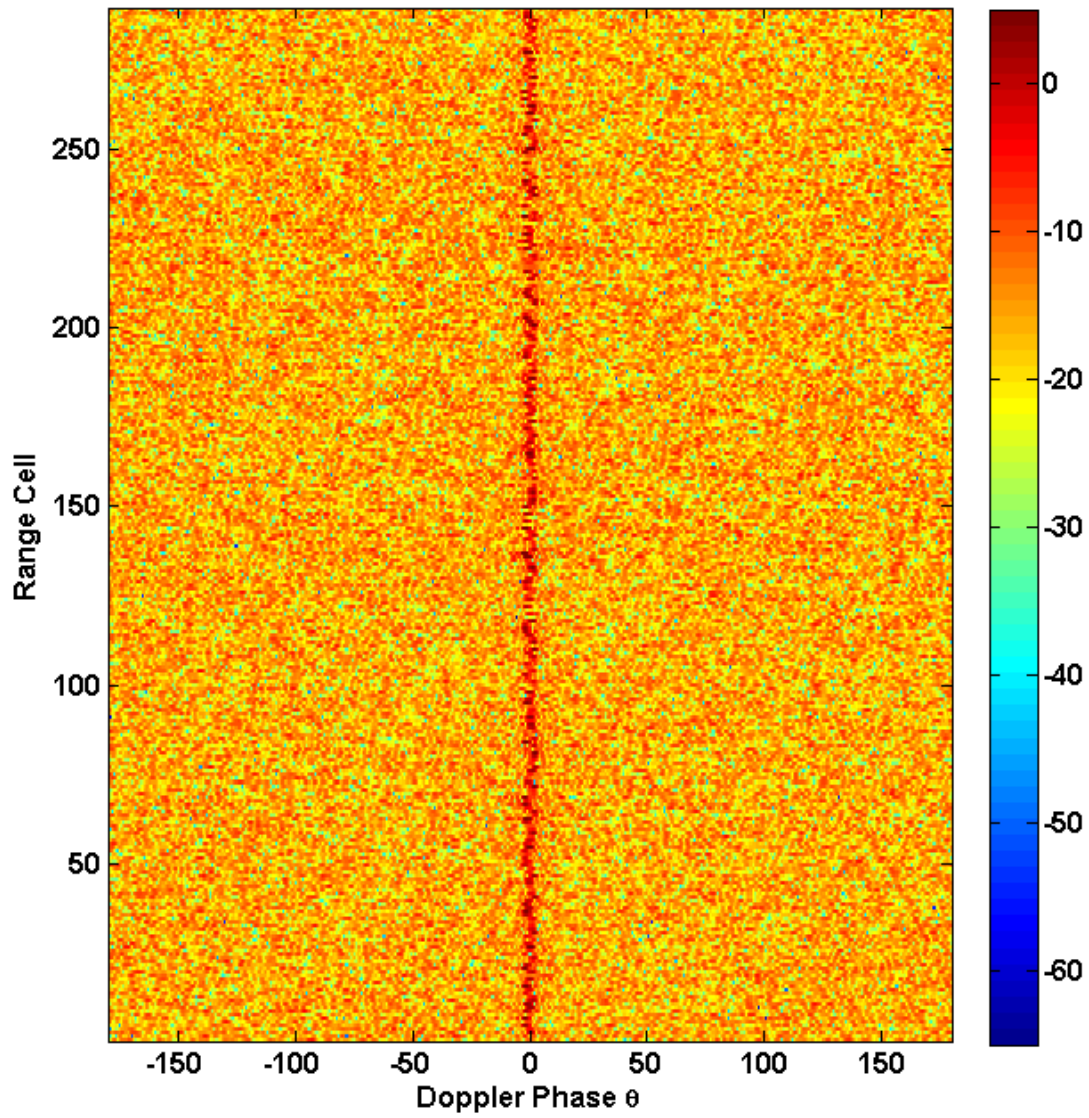


**Figure 6.13** NIMPC estimate (in dB) without clutter cancellation for the first range interval when a different random phase codes is transmitted on each pulse

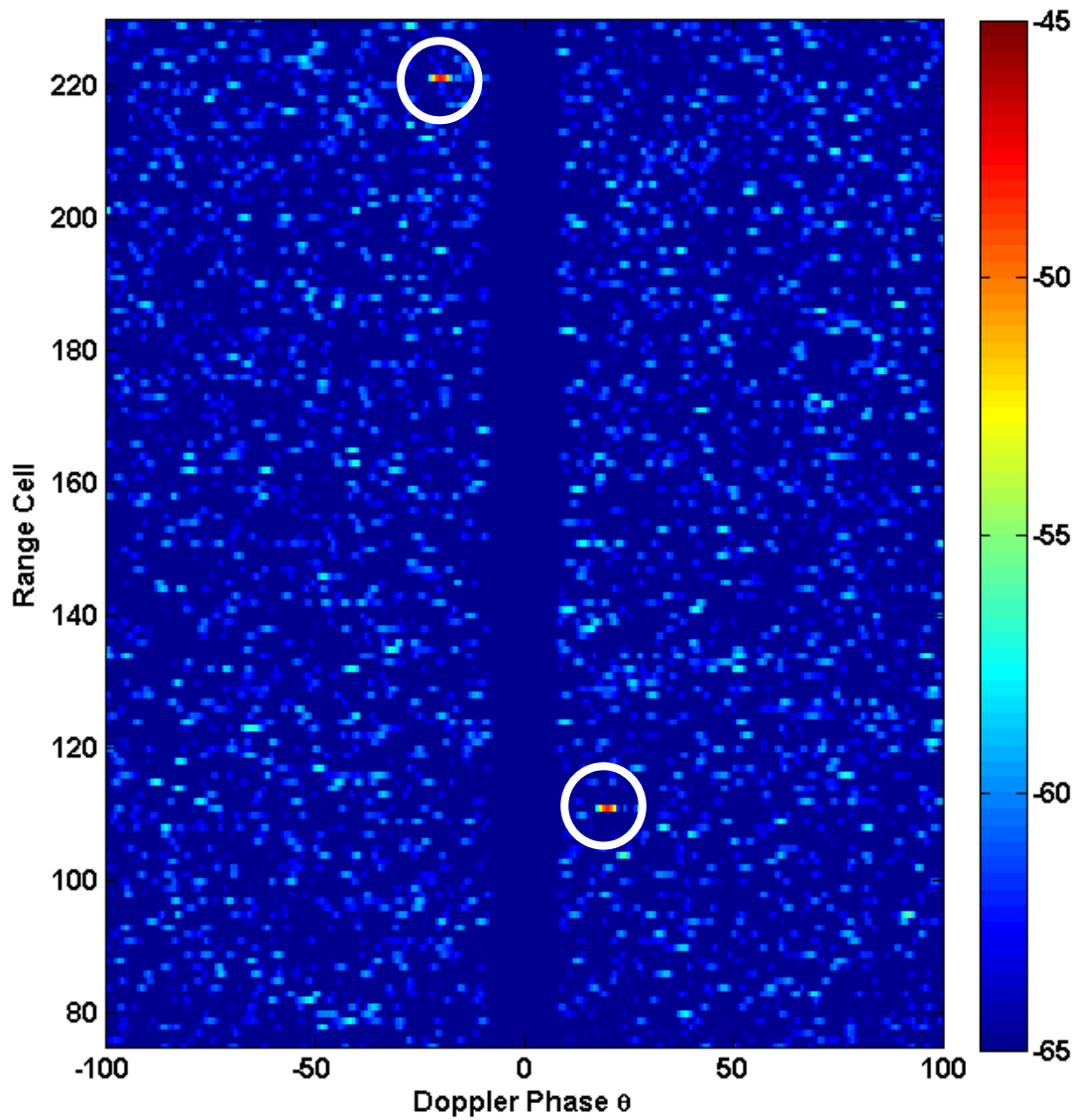


**Figure 6.14** NIMPC estimate (in dB) with clutter cancellation for the first range interval when a different random phase code is transmitted on each pulse

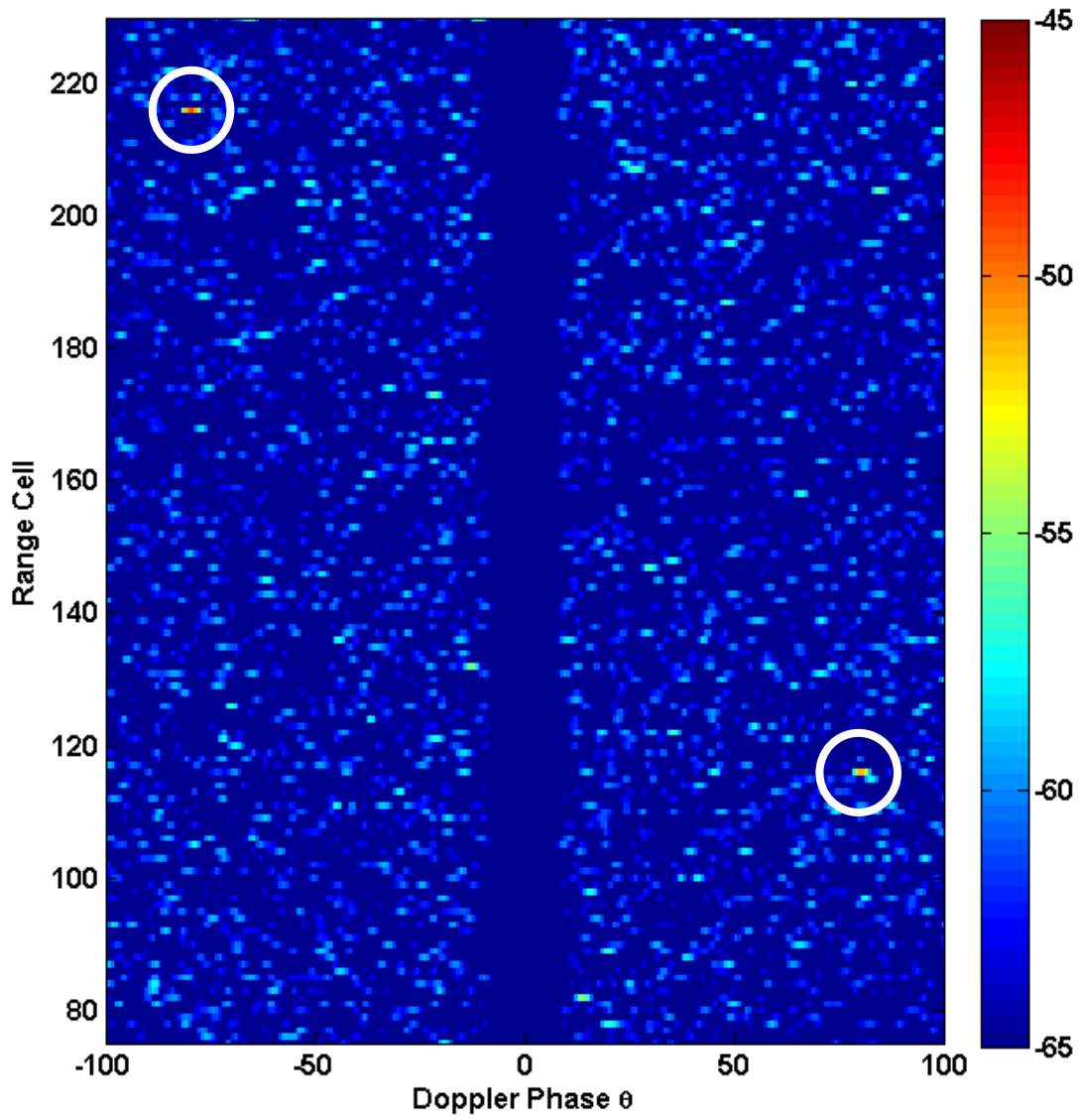


**Figure 6.15** NIMPC estimate (in dB) with clutter cancellation for the second range interval when a different random phase code is transmitted on each pulse

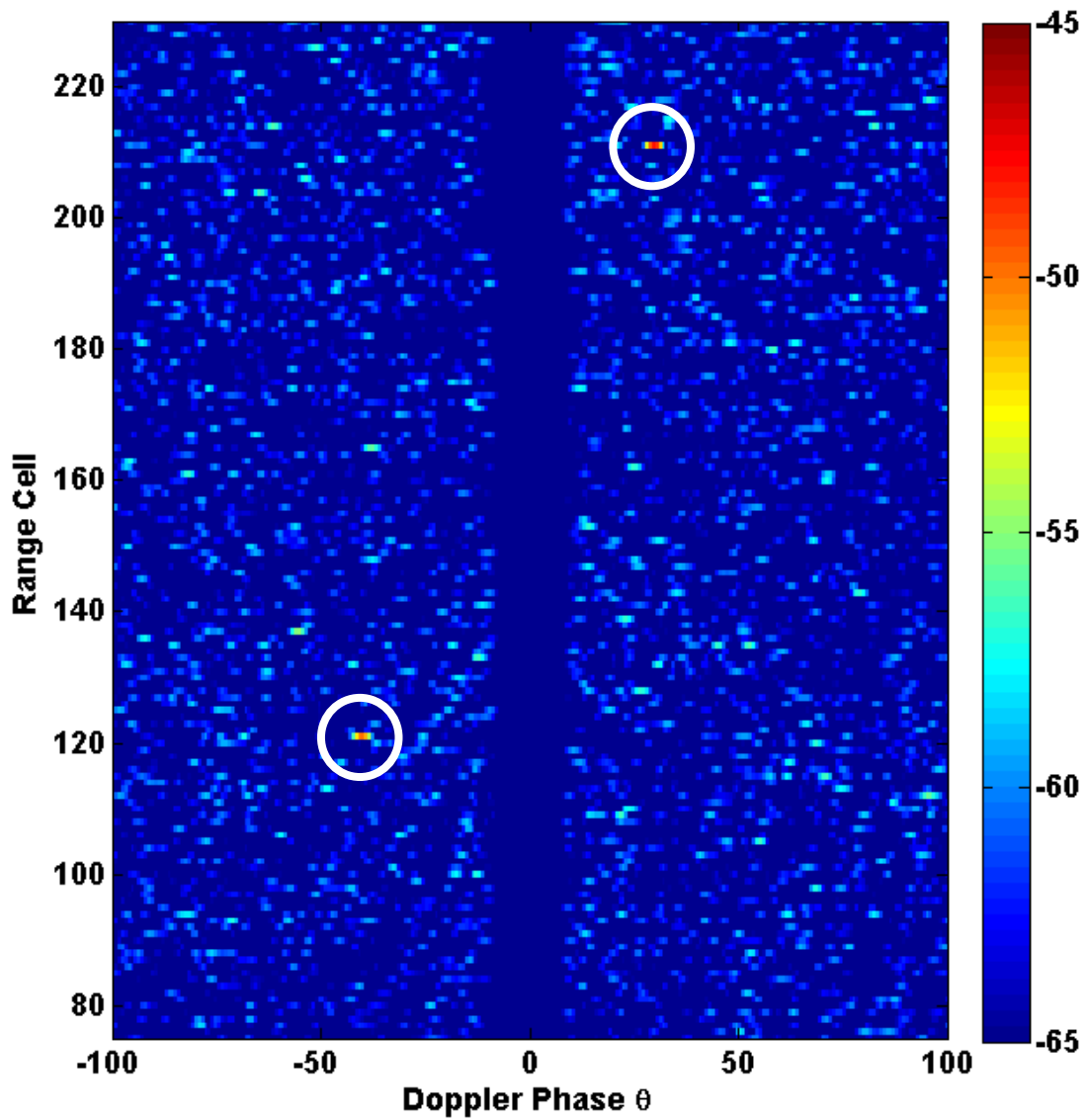


**Figure 6.16** NIMPC estimate (in dB) with clutter cancellation for the third range interval when a different random phase code is transmitted on each pulse

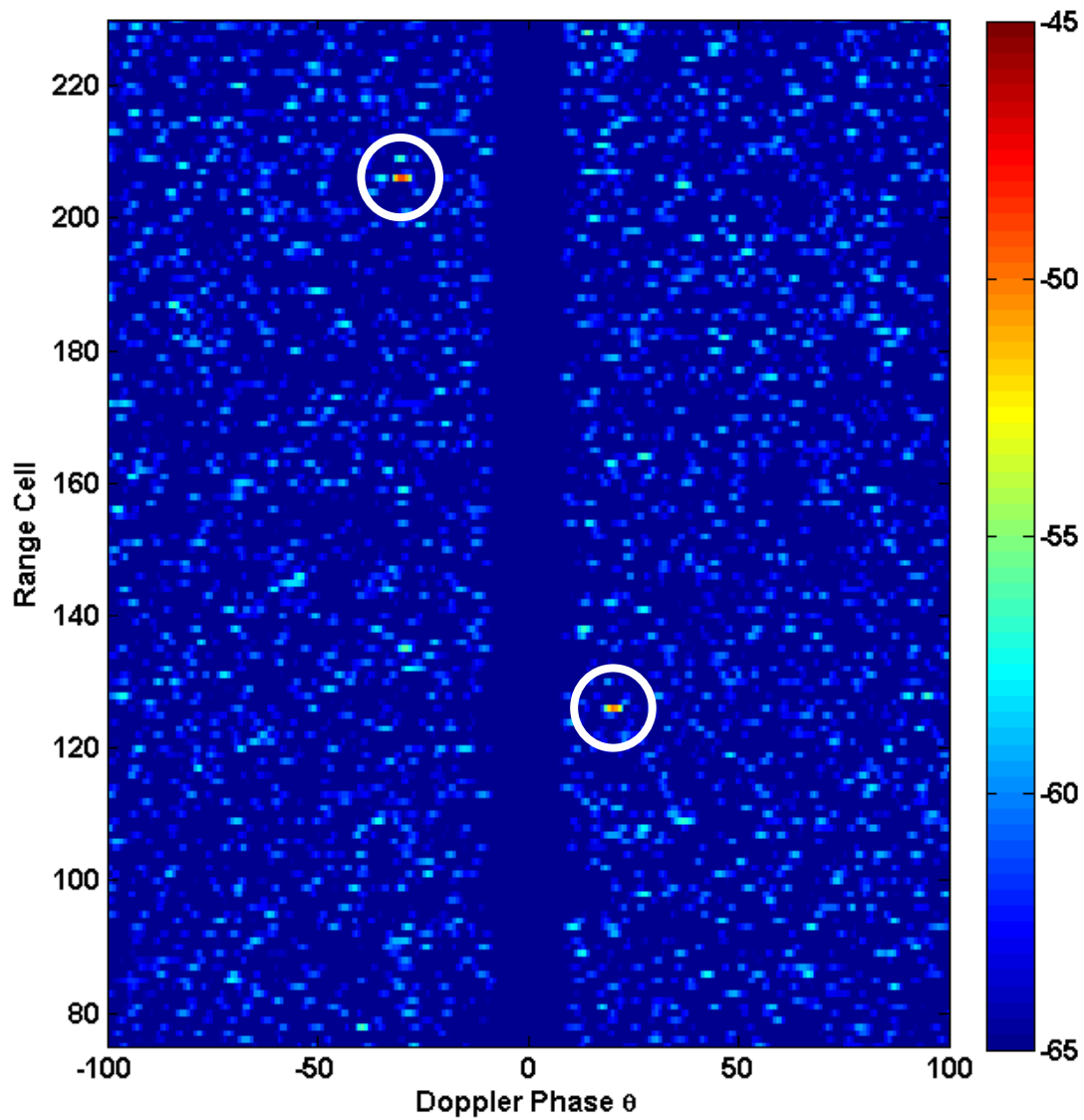


**Figure 6.17** NIMPC estimate (in dB) with clutter cancellation for the fourth range interval when a different random phase code is transmitted on each pulse

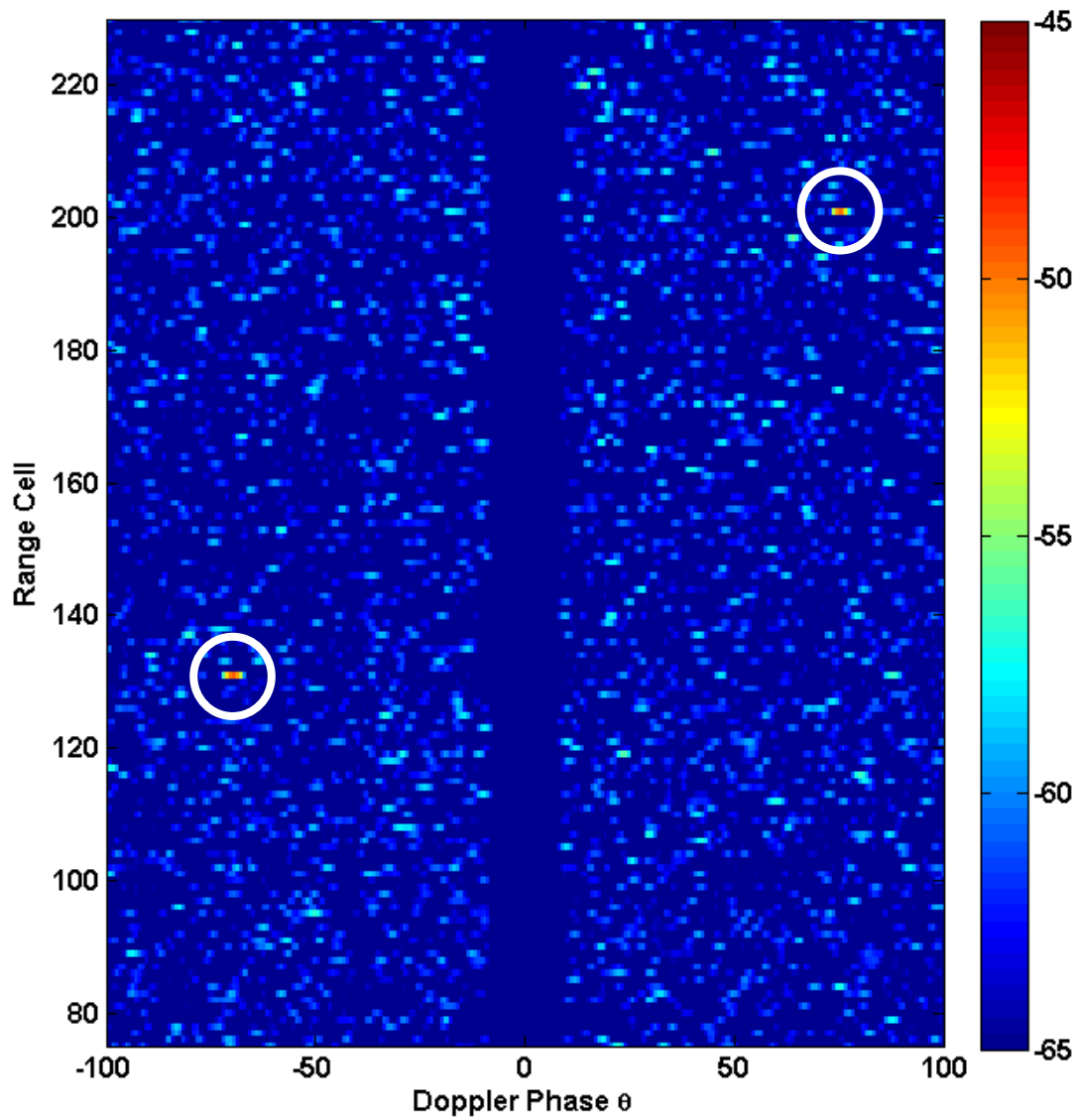


**Figure 6.18** NIMPC estimate (in dB) with clutter cancellation for the fifth range interval when a different random phase code is transmitted on each pulse

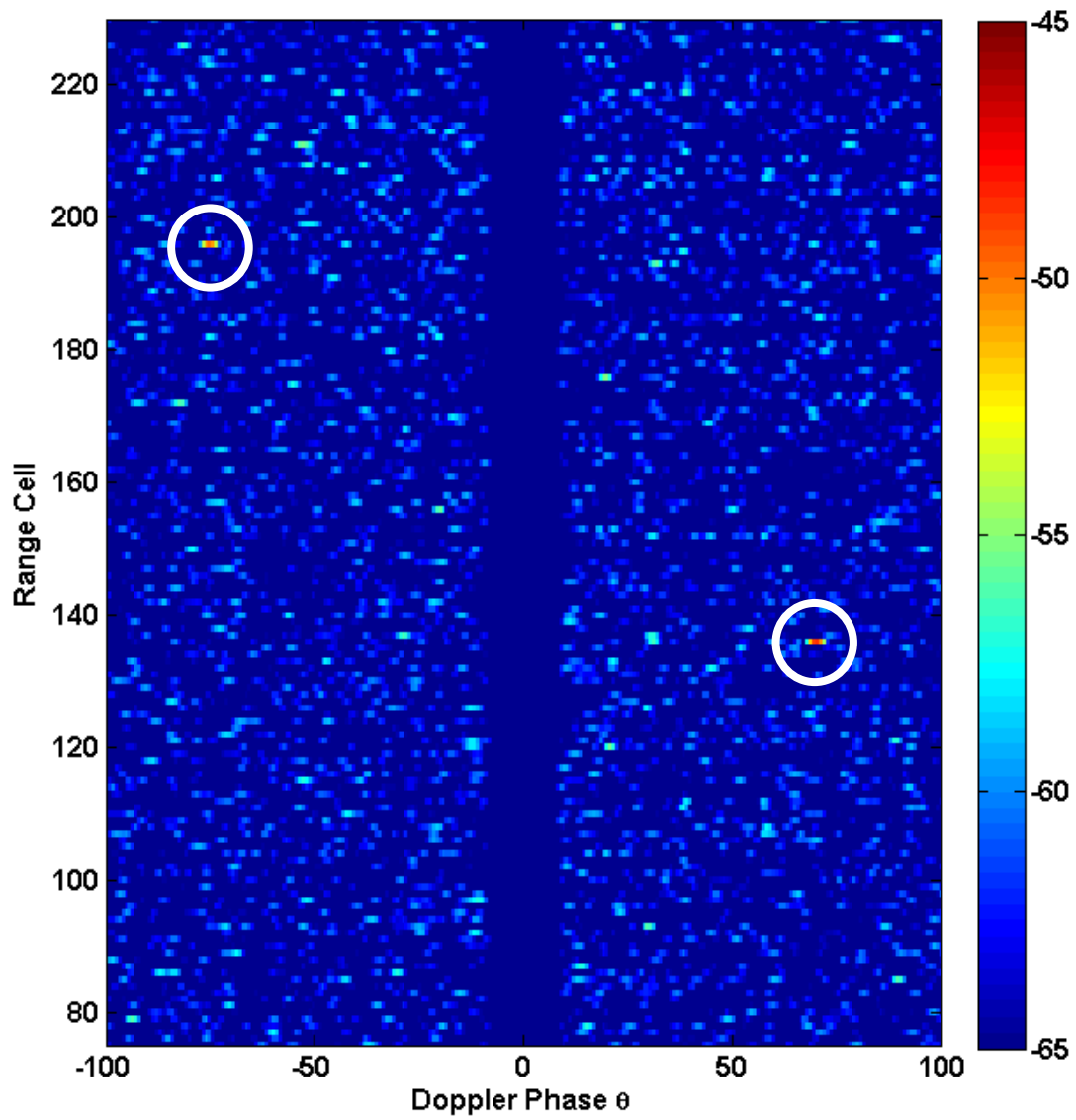


**Figure 6.19** NIMPC estimate (in dB) with clutter cancellation for the sixth range interval when a different random phase code is transmitted on each pulse

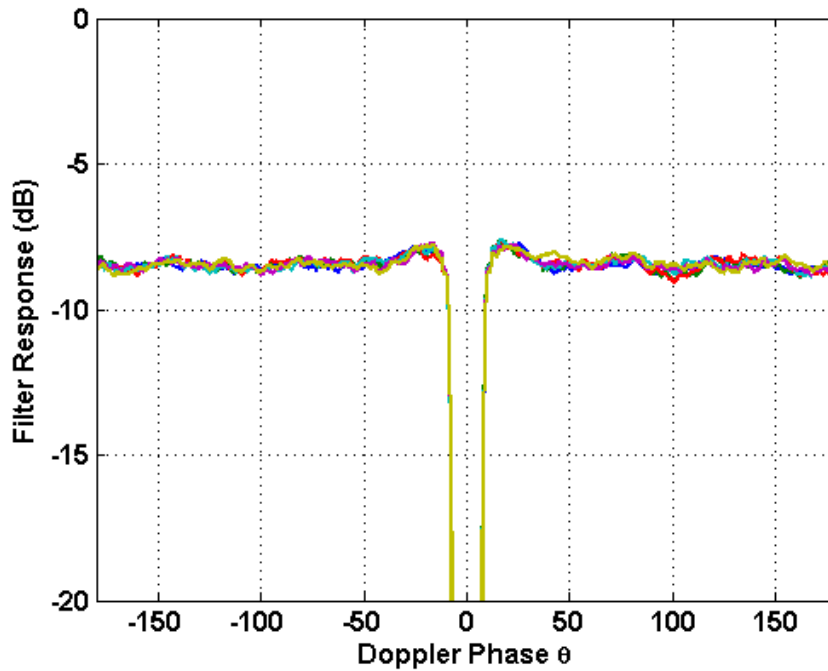


**Figure 6.20** NIMPC filter response when a different random phase code is transmitted on each pulse

### 6.3 CONCLUSION

A new non-adaptive framework, entitled Non-Identical Multiple Pulse Compression (NIMPC), is presented that allows clutter cancellation to be performed for scenarios when the radar waveforms within a CPI change from pulse to pulse. A novel implementation is provided that enables a real-time realization of the NIMPC algorithm via fast convolution techniques. Simulation results for synthetic wideband waveforms in range ambiguous scenarios with multiple-time-around clutter (MTAC) are presented. The effects of Doppler tolerance on MTAC for synthetic wideband waveforms are investigated and it is determined that range-ambiguous clutter from Doppler-tolerant synthetic wideband waveforms induces an artificial clutter-Doppler spread, which can be cancelled using NIMPC but may result in an undesired suppression of slow

moving targets. When a Doppler intolerant waveform is used in the synthetic wideband regime, the artificial clutter-Doppler spread is alleviated and the minimum discernable velocity can be improved. Additionally, NIMPC is shown via simulation to be capable of suppressing multiple intervals of clutter when pulse agile emissions are employed.

## CHAPTER 7      CONCLUSIONS

Advances in electronics technology will allow future generations of radar systems to employ enhanced flexibility and rapid reconfiguration of the waveforms transmitted on each element of an array or pulse within a coherent processing interval (CPI). The benefits of waveform diversity come at a significant cost in sensitivity for radar systems with a modest time-bandwidth product. Multi-dimensional signal models are proposed and utilized to develop coupled-domain signal processing approaches that offer a greater number of degrees of freedom compared to independent adaptation.

Waveform diversity across the elements of an antenna array facilitates broadening of the transmit beam pattern to investigate large angular regions within a single CPI. A technique is presented in Chapter 3 that allows a set of waveforms to be combined and transmitted to a corresponding set of particular spatial angles within a single pulse. The space-range ambiguity diagram in (3.14) is used to illustrate the resulting matched filter performance for this transmission strategy. In Chapter 4, a new reiterative minimum mean squared error (RMMSE) based algorithm entitled Space-Range Adaptive Processing (SRAP) is proposed that is capable of simultaneously adapting in space and range to produce a unique receive filter for each angle-range cell. The increased computational complexity inherent to multi-dimensional adaptivity is alleviated through the development of a reduced-dimensionality version of SRAP (RD-SRAP). Filter responses for independent adaptation and joint adaptation are conceived and used to assess the multi-dimensional framework. SRAP and RD-SRAP are shown to exhibit improved performance relative to both matched filtering and sequentially adapting in angle and range.

In Chapter 5, the multi-dimensional framework is augmented to incorporate waveform diversity in a pulse-Doppler regime, i.e., pulse-to-pulse waveform changes. This genre of waveform diversity offers benefits such as unambiguous ranging and enhanced range resolution. The RMMSE framework is again employed yielding the Time-Range Adaptive Processing (TRAP) algorithm. Akin to the the spatial variant, TRAP is capable of simultaneous adaptation in slow-time (Doppler) and range to enhance sensitivity by suppressing Doppler and range sidelobes of large targets. Furthermore, TRAP is extended to estimate into the eclipsed regions associated with high-power radar systems that use blanking to safeguard the receiver. The performance of TRAP and a reduced dimensionality variant are assessed via simulations utilizing synthetic wideband waveforms and pulse-to-pulse coding changes. TRAP is able to suppress both Doppler and range sidelobes of targets, even when they are eclipsed.

Waveform diversity in pulse-Doppler radars results in complex clutter returns, which cannot be suppressed using traditional clutter cancellation techniques. In Chapter 6, the TRAP signal model is utilized to develop a non-adaptive pulse agile clutter cancellation algorithm, namely Non-Identical Multiple Pulse Compression (NIMPC). The NIMPC clutter suppression filters can be pre-computed offline and applied efficiently using fast-Fourier transforms, due to the non-adaptive nature of the algorithm. Simulations indicate the ability of NIMPC to suppress multiple range intervals of clutter when pulse-to-pulse waveform changes are employed.

## REFERENCES

- [1] M. Skolnik, *Radar Handbook 3<sup>rd</sup> Edition*, New York, NY: McGraw-Hill, 2008.
- [2] Kingsley, S. and Quegan, *Understanding Radar Systems*. Raleigh, NC: SciTech, 1992.
- [3] R.H. Barker, "Group Synchronizing of Binary Digital Sequences," in *Communication Theory*, W. Jackson, Ed., London, England: Butterworths, 1953, pp. 273-287.
- [4] Nathanson, F. E. *Radar Design Principles 2<sup>nd</sup> Edition*, New York, NY : McGraw-Hill, 1991.
- [5] J.P. Costas, "A Study of a Class of Detection Waveforms Having Nearly Ideal Range-Doppler Ambiguity Properties," *Proc. of the IEEE*, vol. 72, pp. 996-1009, August 1984.
- [6] F.L. Frank, "Polyphase Codes with Good Non-Periodic Correlation Properties," *IEEE Trans.*, vol. IT-9, pp. 43-35, January 1963.
- [7] N. Levanon, *Radar Principles*, John Wiley and Sons Inc., 1988.
- [8] B.L. Lewis and F.F. Kretschmer, "Linear Frequency Modulation Derived Polyphase Pulse Compression Codes," *IEEE Trans. Aerospace and Electronic Systems*, vol. 18, pp. 637-641, September 1982.
- [9] C. Balanis, *Antenna Theory: Analysis and Design 2<sup>nd</sup> Edition*, John Wiley and Sons, Inc., 1997.
- [10] P. Stoica, J. Li, and Y. Xie, "On Probing Signal Design for MIMO Radar," *IEEE Trans. Signal Processing*, vol. 55, pp. 4151-4161, January 2008.
- [11] D. Fuhrmann, J.P. Browning, and M. Rangaswamy, "Constant-Modulus Partially Correlated Signal Design for Uniform Linear and Rectangular MIMO Radar Arrays," *Int. Waveform Diversity and Design Conference*, Orlando, FL, February, 2009.
- [12] D. Fuhrman, and G. San Antonio, "Transmit Beamforming for MIMO Radar Systems using Signal Cross Correlations," *IEEE Trans. Aerospace and Electronic Systems*, vol. 44, pp. 171-186, January 2008.
- [13] S.D. Blunt and K. Gerlach, "Adaptive Pulse Compression via MMSE estimation," *IEEE Trans. Aerospace and Electronic Systems*, vol. 42, no. 2, pp. 572-584, April 2006.

- [14] T. Felhauer, "Digital Signal Processing for Optimum Wideband Channel Estimation in the Presence of Noise," *IEE Proceedings-F*, vol. 140, pp. 179-186, June 1993.
- [15] M.H. Ackroyd and F. Ghani, "Optimum Mismatched Filter for Sidelobe Suppression," *IEEE Trans. Aerospace and Electronic Systems*, vol. 9, pp. 214-218, March 1973.
- [16] R.C. Daniels, and V. Gregers-Hansen, "Code Inverse Filtering for Complete Sidelobe Removal in Binary Phase Coded Pulse Compression," *Proc. IEEE Int. Radar Conference*, Washington, DC, May 2005.
- [17] J. Ward, "Space-Time Adaptive Processing for Airborne Radar," Lincoln Laboratory Technical Report 1015, December 1994.
- [18] W. Roberts, J. Li, P. Stoica, and X. Zhu, "MIMO Radar Receiver Design," *Int. Waveform Diversity and Design Conference*, Orlando, FL, February, 2009.
- [19] W. Roberts, T. Yardibi, J. Li, X. Tan, and P. Stoica, "Sparse Signal Representation for MIMO Radar Imaging," *42<sup>nd</sup> Asilomar Conference on Signals Systems and Computers*, Pacific Grove, CA, October 2008.
- [20] W. Roberts, J. Li, P. Stoica, T. Yardibi, and F.A. Sajadi, "MIMO Radar Angle-Range-Doppler Imaging," *Proc. IEEE Radar Conference*, Pasadena, CA, May, 2009.
- [21] S.D. Blunt, T. Chan, and K. Gerlach, "A New Framework for Direction of Arrival Estimation," *IEEE Sensor Array and Multichannel Signal Processing Workshop*, pp. 81-85, Darmstadt, Germany, July 21-23, 2008.
- [22] S.D. Blunt, T. Higgins, and K. Gerlach, "Dimensionality Reduction Techniques for Efficient Adaptive Pulse Compression," *IEEE Trans. Aerospace and Electronic Systems*, vol. 46, no. 1, pp. 349-362.
- [23] S. Haykin, *Adaptive Filter Theory*, Prentice Hall, 2002.
- [24] P. Antonik, M.C. Wicks, H.D. Griffiths, and C. J. Baker, "Range-Dependent Beamforming using Element Level Waveform Diversity," *Int. Waveform Diversity and Design Conference*, Lihue, HI, January, 2006.
- [25] P. Antonik, M.C. Wicks, H.D. Griffiths, and C. J. Baker, "Multi-Mission Multi-Mode Waveform Diversity," *Proc. IEEE Radar Conference*, Verona, NY, April, 2006.
- [26] M. Secmen, S. Demir, A. Hizal, and, T. Eker, "Frequency Diverse Array Antenna with Periodic Time Modulated Pattern in Range and Angle," *Proc. IEEE Radar Conference*, Waltham, MA, April, 2007.

- [27] P. Baizert, T.B. Hale, M.A. Temple, and M.C. Wicks, "Forward-Looking Radar GMTI benefits using a Linear Frequency Diverse Array," *IEE Electronics Letters*, vol. 42, pp. 1311-1312, October 2006.
- [28] S.D. Blunt and K. Gerlach, "Multistatic Adaptive Pulse Compression," *IEEE Trans. Aerospace and Electronic Systems*, vol. 42, no. 3, pp. 891-903, July 2006.
- [29] T.K. Moon and W.C. Stirling, *Mathematical Methods and Algorithms for Signal Processing*, Prentice Hall, 2000.
- [30] F. Lin and M. Steiner, "New Techniques for Radar Coherent Range Ambiguity Resolution," *Proc. IEEE Radar Conference*, Atlanta, GA, May, 2001.
- [31] S.D. Blunt, M.R. Cook, and J. Stiles, "Embedding Information into Radar Emissions via Waveform Implementation," *Int. Waveform Diversity and Design Conference*, Niagara Falls, Canada, 2010.
- [32] D.R. Wehner, *High Resolution Radar*, Norwood: Artech House, 1987.
- [33] A.F. Culmone, "Properties of Uniform Coherent Frequency-Jump Waveforms," MIT Lincoln Lab Technical Report, April 1973.
- [34] S.D. Blunt, K. Gerlach, and T. Higgins, "Aspects of Radar Range Super-Resolution," *Proc. IEEE Radar Conference*, Waltham, MA, April, 2007.
- [35] S.D. Blunt, K. Gerlach, and E.L. Mokole, "Pulse compression eclipsing repair," *Proc. IEEE Radar Conference*, Rome, Italy, May 2008.
- [36] J. D. Jenshak and J.M. Stiles, "A fast method for designing optimal transmit codes for radar," *Proc. IEEE Radar Conference*, Rome, Italy, May, 2008.
- [37] J.D. Jenshak and J.M. Stiles, "Transmit coding with a range ambiguity," *Int. Waveform Diversity and Design Conference*, Orlando, FL, February, 2009.
- [38] D.P. Scholnik, "Range-ambiguous clutter suppression with pulse diverse waveforms," *Proc. IEEE Radar Conference*, Kansas City, MO, May 2011.